

Dielectrophoresis - Utilising a novel electrode geometry

Josh Parker

A thesis submitted in partial fulfilment for the degree of
Doctor of Philosophy

Director of Studies: Carl Brown

Department of Physics and Mathematics

School of Science and Technology

Nottingham Trent University

January 2024

The copyright in this work is held by the author. You may copy up to 5% of this work for private study, or personal, non-commercial research. Any re-use of the information contained within this document should be fully referenced, quoting the author, title, university, degree level and pagination. Queries or requests for any other use, or if a more substantial copy is required, should be directed to the author.

Abstract

In this thesis, the phenomenon of dielectrophoresis (DEP) is explored by utilising a novel MOS capacitor-style geometry. Photolithography was used to pattern metal electrodes onto the polished surface of a doped p-type silicon wafer, which already had a 1-micron thick oxide layer thermally grown onto its surface. Due to the nature of the geometry only having one patterned electrode surface, it allowed for more complex patterns to be etched into the metal electrode than typical coplanar interdigitated electrodes (IDEs). An AC voltage was applied between the top metal electrode and the p-type silicon underside of the wafer, with the oxide layer forming an electrically insulating layer in the middle, therefore producing a MOS capacitor-type structure. By applying this voltage, highly localised non-uniform electric fields were produced along the edges of the top metal electrodes which were utilised to perform a variety of dielectrowetting and particle dielectrophoresis experiments.

Uni-directional dielectrowetting was achieved by etching long thin rectangular stripes into the metal electrode. A relationship of $\cos(\theta)$ vs V^2 was discovered for the contact angle vs voltage measurements. Axi-symmetric dielectrowetting was demonstrated in which the droplet of liquid mirrored the underlying patterns etched into the electrode as it spread, allowing the formation of hexagonal and square-shaped droplets before eventually spreading into a uniform thin film at larger voltages. Thin threads of liquid could be extracted from a parent droplet along the edge of the metal electrode. These threads were observed to follow a Lucas-Washburn type behaviour, as well as length, width and volume voltage dependence. The ability of the geometry to perform particle DEP was observed by placing a droplet suspension of polymer microspheres onto the top surface with a variety of striped and circular array patterns in the underlying electrode. In these experiments, the particles would arrange themselves depending on the voltage and frequency. The formation and evaporation of thousands of sub-picolitre microdroplets was also studied using this geometry. The microdroplets were observed to undergo diffusive evaporation and this was compared to Masoud's theory of the evaporation of multiple droplets with some numerical simulations.

Declaration

The experiments described in this thesis were carried out by myself and, where indicated, in collaboration with colleagues. The data analysis and interpretation is my own work. This thesis has been written entirely by myself.

Josh Parker

Acknowledgements

First and foremost, I would like to say a special thank you to my director of studies, Professor Carl Brown, for his consistent guidance and support throughout my studies. Carl was always willing to have a chat about both the research and any other issues I may have had, and always helped me achieve the most from my work. Carl is truly an expert in the many fields of research that he is involved in and having someone so knowledgeable as a supervisor was a huge help for my PhD. I'd like to thank my co-supervisor Dr Nikolaos Kalfagiannis and internal assessor Dr Demosthenes Koutsogeorgis for their expertise in semiconductor physics and photolithography, as well as their valuable advice and assistance throughout. Thank you to Dr Ian Sage, without whom this PhD would not have been a thing to begin with. It was Ian who had the brilliant idea of using the fringe field MOS capacitor geometry to perform dielectrophoresis, of which this entire PhD is based. Ian then continued to give fantastic guidance throughout. I'd also like to say a big thank you to Dr Andrew Edwards for getting me started with the project. It was Andy who showed me how to use all the equipment and software in the lab as well as how to make the devices using photolithography in the cleanroom. Thank you to all the technicians for sorting me out whenever I needed anything fixing or practical making. A huge thanks to Dr Akhshay Bhadwal and Joey Kilbride for providing me with great support both in and outside the lab, as well as being great friends that I share some fantastic memories with. I certainly wouldn't have been able to make it without having those two around to listen to me venting every now and again. Thank you to Dr David Fairhurst and Dr Fouzia Ouali for their informal group meetings to share our research ideas, as well as always being willing to have a friendly chat in the lab. Finally, I would like to say a massive thank you to my family and friends who have been so supportive throughout. They always believed in me and encouraged me at times when I needed it the most and I hope to make you all proud.

Contents

Abstract	2
Declaration.	3
Acknowledgements.	4
List of Figures	13
Nomenclature	21
1 Introduction	24
1.1 Overview of research	24
1.2 Structure of thesis	25
2 Fluids	28
2.1 Wetting	28
2.1.1 Molecular cohesion and surface tension	28
2.1.2 Surface free energy and adhesion	31
2.1.3 Surface wettability	31

2.1.4	Contact angle and Young's equation	33
2.2	Liquid Flow	34
2.2.1	Continuity equation	34
2.2.2	Navier–Stokes momentum equation	35
2.2.3	Conservation of energy	36
2.2.4	Viscosity and temperature dependence	36
2.2.5	The Reynolds number	38
2.2.6	Poiseuille flow	39
2.2.7	Washburn's equation	40
2.2.8	Planar Couette flow	41
2.2.9	Rivulet flow	42
2.3	Evaporation	43
2.3.1	Fundamentals of evaporation	43
2.3.2	Diffusion-limited evaporation	45
2.3.3	Evaporation of a single sessile droplet	45
2.3.4	Evaporation of multiple droplet arrays	49
3	Electric Fields	52
3.1	Fundamentals of electric fields	52

3.2	Parallel plate capacitor	54
3.3	Semiconductors	55
3.4	MOS Capacitors	56
3.5	Electric Double Layer	58
4	Electrohydrodynamics	60
4.1	Dielectrophoresis overview	60
4.2	Fundamentals of dielectrophoresis	60
4.3	Particle dielectrophoresis	64
4.3.1	Particle DEP of biological particles	64
4.3.2	Particle DEP of non-biological particles	64
4.3.3	Particle DEP in microelectrode geometries	65
4.3.4	Pearl Chains	66
4.4	Liquid dielectrophoresis and dielectrowetting	67
4.4.1	Early L-DEP geometries	68
4.4.2	Coplanar IDE geometries	69
4.5	Other Electrohydrodynamic effects	71
4.5.1	Electrophoresis	71
4.5.2	Electroosmosis	71

	4.5.3	Electrowetting	72
5		Device manufacturing and characterisation	74
	5.1	Device design	74
	5.1.1	General geometry of device	74
	5.1.2	C3A and C3B electrode patterns	76
	5.2	Device fabrication	77
	5.2.1	Silicon wafer cleaving	77
	5.2.2	Overview of photolithography process	78
	5.2.3	Cleaning	79
	5.2.4	Photoresist application	80
	5.2.5	Mask aligner	80
	5.2.6	Developing, sputter coating and metal lift-off	81
	5.2.7	Hydrophobic coating	81
	5.2.8	Soldering and wiring	82
	5.3	Device characterisation	82
	5.3.1	Change of wafer resistivity after 2 years	82
	5.3.2	Characterisation of 1-10 Ω .cm wafers	83
	5.3.3	Frequency related heating of 1-10 Ω .cm wafers	84

5.3.4	Characterisation of 0.1-1 Ω .cm wafers	85
6	Experimental methods	87
6.1	Experimental setup	87
6.1.1	Basic rig setup	87
6.1.2	Electrical setup, waveforms, frequencies, and voltages . . .	88
6.1.3	Making the polymer microsphere suspension	88
6.2	Image processing and data analysis	89
6.2.1	Contact angle measurements	89
6.2.2	Thread measurements	91
6.2.3	Particle analysis	92
6.2.4	Microdroplet measurements	93
7	Dielectrowetting	97
7.1	Uni-directional dielectrowetting	97
7.1.1	Experiment on striped electrodes using TMPTGE	99
7.1.2	Comparing results with microstrip capacitance theory . . .	104
7.1.3	Dielectrowetting frequency dependence	110
7.2	Axi-symmetric dielectrowetting	112
7.2.1	Initial issues with axi-symmetric spreading designs	113

7.2.2	Hexagonal axi-symmetric spreading	114
7.2.3	Other axi-symmetric spreading	117
8	Liquid threads	119
8.1	Formation of a thin liquid thread	119
8.2	Liquid thread statics	120
8.2.1	Thread length vs Voltage	120
8.2.2	Thread width vs Voltage	121
8.2.3	Thread volume vs Voltage	122
8.3	Liquid thread dynamics	123
8.3.1	Dynamic evolution of a non-volatile liquid thread	124
8.3.2	Controlled detwetting of non-volatile liquid threads	128
8.4	Liquid thread evaporation	131
8.4.1	Static length equilibrium of evaporating thread	132
8.4.2	Dynamic evolution of evaporating thread	135
8.5	Microdroplet spreading	137
9	Particle dielectrophoresis	140
9.1	Particle DEP along a single edge	140
9.1.1	Initial movement of particles	141

9.1.2	Particle chains at low frequencies	143
9.2	Particle DEP on striped geometry	143
9.2.1	40 micron wide stripes	144
9.2.2	20 micron wide stripes	148
9.3	Particle DEP on hexagonal array of circles	150
9.3.1	Large circles (C3A)	151
9.3.2	Small circles (C3B)	154
9.4	Particle DEP liquid film thickness dependence	156
10	Microdroplet arrays	162
10.1	Formation of microdroplet arrays	162
10.1.1	Creating a microdroplet array	162
10.1.2	Droplet size consistency across array	163
10.1.3	Droplet size consistency over multiple experiments	167
10.1.4	Large defects in microdroplet arrays	168
10.2	Evaporation of microdroplet arrays	169
10.2.1	C3A evaporation	170
10.2.2	C3B evaporation	173
11	Conclusions	176

11.1	Dielectrowetting conclusions	176
11.2	Liquid threads conclusions	177
11.3	Particle dielectrophoresis conclusions	178
11.4	Microdroplet array conclusions	180
12	Future work	181
12.1	Gradient wetting	181
12.2	Liquid threads	182
12.3	Particle DEP	184
12.4	Different sized microdroplet evaporation	184
	Bibliography	186

List of Figures

2.1	Molecular cohesion of water molecules via hydrogen bonding	29
2.2	Surface tension arises from the net inward force at the liquid/gas interface .	30
2.3	Influence of solid surface energy and liquid surface tension in wettability . .	32
2.4	Equilibrium contact angle of a sessile droplet on solid surface	33
2.5	Incompressible liquid flow in a narrowing pipe	35
2.6	Temperature dependence for the viscosity glycerol	38
2.7	Laminar flow in a pipe	39
2.8	Planar Couette flow between two plates	41
2.9	Rivulet flow velocity profile by solving the Navier-Stokes equation in Comsol	42
2.10	Graph showing molecular energy distribution in a liquid at two temperatures	44
2.11	Geometry for diffusive-limited evaporation of single sessile droplet	46
2.12	Modes of droplet evaporation	47
2.13	Radius and contact angle time dependence for CR and CA modes	48

2.14	Evaporation of multiple droplets in Masoud's model	50
3.1	Simple parallel plate capacitor geometry with two oppositely charged particles	53
3.2	P-type MOS capacitor structure	56
3.3	Accumulation, depletion and inversion of MOS capacitor	57
3.4	CV curve showing the three regimes at high and low frequencies	58
3.5	Electric Double Layer (EDL)	59
4.1	Dipole in a uniform electric field	61
4.2	Dipole in a non-uniform electric field	62
4.3	Beads trapped by DEP forces	66
4.4	Pearl chain formation of nanoparticles in microelectrode gaps by dielectrophoresis	67
4.5	(A) Pellat's height of rise experiment and (B) Jones' dielectric siphon	68
4.6	Coplanar IDE geometry	69
4.7	Droplet splitting using a series of coplanar IDEs	70
4.8	Electroosmosis	72
4.9	Electrowetting on dielectric (EWOD)	73
5.1	Side view of device	75
5.2	Top view of device	76
5.3	Schematic and dimensions for hexagonal array of circles	77

5.4	Silicon wafer cleaving	78
5.5	Overview of the photolithography process	78
5.6	Capacitance vs DC bias measurements for 1-10 Ω .cm wafers	83
5.7	Temperature vs Voltage at several frequencies for 1-10 Ω .cm wafers	84
5.8	Capacitance vs DC bias measurements for 0.1-1 Ω .cm wafers	86
6.1	Raw, cropped and thresholded side view images of droplet	89
6.2	Droplet Analyser V14 Matlab figure	90
6.3	Radius and contact angle graphs from Droplet Analyser V14	91
6.4	Measuring threads in ImageJ	92
6.5	Particle DEP analysis method using ImageJ	93
6.6	Manually measuring microdroplets using length tool in ImageJ	94
6.7	Measuring size of microdroplets using thresholding in ImageJ	95
7.1	Top view of long rectangular stripes	98
7.2	Cross-sectional view of droplet spreading	99
7.3	TMPTGE droplet spreading on 10 μ m stripes at various voltages	100
7.4	TMPTGE droplet spreading on 20 μ m stripes at various voltages	100
7.5	TMPTGE droplet spreading on 40 μ m stripes at various voltages	101
7.6	Contact angle vs Voltage for uni-directional spreading	102

7.7	Cos(θ) vs Voltage squared for uni-directional spreading	103
7.8	Comparing theoretical and experimental plots for uni-directional spreading .	105
7.9	Diagrams show the difference between single and periodic microstrip simulations	106
7.10	ANSYS simulation showing electric potential lines at electrode edge	107
7.11	Energy vs Voltage squared in ANSYS simulation	109
7.12	Contact angle vs $\log_{10}(f)$ of droplet on lower resistivity wafers	111
7.13	Examples of axi-symmetric electrode patterns	113
7.14	TMPTGE droplet unable to cross stagnation lines	114
7.15	Top view of hexagonal spreading	115
7.16	Contact angle vs Voltage for axi-symmetric spreading	116
7.17	Cos(θ) vs Voltage squared for axi-symmetric spreading	116
7.18	Caltrops, crosses, octagons and squares, and hourglass spreading	117
8.1	Thin threads at various voltages	120
8.2	Thread length vs Voltage - Decanol 1kHz	121
8.3	Thread width vs Voltage - Decanol 1kHz	122
8.4	Thread width vs Voltage - Decanol 1kHz	123
8.5	Thread length vs Time for lower voltages - Decanol 1kHz	124
8.6	Thread length vs Time for higher voltages - Decanol 1kHz	125

8.7	Thread length squared vs Time for lower voltages - Decanol 1kHz	126
8.8	Thread length squared vs Time for higher voltages - Decanol 1kHz	126
8.9	Washburn diffusion coefficient vs Voltage for decanol threads	127
8.10	$\text{Length}^2/(V - V_0)^2$ vs Time	128
8.11	Dewetting of wide thread from 180V to 120V - Decanol 1kHz	129
8.12	Dewetting of wide decanol threads at fixed voltages - Length vs Time	130
8.13	Dewetting of wide decanol thread at fixed voltages - L^2 vs Time	131
8.14	Image of two evaporating IPA threads from parent droplet - 150V at 7.5kHz	132
8.15	Final length of IPA threads over time as they evaporate	133
8.16	Images of evaporating IPA threads from parent droplet at various voltages .	134
8.17	Evaporating thread length vs voltage in static equilibrium - IPA 7.5kHz . . .	135
8.18	Evaporating thread length vs time - IPA 7.5kHz	136
8.19	Evaporating thread length squared vs time - IPA 7.5kHz	137
8.20	Spreading of microdroplets along gold/silicon oxide electrode edge	138
8.21	Length vs voltage for all microdroplets	138
8.22	Average length vs voltage of microdroplets	139
8.23	Simulation of microdroplet spreading along electrode edge	139
9.1	Particle DEP $70\mu m$ capped side view diagram	141

9.2	Particle DEP along a single edge at two frequency/voltage combinations . .	142
9.3	Long chains of particles form perpendicular to edge at low frequencies (50V/20Hz)	143
9.4	40 μm /25V: Average particle distance from centre of silicon	145
9.5	40 μm stripes at 25V: Particle distribution at 25Hz	146
9.6	40 μm stripes at 25V: Particle distribution at 200Hz	146
9.7	40 μm stripes at 25V: Particle distribution at 2000Hz	147
9.8	40 μm stripes at 25V: Particle distribution at 20000Hz	147
9.9	Image of particles being attracted to the gold/silicon interface	148
9.10	Particle DEP on 20 μm stripes	149
9.11	20 μm : Average particle distance from the centre of silicon for several voltages	149
9.12	Particles drift at random at some voltage/frequencies	150
9.13	C3A/100V: Average particle distance from the centre of large circles vs frequency	152
9.14	C3A/100V: Particle distribution at 100Hz	152
9.15	C3A/100V: Particle distribution at 1000Hz	153
9.16	C3A/100V: Particle distribution at 5000Hz	153
9.17	C3A/100V: Particle distribution at 10kHz	154
9.18	Image of particle DEP using C3B geometry	155
9.19	C3B: Average particle distance from the centre of small circles vs frequency .	156

9.20	Initial discovery of film thickness effect	157
9.21	Particle DEP for film thickness side view diagram	158
9.22	Particle DEP for film thickness top view image	159
9.23	Particle DEP for film thickness zoomed images - C3B Decanol 100V	160
9.24	Liquid film thickness dependence on C3B geometry at 100V	161
10.1	9 zones of C3A microdroplet array	164
10.2	C3A experiment 1: Droplet size distribution in each zone	165
10.3	C3A experiment 2/3: Droplet size distribution in each zone	166
10.4	Droplet size distribution over 3 experiments for middle column	167
10.5	Droplet size distribution over 3 experiments for left and right columns	167
10.6	Large defect count over multiple droplet array experiments	169
10.7	Images of C3A microdroplet array evaporation	170
10.8	Experimental and simulated normalised droplet lifetimes for C3A array	171
10.9	Droplet base radius vs normalised lifetime along diagonal for C3A array	172
10.10	Images of C3B microdroplet array evaporation	174
10.11	Experimental and simulated normalised droplet lifetimes for C3B array	174
10.12	Droplet base radius vs normalised lifetime along diagonal for C3B array	175
12.1	Gradient wetting - Thinning stripes from left to right	181

12.2 Gradient wetting - Hexagon and caltrop design	182
12.3 Temperature dependence of decanol liquid thread at 240V	183
12.4 Microdroplets of different sizes in same array	185

Nomenclature

η	Electrophoretic mobility
γ	Surface tension
κ	Thermal conductivity
μ	Dynamic viscosity
ν	Kinematic viscosity
ω	Angular frequency
Φ	Dissipation function
ϕ	Dimensionless vapour concentration field
ρ	Density
σ	Electrical conductivity
τ	Droplet evaporation lifetime
θ	Contact angle
ε	Dielectric constant
ε_0	Permittivity of free space (8.854×10^{-12} F.m ⁻¹)
ζ	Zeta potential

A	Area
a	Acceleration
B	Magnetic field
C	Capacitance
c	Vapour concentration
CM	Clausius-Mossotti factor
D	Vapour diffusion coefficient
d	Distance
D_w	Washburn diffusion coefficient
E	Electric field
E_n	Energy
F	Force
f	Frequency
g	Earth's surface gravitational acceleration (9.81 m.s^{-2})
H	Enthalpy
h	Height
J	Droplet volumetric evaporation rate
j	Local evaporative mass flux
K	Electrical conductance
k	Coulomb's constant ($8.988 \times 10^9 \text{ N.m}^2.\text{C}^{-2}$)
L	Length

m	Mass
n	Amount of substance
P	Pressure
Q	Heat
q	Electric charge
R	Droplet base radius
r	Radius
R_g	Gas constant ($8.314 \text{ J.K}^{-1}.\text{mol}^{-1}$)
Re	Reynolds number
s	Inter-droplet spacing
T	Temperature
t	Time
t_h	Thickness
u	Flow speed
V	Voltage
v	Velocity
V_0	Threshold voltage
V_l	Volume
W	Width
W_D	Work done

1 Introduction

The goal of this thesis is to report and explain the work that was done during my PhD, in which a novel MOS capacitor style geometry was utilised to perform research in the areas of dielectrowetting, liquid dielectrophoresis, particle dielectrophoresis and microdroplet evaporation.

1.1 Overview of research

Early on in the PhD the focus was on documenting the effects of dielectrowetting in the novel geometry. Dielectrowetting is the name given to the phenomenon in which strong non-uniform AC electric fields are used to change the wetting properties of a droplet on a solid surface. Dielectrowetting provides the ability to create thin liquid films, overcoming the limitation of contact angle saturation present in electrowetting. Dielectrowetting has the potential for many applications, such as liquid lenses [1], droplet manipulation [2], and in the field of microfluidics [3].

Dielectrowetting is a specific case of a more generalised phenomenon known as liquid dielectrophoresis, which describes the behaviour of polarisable liquids in the presence of strong non-uniform AC electric fields and their tendency to collect in regions of maximum field intensity. The discovery of the ability to create microscopic liquid rivulets (also referred to as ‘liquid threads’) using liquid dielectrophoresis came rather early and became a significant area of study in the PhD. The study of these liquid threads could lead to new advancements in microdroplet dispensing [4], lab-on-chip microfluidics [5] and a better understanding of fluid mechanics on the micrometre scale [6].

In addition to controlling the behaviour of liquids, it was suspected that microscopic particles in liquid suspension could be manipulated using the phenomenon of particle dielectrophoresis. Using the same novel geometry, the behaviour of polymer microspheres in a polarisable liquid

suspension was controlled using a variety of voltage and frequency combinations. Study of particle DEP in this geometry could further enhance current research in the fields of biological cell sorting [7], mineral processing [8] and nanoparticle sorting [9].

The final experimental chapter covers the formation and evaporation of thousands of tiny microdroplets. The ability to create thousands of sub-picolitre droplets in tightly packed 5x5mm arrays was a direct consequence of the unique patterned electrodes used in this novel geometry. It has the potential to lead to more controllable methods of producing microdroplet arrays for a better understanding of the industrial applications of inkjet printing [10] and spray cooling [11]. Understanding the effect of microdroplet evaporation has also become more relevant recently in the medical setting, such as studying the likelihood of survival of coronavirus in respiratory droplets deposited on a solid surface [12].

1.2 Structure of thesis

The thesis has been broken down into the following sections:

- Background information. This has been split into three chapters:
 - Chapter 2 (Fluids), which goes into some detail about the physics of both liquids and gases. This chapter introduces the reader to droplets, wetting, liquid flow and evaporation.
 - Chapter 3 (Electric Fields), which provides an overview of the well-established physics of electric fields, semiconductors and capacitors.
 - Chapter 4 (Electrohydrodynamics), which delves into the past and ongoing research in electrohydrodynamics (EHD), with a main focus on dielectrophoresis. It explores the fundamentals of particle dielectrophoresis, liquid dielectrophoresis and dielectrowetting, in addition to giving details on the various geometries and applications they are used in. It also explores some other EHD effects such as electrophoresis, electrowetting and electroosmosis. This background chapter ties

chapters 2 and 3 together by introducing and presenting previous research of how fluids can be manipulated using electric fields.

- Methodology. This is split into two chapters:
 - Chapter 5 (Device manufacturing and characterisation), which covers the full MOS capacitor device design and manufacturing process from device geometry, electrode design, silicon wafer structure, photolithography, and device setup. It also documents the characterisation process of the devices such as LCR measurements and their thermal properties.
 - Chapter 6 (Experimental methods), which documents the various methods used throughout the research. This first describes the experimental setup, such as the basic rig, camera and electrical setups, as well as how the liquid suspensions are prepared. It explains image processing and data analysis techniques used such as how droplet contact angle, liquid threads, microparticle positions and microdroplet sizes are measured.
- Experimental chapters. This section has been split into four chapters:
 - Chapter 7 (Dielectrowetting), which documents the results and findings of the first major area of research in the PhD. It begins with the study on uni-directional dielectrowetting, in which the contact angle of a droplet can be manipulated along one axis using the highly localised non-uniform electric fields permeating from the stripes on the surface electrodes. The chapter then moves onto axisymmetric dielectrowetting, which uses the same principle, but the underlying electrode pattern is changed from stripes to other geometric shapes in order to spread the droplet into a variety of shapes and eventually a thin liquid film.
 - Chapter 8 (Liquid threads), which explores how the phenomenon of liquid dielectrophoresis can be used to create very thin and long liquid threads from a larger parent droplet. At first, the so-called 'statics' of non-volatile liquid threads are explored, in which their length, width and volume are measured as a function of voltage. The chapter then delves into the 'dynamics' of non-volatile liquid

threads, which aims to explain the time dependence of this phenomenon. It also documents the findings when liquid threads are instead produced from a volatile liquid, which is referred to as ‘liquid thread evaporation’. Finally, the spreading of tiny microdroplets is covered which are produced when the liquid threads break up due to the Rayleigh-Plateau instability.

- Chapter 9 (Particle dielectrophoresis), which documents how particle dielectrophoresis can be utilised in the novel geometry to manipulate the behaviour of polymer microspheres. It takes a look at this behaviour along a single electrode edge, then with a striped electrode and finally using an electrode with an array of tiny circular holes patterned into its surface.
- Chapter 10 (Microdroplet arrays), which covers the final experimental chapter of the thesis. It uses the axi-symmetric spreading of a droplet into a thin liquid film which then has the vast majority of the liquid blown away to create a 5x5mm array of thousands of tiny microdroplets. The chapter first documents the formation and describes the sizes and consistencies of the microdroplets. It then explores the findings on how the microdroplets in the array evaporate and compares this to other research on droplet array evaporation.
- Conclusions and future work. Split into two chapters:
 - Chapter 11 (Conclusions), which summarises the main findings for each experimental chapter and includes any final remarks and conclusions on each area of research.
 - Chapter 12 (Future work), which suggests some further work that could be done using the same novel geometry going forward. This includes gradient dielectrowetting to move droplets along a surface, more work on liquid threads and particle dielectrophoresis, and the evaporation of microdroplet arrays containing different-sized droplets.

2 Fluids

A fluid is a liquid, gas, or other material that may continuously move and deform under an applied external force. In general, gases can be compressed whereas liquids maintain their volume under an applied force.

2.1 Wetting

Wetting is the ability of a liquid to displace a gas (or other liquid) to maintain contact with a solid surface. The degree of wetting is determined by the balance between adhesive and cohesive forces.

2.1.1 Molecular cohesion and surface tension

The effects of molecular cohesion and how liquids remain as a condensed freely flowing state of matter are often easiest to describe using water molecules. The cohesive forces between water molecules can be attributed to the fact it is a polar molecule. This is due to the shape of a water molecule as seen in figure 2.1, and because the oxygen atom attracts the electrons more strongly than the hydrogen atoms, the water molecule is slightly negative around the oxygen and positive around the hydrogen atoms [13]. Due to this dipole, the positive pole of one water molecule will be attracted to the negative pole of another water molecule. This phenomenon is known as hydrogen bonding, and has been extensively studied for both water and other molecules [14] [15]. These bonds are very strong in the case of water which is why it has a relatively high surface tension (72.75 mN/m at 20°C). Surface tension does have some temperature dependence [16], so the temperature must also be taken into account in most situations.

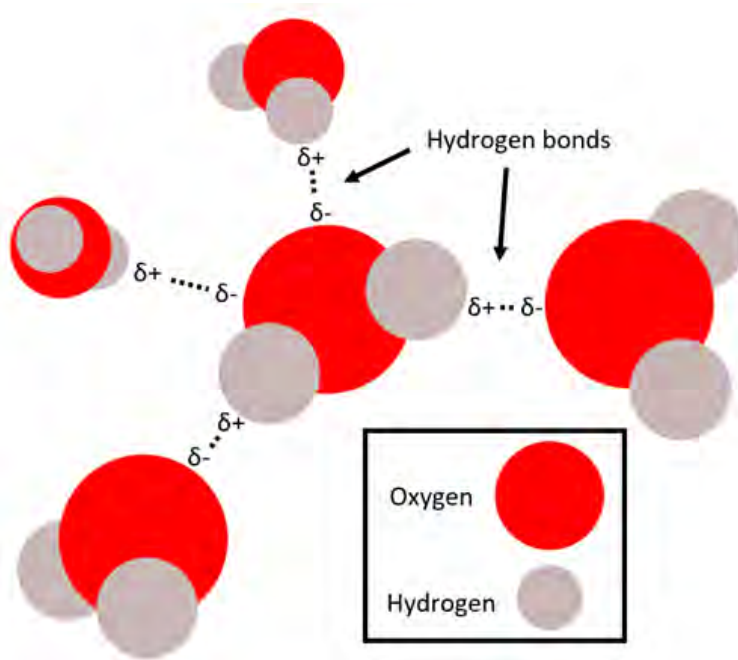


Figure 2.1: Molecular cohesion of water molecules via hydrogen bonding

It is the cohesive forces between liquid molecules that are responsible for the surface tension. Inside the bulk of the liquid, these forces are equal and opposite between neighbouring molecules, resulting in no net force. At the surface of a liquid, we assume that there is very little interaction between the liquid and gas molecules which causes an imbalance in forces due to the lack of an outward pull. This produces a net inward force which attempts to minimise the surface area of a liquid. It is the strength of these cohesive forces that ultimately determines the value of the surface tension, which is often expressed in the units of force per unit length (N/m). When there are no other forces at play, such as solid/liquid interactions or the distortion of a rain droplet due to atmospheric drag, a liquid will minimise this surface area to form a sphere. This has been demonstrated by astronauts in orbit, who are falling in an inertial reference frame and therefore experiencing no net forces. Back on Earth, this is never seen due to the fact gravity pulls the liquid towards the ground resulting in solid/liquid interactions. Liquid/liquid interactions can also occur, such as a film of oil resting on the surface of a puddle of water. This thesis is only concerned about liquids on solids, in which most of the interesting physics will be happening at the solid/liquid/gas three-phase contact line.

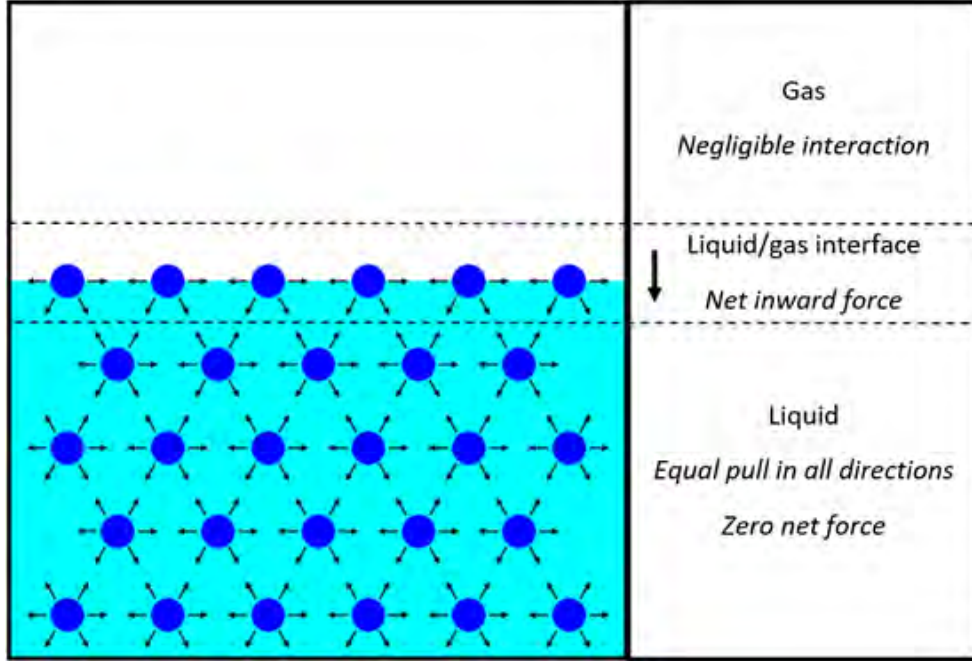


Figure 2.2: Surface tension arises from the net inward force at the liquid/gas interface

It is often useful to define surface tension in terms of the surface energy and surface area of a liquid. This is because when we consider liquid/solid interactions the surface free energy of the solid comes into play, and the two energies can be used to determine the wettability of the surface. To do this, we define the surface tension as a linear scaling coefficient for the energy required to increase the surface area by one unit. This can be expressed as:

$$dE_n = \gamma dA \quad (2.1)$$

In this case, it makes more sense to think of the units of surface tension as energy per unit area (J/m^2) instead of force per unit length (N/m). This definition can be correlated directly to the cohesive forces between the molecules of a liquid. A liquid with high cohesion, such as water due to the strong hydrogen bonds, would require more energy to increase its surface area. This corresponds to a higher surface tension. Likewise, liquids with lower cohesion will require less energy to increase their surface area and therefore have a lower surface tension. Alcohols are a typical example of this, whose surface tension tends to be roughly 3-4 times lower than that of water at room temperature [17].

2.1.2 Surface free energy and adhesion

Like liquids, the surface of a solid also has a surface-free energy which is correlated to the internal bonding force of the solid [18]. These bonds are much stronger than cohesive bonds in a liquid, so one might question why solids do not also contract into spheres on the international space station. The explanation is that, unlike liquids, the molecules in the bulk of the solid are much more strongly bound to each other via covalent, metallic, or ionic bonds. This gives the material elastic properties that dominate over the contractive forces at the surface. Therefore, when it comes to the bulk and shape of a solid it does not care much for its surface free energy. It does, however, play an important role in the wettability of its surface.

2.1.3 Surface wettability

Wettability is defined as the tendency of one fluid to spread on, or adhere to, a solid surface in the presence of other immiscible fluids [19]. The degree of wetting that a given liquid will exhibit on a solid surface is determined by both the liquid's surface tension and the surface free energy of the solid. Liquids with low surface tension will wet a given surface more strongly than liquids with high surface tension. Meanwhile, a solid with a high surface energy will be wet more strongly than one with a low surface energy (see figure 2.3).




Image removed due to 3rd
party copyright restrictions

Figure 2.3: Influence of solid surface energy and liquid surface tension in wettability [20]

Surfaces can be classified as either high-energy or low-energy depending on what they are made from, which in turn influences their wettability. High-energy surfaces are called hard solids which have strong chemical bonds (metallic, ionic or covalent). Examples of high-energy surfaces include glass, metals and ceramics. These surfaces have typical surface free energies of $\gamma_{sv} \approx 0.5$ to 5J/m^2 and therefore a high wettability. Low-energy surfaces are in the form of weak molecular crystals such as fluorocarbons and hydrocarbons. These solids have much weaker bonds and are held together by physical forces such as van de Waals forces [21] or hydrogen bonds [22]. Low-energy surfaces typically have free surface energies in the region of $\gamma_{sv} \approx 0.05\text{J/m}^2$ and therefore a low wettability [23]. Surfaces with high wettability are commonly referred to as hydrophilic whilst surfaces with low wettability are referred to as hydrophobic.

2.1.4 Contact angle and Young's equation

When a liquid droplet is placed onto a solid surface the angle at which its perimeter makes contact with the surface is called its contact angle.

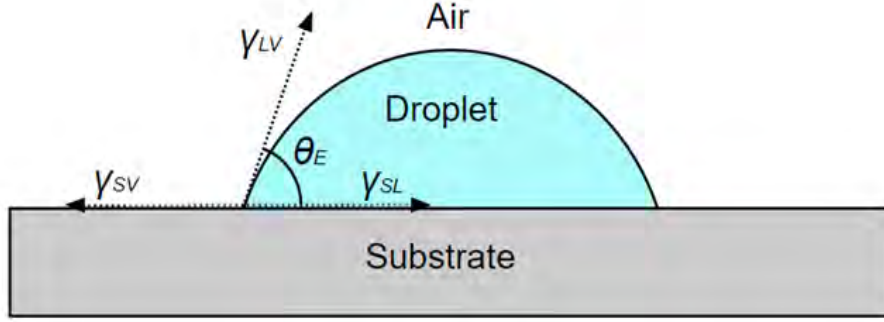


Figure 2.4: Equilibrium contact angle of a sessile droplet on solid surface

In 1804, it was Thomas Young [24] who first derived the relationship between the equilibrium contact angle of a sessile droplet and the surface energies on a smooth flat homogeneous solid surface. This can be written as the simple equation [25]:

$$\gamma_{sv} = \gamma_{sl} + \gamma_{lv} \cos \theta \quad (2.2)$$

where γ_{sv} is the surface free energy of the solid, γ_{sl} is the interfacial tension between the liquid and the solid, γ_{lv} is the surface tension of the liquid and θ is the contact angle of the droplet. Young's equation for the equilibrium contact angle is only accurate for perfectly smooth surfaces without any roughness, which in reality do not exist. The contact angle of droplets on real surfaces always sits between two extremes, known as the advancing (θ_A) and receding (θ_R) contact angles. This phenomenon is known as contact angle hysteresis [26].

2.2 Liquid Flow

Fluid mechanics is the study of the forces acting on gases and liquids. Fluid mechanics includes both fluid statics (the study of fluids at rest) and fluid dynamics (the study of fluids in motion). Fluid dynamics revolves around some fundamental axioms - the conservation of mass, conservation of linear momentum, conservation of energy, as well as the assumption that fluids are continuous entities and can be well-defined at infinitesimally small points in space-time. There are several parameters that influence how fluids flow, such as viscosity, temperature, density and pressure. As stated earlier, the word fluid can mean a gas or a liquid, but for the purposes of this thesis, we will only be considering liquids so the terms are often used interchangeably.

2.2.1 Continuity equation

For the mass continuity law, it is assumed that when a fluid moves it must do so in such a way that its mass is conserved. The continuity equation (eq 2.3) states that the rate at which mass leaves a system of fluid is equal to the rate at which mass enters the system plus the accumulation of any mass within the system [27].

$$\frac{\partial \rho}{\partial t} + \nabla \cdot (\rho \mathbf{u}) = 0 \quad (2.3)$$

The differential form of the mass continuity equation is given above [28], where ρ is the fluid density, t is time and \mathbf{u} is the flow velocity vector. Although all fluids are compressible to a certain extent (such as water [29]), all fluids in this thesis are assumed to be incompressible, and therefore the $\partial \rho / \partial t$ term of the equation becomes zero since the density of the fluid does not change with time. Therefore the equation for incompressible flow simply reduces to

$$\nabla \cdot \mathbf{u} = \frac{\partial u}{\partial x} + \frac{\partial v}{\partial y} + \frac{\partial w}{\partial z} = 0 \quad (2.4)$$

One can interpret equation 2.4 as the velocity of an incompressible fluid converges along an axis, it must increase along the other to satisfy mass continuity. An example is when fluid gets squeezed from a wider pipe into a thinner pipe (see figure 2.5).

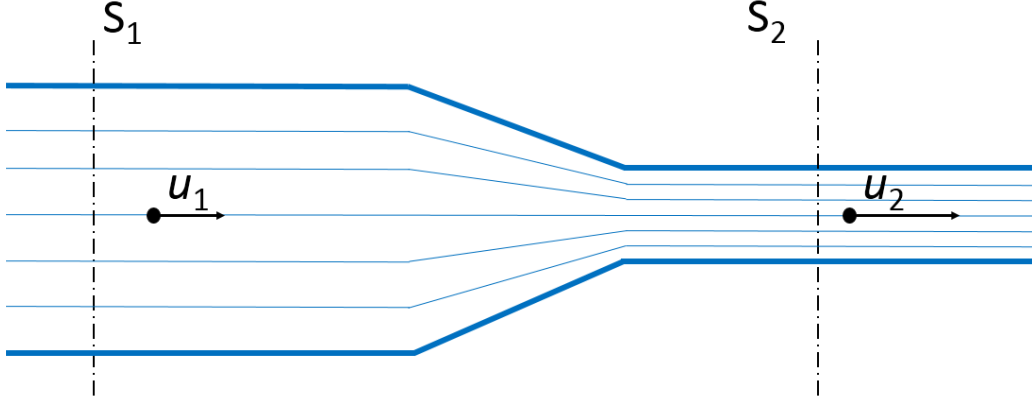


Figure 2.5: Incompressible liquid flow in a narrowing pipe [30]

2.2.2 Navier–Stokes momentum equation

Newton’s second law is also relevant in fluid dynamics and plays a role in the conservation of momentum law. It states that “the net force acting on a body or system of bodies in a particular direction is equal to the rate of change of momentum of the body” [31]. When applied to a control volume of fluid, it is a statement that any change in momentum will be due to either a net flow of fluid into the volume, or the influence of an external force acting on the fluid such as a mechanical force, gravity, or an electromagnetic field. The Navier-Stokes momentum equation, which can be derived as a particular form of the Cauchy momentum equation [32], can be written as

$$\rho \left(\frac{\partial \mathbf{u}}{\partial t} + \mathbf{u} \cdot \nabla \mathbf{u} \right) = \rho \mathbf{g} - \nabla P + \mu \nabla^2 \mathbf{u} \quad (2.5)$$

where ρ is the density, \mathbf{u} is flow velocity, t is time, P is pressure, μ is the dynamic viscosity and \mathbf{g} represents any body accelerations acting on the fluid such as inertial forces, gravity or electromagnetic forces [33]. The key takeaway is that there will be no net change in the overall momentum of an isolated system of fluid unless it is acted upon by an external force.

2.2.3 Conservation of energy

Fluid dynamics must also obey the conservation of energy. The first law of thermodynamics states that it is the combined sum of the work done and heat added to a system that will increase the total energy of the system, which can be expressed as

$$dE_n = dW_D + dQ \quad (2.6)$$

where dE_n is the total increase in energy of the system, dW_D is the work done on the system and dQ is the heat added to the system. A common equation used in fluid dynamics to express the conservation of energy is given by

$$\rho \left(\underbrace{\frac{\partial H}{\partial t}}_I + \underbrace{\nabla \cdot (H \mathbf{u})}_{II} \right) = - \underbrace{\frac{DP}{Dt}}_{III} + \underbrace{\nabla \cdot (\kappa \nabla T)}_{IV} + \underbrace{\Phi}_V \quad (2.7)$$

where ρ is the density, t is time, \mathbf{u} is flow velocity, P is pressure, κ is thermal conductivity, T is temperature, H is enthalpy and Φ is the dissipation function representing the work done against viscous forces, which is irreversibly converted into internal heat energy [34]. The five separate terms in the equation can be thought of as:

I: Local changes in the system's energy with time

II: Convective term

III: Pressure work term

IV: Heat flux term

V: Viscous to heat dissipation term

2.2.4 Viscosity and temperature dependence

A fluid's viscosity provides the measurement of its resistance to the rate of deformation [35]. In layman's terms, it can be thought of as how thick and 'syrupy' the liquid is. There are two

different scientific types of viscosity, called dynamic and kinematic viscosity. The dynamic viscosity (μ) is most commonly used and has units of pressure multiplied by time (Pa.s). The kinematic viscosity (ν) is simply the dynamic viscosity divided by the liquid's density for a given temperature:

$$\nu = \frac{\mu}{\rho} \quad (2.8)$$

In this thesis, dynamic viscosity is always used, and when the term ‘viscosity’ is mentioned it should be assumed that it is the dynamic viscosity that is being referred to. Examples of liquids with a low dynamic viscosity include water (1 mPa.s at 20° C), ethanol (1.074 mPa.s at 20° C) and mercury (1.526 mPa.s at 20° C) [36]. Examples of liquids with high dynamic viscosity include glycerol (1412 mPa.s at 20° C [37]) and honey whose viscosity can be anywhere in the range of 400 to 23000 mPa.s depending on the temperature and moisture content [38].

The viscosity of a liquid has a very strong temperature dependence, with it increasing exponentially as the temperature decreases up until the point of freezing. An equation for the relationship between the dynamic viscosity and temperature was first proposed in 1913 and is known as the Andrade equation, named after British physicist Edward Andrade [39]:

$$\mu = \alpha e^{\beta/T} \quad (2.9)$$

where μ is the dynamic viscosity, T is the temperature, and α and β are constants that are characteristic of the liquid. This relationship can be seen in figure 2.6, which shows the temperature dependence for the viscosity of glycerol.



Figure 2.6: Temperature dependence for the viscosity glycerol [40]

2.2.5 The Reynolds number

It is often useful to know whether the flow will be laminar (sheet-like) or turbulent. The Reynolds number (Re) is a dimensionless quantity that measures the ratio between inertial and viscous forces in the liquid. The Reynolds number is defined by equation 2.10.

$$Re = \frac{\rho u L}{\mu} \quad (2.10)$$

where ρ is the density of the fluid, u is the flow speed, L is the characteristic length scale of the system and μ is the dynamic viscosity of the fluid. At small Reynolds numbers, the flow will be laminar, with an example being honey flowing down the side of a jar. At larger Reynolds numbers the flow will be turbulent, with an example being fast-flowing river rapids. Based on the API 13D recommendations, it is assumed that a Reynolds number less than or equal to 2100 indicates laminar flow and a Reynolds number greater than 2100 indicates turbulent flow [41], although slightly different recommendations have been used by others.

2.2.6 Poiseuille flow

One of the most useful solutions to the Navier-Stokes equations is that of Poiseuille flow. It assumes the fluid is incompressible and that it exhibits laminar flow through a confined constant cross-section, such as a water pipe or drinking straw. Poiseuille flow assumes that the flow is sheet-like and parallel to the walls of the pipe and that the flow velocity is zero at the walls, gradually increasing towards a maximum value in the centre of the pipe.

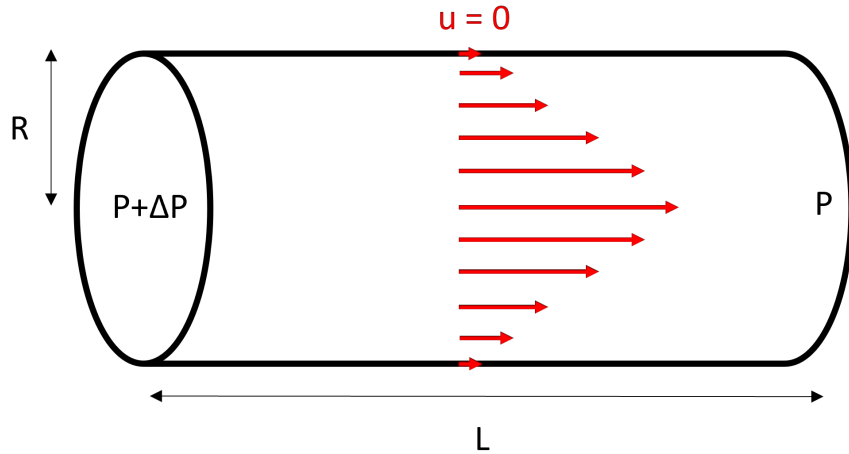


Figure 2.7: Laminar flow in a pipe

It is also known as the Hagen–Poiseuille law since it was experimentally discovered by Jean Léonard Marie Poiseuille and Gotthilf Heinrich Ludwig Hagen in 1838 but was not published by Poiseuille until 1840 [42]. It was not until 1845 that George Stokes produced a theoretical justification for the law [43]. The law can be written as

$$\frac{dV_l}{dt} = \frac{\Delta P \pi R^4}{8\mu L} \quad (2.11)$$

where dV_l/dt is the volumetric flow rate, ΔP is the pressure difference between each end of the pipe, R is the radius of the pipe, μ is the dynamic viscosity and L is the length of the pipe [44]. Poiseuille flow shows how the volumetric flow rate is linearly proportional to the pressure difference between the two ends of the pipe while being inversely proportional to

the length. Hence, if the length of the pipe is doubled the pressure gradient would have to be doubled to maintain the same volumetric flow rate. An example of this is that it is harder to suck a drink up through a longer straw. On the other hand, the volumetric flow rate is proportional to the radius to the fourth power. Therefore, doubling the width of the pipe would lead to a 16 times greater flow rate for the same gradient in pressure.

2.2.7 Washburn's equation

Washburn's equation is primarily used to describe the flow of liquid in tubes and porous materials. It is named after Edward Washburn [45], although it is sometimes referred to as the Lucas-Washburn equation since Richard Lucas wrote a paper on something similar three years prior [46]. The most general form of Washburn's equation can be written as

$$L = (D_w t)^{1/2} \quad (2.12)$$

where L is the liquid penetration depth into the tube, t is time and D_w is the simplified diffusion coefficient depending on tube size and liquid properties [47]. Although the physical constants that contribute to the diffusion coefficient vary, this $L \propto t^{1/2}$ relationship holds for many physical systems in both nature and engineering such as agriculture [48], textiles [49], oil mining [50], medical diagnostics [51], force tensiometers [52] and more [53].

It is possible to derive a Washburn relationship from Poiseuille flow in a capillary tube. If we assume it is the capillary pressure (eq 2.13) driving the pressure gradient between each end of the tube, with gravity and atmospheric pressure being equal at both ends

$$P_c = \frac{2\gamma \cos(\theta)}{R} \quad (2.13)$$

where P_c is the capillary pressure, γ is the surface tension of the liquid, θ is the contact angle of the liquid with the walls of the tube, and R is the radius of the tube. Poiseuille's law can

be used to obtain the following Washburn relationship

$$L = \sqrt{\frac{\gamma R \cos(\theta)}{2\mu} t} \quad (2.14)$$

where μ is the dynamic viscosity [53]. Although in the case of equation 2.14 it is specifically the capillary forces that are causing the pressure gradient, the Washburn relationship can be expected via any other pressure gradient, such as a difference in water pressure at each end of the pipe. The only requirement is that the pressure gradient remains constant.

Another important factor when it comes to the Washburn law is that the inertia of the liquid does not come into play. It is only once length and momentum scales get sufficiently large that the system starts to deviate from the Lucas-Washburn relationship towards having some dependence on inertial flow, as predicted by Bosanquet [54] [55].

2.2.8 Planar Couette flow

Planar Couette flow refers to that of viscous flow between two parallel plates when one plate is moving tangentially relative to the other. It is in the laminar flow regime (see section 2.2.5) and the flow is driven by the shear stress imposed by the moving surface [56].

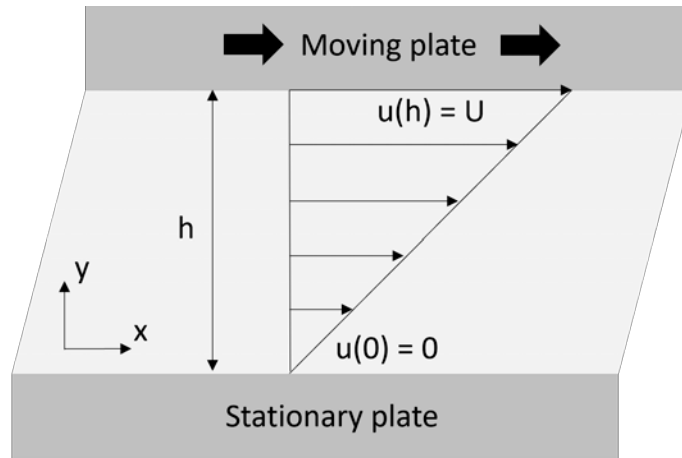


Figure 2.8: Planar Couette flow between two plates

In the most simple case, the velocity flow profile in planar Couette flow (figure 2.8) varies linearly in the y -axis, and therefore the Navier-Stokes equations simplify to

$$\frac{d^2u}{dy^2} = 0 \quad (2.15)$$

When the boundary conditions are such that the top plate is moving at $u(h) = U$ and the bottom plate is stationary at $u(0) = 0$, the solution becomes

$$u(y) = U \frac{y}{h} \quad (2.16)$$

2.2.9 Rivulet flow

A rivulet is a very small stream of liquid flowing on a solid surface. There are models for the flow of rivulets on both impermeable [57] and permeable [58] inclined planes, which use gravity as the driving mechanism for the flow. The flow [59] and mixing [60] of rivulets in micro-channels, as well as their stability [61] has been studied. Figure 2.9 shows the velocity profile of the flow regime for a rivulet in a straight open channel calculated by solving the Navier-Stokes equation in Comsol Multiphysics.



Figure 2.9: Rivulet flow velocity profile by solving the Navier-Stokes equation in Comsol [60]

An interesting thing to note about rivulet flow is that it shares some characteristics of both Poiseuille and Couette flow, and these primarily depend on the aspect ratio of the rivulet. For example, when looking from the top down on the flow profile in figure 2.9 and integrating along the y-axis to get a 2D flow rate in the x-axis, a Poiseuille flow profile is produced. Alternatively, it is apparent from looking at figure 2.9 that it is very similar to a Couette flow velocity profile, being faster on the top and slower on the bottom. Hence, if the rivulet is tall and narrow the more dominant flow mechanism is that of a Couette-type flow, whereas if it is flat and wide it could be approximated as a Poiseuille-type flow.

2.3 Evaporation

The physical phenomenon when a liquid changes state into a gas is called evaporation. It is a very well-studied area of physics and has a multitude of applications including medical science [62], food industry [63], pharmaceutical industry [64], cosmetics [65], spray coating [66], printing [67], thin film deposition [68], evaporative cooling [69], climate science [70] and desalination [71], to give just a few examples. This subsection first delves into the basic principles of evaporation in section 2.3.1, then looks into the evaporation of a single sessile droplet in section 2.3.3, before finally expanding to the evaporation of multiple droplet arrays in section 2.3.4.

2.3.1 Fundamentals of evaporation

The most intuitive way of thinking about evaporation is on the molecular scale. Like an ideal gas, the molecules in a body of liquid follow the Maxwell-Boltzmann distribution [72], and the shape of this distribution is determined by the temperature. Although formulating a rigorous mathematical description is much more difficult for liquids than with gases [73], knowing the exact distribution of the energies is not relevant for evaporation theory. Figure 2.10 shows an example of the kinetic energy distribution of the liquid molecules at two

different temperatures. It shows how at the lower temperature T_1 more of the molecules have a lower energy and the peak is sharper, whilst at the higher temperature T_2 the distribution is flatter with more molecules having a higher energy.

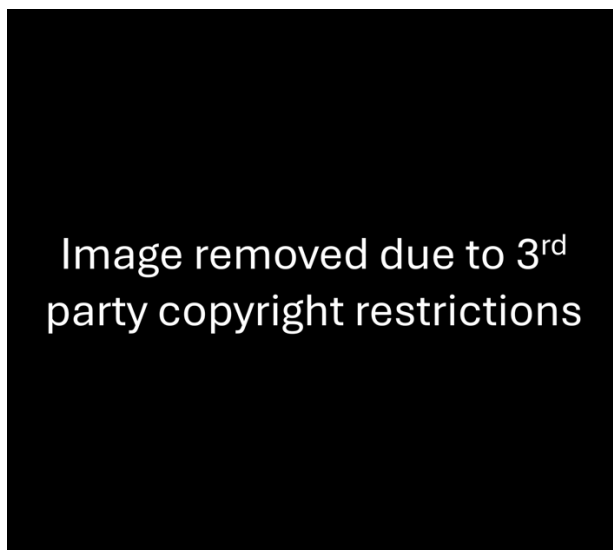


Figure 2.10: Graph showing molecular energy distribution in a liquid at two temperatures [74]

At the surface of the liquid there is a certain kinetic energy that a molecule requires in order to escape the surface, which is denoted as E in figure 2.10. Therefore any molecules at the surface of the liquid that have a surface perpendicular component of their energy of E or greater will evaporate and contribute to a vapour pressure above the liquid surface. Since there are more molecules at higher energies when the temperature is higher this increases the evaporation rate as expected. This model also explains the phenomenon of evaporative cooling since as more molecules evaporate the liquid loses energy overall, therefore shifting the energy distribution towards the left, which is felt as a reduced temperature on the macroscopic scale.

2.3.2 Diffusion-limited evaporation

Diffusion-limited evaporation is used in many models for the evaporation of liquid droplets or films on a solid surface [75]. It assumes that the phase transition from liquid to gas happens at a much faster rate than the vapour particles can diffuse away. Therefore the liquid/gas interface will have a saturated vapour concentration [76]. Consequently, the local evaporation rate is controlled entirely by the vapour diffusion away from the interface. Diffusion-limited evaporation has been shown to have good predictive power for the evaporation of multiple droplets on small scales [77]. This model ignores the effects of convection, which is driven by temperature and density gradients. It has been shown that things stay relatively close to a diffusion-limited regime for droplets of less than 20mm in radius [78], at which point the effects of convection begin to become more influential on evaporation rate.

2.3.3 Evaporation of a single sessile droplet

The evaporation of droplets is a large area of scientific research for both theoreticians and experimentalists. From the explanation of everyday phenomena such as the coffee-ring effect [79], to technological ones like inkjet printers [80] and many more [81]. In his recent review paper, Wilson states “The most widely studied situation is that in which the rate-limiting process controlling evaporation is the diffusive transport of vapour away from the droplet in the atmosphere and the simplest model for this situation is the basic diffusion-limited model [82]”. It describes the evaporation of a small, isolated, axi-symmetric droplet that is resting on a flat horizontal surface as shown in figure 2.11.

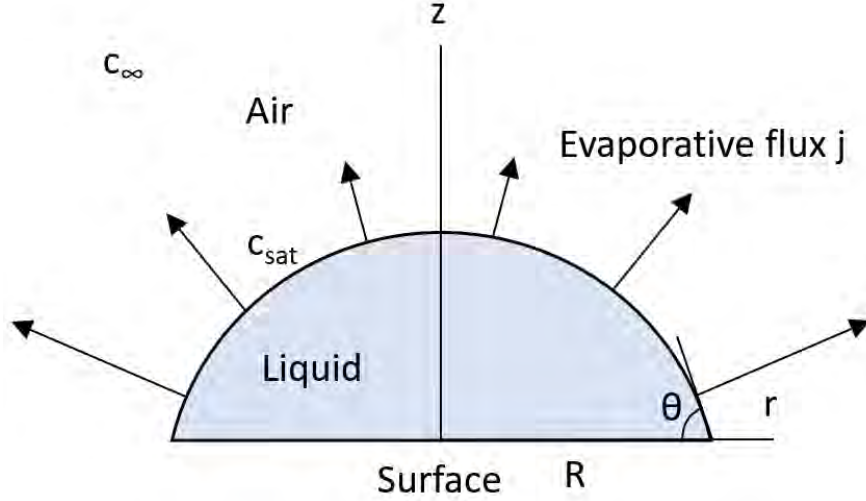


Figure 2.11: Geometry for diffusive-limited evaporation of single sessile droplet

In the case of diffusive-limited evaporation, the air at the free surface of the droplet is saturated with a concentration denoted as c_{sat} , and the ambient vapour concentration is denoted as c_∞ . There must always be the condition that $c_\infty \leq c_{sat}$ for diffusive evaporation to occur. To determine the vapour concentration in the atmosphere at any given location and time, Laplace's equation can be solved

$$\nabla^2 c = 0 \quad (2.17)$$

with the boundary conditions that $c = c_{sat}$ at the droplet's free surface, $c \rightarrow c_\infty$ far from the droplet and a no-flux condition of $\partial c / \partial z = 0$ everywhere else on the surface, where $z = 0$. The local evaporative mass flux from the surface of the droplet is given by

$$j = -D \nabla c \cdot \mathbf{n} \quad (2.18)$$

where j is the local evaporative mass flux at the droplet surface, D is the diffusion coefficient of the vapour in the atmosphere, and \mathbf{n} is the normal unit vector outward from the droplet surface.

In 1977, Picknett [83] modelled the evaporation rate of an isolated sessile droplet to be

$$\rho J = R\pi D(c_{sat} - c_{\infty})f(\theta) \quad (2.19)$$

where ρ is the density of the liquid, J is the volumetric evaporation rate of the droplet, R is the droplet base radius and $f(\theta)$ is a term representing the effect of the substrate which depends on the contact angle. One simplified example of this was given by Hu in 2014 [84] as

$$f(\theta) = \frac{2}{\sqrt{1 + \cos \theta}} \quad (2.20)$$

There are two extreme modes of sessile droplet evaporation, called the constant contact radius (CR) and constant contact angle (CA) modes. The CR mode occurs on rough surfaces when the contact line gets pinned, which causes the droplet radius to stay constant and therefore the contact angle shrinks as the droplet evaporates (figure 2.12b). The CA mode occurs on perfectly smooth surfaces when there is no pinning of the contact line and the droplet radius shrinks while the contact angle stays fixed (figure 2.12c). In reality, droplets evaporate via a combination of mixed modes between these two extremes [85].



Figure 2.12: (a) Sessile drop (b) Constant contact radius (c) Constant contact angle [86]

Depending on the mode of evaporation, various relationships for the evolution of contact angle, droplet radius and droplet lifetime have been formulated, which are summed up in the review paper by Wilson [82]. Regardless of the mode of evaporation, the lifetime of an isolated diffusion-limited evaporating sessile droplet is of order

$$\tau \propto \frac{\rho R_0^2}{D(c_{sat} - c_{\infty})} \quad (2.21)$$

where τ is the droplet lifetime, ρ is the density of the liquid and R_0 is the droplet's initial base radius.



Figure 2.13: Radius and contact angle time dependence for CR and CA modes [82]

Figure 2.13 shows how the radius and contact angle evolve for the CR and CA modes as the droplet evaporates. For the CR mode, the contact angle evolves as

$$\theta = \theta_0 - \alpha t \quad (2.22)$$

where θ_0 is the initial contact angle and α is a parameter that is influenced by the droplet vapour concentration, diffusion coefficient, droplet radius and liquid density. For the CA mode, the droplet base radius evolves as

$$R = R_0(1 - \beta t)^{1/2} \quad (2.23)$$

where R_0 is the initial droplet base radius and β is a parameter that is influenced by the vapour concentrations, diffusion coefficient, contact angle, and liquid density.

2.3.4 Evaporation of multiple droplet arrays

Although the vast majority of the literature has focused on the evaporation of isolated droplets, in nature droplets seldom occur on their own. Some studies done on the evaporation of multiple droplets, both experimentally and theoretically include Schäffle in 1999 [87], Sokuler in 2010 [88], Carrier in 2016 [89].

An important concept that distinguishes multiple droplet from single droplet evaporation is the so-called ‘shielding’ effect [90]. This refers to the mechanism in which the evaporation of neighbouring droplets increases the vapour concentration in the air, therefore reducing the evaporation rate of a droplet compared to what it would be if it were isolated. The more neighbouring droplets there are, the higher the vapour concentration and therefore the slower the evaporation rate. For a 2D array of droplets, the droplets in the centre of the array have more neighbouring droplets than those on the outer edges, therefore causing them to evaporate at a slower rate. In 2020, Wray [91] produced a model for the competitive diffusion-limited evaporation of multiple thin sessile droplets, which assumed a very small contact angle or that the droplets were “flat”. They first predicted the evaporation rate of a pair of droplets and then applied it to polygonal arrays of droplets. Edwards et al. [92] were able to get very good experimental agreement with this theory in 2021 by taking precise interferometric measurements of 2D evaporating droplet arrays in the microlitre range.

A recent model for the evaporation of arrays of multiple sessile droplets was given by Masoud in 2021 [93]. Although Masoud’s model gives similar qualitative predictions to that of Wray’s [94], the theory is not limited to small contact angles. For Masoud’s model, we consider an array of droplets of the same liquid, that might not necessarily be the same size, numbered $n = 1, 2, \dots, N$. Like in the case of single droplet evaporation (section 2.3.3), there is a vapour concentration field in the atmosphere around the droplets. Here we define the dimensionless vapour concentration field

$$\phi = \frac{c - c_\infty}{c_{sat} - c_\infty} \quad (2.24)$$

Similarly to the single droplet case (eqn 2.17), the quasi-static solution for the vapour con-

centration dominated by diffusion is given by

$$\nabla^2 \phi = 0 \quad (2.25)$$

with the boundary conditions of $\phi = 1$ at each droplet's surface ($S_1, S_2 \dots S_N$), $\mathbf{n} \cdot \nabla \phi = 0$ on the exposed substrate surface (S_s) and $\phi \rightarrow 0$ as $r \rightarrow \infty$, where r is the position vector and \mathbf{n} is the unit normal vector pointing into the vapour phase. Figure 2.14 shows this geometry, which is taken directly from Masoud's 2021 paper.

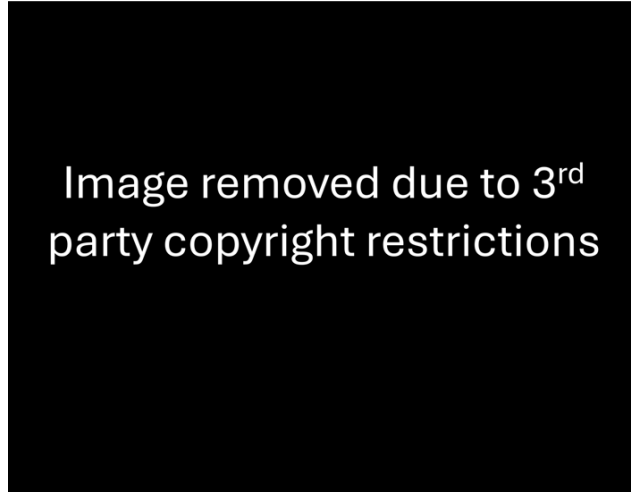


Figure 2.14: Evaporation of multiple droplets in Masoud's model [93]

The rate at which the n -th droplet loses mass J_n , can be obtained by integrating the flux of c over S_n

$$J_n = -D(c_{sat} - c_\infty) \int_{S_n} \mathbf{n} \cdot \nabla \phi \, dS \quad (2.26)$$

where D is the diffusion coefficient. However, rather than having to solve for ϕ directly, Masoud was able to use Green's second identity to obtain an exact relationship between the local flux and total evaporation rate from the droplets [95]. Using the method of reflections and by solving a system of N linear equations for the evaporation rates of each droplet J_n as a function of its isolated evaporation rate \hat{J}_n , and the dimensionless vapour concentration field at the location of the m -th droplet ϕ_{nm} , Masoud obtained the normalised evaporation

rate of the n-th droplet F_n

$$F_n = \frac{J_n}{\hat{J}_n} = 1 - \sum_{m=1}^N \phi_{nm} \frac{J_m}{\hat{J}_n} \quad (2.27)$$

It is easiest to think of ϕ_{nm} as an $N \times N$ matrix, whose off-diagonal elements describe the interactions between droplets n and m. The value of the evaluated point in the concentration field is given by

$$\phi_{nm} = 4I_1 \frac{R_m}{s_{nm}} + (I_1 + 4I_2) \frac{R^3(s_{nm}^2 - 3h_n^2)}{s_{nm}^5} \quad (2.28)$$

where R_m is the droplet base radius, s_{nm} is the inter-droplet spacing from centre to centre and h_n is the droplet height. I_1 and I_2 are integrals defined as

$$I_1 = \int_0^\infty \left[1 + \frac{\cosh((2\pi - \theta)\tau)}{\cosh(\theta\tau)} \right]^{-1} d\tau \quad (2.29)$$

and

$$I_2 = \int_0^\infty \left[1 + \frac{\cosh((2\pi - \theta)\tau)}{\cosh(\theta\tau)} \right]^{-1} \tau^2 d\tau \quad (2.30)$$

where θ is the contact angle and τ is the droplet evaporation lifetime. By inverting the matrix ϕ , the system of equations can be solved for the unknown evaporation rates of each droplet J

$$J = \hat{J}\phi^{-1} \quad (2.31)$$

given that the isolated droplet evaporation rate \hat{J} is known (see eq 2.19).

3 Electric Fields

3.1 Fundamentals of electric fields

Oxford’s ‘A Dictionary of Physics’ defines an electric field as “A region in which an electric charge experiences a force usually because of a distribution of other charges. The electric field strength or electric intensity (E) at any point in an electric field is defined as the force per unit charge experienced by a small charge placed at that point. This is equivalent to a potential gradient along the field and is measured in volts per metre [96].” Purcell’s classic textbook on Electricity and Magnetism states “The electric field attaches to every point in a system a local property, in this sense: if we know E in some small neighbourhood, we know, without further inquiry, what will happen to any charges in that neighbourhood. We do not need to ask what produced the field [97].” The important takeaway from this is that as long as the direction and strength of the electric field at a point in space is known, it does not matter how the field is produced from the perspective of the particles it is acting on.

Linear uniform electric fields are the simplest in nature. As an example, take two large flat metallic plates in a vacuum, separate them by a distance d , and apply a potential difference V across them. The electric field strength E at every point between the plates will be the voltage divided by the distance (Eq 3.1). The S.I. units for an electric field are in volts per metre.

$$E = \frac{V}{d} \tag{3.1}$$

In this simple geometry, doubling the voltage would have the same effect on the electric field as halving the distance between the plates. Due to this effect, it is possible to get very strong electric fields at relatively low voltages if the distance between the plates is very small. This geometry is known as a parallel-plate capacitor (Figure 3.1).

The technical definition for the electric field is the divergence of the potential difference:

$$\vec{E} = -\nabla V \quad (3.2)$$

Electric fields are either attractive or repulsive depending on the polarity of the field and the net charge of the particles it is acting on. In a simple parallel plate geometry, negative particles are attracted to the positive plate and positive particles are attracted to the negative plate. In diagrams, the electric field lines are always drawn to point from positive to negative, as seen in figure 3.1.

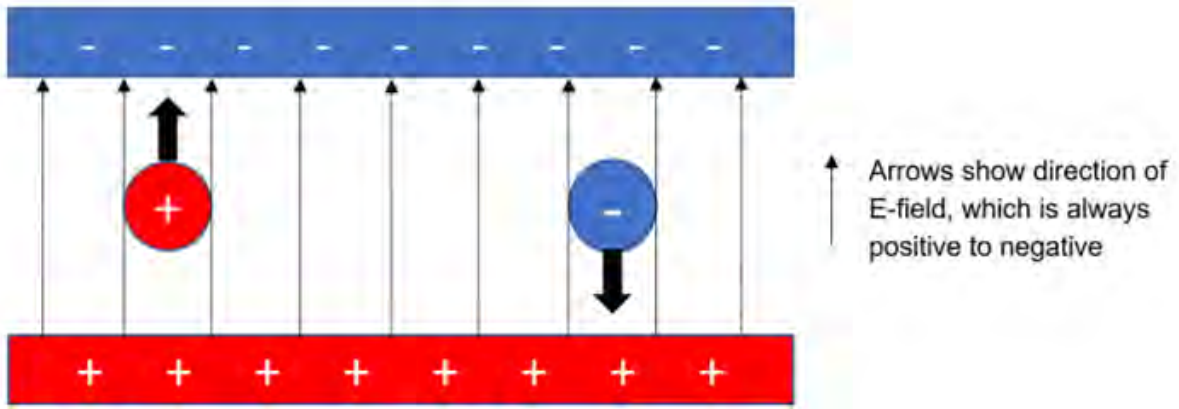


Figure 3.1: Simple parallel plate capacitor geometry with two oppositely charged particles

The Lorentz force law can be used to calculate the force felt by a charged test particle in an electric or magnetic field [98]. The full law (Eq 3.3) can be written as the equation:

$$\vec{F} = q(\vec{E} + \vec{v} \times \vec{B}) \quad (3.3)$$

Since this thesis is only concerned with the electric field contribution, the force (\vec{F}) on a charged particle in an electric field is simply the particle charge (q) multiplied by the electric field strength (\vec{E}). Note that vector notation is used since the direction of the E-field and corresponding force are relevant.

$$\vec{F} = q\vec{E} \quad (3.4)$$

This can be equated to Newton's second law to determine the acceleration of a charged particle with a mass m :

$$\vec{a} = \frac{q\vec{E}}{m} \quad (3.5)$$

Except in simple geometries like the parallel plate capacitor, most electric fields in reality are non-uniform. A non-uniform field does not have a constant magnitude and/or direction at every single point in space. Consequently, the forces felt by charges in the field will vary depending on their location. Non-uniform electric fields come in many different geometries. For example, the electric field produced by a concentrated sphere of charges will shrink inversely proportional to the square of the distance from the centre of charge. This also works for two single-point charged particles and is referred to as Coulomb's law (Eq 3.6). The force (F) felt by each particle in this geometry is given as:

$$\vec{F} = k \frac{q_1 q_2}{r^2} \quad (3.6)$$

where k is Coulomb's constant, q_1 is the charge of one particle, q_2 is the charge of the other particle, and r is the distance between the two particles. Note that if the charges are of the same polarity, the force will be positive and therefore repel each other. If they are opposite polarity the force will be negative and attract each other. The force on each particle will be equal in magnitude and opposite in direction.

3.2 Parallel plate capacitor

A simple parallel plate capacitor has a capacitance given by the formula [97]:

$$C = \frac{\varepsilon_r \varepsilon_0 A}{d} \quad (3.7)$$

where ε_r is the relative dielectric constant of the material between the plates, ε_0 is the permittivity of free space, A is the area of one of the plates, and d is the distance between the plates.

3.3 Semiconductors

A semiconductor material is defined as a material that exhibits properties between those of a conductor and an insulator. Unlike metals whose electrical conductivity decreases as a function of temperature, a semiconductor's electrical conductivity increases as the temperature increases, which was first reported by Michael Faraday in 1833 [99].

Semiconductors belong to two types - intrinsic or extrinsic. By definition, intrinsic semiconductors have the same number of free electrons to holes, where a hole refers to the absence of an electron in a particular place in the semiconductor lattice. A common intrinsic semiconductor is silicon (Si). This is because each silicon atom is surrounded by four other silicon atoms in a crystalline structure, with each atom sharing one of its four valence electrons with each neighbour. These shared electrons are referred to as covalent bonds, which are very strong [100]. At low temperatures these electrons remain covalently bonded and can therefore not contribute to any electrical conductivity, making the overall conductivity of the material low. As the temperature increases there is enough energy to break some of these bonds, which produces electron-hole pairs. These free electrons are then able to move under the influence of an applied electric field. Likewise, the virtual holes are free to move in the opposite direction to the free electrons, although what is effectively happening is that all the real bonded electrons are just 'shuffling' from one atom to the next as the holes move backwards. Increasing the temperature creates more electron-hole pairs which further increases the conductivity of the material.

By adding trace impurities to the semiconductor lattice, an intrinsic semiconductor such as pure silicon can be changed into an extrinsic semiconductor in which the number of free electrons is different to the number of holes. This process is called doping. Extrinsic semiconductors can either be n-type if they have more free electrons, or p-type if they have more holes. The type is determined by whether the dopant belongs to an element in group III or V of the periodic table. If the element belongs in group V it is called a donor since it has five electrons in its outer shell and is therefore able to donate one free electron when its

other four bond with the four neighbouring silicon atoms in the lattice. Some examples of group V donors are phosphorous (P), arsenic (As) and antimony (Sb). Alternatively, if the element belongs to group III it is called an acceptor since it only has three electrons in its outer shell, and hence there is already a natural hole present in the crystal structure when its other three electrons bond to the neighbouring silicon atoms. Some examples of group III acceptors are boron (B), aluminium (Al) and gallium (Ga) [101].

3.4 MOS Capacitors

The Metal-Oxide-Semiconductor capacitor, otherwise known as a MOS capacitor, is made of a semiconductor body, a thin insulating oxide layer and a metal electrode called a gate. While much effort is currently being made to integrate new dielectric or ferroelectric materials, the most common oxide used between the capacitor plates remains to be silicon dioxide (SiO_2) [102]. The metal acts as one plate of the capacitor and the semiconductor layer, which may be n-type or p-type, acts as another plate.

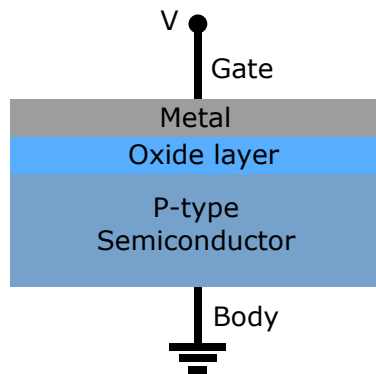


Figure 3.2: P-type MOS capacitor structure

Due to the nature of semiconductors, the capacitance of the MOS capacitor depends upon the voltage applied. The body is typically grounded whilst voltage is applied to the gate ¹.

¹This is the most common configuration and will be maintained in this section. However, it is important to note the actual devices used were reversed, where the voltage is applied to the semiconductor and the metal is grounded.

There are three regions of interest when applying a DC bias voltage to the gate of a MOS capacitor. These are the accumulation, depletion and inversion regions. These regions are tied directly to three voltages, referred to as the flatband voltage V_{fb} , the gate voltage V_G and the threshold voltage V_T . The flatband and threshold voltages are determined by the dimensions of the capacitor and the materials it is made from, including oxide thickness and doping levels. For a MOS capacitor with a p-type substrate, the accumulation regime happens when a negative DC bias voltage is applied to the gate and therefore holes are attracted to the semiconductor/oxide interface (figure 3.3a). In this case, the gate voltage is less than the flatband voltage. If the gate voltage is positive and exceeds the flatband voltage but remains lower than the threshold voltage, the depletion regime is reached. During depletion, positive holes are pushed away from the semiconductor/oxide interface and a negative charge region is produced near the interface, which increases in size as the gate voltage increases (figure 3.3b). When the gate voltage is further increased beyond the threshold voltage the inversion regime is entered. During inversion, there exists a negatively charged inversion layer at the semiconductor/oxide interface in addition to the increased size of the depletion region. This inversion layer is caused by a build-up of electrons caused by the high positive gate voltage (figure 3.3c). As the gate voltage increases further, more electrons are pulled towards the interface but the depletion region does not grow in size much more [103].

Image removed due to 3rd
party copyright restrictions

Figure 3.3: Accumulation, depletion and inversion of MOS capacitor [103]

By using an LCR meter that applies a DC bias voltage in addition to a smaller sinusoidal alternating voltage of a chosen frequency, a CV curve can be plotted to determine the three regimes. From this curve, parameters such as carrier mobility, charge density and charge inversion can be extrapolated. Depending on whether the AC voltage applied is at a high or low frequency, the capacitance of the MOS capacitor during the inversion regime will vary. When a high-frequency AC voltage is applied, the capacitance during inversion is lower than that when compared to a low-frequency AC voltage. This leads to a lower overall average capacitance when applying large AC voltages at higher frequencies. This effect is shown in figure 3.4.



Figure 3.4: CV curve showing the three regimes at high and low frequencies [104]

3.5 Electric Double Layer

“A double layer around a charged particle [or surface] is formed by the particle surface charge and its counter ions, forming an ionic cloud surrounding the particle” [105]. This is known as the Electric Double Layer (EDL) and was first described by Helmholtz in 1879 [106].




Image removed due to 3rd
party copyright restrictions

Figure 3.5: Electric Double Layer (EDL) [107]

This double layer creates an electrokinetic potential, also called the zeta potential ζ , which has an influence on the behaviour of the particle (section 4.5.1) or fluid along the surface (section 4.5.2) under an applied electric field.

4 Electrohydrodynamics

4.1 Dielectrophoresis overview

Dielectrophoresis, or DEP for short, is the name given to the phenomenon when a force is exerted on a dielectric particle under the influence of a non-uniform electric field. It was first explained in 1951 by Herbert Pohl [108]. 15 years later, a paper was published by Pohl and his master's student, Ira Hawk, on the separation of live and dead yeast cells using inhomogeneous electric fields [109], which paved the way for DEP becoming a significant area of academic and industrial research.

Since research into dielectrophoresis began, it has been utilised in many geometries and applications. The majority of these applications are based around particle dielectrophoresis, especially in the field of biomedical research [110]. Particle DEP has been explored extensively in both industry and academia and has many potential prospects for both [111]. Meanwhile, liquid dielectrophoresis has mainly been limited to academic research only, due to it not having many profitable applications thus far. However, with the increase of lab-on-a-chip (LoC) devices, liquid DEP is becoming more useful in the field of microfluidics [112]. The following sections will first cover the fundamentals and theory of dielectrophoresis and then explore the geometries and applications for both particle and liquid DEP.

4.2 Fundamentals of dielectrophoresis

Particles do not need to have a net electric charge to undergo dielectrophoresis, and in most cases are neutral. The particles do have to be polarisable, however, via either a permanent or induced electric dipole. Although polarizable particles can be placed into a uniform electric field, such as that between two plates of a parallel plate capacitor, they will not feel a net force due to the attractive and repulsive forces on each end of the dipole being equal and

opposite (Figure 4.1).

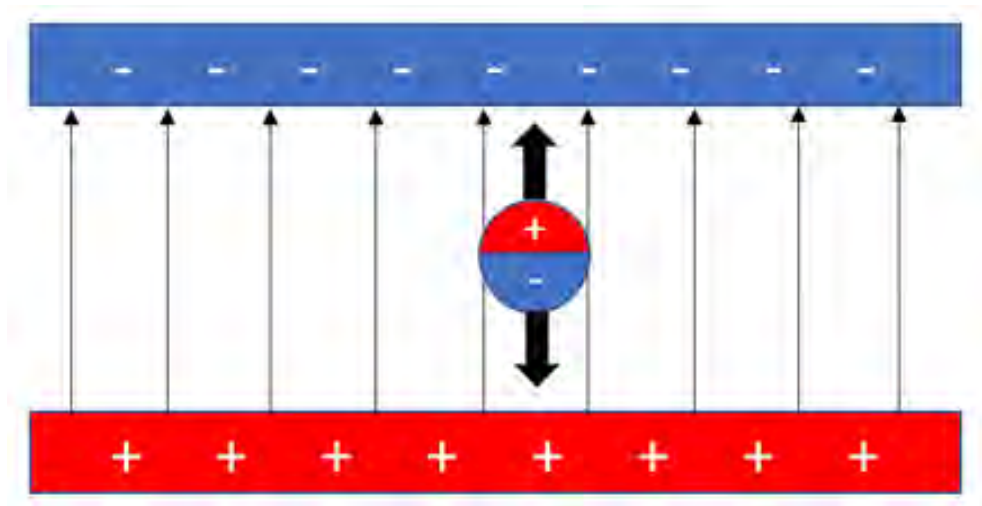


Figure 4.1: Dipole in a uniform electric field

In the case of a non-uniform electric field such as that at the edge of an electrode (Figure 4.2), the particles will still orient along the direction of the field, but the attractive force on the end of the dipole in the region of higher electric field density will be greater than the repulsive force in the region of lower electric field density. In this case, the polarity of the electrode does not matter, since if it were reversed the particle would flip 180 degrees to realign itself and still be attracted to the area of highest electric field density. Therefore, this phenomenon can be utilised using AC electric fields. In this case, when the particle is attracted to the area of higher field density, it is referred to as positive dielectrophoresis or pDEP.

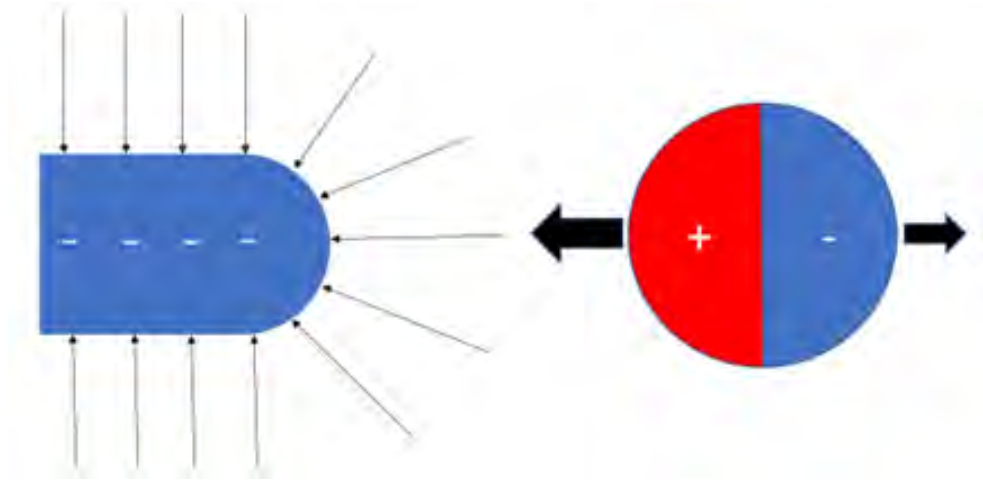


Figure 4.2: Dipole in a non-uniform electric field

Although positive dielectrophoresis is the most intuitive way of understanding this phenomenon, it is only half the story. It is also possible for particles to undergo negative dielectrophoresis, or nDEP. During negative dielectrophoresis, rather than the particle being attracted to the region of highest field density they are instead repelled away from it. This is because the polarizable particles are not the only thing that must be considered when examining dielectrophoresis; the electrical properties of the medium it is suspended in must also be considered.

To keep things simple for now, only the limit in which the electrical permittivity (or dielectric constant) of the particle and medium are considered. This is the case when the frequency of the electric field gets very large (typically in the MHz range). Later, the role of conductivity will be introduced, which typically comes into play at lower frequencies. In the high-frequency limit, the equation for the force on a homogeneous sphere surrounded by a dielectric medium is written as [113]:

$$\vec{F}_{DEP} = 2\pi\epsilon_m\epsilon_0r^3 \left[\frac{\epsilon_p - \epsilon_m}{\epsilon_p + 2\epsilon_m} \right] \nabla |\vec{E}_{rms}|^2 \quad (4.1)$$

Where r is the radius of the sphere, ϵ_m and ϵ_p are the relative permittivities of the medium

and particle, and E_{rms} is the applied electric field. It should be noted that all these values, except for the electric field, are always positive. Since the electric field term is squared in equation 4.1, this part is always positive. Therefore, the only thing that determines whether the force is positive or negative is the term in the square brackets, which is referred to as the high-frequency limit of the real part of the Clausius-Mossotti factor (Eq 4.2) [114].

$$Re[CM(\omega \rightarrow \infty)] = \frac{\varepsilon_p - \varepsilon_m}{\varepsilon_p + 2\varepsilon_m} \quad (4.2)$$

This term is positive when the relative permittivity of the particle is greater than that of the medium and negative when the relative permittivity of the particle is smaller than that of the medium. Hence, we see negative dielectrophoresis when the permittivity of the particle is lower than that of the surrounding medium.

If the force on a dielectric particle was only ever determined by the permittivity of itself and the surrounding medium, dielectrophoresis would not be nearly as useful as it is in a variety of applications today. The property that makes DEP so useful is that it is possible to change the magnitude and direction of the force on a particle by changing the frequency of the electric field applied, allowing for applications such as biological cell sorting [115]. This is where the conductivity of the particle and medium becomes an important factor. In this case, the Clausius-Mossotti factor must be written in full, which incorporates the frequency dependence by using the complex dielectric permittivities of both the particle and medium [114]:

$$CM(\omega) = \frac{\varepsilon_p^* - \varepsilon_m^*}{\varepsilon_p^* + 2\varepsilon_m^*} \quad (4.3)$$

Where ε_p^* and ε_m^* are the complex permittivities of the particle and medium respectively, with $\varepsilon_p^* = \varepsilon_p - j\frac{\sigma_p}{\omega}$ and $\varepsilon_m^* = \varepsilon_m - j\frac{\sigma_m}{\omega}$ where ε_p and ε_m are the permittivities, σ_p and σ_m are the conductivities, ω is the angular frequency and $j = \sqrt{-1}$. From these expressions, we see that as $\omega \rightarrow \infty$ the complex permittivity becomes the standard dielectric permittivity,

as seen in equation 4.2. Alternatively, as $\omega \rightarrow 0$ the term involving the conductivity becomes dominant. Due to this dependence, there becomes a certain frequency where the direction of the felt force switches from positive to negative or vice versa, and this is defined as the crossover frequency.

4.3 Particle dielectrophoresis

4.3.1 Particle DEP of biological particles

One of the earliest examples of the use of particle DEP on biological particles was that done by Herbert Pohl in 1966, where he was able to separate living yeast cells from dead ones in an aqueous medium by carefully tuning the frequency of the AC electric field [109]. In 1978, Pohl released a book on the subject which described the phenomenon and his work over the years in detail [116]. In 1988, Price used a spectrophotometer in an optical chamber to more accurately measure the frequency-dependent behaviour of several species of bacteria [117]. Since biological cells are not homogeneous, they can be modelled to account for their non-homogeneous structures using the so-called ‘multishell model’, which was presented by Irimajiri in 1979 [118]. This multishell model was extended to describe non-spherical cells [119] and then to factor in the effects of the dielectric anisotropy of the plasma membrane of the cell [120]. In 1996, Müller used particle DEP via high-frequency electric fields to successfully trap viruses [121]. More recent advances in the use of DEP for biological applications include discriminating dengue-infected hepatic cells [122], the separation of tumour cells [123], the separation of DNA molecules by size [124] and many more [110].

4.3.2 Particle DEP of non-biological particles

In addition to biological particles, the use of DEP for the separation of non-biological particles has become a significant area in the field [125]. The earliest use of non-biological DEP was

in 1924 when Hatfield was the first to apply dielectrophoresis in minerals processing by using low-frequency AC electric fields to separate minerals based on their permittivities [8]. Although most famous for the yeast cell separation experiment [109], Pohl’s earliest work came in the form of non-biological DEP, with the separation of carbon black from polyvinyl chloride in di-isopropyl ketone in 1951 [108]. He then went on to design a foil-lined Pyrex Tube of 20 mm in diameter with a Teflon-coated metal wire as the inner electrode to produce a continuous DEP separator [126]. In 1960, Pohl and Plymale were able to separate PVC from a liquid medium at a flow rate of 750mL/h, in addition to various other particles from each other (e.g. SiC from Al_2O_3 and zirconia from rutile) [127].

Since the early experiments there have been many experiments using polystyrene beads [128], which had some crossover with biological particle DEP due to a lot of biological particle work being modelled on the polystyrene bead behaviour. In 1997, Green explored the dielectrophoretic behaviour of sub-micron latex spheres [129], which was then further expanded upon in 2002 to study the influence of the Stern layer conductance on the spheres [130]. Non-biological DEP has also been used on the nanoscale by trapping and separating nanoparticles [131][132], and for the assembly of nanostructures [133][134].

4.3.3 Particle DEP in microelectrode geometries

In the early days of DEP research and applications, larger electrode designs were used with wires up to 1.59mm in diameter and voltages of up to 11kV being used by Pohl [116]. Using high voltages often leads to fluid motion from thermal effects, which interfered with the effects of DEP alone. As technology for the fabrication of microdevices progressed, groups were able to scale down the size of the geometries. In 1998, Green and Morgan [135] were able to separate submicrometre particles of two different sizes using a combination of dielectrophoretic and other electrohydrodynamic forces using microelectrodes, as seen in figure 4.3. In this geometry, the smaller beads were trapped at the electrode edges via the DEP force, whilst the larger beads were carried with the liquid flow to the centre via other EHD forces, where they moved upwards and became trapped in “stagnation points”. This is due to the

phenomenon that as the bead radius changes, the total conductivity of the particles changes as given by the equation:

$$\sigma_p = \sigma_b + \frac{2K_s}{r} \quad (4.4)$$

where σ_p is the particle conductivity, σ_b is the bulk conductivity of the particle (which is approximately zero for latex spheres), K_s is the surface conductance and r is the particle radius [136]. Due to this, smaller particles have a higher conductivity which affects the crossover frequency from the CM-factor (section 4.2).



Figure 4.3: Small beads trapped by DEP forces whilst large beads move with liquid to stagnation point [135]

In 2003, Maverick [137] used platinum wires of $100\mu m$ in diameter and peak-to-peak voltages of just 15V to manipulate and characterise red blood cells. More on the use of microelectrodes for particle DEP are discussed in the review paper [138] as well as the microfabrication techniques to make them [139].

4.3.4 Pearl Chains

‘Pearl chain’ formation is a phenomenon where particles align and form long chains when immersed in a liquid and subjected to an electric field. They only occur when the field

strength is greater than a certain minimum value [140]. Pearl chains have previously been referenced in the literature [141] in which particles close to the edge of an electrode orient themselves along field lines, and the interaction of neighbouring particles has been discussed by Stoy in 1994 [142].




Image removed due to 3rd
party copyright restrictions

Figure 4.4: Pearl chain formation of nanoparticles in microelectrode gaps by dielectrophoresis [143].

4.4 Liquid dielectrophoresis and dielectrowetting

Liquid dielectrophoresis (L-DEP) utilises the same concept as particle DEP, but instead of solid particles being the objects of interest in a liquid medium, it can be thought of as the liquid molecules being dielectric ‘particles’ in a medium of air. Since all liquids have a higher dielectric permittivity than air, positive L-DEP is always observed by a liquid in air. Liquid-in-liquid dielectrophoresis has also been demonstrated [144], which relies on the permittivities and conductivities of each liquid being different.

4.4.1 Early L-DEP geometries

In 1894, prior to the invention of the word ‘dielectrophoresis’, Pellat demonstrated the effect of liquid dielectrophoresis by applying a voltage V to two plate electrodes separated by a distance d that were partially submerged in a dielectric liquid with a permittivity of ε . This caused the liquid to rise to a new height of:

$$h = \frac{(\varepsilon - \varepsilon_0)V^2}{2\rho g d^2} \quad (4.5)$$

where ρ is the density of the liquid and g is the acceleration due to gravity [145]. This principle was later used by Jones in 1971 to create a dielectric siphon which used a voltage to siphon a liquid from a higher reservoir to a lower one [146]. In this case, it was not the voltage that did the pumping of the liquid but rather caused the siphon to be ‘primed’, allowing gravity to do the pumping. This meant that the flow rate was independent of the voltage applied, but it could still be switched off when the voltage was not high enough to connect the reservoirs (if $h < h_u$ as produced by equation 4.5 and seen in figure 4.5).



Figure 4.5: (A) Pellat’s height of rise experiment and (B) Jones’ dielectric siphon [147]

In these early DEP geometries, the voltages required to achieve any substantial movement of the liquid were very high (19kV in Jones' case), which is because the DEP force scales proportionally to the electric field squared as seen in equation 4.1. Since the electric field is voltage divided by distance (equation 3.1), high electric field strength could only be produced by applying a very high voltage due to the large distances between the plates in these experiments. In 2001, Jones was able to miniaturise this geometry by creating a “wall-less” electrode structure capable of moving a dielectric oil up against gravity by several centimetres with only 200V [148]. In 2006, Cheng was able to demonstrate a recoverable 25° contact angle change of a liquid crystal droplet at 200V, which could be used to make a liquid lens [1].

4.4.2 Coplanar IDE geometries

A common geometry for dielectrowetting in particular has been that of coplanar interdigitated electrodes (IDEs). This refers to the geometry in which two electrodes share the same x-y plane and are interdigitated so that the electrode fingers interlock leaving a fixed spacing between them (figure 4.6). A voltage can then be applied across the electrodes, which creates a non-uniform electric field that permeates into the surrounding material, air and liquid. Coplanar IDEs are typically patterned via photolithography onto a glass substrate.



Figure 4.6: Coplanar IDE geometry - Shows before and after voltage is applied [149]

In 2009, Brown used coplanar IDEs to spread a droplet of decanol into a thin film of $12\mu m$ in thickness, therefore overcoming the contact angle saturation seen in electrowetting experiments. The ability to create wrinkles using this method on the air/liquid interface of the thin film allowed them to create a voltage-programmable diffraction grating [150]. A relationship between the contact angle and voltage for a uni-directional spreading of a sessile droplet was determined to be $\cos(\theta) \propto V^2$ by McHale in 2011. It was in this paper that the term ‘dielectrowetting’ was first introduced [151]. In 2021, Quetzeri-Santiago used dielectrowetting to control the splashing and bouncing of droplets onto a flat surface with coplanar IDEs [152]. The principle of dielectrowetting was also used to split and transport droplets [2] by using a series of droplet-sized adjacent coplanar IDEs as seen in figure 4.7.

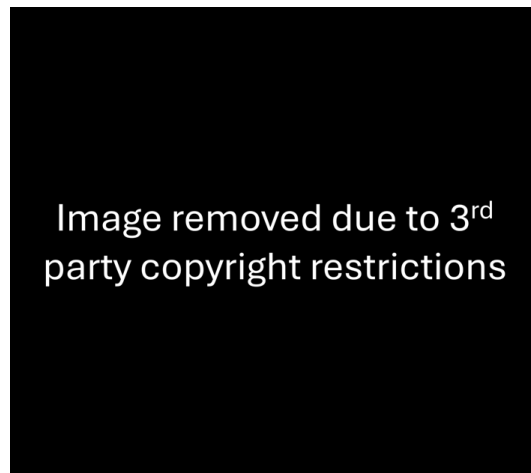


Figure 4.7: Droplet splitting using a series of coplanar IDEs [112]. By selecting when each small coplanar electrode is switched on or off it is possible to split and transport the droplet.

4.5 Other Electrohydrodynamic effects

4.5.1 Electrophoresis

Electrophoresis is perhaps the simplest of all the electrohydrodynamic effects to comprehend. It was first discovered by Peter Ivanovich Strakhov and Ferdinand Frederic Reuss at Moscow University in 1807 who noticed that clay particles dispersed in water began to migrate under an applied electric field [153]. It describes the migration and separation of charged particles or molecules under the influence of a spatially uniform electric field [154]. The particles are held in a liquid suspension between an anode and a cathode, and when an electric field E is applied they move with a velocity v , where η is a constant that represents the electrophoretic mobility.

$$v = \eta E \quad (4.6)$$

The mobility η of the particle depends on several factors such as the particle's shape, size and charge, as well as the temperature and viscosity of the liquid medium. The most widely used theory of electrophoresis was developed by the Polish physicist Marian Smoluchowski in 1903 [155]:

$$\eta = \frac{\varepsilon_m \varepsilon_0 \zeta}{\mu} \quad (4.7)$$

where ε_m is the dielectric constant of the liquid, μ is the dynamic viscosity of the liquid and ζ is the zeta potential (see section 3.5).

4.5.2 Electroosmosis

Electroosmosis, sometimes referred to as electroosmotic flow (EOF), is the motion a liquid solution that is induced when a potential is applied across a conduit such as a capillary tube or porous material. Due to the presence of the electric double layer (see section 3.5) the walls of the tube are electrically charged (negative in the case of figure 4.8) and they attract the

positive ions in the solution. These positive ions then move towards the cathode when an electric field is applied, creating a flow within the tube.



Figure 4.8: Simple diagram of electroosmosis [156]

4.5.3 Electrowetting

Although the research presented in this thesis focused on the effects of dielectrophoresis and dielectrowetting, it is important to distinguish the difference between this and a similar phenomenon called electrowetting. The basis of modern electrowetting was first described by Gabriel Lippmann in 1875 [157]. He found that the capillary depression of mercury in contact with electrolyte solutions could be varied by applying a voltage between the mercury and electrolyte. This led to the invention of his capillary electrometer [158]. The practical applications of this were somewhat limited due to the electrolytic decomposition of water upon applying voltages beyond a few hundred millivolts [159]. It was not until 1993 that Berge [160] introduced the idea of using a thin insulating layer to separate the conductive liquid from the metal electrode, allowing them to overcome the problem of electrolysis. This concept became known as electrowetting on dielectric, or EWOD for short.



Figure 4.9: Electrowetting on dielectric (EWOD) [161]

5 Device manufacturing and characterisation

This chapter covers the design, manufacturing process and characterisation of the silicon wafer devices used. Section 5.1 describes the general device geometry and electrode design. Section 5.2 explains the process of device fabrication, including device cleaning, photolithography, sputter coating, hydrophobic layer deposition and device wiring. In section 5.3 the devices are characterised using LCR measurements and their temperature/frequency dependence is measured.

5.1 Device design

5.1.1 General geometry of device

The general geometry of the devices used remained consistent throughout, with the only major difference being the pattern on the gold-titanium electrodes. The main structure of the device is shown in Figure 5.1. It consists of a boron-doped p-type silicon wafer with a $1\mu\text{m}$ thermally grown oxide layer (SiO_2), of which a single side has been polished by the manufacturer (Mi-Net Technology Ltd). The wafers have a thickness of $525\mu\text{m}$, a crystal orientation of $\langle 100 \rangle$ and a resistivity of $1\text{-}10\ \Omega\cdot\text{cm}$. Towards the end of the PhD, new wafers were used with the same parameters except for their resistivity, which was in the range of $0.1\text{-}1\ \Omega\cdot\text{cm}$ instead. This is discussed more in section 5.3. The 4" wafer is cut up into $35\text{x}25\text{mm}$ rectangular devices. Gold-titanium electrodes are patterned onto the polished top side of the device using thin-film photolithography. A layer of the hydrophobic fluoropolymer coating Novec 2702 can be deposited onto the top surface. The underside p-type silicon is connected to the live terminal of the amplifier and the top gold-titanium electrode is connected to 0V on the amplifier, with indium solder being used to connect each wire to the device.

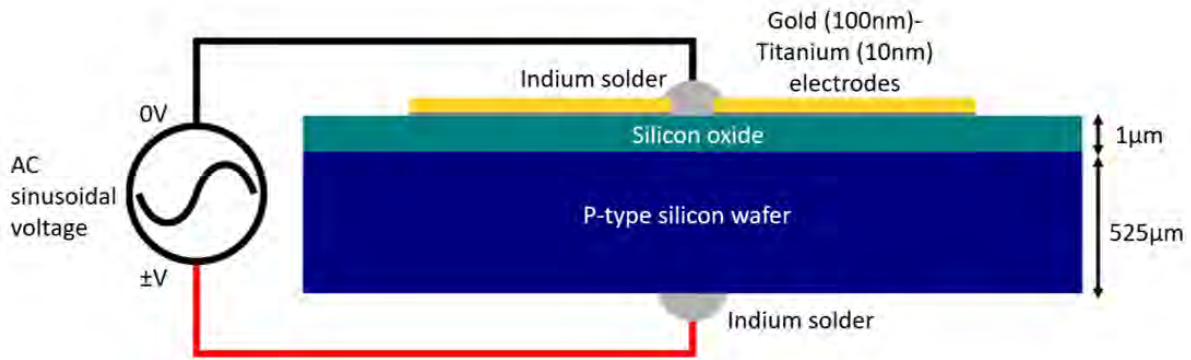


Figure 5.1: Side view of device

Each 35x25mm rectangle contains four 9x7mm electrodes with different patterns in order to utilise all the space available and make it easier to compare similar patterns on a single device (Figure 5.2). The patterned area on each 9x7mm electrode is a 5x5mm square, which is offset to allow enough space for soldering. The four electrodes were purposely designed to be isolated from each other so that they could be connected individually, mainly because the amplifier had difficulty driving the device if the electrode area was too large, particularly at higher AC frequencies ($>10\text{kHz}$). However, the electrodes were close enough together so a single piece of solder could connect them all to the amplifier if higher frequencies were not required. Figure 5.2 shows an example where the indium solder would connect two electrodes to the amplifier at once.

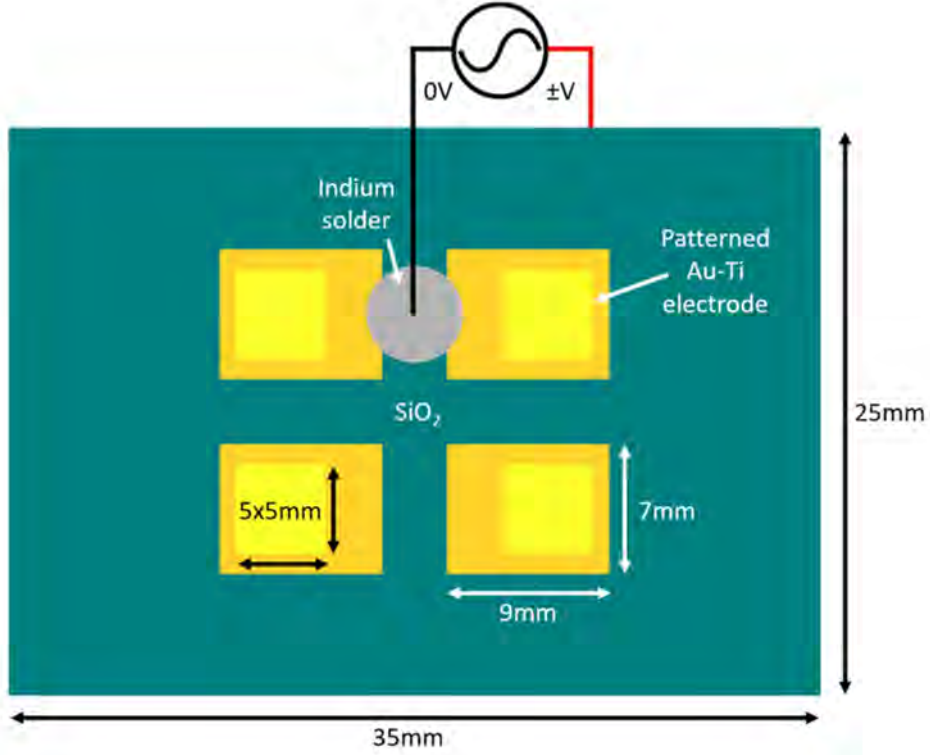


Figure 5.2: Top view of device

5.1.2 C3A and C3B electrode patterns

Two electrode patterns that come up quite regularly in both the particle DEP (section 9) and microdroplet arrays (section 10) are referred to as C3A and C3B to keep things brief. The reason for this naming convention came quite early in the PhD and refers solely to their location on the photomask. Figure 5.3 shows the schematic and associated dimensions for these two patterns, with the only difference being the circle size and pitch. C3A (large circles) refers to the electrode pattern with a pitch of $p = 60.5\mu m$ and a radius of $r = 20.2\mu m$. C3B (small circles) refers to the electrode pattern with a pitch of $p = 45.3\mu m$ and a radius of $r = 11.6\mu m$. The seemingly random non-integer dimensions for these patterns were again established early in the PhD when there was an idea to keep the edge length per unit area fixed for the axi-symmetric spreading experiments (section 7.2). However, due to the presence of stagnation lines not allowing for the droplets to spread, this idea was not pursued further.

but the patterns were used for other things.

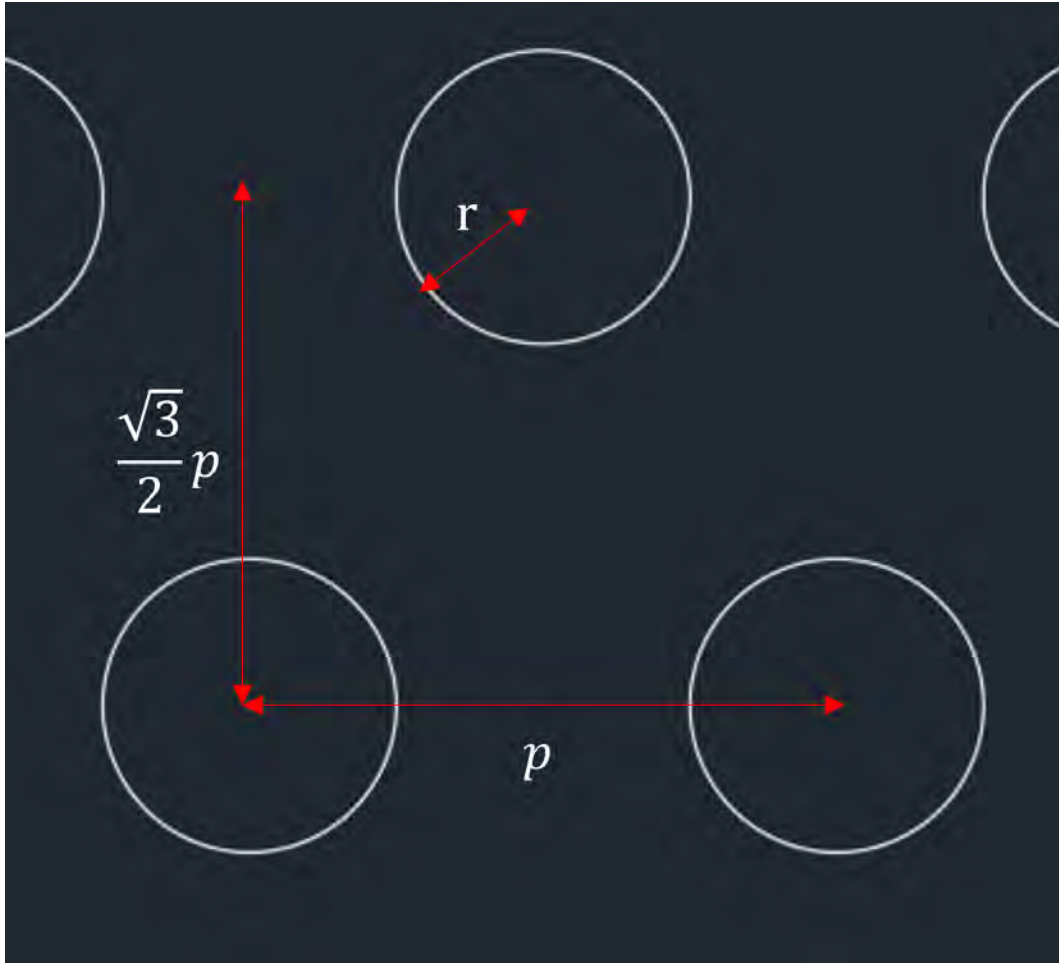


Figure 5.3: Schematic and dimensions for hexagonal array of circles

5.2 Device fabrication

5.2.1 Silicon wafer cleaving

4-inch boron-doped p-type silicon wafers were cleaved into 35x25mm rectangular devices using the diamond pen cleaving method. Six devices could be made from each 4" wafer.

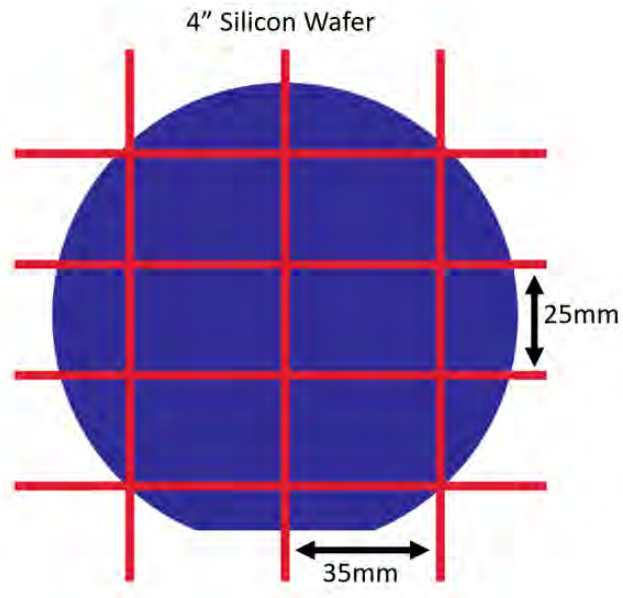


Figure 5.4: Silicon wafer cleaving

5.2.2 Overview of photolithography process

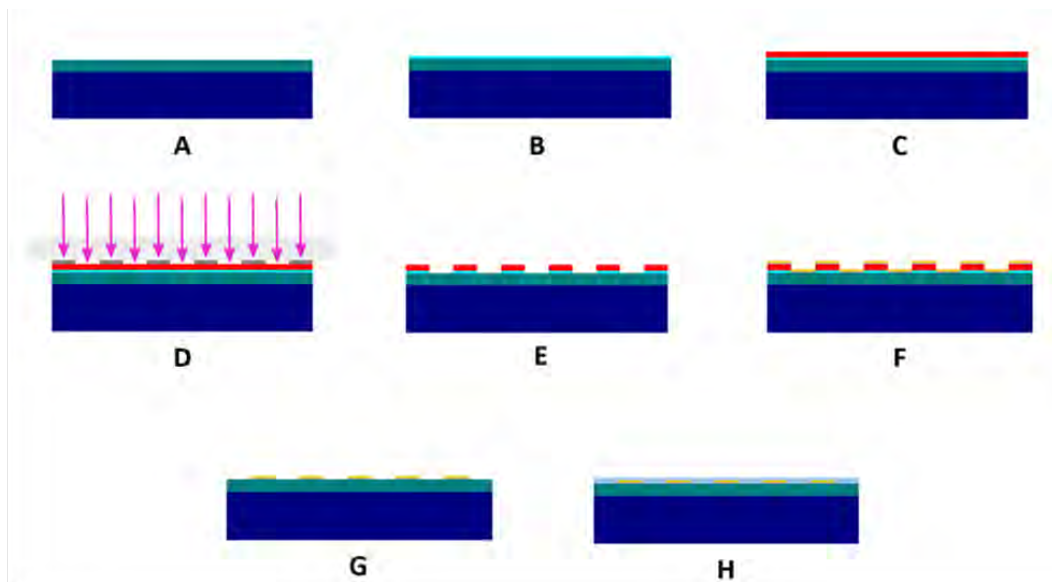


Figure 5.5: Overview of the photolithography process

[A] – Cross-sectional view of 35x25mm p-type wafer (blue) with polished $1\mu\text{m}$ oxide layer (green).

[B] – A monolayer of hexamethyldisilazane (turquoise) is evaporated onto the oxide surface. Hexamethyldisilazane, commonly abbreviated to HMDS, is a colourless, flammable liquid that is used to promote adhesion of the photoresist.

[C] – S1813 positive photoresist (red) is spin-coated onto the surface.

[D] – Mask aligner used with a chrome (dark grey) class 4 quartz glass (light grey) inverted photomask to expose areas of photoresist to UV light.

[E] – Device placed into developer solution which removes the photoresist and HMDS in the areas exposed to UV light.

[F] – 10nm layer of titanium (grey) and 100nm of gold (yellow) sputter coated onto the whole surface.

[G] – Device placed into acetone and sonicated to remove remaining photoresist and HMDS, therefore lifting off the metal above it. This leaves the metal electrode pattern on the area which was exposed to UV light.

[H] – A $0.2\mu\text{m}$ layer of Novec 2702 (light blue) can be spin coated or dip coated when a hydrophobic surface is required.

5.2.3 Cleaning

The devices [A] were air dusted, rinsed with isopropyl alcohol, and placed into Petri dishes to be cleaned thoroughly. In the cleanroom, the devices were cleaned in a series of ultrasonic bath cycles for 5 minutes each. The first and second baths contained 5% and 0.5% Decon 90/DI water solution respectively. The final bath consisted of only DI water. Each device was rinsed with isopropyl alcohol and blow-dried with nitrogen after each cycle. After the final

bath, the devices were rinsed with isopropyl alcohol, blow-dried with nitrogen, and placed on a hotplate at 200°C for at least 10 minutes, although each device was left on the hotplate until the application of the HMDS (see 5.2.4). The purpose of keeping them on the hotplate was to ensure that they were as dehydrated as possible for the next step.

5.2.4 Photoresist application

Each device was taken off the hotplate one at a time for this step. In the fume cupboard, another hotplate was set to 110°C, and a clean glass slide was placed on it. A device was taken off the 200°C hotplate, rinsed with isopropyl alcohol, blow-dried with nitrogen, and placed onto the 110°C hotplate next to the glass slide. Reagent grade hexamethyldisilazane (HMDS) was extracted from the bottle using a needle and syringe, and a few small drops ($\approx 10\mu\text{L}$) were dispensed onto the glass slide. A petri dish was used to quickly cover both the glass and device for 45 seconds, allowing enough time for the HMDS to evaporate and form a monolayer [B] on the polished silicon oxide surface to help promote adhesion of the photoresist. The device was placed onto the spincoater chuck, S1813 photoresist was dispensed onto it using a plastic pipette, and it was spun at 500RPM for 10 seconds and 3000RPM for 30 seconds. This produces a thin film of S1813 roughly $1.5\mu\text{m}$ in thickness. Immediately after spin coating, the device was placed onto the 110°C hotplate and covered with a petri dish to bake for 75 seconds. The device was stored in a clean petri dish and this step was repeated until all devices had been coated [C].

5.2.5 Mask aligner

The UV mask aligner was then used to expose the devices [D]. Since S1813 is a positive photoresist, it is the areas that receive an exposure that are removed in the developing stage. Hence, the photomask was required to be the inverse of the final electrode design. AutoCad was used to design the photomasks as a .dwg file and this was sent to JD Photo Data for manufacturing. The 5" chrome photomasks were made from quartz glass and had class 4

(500k dpi) resolution to get the best possible minimum feature size. The mask was placed chrome side down on the mask aligner and held in place by a vacuum. Soft contact exposure at a brightness of 30 kilolux for five seconds was performed on one device at a time. These devices could then be stored in a petri dish under dim yellow light conditions for several days if required, although moving onto the developing stage was always done on either the same or the following day.

5.2.6 Developing, sputter coating and metal lift-off

One at a time, the devices were placed into a microposit MF-319 developer solution. Slight agitation was needed to remove the areas of photoresist that had been exposed to the UV light on the mask aligner [E]. This typically took about one minute. The device was then rinsed in a beaker of DI water for 30 seconds to remove any excess developer before being blow-dried with nitrogen. The devices were placed into the sputter coater and coated with a 10nm adhesion layer of titanium and then 100nm of gold [F]. Titanium is regularly used as an adhesion layer to prevent the gold from peeling off the silicon oxide surface [162]. The calibrated deposition rate for titanium was 2.5nm/min at 150mA and for gold it was 15nm/min at 40mA. Finally, the sputter-coated devices were placed into some 99.8% purity acetone in an ultrasonic bath for five minutes to remove the remaining photoresist [G]. This lifted off any metal that was sitting on top of the photoresist, leaving the patterned metal electrode where the photoresist was removed during the developing stage. The devices were wiped with a lens tissue soaked in acetone to ensure all photoresist was removed, rinsed with isopropyl alcohol, and blow-dried with nitrogen.

5.2.7 Hydrophobic coating

When required, a robust fluoropolymer hydrophobic coating called Novec 2702 was used to increase the initial contact angle of the liquids used in the experiments. Novec 2702 can be coated using various methods, but the two used during this PhD were spin coating and dip

coating. To spin coat, a syringe was used to place a small amount onto the surface, and it was spun at 1000RPM for 20 seconds. To dip coat, the device was submerged into a small bottle of Novec 2702 for 5 seconds and then held sideways for 30 seconds so that any excess dripped off onto a paper tissue. A short bake on a hotplate at 80°C for 1 minute ensured the solvent had fully evaporated, leaving the hydrophobic fluoropolymer surface [**H**]. The coating was measured to have a thickness of $0.2\mu\text{m}(\pm 20\%)$ using ellipsometry [163].

5.2.8 Soldering and wiring

Indium solder was used throughout due to its ability to create an ohmic contact with the silicon and its low melting point. All soldering was performed on a hotplate set to 120°C, which is 36.6°C below the melting point of indium [164], making it easier to solder due to the high thermal conductivity of the silicon wafer. To make the electrical connection to the underside of the device, a diamond scribing pen was used to scratch the oxide layer directly through some molten indium. This allowed the molten indium to flow into the scratches made, ensuring a good electrical contact.

5.3 Device characterisation

5.3.1 Change of wafer resistivity after 2 years

Throughout the first 2 years of the PhD the wafers used had a bulk resistivity of 1-10 $\Omega\cdot\text{cm}$. At higher frequencies there appeared to be some heating (section 5.3.3), and therefore it was decided that the next batch of wafers ordered would have a lower resistivity (0.1-1 $\Omega\cdot\text{cm}$) to see if this reduced the heating effect. In addition, due to the nature of MOS structures (see section 3.4), the capacitance of the system can also change as a function of frequency, and this can be measured using an LCR meter.

5.3.2 Characterisation of 1-10 $\Omega\cdot\text{cm}$ wafers

A Keysight E4980A LCR meter was used to measure the capacitance across two 9mm x 7mm electrodes simultaneously since this was often the most common configuration when performing experiments. This meant the total electrode area was $2 \times 9 \times 7 = 126 \text{mm}^2$. For an ideal parallel plate capacitor with plates of this area, a dielectric thickness of $1 \mu\text{m}$ and a dielectric constant of $\epsilon_r = 4$, the capacitance given by the basic formula (eq 3.7) is 4.46nF . This simple calculation was used to check that the LCR readings were giving reasonable results so that the wafers could be characterised. Figure 5.6 shows the data for how the capacitance of the device changes as a function of DC bias for frequencies ranging from 300Hz to 100kHz. Firstly, it is important to note that the capacitance ranges from 3.5nF to 4.4nF so that it is in the right ballpark concerning what is expected in an ideal case.

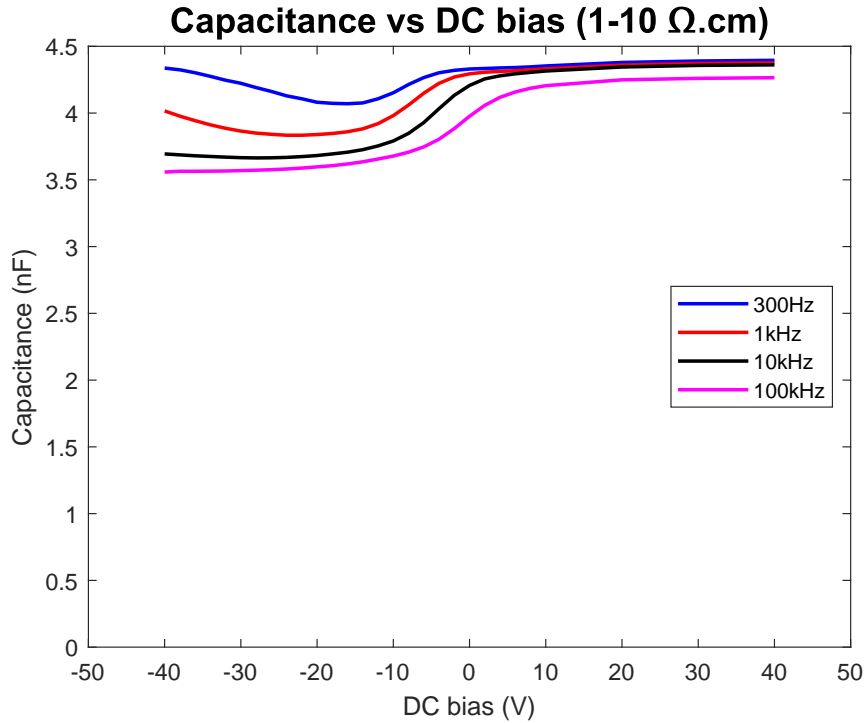


Figure 5.6: Capacitance vs DC bias measurements for 1-10 $\Omega\cdot\text{cm}$ wafers

In the measurements shown in figure 5.6, the live terminal was connected to the P-type silicon whilst 0V was connected to the top electrode. This is important to note since it affects which

polarity the inversion and depletion regions of the C-V curve will lie (see section 3.4). The results from the LCR measurements for these wafers show some inversion and depletion which is dependent on the frequency, revealing that the average capacitance of the system will be around 10% lower at 100kHz ($\approx 3.8\text{nF}$) compared to 300Hz ($\approx 4.2\text{nF}$).

5.3.3 Frequency related heating of 1-10 $\Omega\cdot\text{cm}$ wafers

It was noticed that at higher frequencies the devices tended to get hot. To quantify this, one 9x7mm electrode was connected to the amplifier on the 35x25mm device, the device was attached to the plastic holder as usual, and various frequencies were tested for voltages of up to 200V. For frequencies above 30kHz, the amplifier could no longer drive the device to higher voltages, so only the highest possible voltage for those frequencies has been recorded. Since the top surface of the wafer is very reflective in the infrared range that the FLIR-E63900 thermal camera uses, some masking tape was stuck onto the top surface of the wafer and its temperature was instead recorded on the thermal camera. Figure 5.7 shows the results of this experiment.

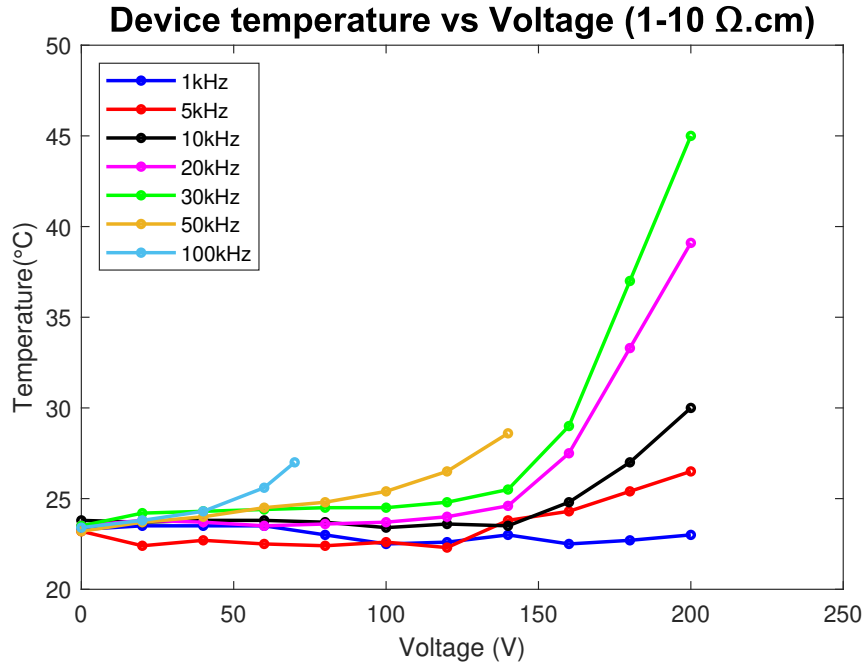


Figure 5.7: Temperature vs Voltage at several frequencies for 1-10 $\Omega\cdot\text{cm}$ wafers

The results show that even at frequencies as low as 5kHz, there is some heating effect causing the device temperature to increase at voltages above 150V. This gets especially noticeable at frequencies $>10\text{kHz}$, with the device managing to reach a temperature of 45°C at 200V at 30kHz. This increased temperature could potentially have a few effects on any experiments performed at these parameters. The first is that the resistivity of the device will increase with temperature. In addition, heating the device will also heat the liquid, which will in turn decrease its viscosity and increase its evaporation rate. This is something that must be taken into account and therefore voltage/frequency combinations that could cause the wafer temperature to exceed 30°C were never used in experiments to minimise this heating effect (e.g. 8kHz at $<200\text{V}$ was used in chapter 7.1 to keep within this limit).

5.3.4 Characterisation of 0.1-1 $\Omega\cdot\text{cm}$ wafers

The second batch of wafers purchased from Mi-Net Technology Ltd were identical to the first, except for having a resistivity in the range of 0.1-1 $\Omega\cdot\text{cm}$. The LCR meter was again used to measure the capacitance vs DC bias for frequencies from 300Hz to 100kHz. Similarly to the higher resistivity wafers, it was measured for two 9mm x 7mm electrodes simultaneously, which would give an ideal capacitance value of 4.46nF. As seen in figure 5.8, the LCR measurements also gave values close to this value. However, one major difference between these newer lower-resistivity wafers and the older higher-resistivity ones is the obvious flatness of the data across the entire DC bias range. For all practical purposes, the capacitance is constant as both a function of DC bias and frequency for the 0.1-1 $\Omega\cdot\text{cm}$ wafers. This effectively means the system is behaving more like a metal-insulator-metal capacitor instead of a metal-insulator-semiconductor capacitor. It is speculated that due to the higher doping of boron in the lower resistivity wafers, there are enough free holes for the silicon to effectively behave like a conductive metal, also known as a degenerate semiconductor [101]. Unlike the higher resistivity wafers, the 0.1-1 $\Omega\cdot\text{cm}$ wafers did not undergo a net heating effect for the frequencies and voltages that were applied to the devices in the experiments. This was confirmed using the thermal camera, and no increase above room temperature was observed

for any sensible voltage/frequency combination for these lower resistivity wafers.

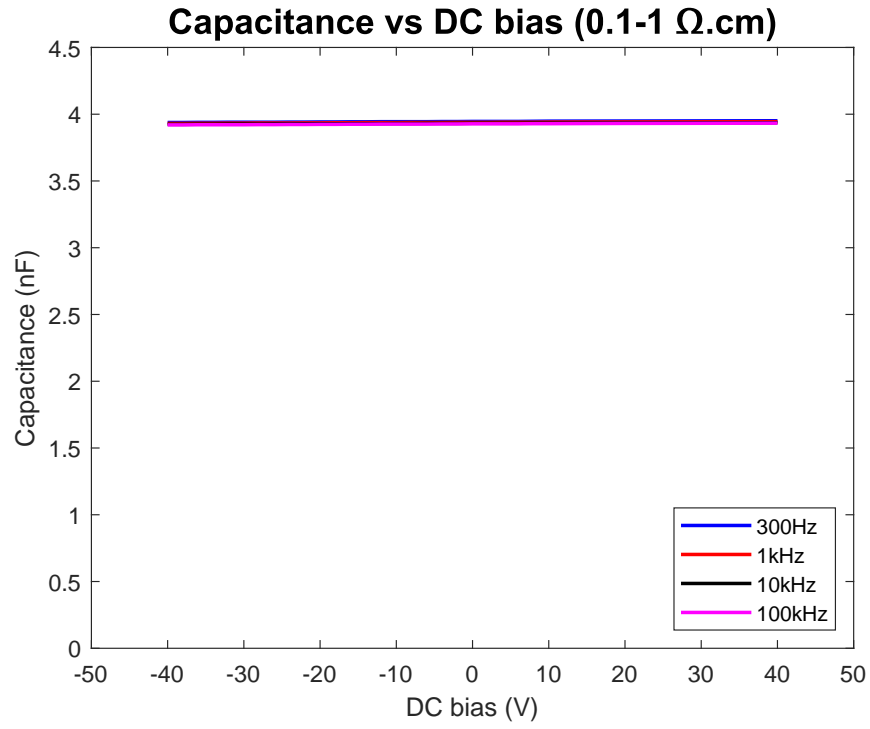


Figure 5.8: Capacitance vs DC bias measurements for 0.1-1 $\Omega\cdot\text{cm}$ wafers

6 Experimental methods

This chapter covers the experimental methods used throughout the PhD. Section 6.1 describes the experimental setup, including the basic rig setup, electrical equipment setup and the method for creating the particle suspension used in chapter 9 of the thesis. Section 6.2 explains the techniques used for image processing and data analysis.

6.1 Experimental setup

6.1.1 Basic rig setup

Throughout the PhD, there was very little change to the fundamental experimental setup. It consisted of a custom-made plastic holder to which one end of the device was secured. The holder was attached to an x-y translation stage which was attached to a Thorlabs breadboard table. A Thorlabs DCC1545M side view camera was used to look at the droplets along the y-axis to measure their height, width and contact angle. This side view camera had x-z-translation for viewing different areas of the droplet and y-translation for adjusting focus. The height of the camera was adjusted manually on its post holder to change the z-direction. A Thorlabs DCC1645C top view camera was attached to a z-translation stage for fine focus adjustment which was then attached to a large z-translation beam. The x-y translation and rotation of the top camera were controlled manually by adjusting the post holders attaching it to the main beam. Both cameras were connected to a Windows 10 PC where uEye Cockpit camera software was used to take photos and record videos.

6.1.2 Electrical setup, waveforms, frequencies, and voltages

To supply voltage to the device, a Keysight 33500B Series waveform generator and TRek Model PZD700 piezo driver/amplifier were connected to the device wires using large crocodile clips. A Tektronix TDS 2014 four channel digital oscilloscope and Agilent 34401A $6\frac{1}{2}$ digit multimeter were placed in parallel to measure the waveform and RMS voltage across the device. The breadboard was also earthed for safety.

AC sinusoidal waveforms were always used throughout the entire PhD. Frequencies used were limited by the capacitive nature of the device, which ranged from 10Hz to 30kHz. At frequencies greater than 30kHz the amplifier had difficulty driving the voltage due to the large capacitance, with heating also becoming an issue at higher frequencies and voltages. A FLIR-E63900 thermal camera was used to measure the temperature of the device at several frequency/voltage combinations. Since gold and polished silicon oxide are very good reflectors of infrared light, the temperature of some masking tape stuck on a small area of the device was measured to make sure the readings were accurate. The results of this are shown in section 5.3.3.

6.1.3 Making the polymer microsphere suspension

To get the right concentration of polystyrene microsphere to liquid suspension, a $10\mu L$ droplet from the bottled suspension of Fisher Scientific FluoSpheres™ $10\mu m$ yellow-green fluorescent polystyrene microspheres was dispensed into a small glass vial using a micropipette. This was then heated at a low temperature of $50^\circ C$ until all the liquid had evaporated. It was allowed to cool, $200\mu L$ of liquid was added to the vial and then it was stirred and sonicated to make sure the particles were as separated as possible. If left for a while the suspension would separate, so it always required to be sonified before any experiments.

6.2 Image processing and data analysis

The main method of obtaining data throughout the PhD was through the side and top view visual cameras and using image processing software to translate photos and videos into spatial coordinates of the liquid and/or particles.

6.2.1 Contact angle measurements

To measure the contact angle of the droplet for both the uni-directional (section 7.1) and axi-symmetric dielectrowetting (section 7.2) experiments, monochromatic images were taken from the side view camera using a 5x lens with a white back-light, with extra care being taken to focus the camera on the point at which the droplet makes contact with the surface of the device. A small ‘letter-box’ slit was stuck onto the front of the backlight using cardboard and blue-tac, which helped get the best contrast possible between the droplet (black) and the background (white). The reflection of the droplet was always seen below it, which helped reveal the surface and hence the baseline at which the contact angle could be taken.

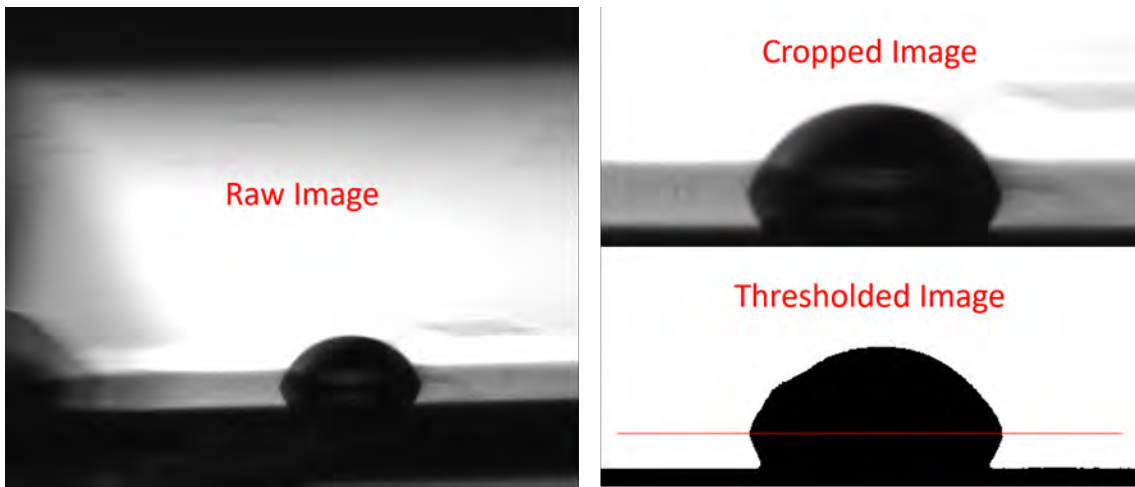


Figure 6.1: Raw, cropped and thresholded side view images of droplet

Once the photos were taken, they were imported into the image processing software, ImageJ. In ImageJ, the photos were cropped so that only the droplet and its reflection were in the

image, rotated so that the device surface was parallel to the x-axis, and finally thresholded using the Otsu algorithm so that the droplet and its reflection were completely black and the background was completely white. For a given set of measurements, such as a voltage sweep from 0V to 200V at 10kHz for example, all the droplet images were stacked and saved as .avi file ready for the next step.

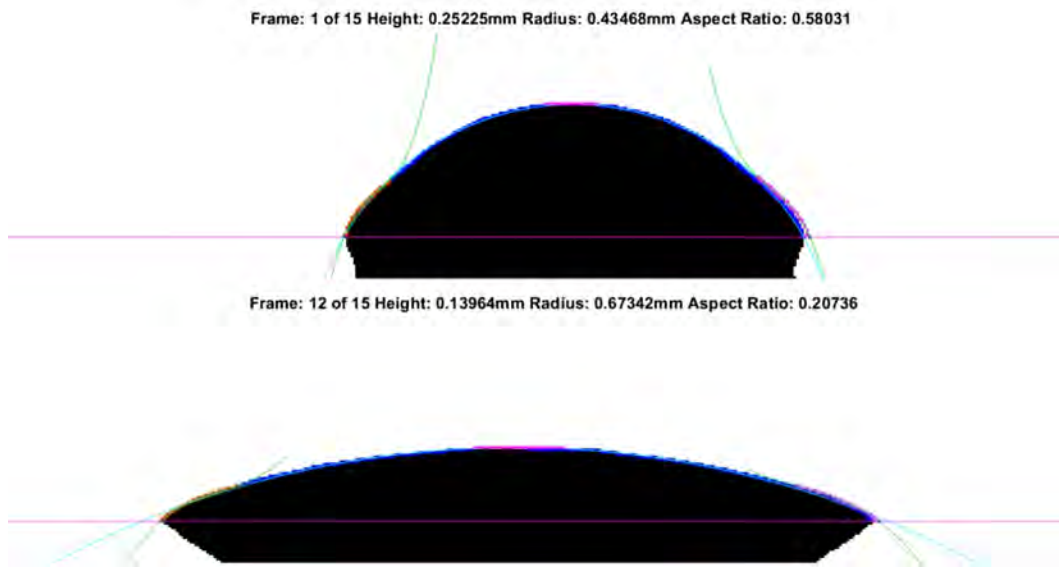


Figure 6.2: Droplet Analyser V14 Matlab figure - Green lines show polynomial fit, the dark blue line shows circle fit and the straight pink line is a baseline set by the user.

To measure the contact angle of the thresholded droplets, the .avi file was saved into the same folder as the Droplet Analyser V14 Matlab code, which was developed by previous colleagues and students at NTU, with the most recent version being developed by Dr Andrew Edwards. This code can determine the contact angles of both the left and right sides of the droplet by setting a baseline to measure from, which is the pink line in figure 6.2. Either a circle fitting (dark blue line) or a polynomial fitting (green lines) algorithm could be chosen as the preferred method of measuring the contact angle. In most cases the discrepancy between the two methods was minimal, but the average of the two methods was always taken in case there was some disagreement. The radius and height of the droplet could also be measured using the software. Figure 6.3 shows two graphs produced by the droplet analyser code, the left one showing the radius measurements and the right one showing the two fitting algorithms and their moving average (light green line). The x-axis on the graphs is time due to the

fact it is several stacked images in a .avi file and it represents the time in the video. The x-axis was later manually changed when importing the outputted values into Excel to a more appropriate unit, such as voltage.

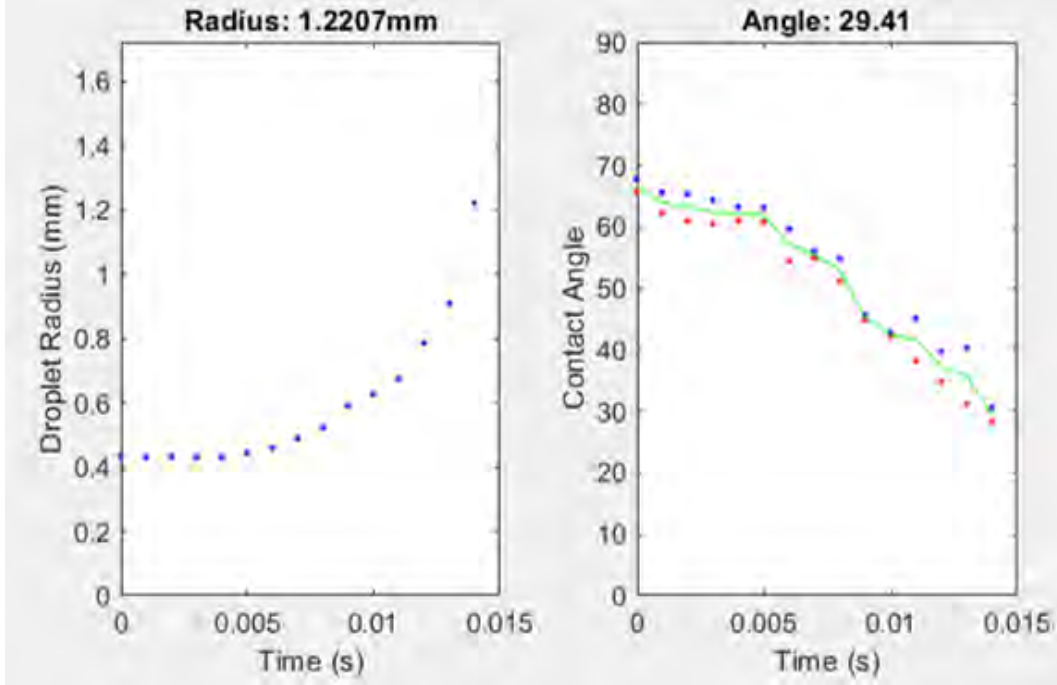


Figure 6.3: Radius and contact angle graphs from Droplet Analyser V14 code - Contact angle plot shows the circle fit (blue dots), polynomial fit (red dots) and the moving average of both (light green line).

6.2.2 Thread measurements

All data for the length and width of liquid threads (section 8) was achieved via manual measurements in ImageJ using photos taken from the top view camera with either a 5x or 10x lens with an LED ring light for illumination. The devices always had some sort of inbuilt scale bar, such as the 5x5mm central area, so no external calibration scale ever had to be used to calibrate the measurements. For dynamic thread measurements with time dependence, videos were taken and saved as .avi files with frame rates typically around 20FPS. These .avi files could then be uploaded as image stacks into ImageJ where the length can be measured when the exact time in the video is known.

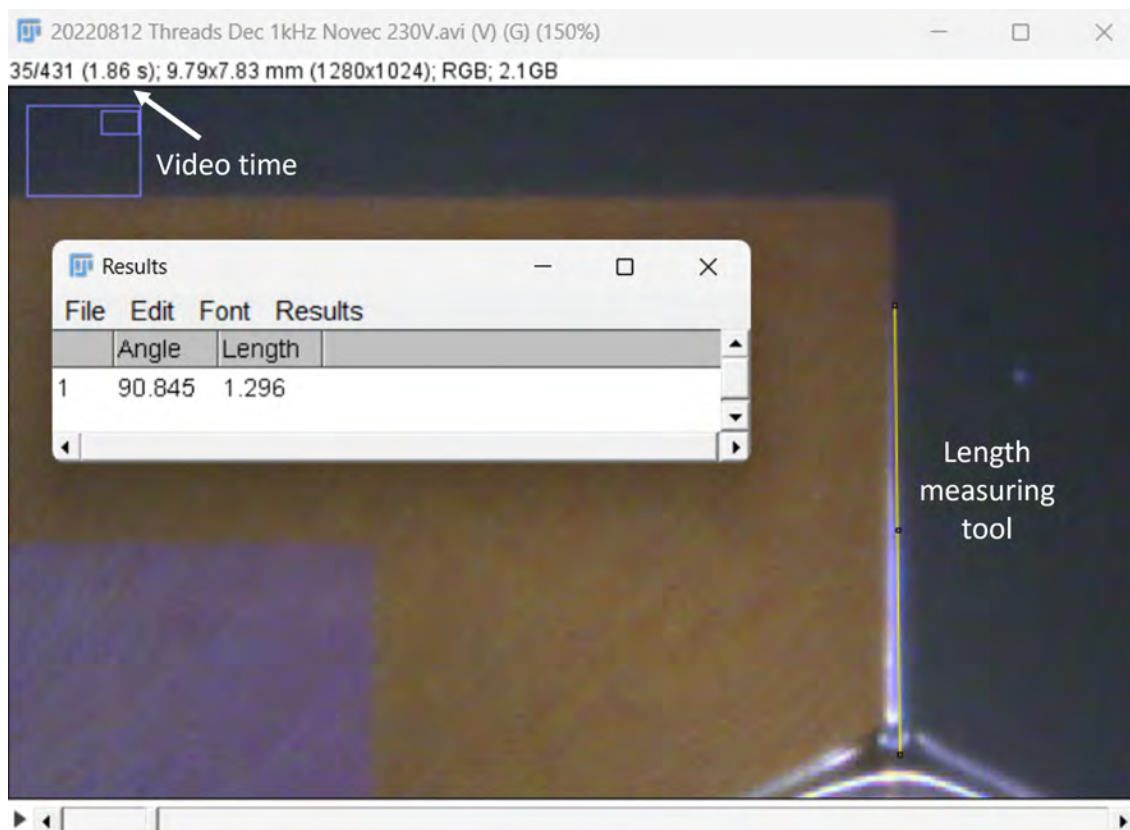


Figure 6.4: Measuring threads in ImageJ

6.2.3 Particle analysis

To determine the locations of the polymer microspheres in section 9, it would have been impractical and very time-consuming to measure the distance of each one from the centre of each hole or stripe manually by using the distance tool that was used to measure the length of the threads (figure 6.4). Instead, the images needed to be rotated, cropped, converted to greyscale, thresholded and put into the ImageJ ‘analyse particles’ function. The minimum and maximum area were set to a range so that only single microspheres were selected, and any clumps or small other bits of debris were ignored. This was typically between $100\text{-}300\mu\text{m}^2$ since the area of the particles could vary with things such as focus, light intensity, and the way they were thresholded. The circularity was also set to 0.8 to further ensure only microspheres were analysed. The centre x-y coordinates outputted by this function could then be used to

determine the relative positions of the microspheres to the background electrode depending on the pattern, either using MOD functions in Excel (for striped geometry) or a Matlab code (for circle geometry).

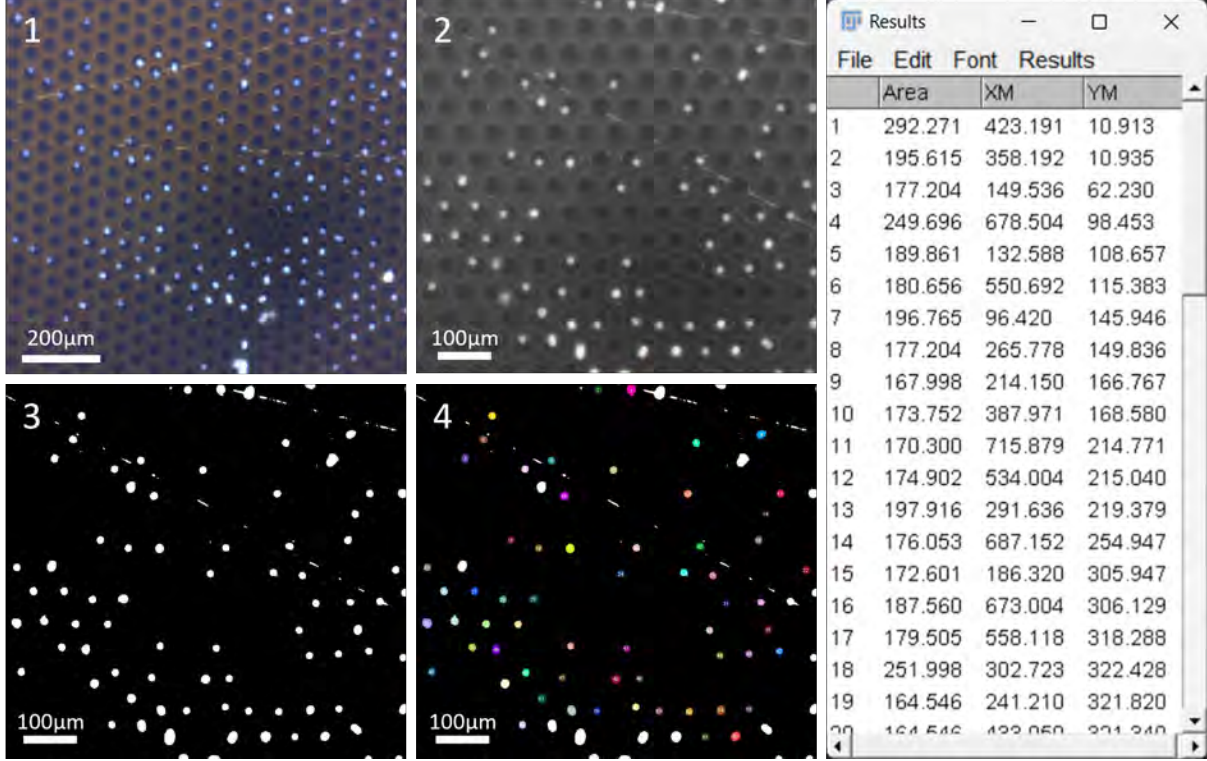


Figure 6.5: Particle DEP analysis method using ImageJ

6.2.4 Microdroplet measurements

There were a couple of methods used to measure the size of the microdroplets in sections 8.5 and 10. The simplest was to use the length tool in ImageJ on a zoomed-in image. For section 8.5 this was only done along the axis of spreading and 3 measurements were taken for each before being averaged. For section 10 this was done along multiple axes (as seen in figure 6.6) which were then averaged. In addition to being very time-consuming to measure the droplets manually, a major flaw in this method was that there was never a well-defined edge to the droplet which meant there was a certain degree of subjective interpretation to the data.

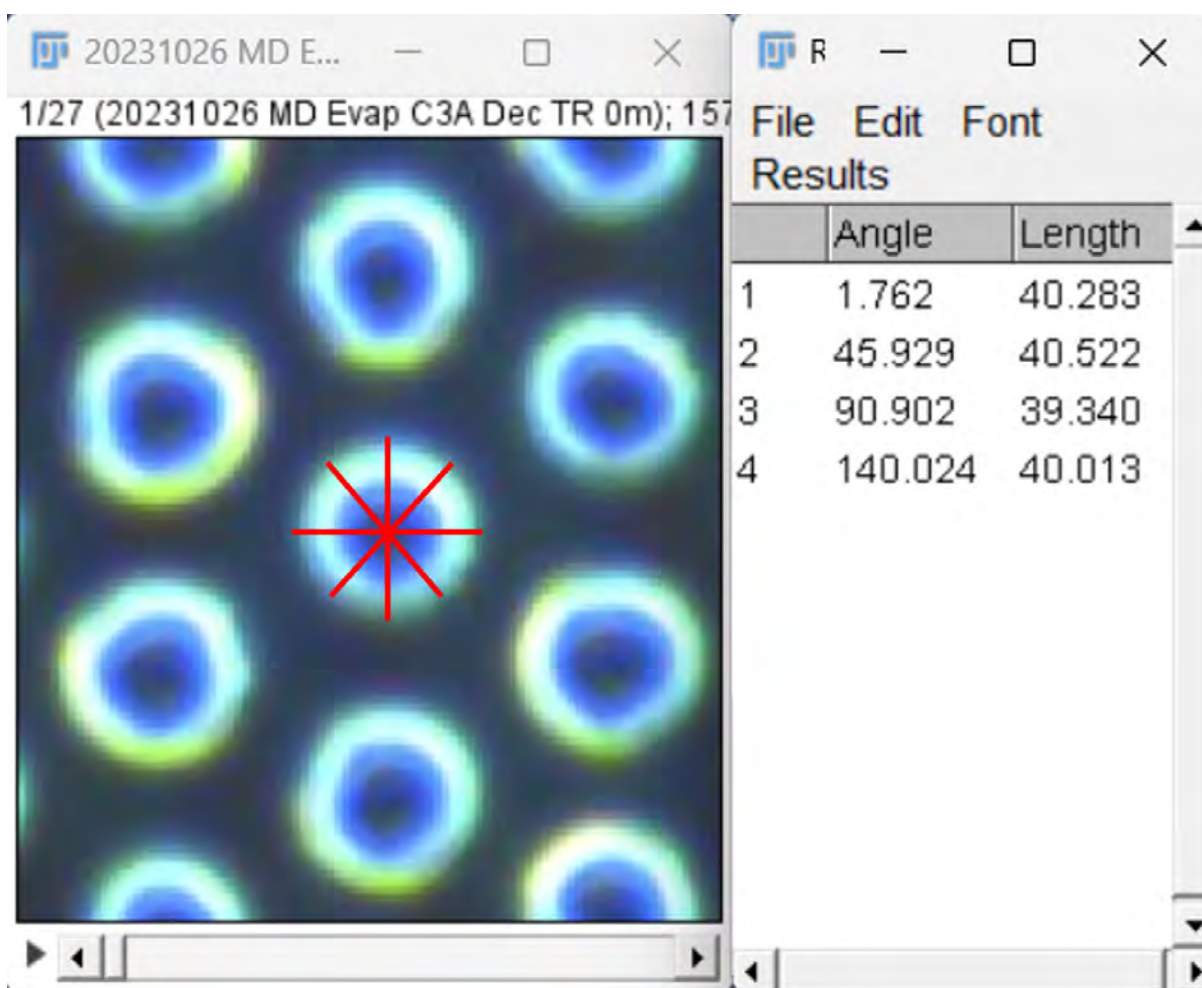


Figure 6.6: Manually measuring microdroplets using length tool in ImageJ

For a quicker and less subjective analysis of microdroplet size, a thresholding method was used in ImageJ. However, this did come with its issues since lighting levels and focus affected the final thresholded size of the microdroplets. Therefore, cross-checking the size of the thresholded droplets with their size measured using the manual length method was important to make sure the correct threshold algorithm was used in ImageJ to get the most accurate result.

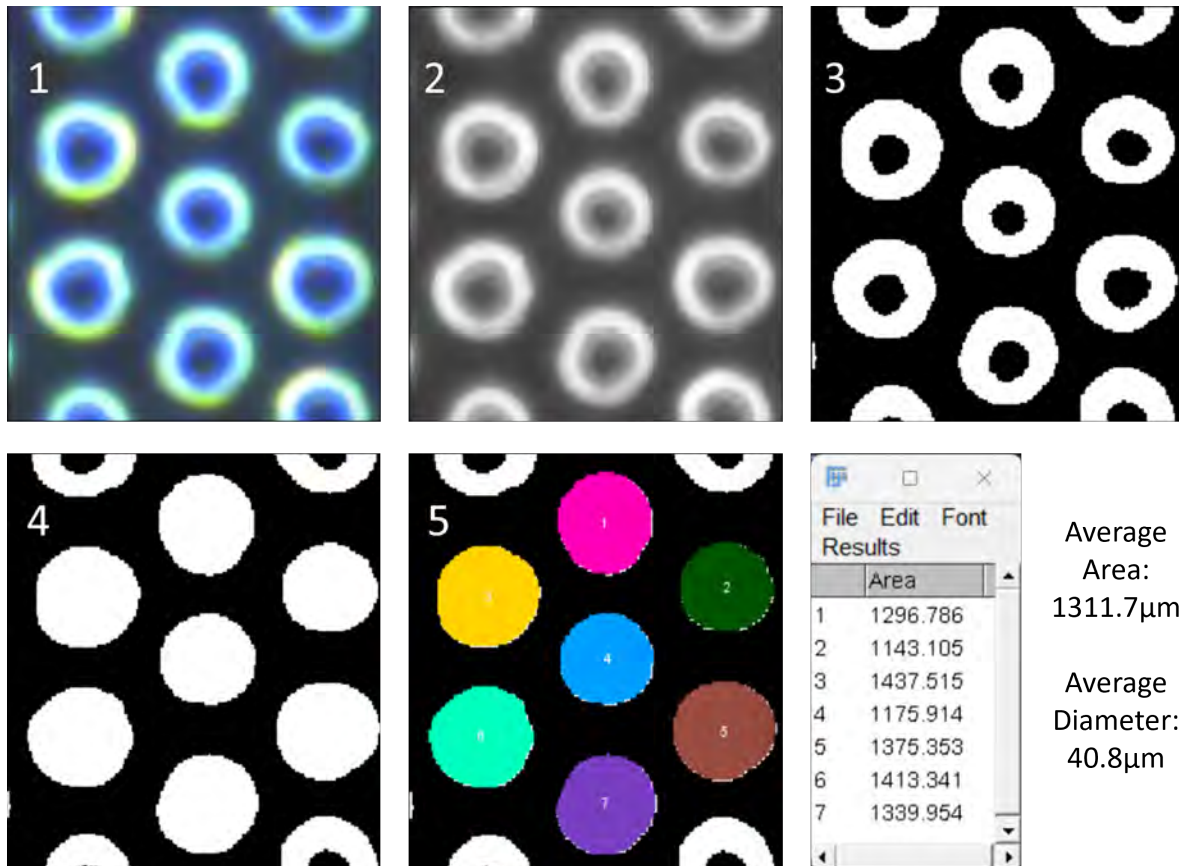


Figure 6.7: Measuring size of microdroplets using thresholding in ImageJ

Figure 6.7 shows the steps that were used to obtain the microdroplet area in ImageJ. They are as follows:

1. Obtain a clear zoomed-in image of the microdroplets. This was done using either a 10x or 20x microscopic lens on the camera.
2. Convert the coloured image to an 8-bit black and white image in ImageJ.
3. Use one of the appropriate thresholding algorithms built into ImageJ. This needed testing to see which one gave the best result and cross-checking against the manual measurements. The most common thresholding algorithms used were Default, Otsu, Max Entropy and Li.
4. Use the 'fill holes' function to fill in the thresholded white rings. This is due to the fact

a ring light was being used, which gave a black interior after thresholding.

5. Use the ‘analyse particles’ function to detect all the thresholded droplets. The minimum area and circularity were often tweaked to ensure only the droplets were getting picked up and not other things such as specks of dust or scratches.
6. Once the area is given by the function, the diameter/base radius can then be extrapolated if we assume that they are circular.

7 Dielectrowetting

The first major area of research of the PhD was to investigate the dielectrophoresis-induced wetting of a sessile droplet. This has been done several times in the past using coplanar interdigitated electrodes on a glass substrate with a thin dielectric layer on top [151] [165]. In addition to spreading a droplet, the same geometry was used to study the dewetting of a thin film into a sessile droplet [166] [167]. This chapter aims to describe and explain how the novel MOS capacitor geometry was not only able to reproduce the results of previous dielectrowetting experiments, but also produce new phenomena that are not possible with the coplanar IDE geometry which are documented in 4.4.2.

7.1 Uni-directional dielectrowetting

The first step was to reproduce what is known as ‘uni-directional dielectrophoresis induced wetting’ or ‘uni-directional dielectrowetting’. This refers to the ability to spread a sessile droplet along only one axis so that its length, but not width, increases as a function of the voltage applied. The droplet’s contact angle along the axis of spreading also decreases as a function of the voltage. On previous coplanar IDE geometries [151] [165], a linear relationship between the cosine of the contact angle and the square of the voltage was established. This relationship was analytically derived using the surface energy of the droplet, Young’s equation and the electrostatic potential energy from Maxwell’s equations. Due to the electrostatic potential energy in a capacitor being proportional to voltage squared [168] and the fact we were using a sessile droplet that obeys Young’s equation, the same linear relationship was expected from the new geometry.

To achieve uni-directional dielectrowetting, long rectangular holes (or stripes), were patterned into the metal electrode via photolithography. The overall electrode size was 9x7mm and the striped area was 5x5mm. Indium solder was used to connect the metal electrode to 0V whilst

the live voltage terminal was soldered to the p-type silicon underneath the oxide layer. More information on this can be found in section 5.1. The length of the stripes was 5mm and four different widths were tested, of which three are presented in the analysis below. The stripe widths were $5\mu\text{m}$, $10\mu\text{m}$, $20\mu\text{m}$ and $40\mu\text{m}$. The width of the metal in between each stripe was chosen to always be the same as the stripe width. For example, the $20\mu\text{m}$ stripes would be a $20\mu\text{m}$ stripe of silicon oxide, then a $20\mu\text{m}$ stripe of metal, then a $20\mu\text{m}$ stripe of silicon oxide and so on. This pattern repeats over the entire 5mm area of interest, giving a total of 125 silicon oxide stripes and 123 metal stripes. Hence, the thinner the stripes, the more of them will be under a droplet of a given size. This is important since the number of edges per unit area increases with thinner stripes.

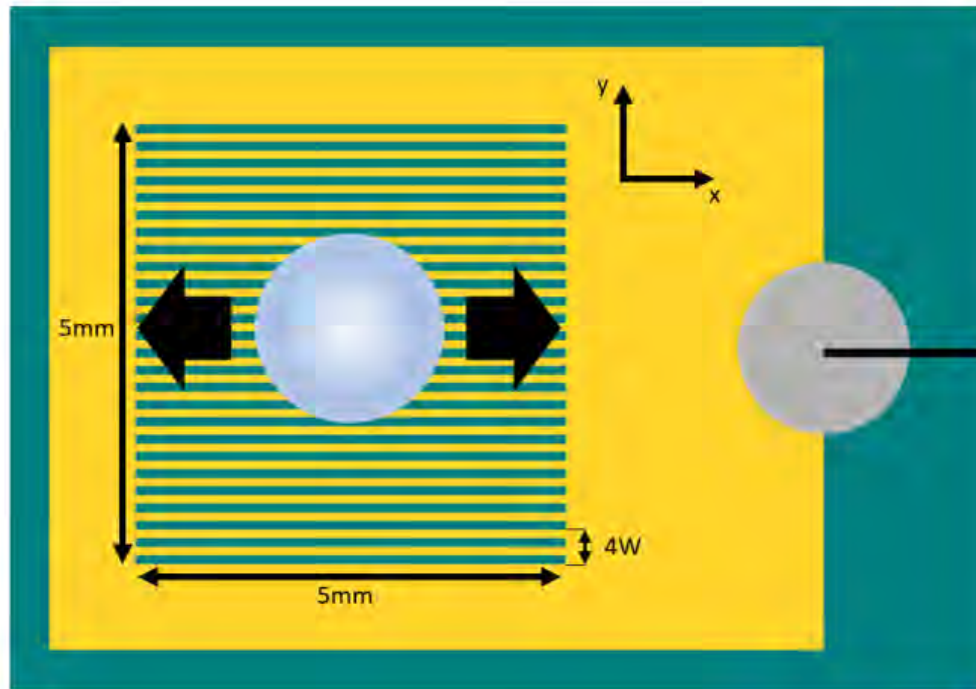


Figure 7.1: Top view of long rectangular stripes. Droplet spreads along the x-axis when a voltage is applied.

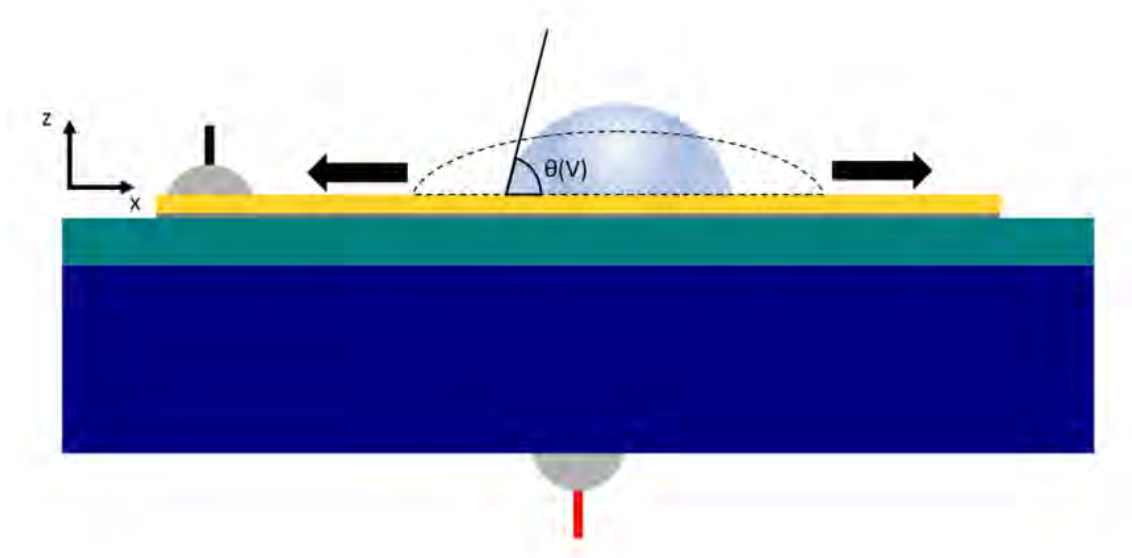


Figure 7.2: Cross-sectional view of device. Droplet spreads along the x-axis and the contact angle decreases as a function of voltage.

7.1.1 Experiment on striped electrodes using TMPTGE

In the early stages of the PhD, the liquid of choice was Trimethylolpropane triglycidyl ether, or TMPTGE for short. This liquid was chosen because of its excellent dielectric properties, non-volatility, low conductivity and relatively high equilibrium contact angle ($\approx 75^\circ$) on the hydrophobic coating of choice, NOVEC 2702. It has been used previously at NTU [166] [167] and produced reliable and consistent results.

A $2\mu\text{L}$ droplet of TMPTGE was dispensed into the centre of the $5\times 5\text{mm}$ striped electrode pattern. The three stripe widths chosen for this experiment were $10\mu\text{m}$, $20\mu\text{m}$ and $40\mu\text{m}$. Each stripe width was tested one at a time on the same device to ensure consistency throughout the experiment. An AC sinusoidal voltage was applied to the device at a frequency of 8kHz . Figures 7.3, 7.4 and 7.5 show the voltages required to spread the droplet for each stripe width.

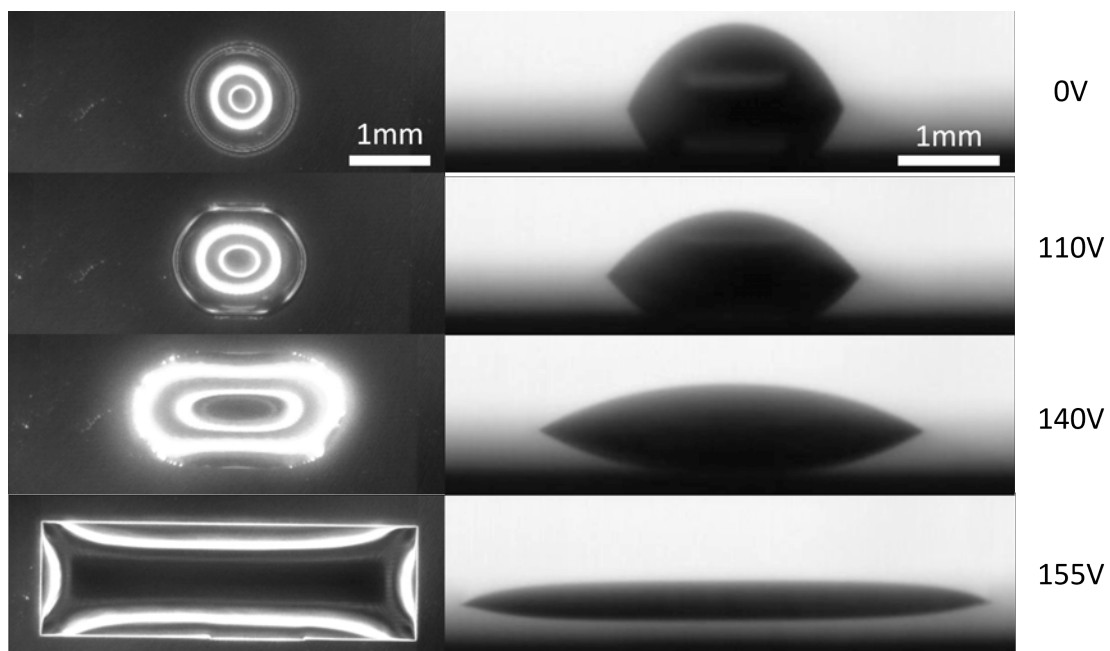


Figure 7.3: TMPTGE droplet spreading on $10\mu\text{m}$ stripes at various voltages

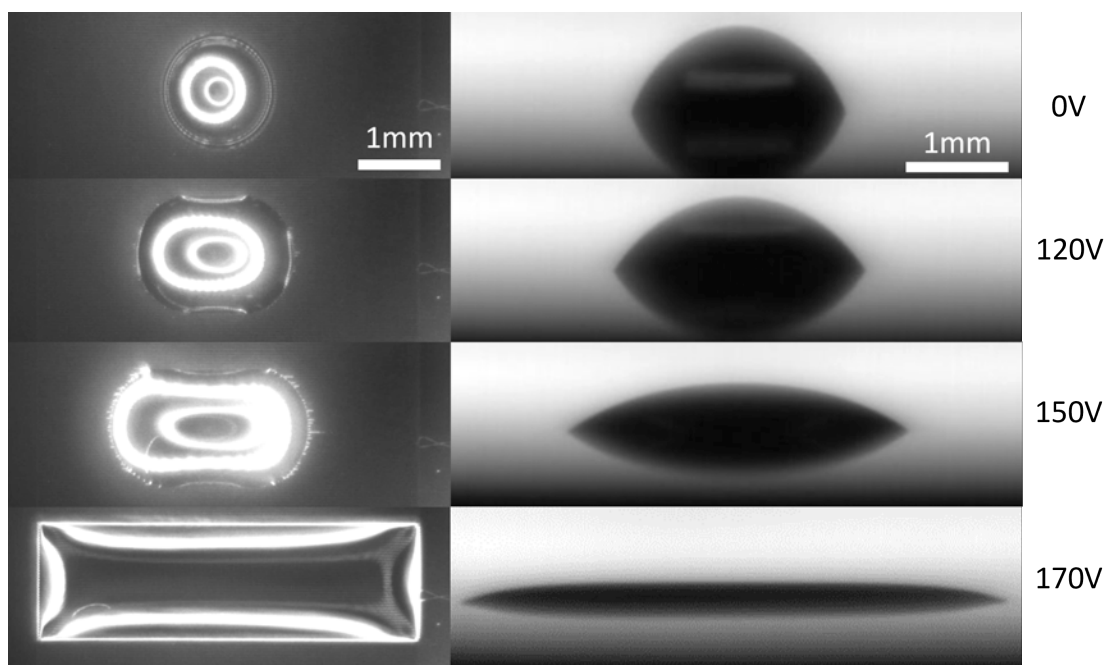


Figure 7.4: TMPTGE droplet spreading on $20\mu\text{m}$ stripes at various voltages

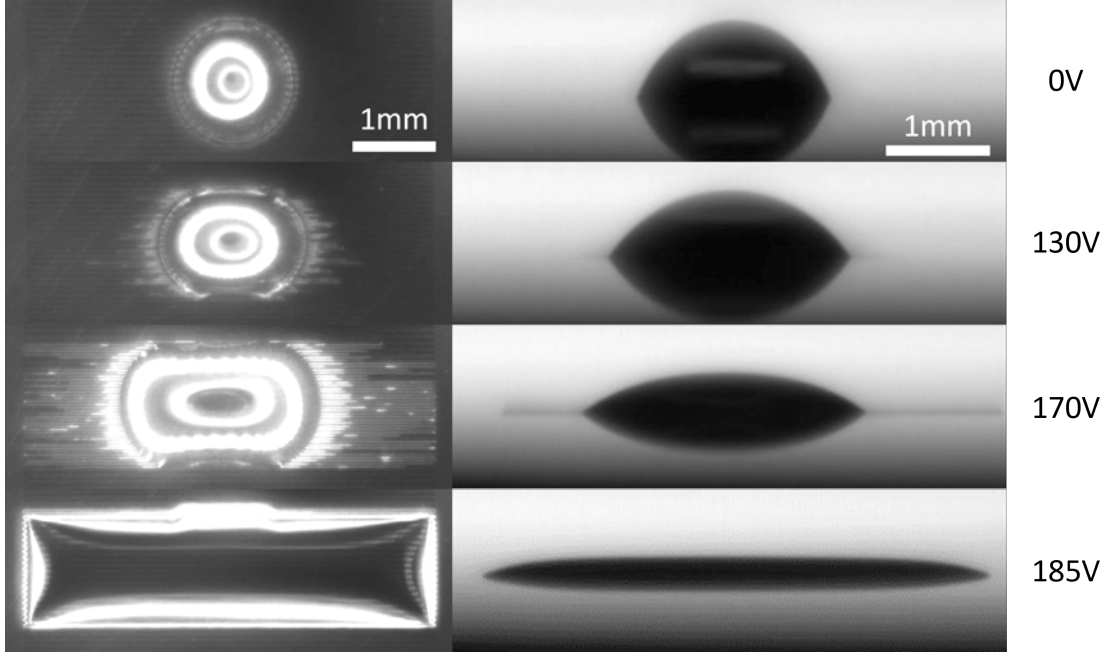


Figure 7.5: TMPTGE droplet spreading on $40\mu\text{m}$ stripes at various voltages

Figures 7.3, 7.4 and 7.5 illustrate how the droplets always spread along the direction of the stripes and do not cross over to neighbouring stripes, therefore elongating and reducing the contact angle of the droplet along the x -axis. Similarly to previous experiments on IDE coplanar electrodes [151], the contact angle is reduced as a function of voltage until the droplet fully spreads to the edge of the patterned area. For the $10\mu\text{m}$ and $20\mu\text{m}$ stripes, the droplet spreads uniformly without any deformities. In contrast, for the $40\mu\text{m}$ stripes, there are thin liquid rivulets or “threads” that get pulled out ahead of the main droplet which extend to the edges of the patterned electrode before the rest of the droplet catches up at a higher voltage. This phenomenon led to a large area of study for this thesis and is documented in chapter 8.

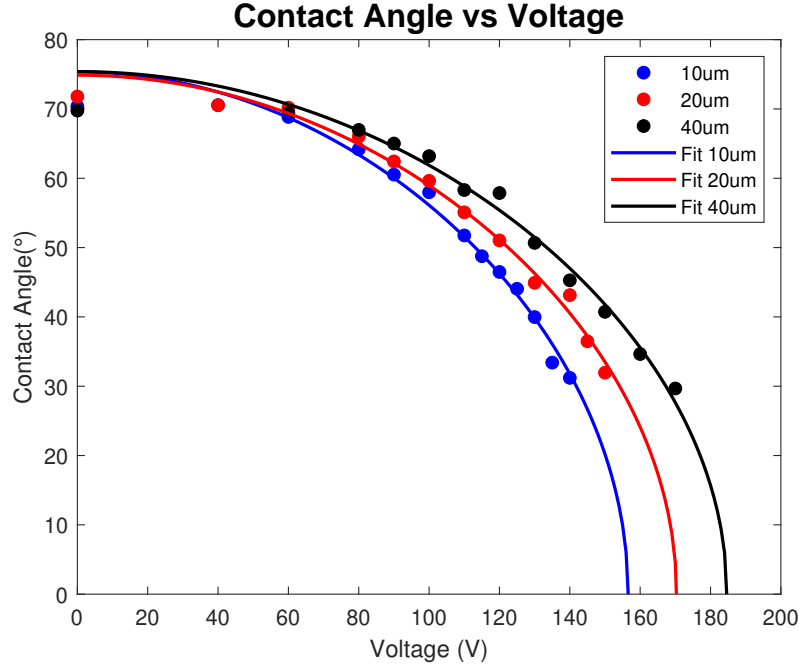


Figure 7.6: Contact angle vs Voltage for uni-directional spreading

The points on figure 7.6 show the contact angle measured using a droplet analyser MATLAB program developed by Dr Andrew Edwards across a range of voltages for three different electrodes with stripe widths of $10\mu\text{m}$, $20\mu\text{m}$ and $40\mu\text{m}$. From the $\text{Cos}(\theta)$ vs voltage squared graph (figure 7.7), the linear gradient was extrapolated to produce best-fit lines on the contact angle versus voltage graph. When calculating the linear gradients from the cosine graph, the initial data point at 0V was not included in the LINEST function. It was decided this was best since the contact angle measurement at 0V was most likely not the true advancing contact angle of the droplet due to the way it had been dispensed onto the substrate using a handheld pipette. The phenomenon of contact angle hysteresis [169] meant that the contact angle of the newly placed droplet was somewhere between TMPTGE's advancing and receding angle on the Novec 2702. It was only once the dielectrophoretic force started to spread the droplet that the true advancing contact angle for that given voltage was achieved. This notion is backed up by figure 7.6, since the measured initial contact angles for the three droplets range from 69.8° to 71.8° , but the best fit lines all intersect the y-axis between 74.8° and 75.4° . This would suggest that the true advancing contact angle at 0V would fall somewhere in this

range.

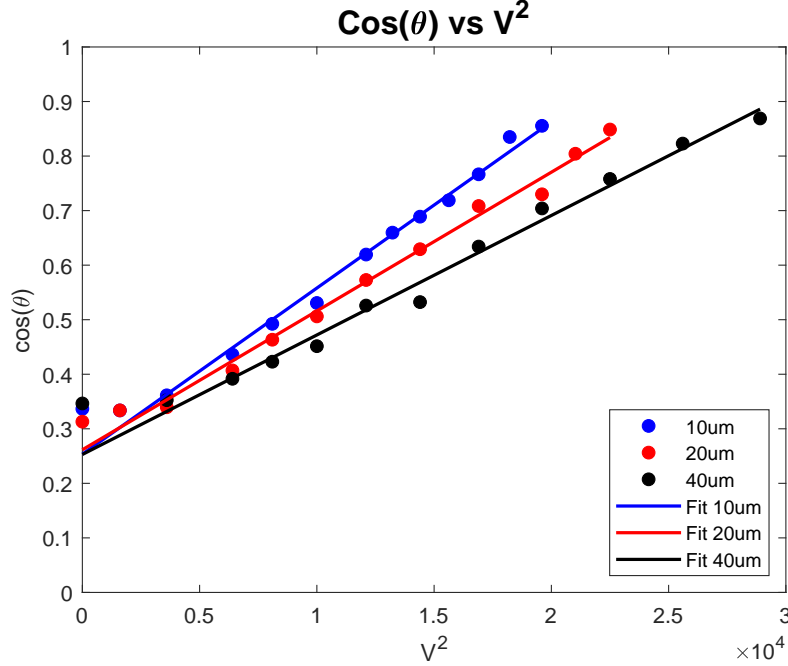


Figure 7.7: $\cos(\theta)$ vs Voltage squared for uni-directional spreading

Like the IDE co-planar geometry, a clear linear relationship between the cosine of the contact angle and voltage squared was achieved for all three stripe widths. The expectation that the thinner stripes, with more edges per unit area, would spread the droplet more strongly at a given voltage was also confirmed by this experiment. The gradients for the $10\mu m$ and $20\mu m$ stripes are 1.39 and 1.16 times that of the $40\mu m$ stripes respectively. Due to the limited size of the electrodes and the reduced accuracy in measuring small contact angles of a small droplet, voltage readings that reduced the contact angle below 30° were not taken. If instead the trend is followed to see at what voltage a theoretical contact angle of 0° and hence full wetting is achieved, the results are 156.6V at $10\mu m$, 170.3V at $20\mu m$ and 184.6V at $40\mu m$. Before reaching these theoretical voltage values the droplet fully spreads along the entire 5mm length of the electrode, keeping the contact angle at a fixed value above zero. It can also be seen from the photos (figures 7.3-7.5) that once the droplet fully spreads it no longer maintains a sessile circular cap geometry, but instead has a horizontal flat top with a gradual slope at each end.

7.1.2 Comparing results with microstrip capacitance theory

These experimental values can be compared to the values predicted by the modified version of Young's Law for multiple parallel microstrip capacitors. These equations were derived by incorporating microstrip capacitance theory from Kwok [170] and Barbuto [171] into previous dielectrowetting theory from Mchale [151]. In its full form, the modified equation is:

$$\cos(\theta(V)) = \cos(\theta_Y) + xy \frac{\varepsilon_0 V^2}{4W\gamma_{LV}} \quad (7.1)$$

$$x = \frac{\varepsilon_{liq} - \varepsilon_{air}}{2} + \frac{\varepsilon_{air} - \varepsilon_{liq}}{2} \left(1 + \frac{12t_h}{W}\right)^{-0.5} \quad (7.2)$$

$$y = \frac{W}{t_h} + 2\pi \left(\frac{1}{\ln\left(\frac{8t_h}{W} + 1\right)} - \frac{W}{8t_h} \right) \quad (7.3)$$

When plugging in the relevant values for liquid permittivity ($\varepsilon_{liq} = 13.8$ [172]), air permittivity ($\varepsilon_{air} = 1$), oxide thickness ($t_h = 1\mu m$), stripe width ($W = 10\mu m, 20\mu m$ and $40\mu m$), permittivity of free space ($\varepsilon_0 = 8.854 \times 10^{-12} m^{-3} kg^{-1} s^4 A^2$ [173]) and liquid surface tension ($\gamma_{LV} = 43 mN/m$ [172]), the theoretical coefficient of the V^2 term for each stripe width can be determined. The ratio of these coefficients can be compared to the experimental values, and they can be used to plot a theoretical contact angle versus voltage graph which can be compared to the experimental graph.

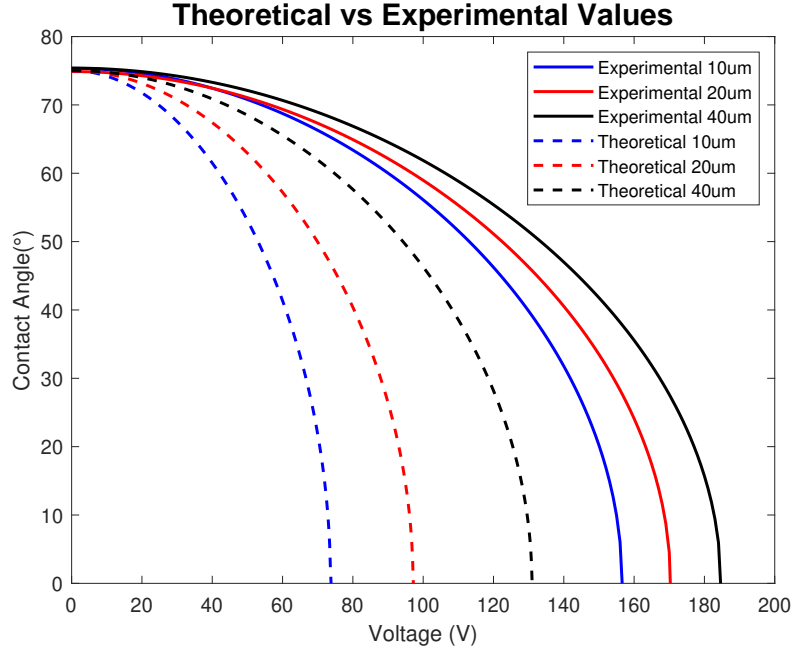


Figure 7.8: Comparing theoretical and experimental plots for uni-directional spreading

Figure 7.8 shows that the theory predicts the droplet's contact angle should decrease at a faster rate than seen in the experiments. The theory also predicts that the ratios between the coefficients of V^2 for the different stripe widths should also be larger than what the experimental results produced. Several mechanisms were postulated to explain this. Before exploring these, it is worth noting that the theory at least falls within the same order of magnitude as the experimental results. It is also important that the theory predicts a lower voltage, and hence energy, requirement to spread the droplet than the experimental results. This is because the theory predicts a perfect system where no energy is lost, so it should be expected for the experimental results to require a higher voltage.

A potential explanation for why the experimental droplets require a higher voltage to spread is due to the friction on the surface, which exerts a force against the direction of spreading. Additional work would be required by the dielectrophoretic force to overcome this, requiring a higher voltage. It is also possible that the parallel microstrip capacitor theory is an overly simplistic way of modelling the geometry used in the experiments. For example, the real devices are not perfect conductors on the bottom plate and there is a thin layer of hydrophobic

coating above the electrodes. In addition, the microstrip capacitor theory is used to determine the capacitance of a single microstrip. To derive the energy for the modified Young's law (eq 7.1), it is assumed that the capacitance of a single microstrip can be multiplied by the number of stripes in parallel. However, placing them in close proximity would cause some interaction between the neighbouring microstrips and their fringing fields, reducing the overall capacitance and electric field strength and therefore requiring a higher voltage to spread the droplet. This may also explain why the V^2 coefficients for the three widths are closer in the experiment than in theory, due to the thinner stripes being in closer proximity than the wider stripes and hence having stronger interference with their neighbouring stripes.

To justify the hypothesis that the electric fields of neighbouring microstrips interact with each other, 2D electrostatic simulations were carried out on ANSYS Electromagnetics Suite 19.2. The first scenario tested was that of a single microstrip with a sufficiently large gap to ensure it would not interact with its neighbour under periodic boundary conditions. A gap of 1mm was assumed to be sufficient in this case (figure 7.9 A). The second scenario tested was for a microstrip with width W , which had periodic boundary conditions of $2W$ that reflected the geometry of the real electrodes (figure 7.9 B).

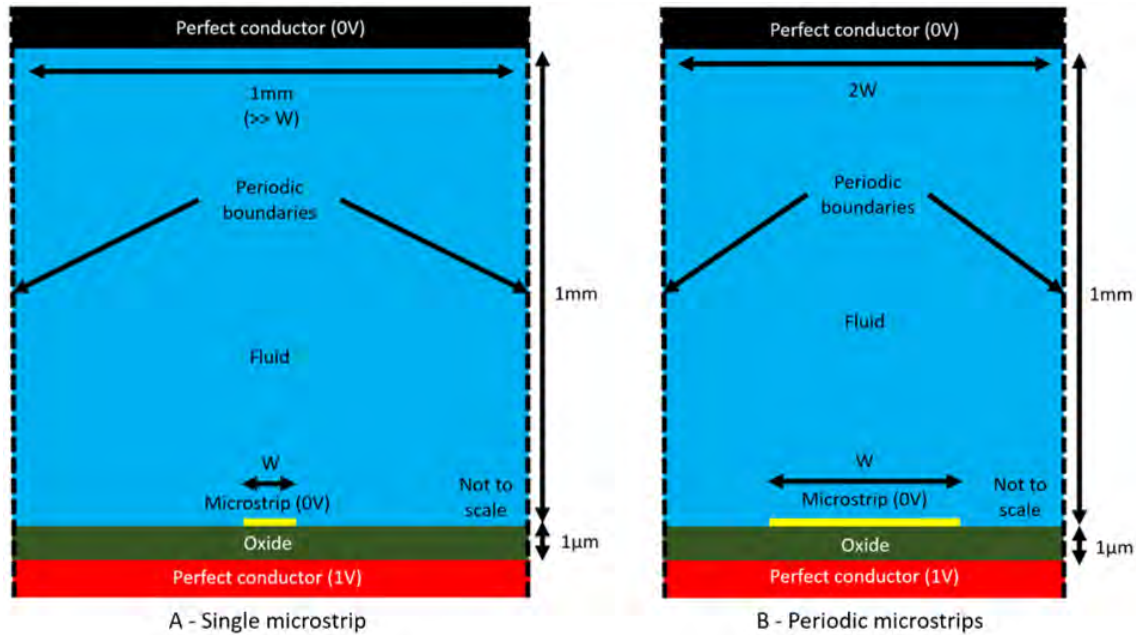


Figure 7.9: Diagrams show the difference between single and periodic microstrip simulations

An important consideration when designing the geometry of these simulations was the electrode potential configuration. In addition to the potentials of the microstrip and p-type silicon, it must be assumed that the potential at infinity is 0V. This means having to introduce another electrode above the fluid. However, this effectively makes a second parallel plate capacitor between this electrode and the p-type silicon, creating an additional electric field independent of the microstrip capacitor. To ensure this field is negligible to that produced by the microstrip capacitor, the top electrode had to be at a sufficiently large enough distance to ensure the capacitance of this additional parallel plate capacitor was small. To check that most of the energy in the system was concentrated in the oxide and around the vicinity of the microstrip ($< 100\mu m$) above the surface), a simulation was run with the fluid broken down into ten blocks of height $< 100\mu m$ up to $1mm$ above the surface. The parameters used for the simulation were:

$1mm$ wide periodic boundary

$20\mu m$ wide single microstrip (0V)

$1mm$ distance ground electrode (0V)

P-type silicon electrode (1V)

$1\mu m$ thick silicon oxide ($\epsilon = 4$)

$100nm$ thick gold microstrip electrode

TMPTGE as fluid ($\epsilon = 13.8$)

Air as fluid ($\epsilon = 1$)

All electrodes were set as ‘perfect conductors’

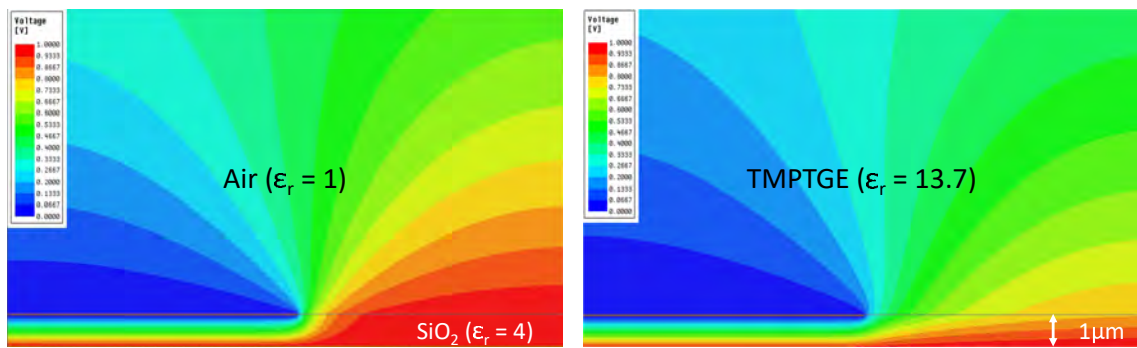


Figure 7.10: ANSYS simulation showing electric potential lines at electrode edge

The simulation was run for both TMPTGE and air. The energy for each block is listed in table 1.

	TMPTGE (J/m)	Air (J/m)
Total Energy	5.59×10^{-10}	3.87×10^{-10}
Oxide	3.94×10^{-10}	3.71×10^{-10}
0-100 μm	1.138×10^{-10}	1.27×10^{-11}
100-200 μm	5.95×10^{-12}	4.35×10^{-13}
200-300 μm	5.73×10^{-12}	4.25×10^{-13}
300-400 μm	5.70×10^{-12}	4.24×10^{-13}
400-500 μm	5.688×10^{-12}	4.23×10^{-13}
500-600 μm	5.686×10^{-12}	4.23×10^{-13}
600-700 μm	5.685×10^{-12}	4.23×10^{-13}
700-800 μm	5.685×10^{-12}	4.23×10^{-13}
800-900 μm	5.685×10^{-12}	4.23×10^{-13}
900-1000 μm	5.685×10^{-12}	4.23×10^{-13}
SUM 100-1000 μm	5.15×10^{-11}	3.82×10^{-12}

Table 1: Table of energies for the oxide and 100 μm blocks of fluid above it

The results from the simulations show most of the energy in the system is stored in the oxide layer for both air and TMPTGE. For TMPTGE, 20% of the total energy is stored in the fluid between 0 – 100 μm . This value is only 3% for air. For both fluids, the energy from 100 – 1000 μm was summed to see how much energy was being stored by the larger parallel plate capacitor. This amounted to 9% for TMPTGE and 1% for air. This was considered small enough for the purposes of the test. Table 1 also shows that for both fluids, the energy stored per 100 μm block drops off by more than an order of magnitude at more than 100 μm above the surface. Note that the energy dimensions are in J/m since this simulation is a 2D cross-section of the geometry.

Once it was established that most of the energy in the system comes from the microstrip capacitor, the next step was to test whether the electrode potential configurations (1V/0V/0V), (0V/1V/0V) or (-0.5V/0.5V/0V) played a significant role in the energy. The simulations showed the difference was only 2%, so the configuration is not an important factor and the

(1V/0V/0V) configuration was chosen for all future simulations.

The final check to make sure everything was being simulated correctly was to make sure the energy in the simulation scaled as a function of the voltage squared, as by:

$$E_n = \frac{\varepsilon}{2} \int_{V_l} |E|^2 dV_l \quad (7.4)$$

where E_n is the energy stored in an electric field, ε is the dielectric permittivity of the material, E is the electric field, and V_l is the volume. Since the electric field is proportional to voltage and the energy is proportional to the electric field squared, the energy is therefore proportional to the voltage squared.

Voltages from 0V to 10V were tested on a $20\mu m$ microstrip for both air and TMPTGE, and the total energy in the system was plotted against voltage squared. The energy was indeed linearly proportional to voltage squared as seen in figure 7.11, verifying the simulation was correctly calculating the energy in the system.

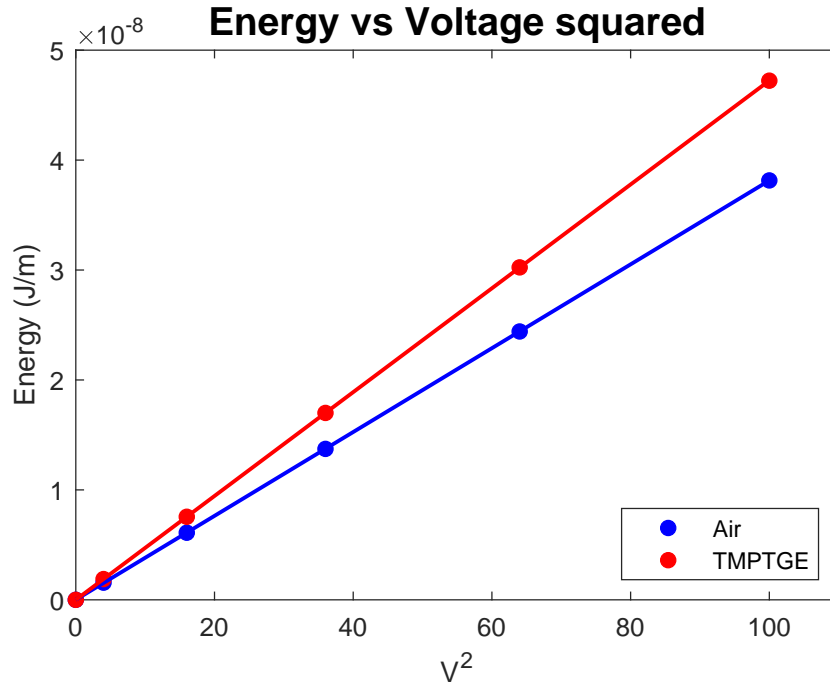


Figure 7.11: Energy vs Voltage squared in ANSYS simulation

Once all preliminary checks were done on the ANSYS simulation, the two scenarios in figure 7.9 were tested for the three microstrip widths. Table 2 shows the results of these simulations.

	Width (μm)	Periodic (J/m)	Single (J/m)	Difference (%)
Air	10	2.02E-10	2.07E-10	2.75
	20	3.81E-10	3.83E-10	0.47
	40	7.37E-10	7.41E-10	0.35
TMPTGE	10	2.64E-10	3.11E-10	17.76
	20	4.69E-10	5.08E-10	8.11
	40	8.53E-10	8.84E-10	3.63
TMPTGE - Air	10	6.18E-11	1.03E-10	66.85
	20	8.87E-11	1.25E-10	40.92
	40	1.15E-10	1.44E-10	24.56

Table 2: Energies for each condition in air, TMPTGE and the difference between them

The results of the simulation reveal that there is very little difference between the single microstrip and periodic boundary case in air, for all widths. On the other hand, in TMPTGE there becomes a significant reduction in energy in the periodic boundary case compared to the single microstrip, especially for the $10\mu\text{m}$ case (17.76%). This infers there is some interaction going on between the electric fields of neighbouring microstrips. Additionally, what creates an even larger discrepancy between the single and periodic case is when the energy difference between TMPTGE and air is calculated. Here we see that there is a difference of 67.85% for $10\mu\text{m}$, 40.92% for $20\mu\text{m}$, and 24.56% for $40\mu\text{m}$. Since it is ultimately the difference in the potential energy of the electric field between the two fluids that produce the DEP force, a large reduction in this difference could be the reason why the experimental results require a higher voltage (and thus energy) than that predicted by the theory in equation 7.1, which assumes many non-interacting microstrips in parallel.

7.1.3 Dielectrowetting frequency dependence

In addition to the obvious voltage dependence that we expect due to a higher electric field strength producing a higher DEP force, there was also a frequency dependence associated

with the dielectrowetting effect. Figure 7.12 shows how the contact angle of a droplet of decanol is affected by the frequency of the electric field at three different voltages on the 0.1-1 Ohm.cm wafers. For each voltage, the frequency was swept from the lowest (50Hz) to the highest (30kHz), and the contact angle decreased as the frequency increased until a saturation frequency of around 2-5kHz, depending on the voltage.

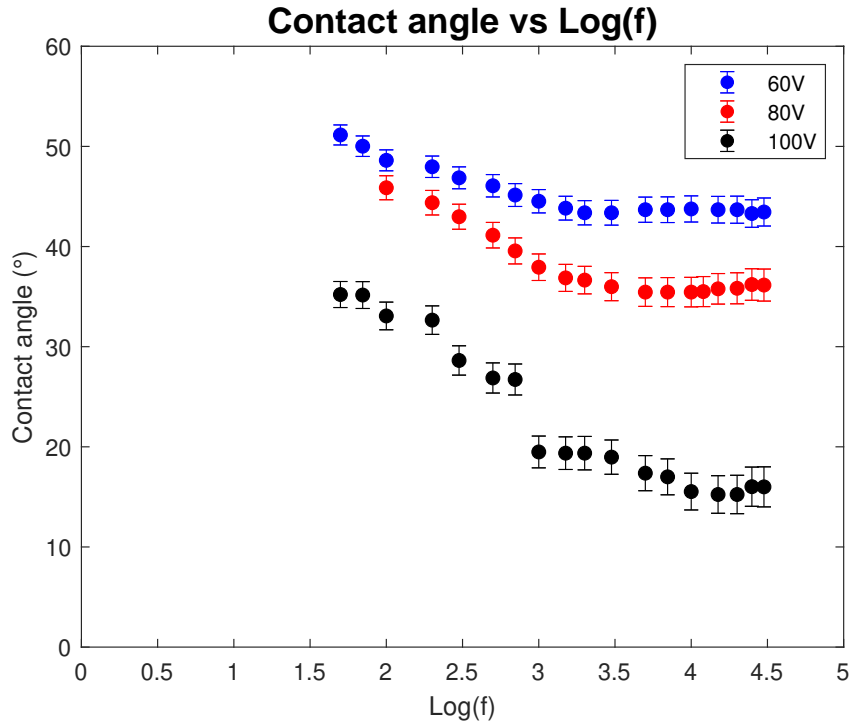


Figure 7.12: Contact angle versus $\log_{10}(f)$ of a decanol droplet on the lower resistivity 0.1-1 Ohm.cm wafers

Since the capacitance of the 0.1-1 Ohm.cm wafers was measured to be practically constant across all frequencies tested (figure 5.8), it can be considered a safe assumption that it is not the wafer that is causing this frequency dependence on the contact angle. Similar frequency dependence was also seen on the higher resistivity 1-10 Ohm.cm wafers, but they were not chosen for this experiment since it was the liquid's frequency dependence that was being tested. Instead, it is hypothesised that the dielectrowetting effect is diminished at lower frequencies due to the conductivity of the liquid. This was also briefly observed in the early stages of the PhD when older propylene glycol that had been left in a small vial for a few weeks tended to require a higher voltage to spread than fresh propylene glycol. Since propylene

glycol is hygroscopic it will absorb water vapour from the air over time, therefore increasing its conductivity and diminishing the dielectrowetting effect. This ageing effect of propylene glycol was the reason its use was discontinued very early on in the project.

7.2 Axi-symmetric dielectrowetting

Since previous coplanar IDE geometries have been limited to having their electrodes separated by equally spaced fingers, this has put severe restraints on the possible electrode designs and therefore limited the ways liquids can be spread using the dielectrowetting phenomenon. Although previous attempts have been made to produce axi-symmetric dielectrowetting by producing a ‘zipper’ style electrode geometry, these produce droplets with wrinkly top surfaces as seen in the 2015 paper by Russell et al. [174]. Due to the nature of the MOS geometry used in this PhD, in which one electrode sits underneath the pattern instead of being part of it, it opens many possibilities in the way the top electrode can be patterned. Consistent repeating patterns can be produced with the same logic as tiling a kitchen floor, which allows for all sorts of shapes of different sizes and combinations. This leads to being able to spread liquids in multiple directions to form a variety of droplet shapes and uniform thin films. Figure 7.13 shows just four patterns used during this project. Yellow in the figure represents where the gold is deposited and black is where there is silicon oxide, similar to the previous striped geometry in section 7.1. From top left to bottom right we have a tessellated array of hexagons, an array of octagons with small squares in between, tessellated crosses, and interlinking “hourglasses”. In all patterns, the width of the gold separating the shapes was kept at a constant $10\mu m$.

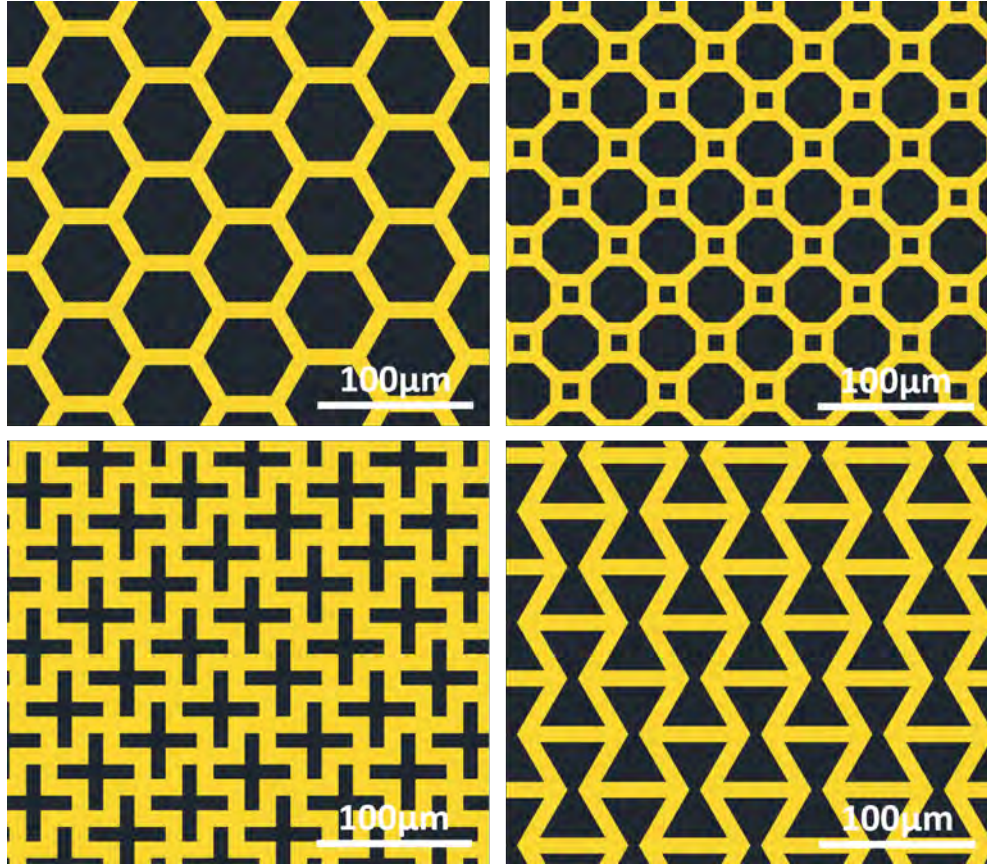


Figure 7.13: Examples of axi-symmetric electrode patterns used. From top left to bottom right - hexagons, octagons and squares, crosses and hourglasses.

7.2.1 Initial issues with axi-symmetric spreading designs

Prior to designing and making the patterns in figure 7.13, earlier attempts for axi-symmetric spreading did not go according to plan. The first design for axi-symmetric spreading produced hexagonal arrays of circular holes of various diameters and spacing. It was expected that the liquid would feel an equal force in all directions by this uniform array and therefore spread as a circular droplet equally in all directions. However, one fundamental problem with this circular hole design was that we ended up with “stagnation lines” between the holes, in which there was no overlap between neighbouring shapes, therefore not allowing the meniscus of the liquid to get close enough to the fringing field of the next shape to “jump across” the gap of gold (figure 7.14). Later on, using liquids with lower contact angles could overcome

this, but since the initial tests were done with TMPTGE it was considered a big hurdle at the time.

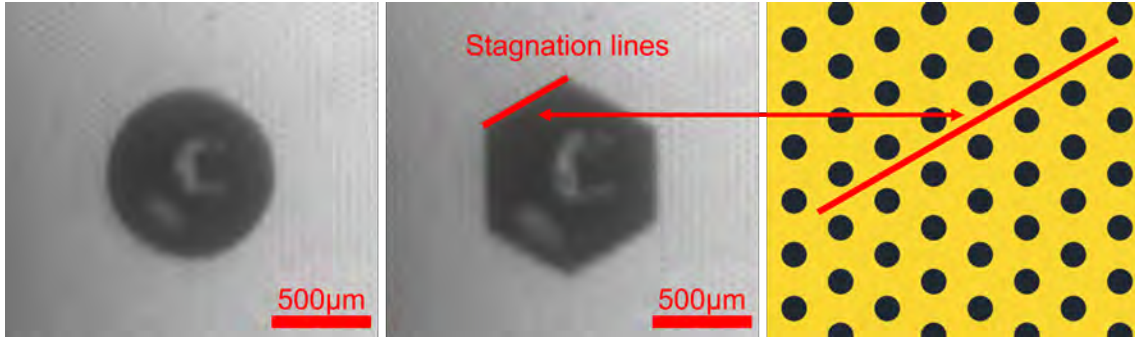


Figure 7.14: TMPTGE droplet unable to cross stagnation lines

When designing new patterns of axi-symmetric spreading, a rule of thumb was to see if a straight line could be drawn from one point on the array to another without crossing the edge of a shape. If this was the case, it was very likely that this line would become a point of stagnation in which the droplet could not spread across. This is what inspired the tessellated array designs in figure 7.13, in which it is not possible to draw a large straight line across the pattern without intercepting the edge of a shape, which always gives the liquid the ability to spread to the neighbouring holes.

7.2.2 Hexagonal axi-symmetric spreading

The easiest solution for the stagnation line issue was to keep a hexagonal array but change from circular holes to hexagonal holes. As seen in the top left of figure 7.13, it is not possible to draw a straight line across the array of tessellated hexagons as long as the gap between them was kept relatively narrow compared to their width.



Figure 7.15: Top view of hexagonal spreading. It shows how the underlying hexagonal electrode geometry (see figure 7.13) influences the symmetry of the droplet. At higher voltages (150V) the droplet is fully spread over the entire electrode area into a thin film.

Measuring the contact angle of axi-symmetric spreading droplets is not as simple as that of uni-directional droplets, as seen in section 7.1. With a uni-directional droplet, a side view camera can be set up so that it is perpendicular to the direction of spreading, and the point of the droplet that is being measured remains at a relatively constant distance away from the camera and in focus. With an axi-symmetrically spread droplet the contact angle changes in all directions, and the droplet is deformed into a polygonal shape (see figure 7.15). This made measuring the true contact angle of the droplet a little more difficult, and thus there are likely to be more errors associated with the data.

Similarly to how different stripe widths were tested in section 7.1, three different hexagon sizes were tested which had edges of length $20\mu m$, $30\mu m$ and $40\mu m$. There was always a fixed gap of $10\mu m$ between the hexagons for all sizes. These are referred to as Hex20, Hex30 and Hex40. Figure 7.16 reveals how the contact angle of a decanol droplet on Novec 2702

changes as a function of voltage at 8kHz for the three different sized hexagonal holes.

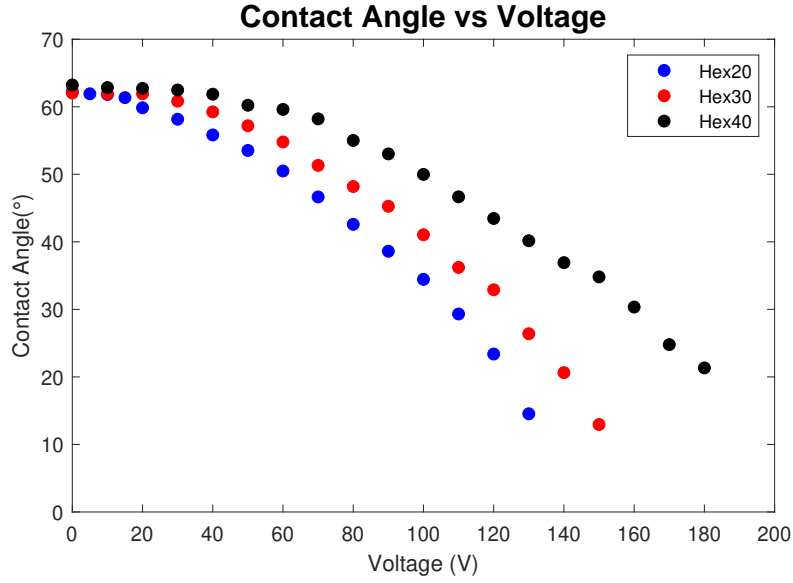


Figure 7.16: Contact angle vs Voltage for axi-symmetric spreading

At first glance, there appears to be a similar relationship to the uni-directional case, but when we plot $\cos(\theta)$ vs V^2 (figure 7.17) it can be seen that there is no longer a linear dependence and that a higher voltage is required to fully wet the droplet in the axi-symmetric case.

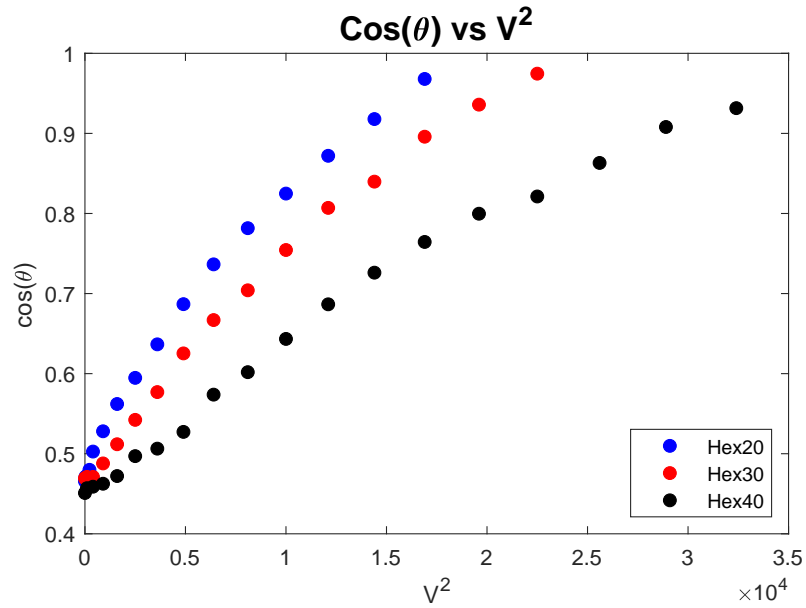


Figure 7.17: $\cos(\theta)$ vs Voltage squared for axi-symmetric spreading

The divergence from the $\cos(\theta)$ vs V^2 relationship is not surprising, since the theory described in section 7.1 only takes into account one direction of spreading, whereas here there are two.

7.2.3 Other axi-symmetric spreading

In addition to tessellated hexagons, several other patterns were tested to see how well they spread in two directions. Figure 7.18 shows some examples of these. The general rule of thumb is that the droplet tended to loosely follow the underlying geometry, albeit at a much lower resolution due to surface tension wanting to pull the droplet into a spherical cap again.

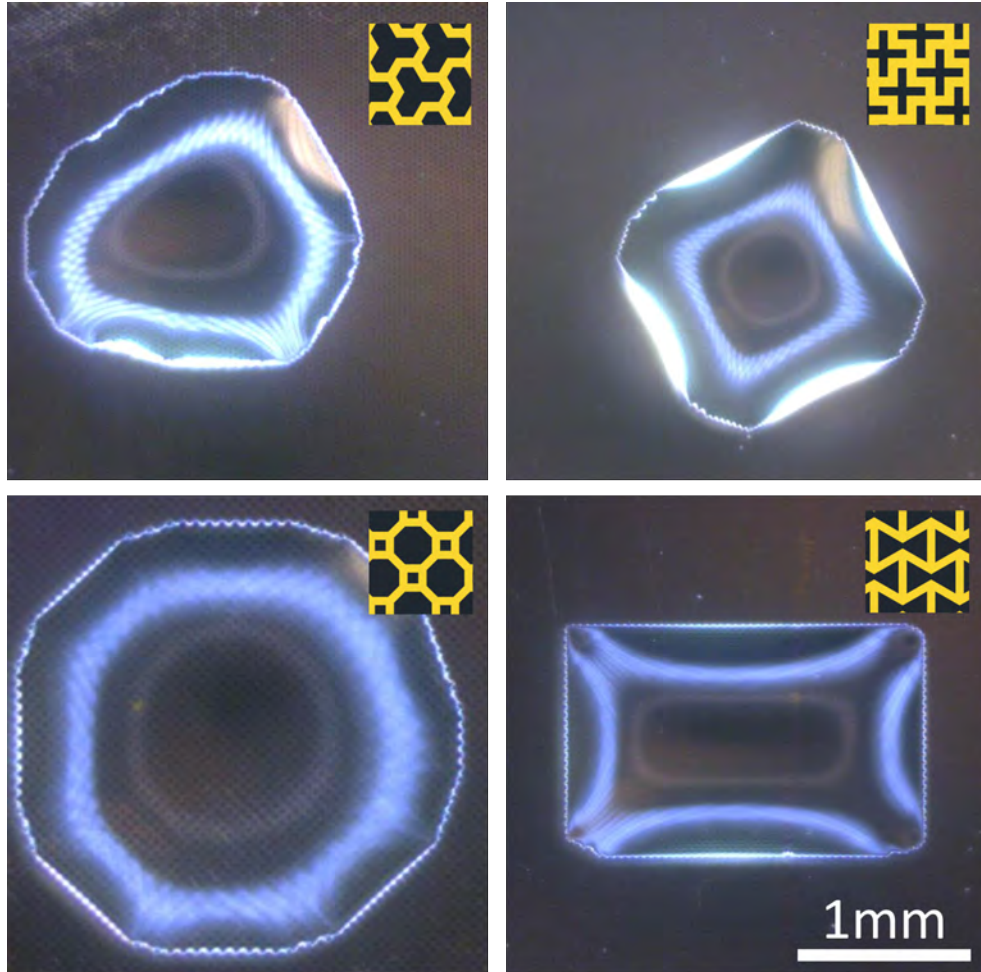


Figure 7.18: Caltrops, crosses, octagons and squares, and hourglass spreading

When the underlying array has symmetry along both axes, the shape will spread equally in both directions and eventually form a thin film. This is the case for the caltrops, crosses, hexagons and octagons/squares. When there is some asymmetry along the x and y-axis of the underlying array, such as that of the hourglass pattern, the droplet tends to spread in one direction more strongly than the other, as seen in the bottom right image of Figure 7.18. It is important to emphasise that the orientation of the patterns shown in the top right corner of each image is correct with respect to the droplet. When looking at the caltrops pattern, for example, the 3 corners of the droplet form at 60° rotation to the corners of those in the underlying pattern. Therefore, it cannot be assumed that the droplet will necessarily mimic the absolute rotational symmetry of the pattern underneath, but only its relative rotational symmetry (e.g. 3 vertices for caltrop pattern).

8 Liquid threads

Something that became apparent in the early stages of the PhD was the ability of this geometry to produce very thin and long liquid rivulets from a parent droplet along the edge of the metal electrode. These were given the informal name of 'liquid threads', which is what they will be referred to as in this thesis. Similarly to the uni-directional spreading model (section 7.1), it is at the liquid/air interface at which the L-DEP force is felt. When this overcomes the surface tension, Laplace pressure, surface friction and viscous forces, a liquid thread is formed. Initially in the PhD, liquid threads were created along only one edge of the metal/oxide interface, which will be referred to as 'thin' or 'single edge' liquid threads. Later on, 'wide' or 'double edge' liquid threads were produced by having two electrode edges close enough together so that two thin threads merged into a single wide one. Both the statics and dynamics of non-volatile and volatile liquid threads are covered in this chapter, as well as the spreading of microdroplets if the threads are allowed to break up.

8.1 Formation of a thin liquid thread

To produce thin or single-edge liquid threads, a parent droplet can be placed on the edge of the 7x9mm electrode. This gives only one metal/oxide interface along which the thread can be drawn out by the non-uniform electric fields produced at this interface. When a high enough voltage is applied, a very thin thread of roughly $10\mu m$ in width is pulled along the edge of the electrode. Figure 8.1 shows this for a few voltages, as well as zoomed-in images of the thread at various distances along its length at 200V. There is a voltage dependence on both the length and width of the thread, which are quantified in sections 8.2.1 and 8.2.2. There is also a voltage dependence on the dynamics of how quickly the thread is pulled out, which is quantified in section 8.3.1.

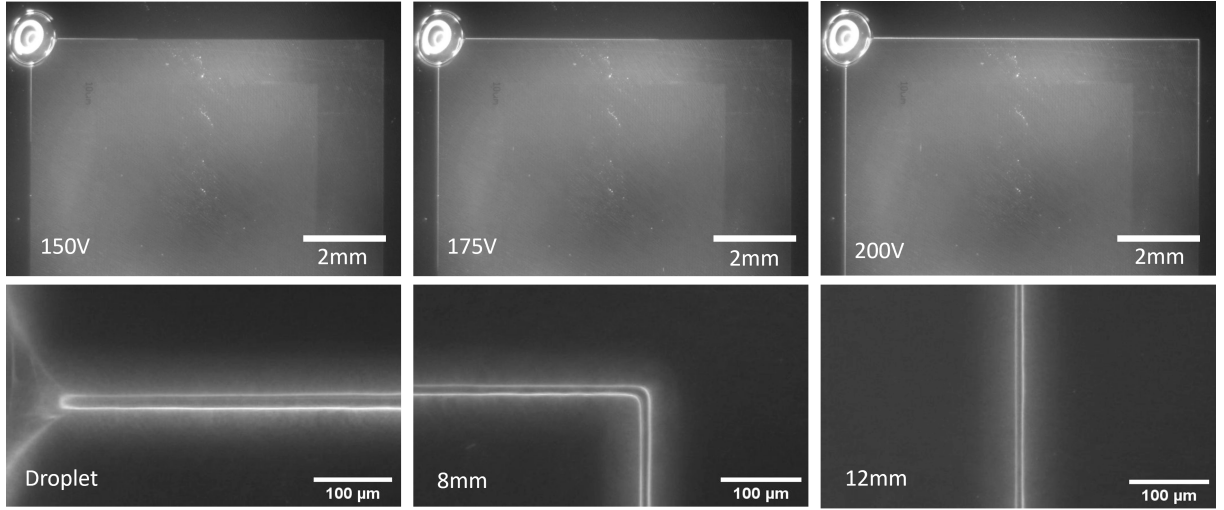


Figure 8.1: Thin threads at various voltages. The top 3 images show the entire thread at various voltages as it is pulled from the parent droplet (top left of image). The bottom 3 images show a close-up of the 200V thread at various points along the thread.

8.2 Liquid thread statics

In this subsection, we take a look at the time-independent behaviour of liquid threads. We look at how their length, width and volume vary as a function of voltage once an equilibrium has been reached.

8.2.1 Thread length vs Voltage

Figure 8.2 shows how the length of a decanol thread depends on the voltage applied. Up until a certain threshold voltage, the L-DEP force is not strong enough to overcome the surface tension and Laplace pressure, and therefore no thread is produced. Just above this theoretical threshold voltage (V_0), the droplet starts to wet slightly along the electrode edge but there is still no visible liquid thread. Only once the voltage is about 10-15 volts above V_0 does a visible liquid thread form. Once a thread has formed its length has a very strong voltage dependence, and in the case of figure 8.2 we get $\text{Length} \propto (V - V_0)^{3.5}$, where $V_0 = 110V$. Since the length at which the thread grows can often be influenced by imperfections on the

surface where it gets pinned, several experiments were done and then the lengths of the threads were averaged.

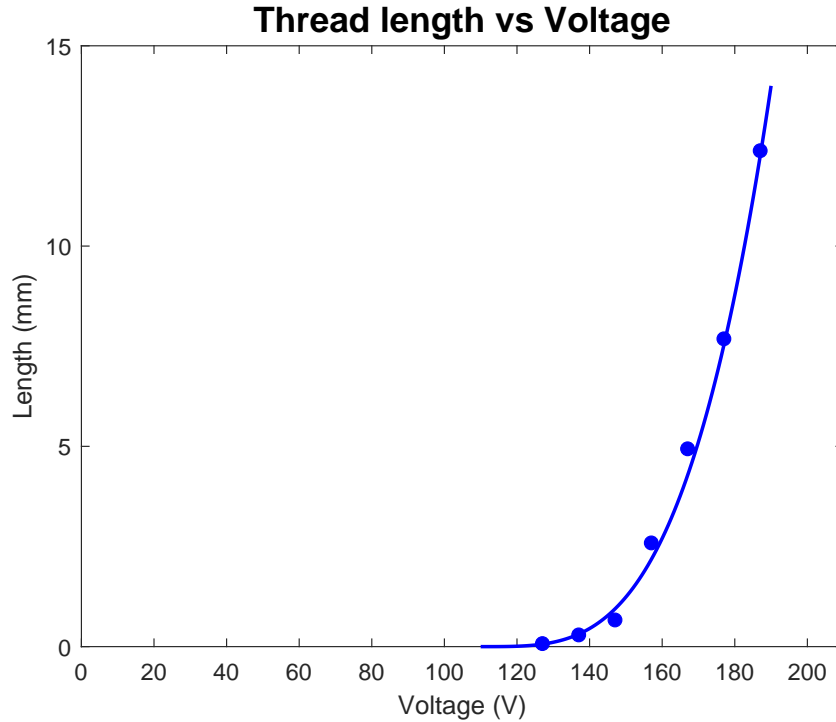


Figure 8.2: Thread length vs Voltage - Decanol 1kHz

8.2.2 Thread width vs Voltage

In addition to the length of the thread changing as a function of voltage, the width of a thread also increases as the voltage is increased. However, unlike the length which has one measurable value, the width of a thread will taper, getting smaller towards the end of the thread and wider closer to the parent droplet.

To achieve a thread of uniform width across its entire length, two decanol threads were pulled out of two separate parent droplets so that they joined together in the centre. Its width was then measured as a function of voltage at five equally spaced points along its entire length. The average width W was then calculated and plotted against the voltage V . Figure 8.3 reveals how there is a very strong linear dependence of thread width versus

voltage. Assuming a cylindrical type structure, since we have $A \propto W^2$, this effectively means the cross-sectional area of the thread A , is proportional to voltage squared and hence the energy.

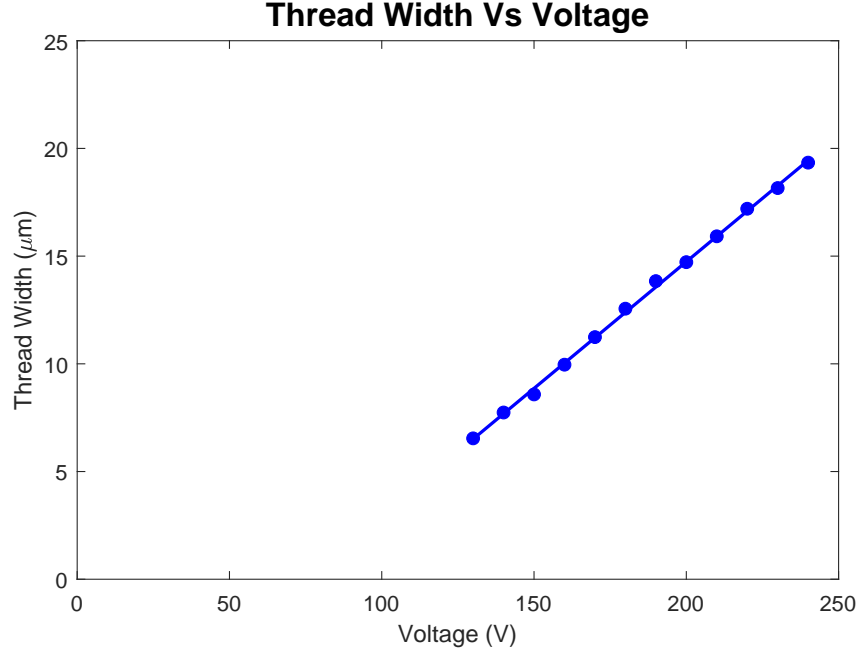


Figure 8.3: Thread width vs Voltage - Decanol 1kHz

For voltages lower than those shown in figure 8.3, the threads were never able to connect to form a uniform thread, so they are not shown on the graph. It is expected that the linear relationship shown would not continue down to widths much below $5\mu m$, and that instead there would be a point at which the surface tension overcomes the DEP force causing Plateau-Rayleigh breakup [175].

8.2.3 Thread volume vs Voltage

Using the same connected decanol threads from section 8.2.2, for each thread the voltage was switched off so that the Rayleigh-Plateau breakup of the threads into small droplets could be used to determine the overall volume of the droplets by using the receding contact angle of decanol on Novec 2702 ($\approx 40^\circ$) and the droplet width, assuming a spherical cap. The

individual droplet volumes were then added up and divided by the total length of the thread to get the volume per unit length of the thread for each voltage.

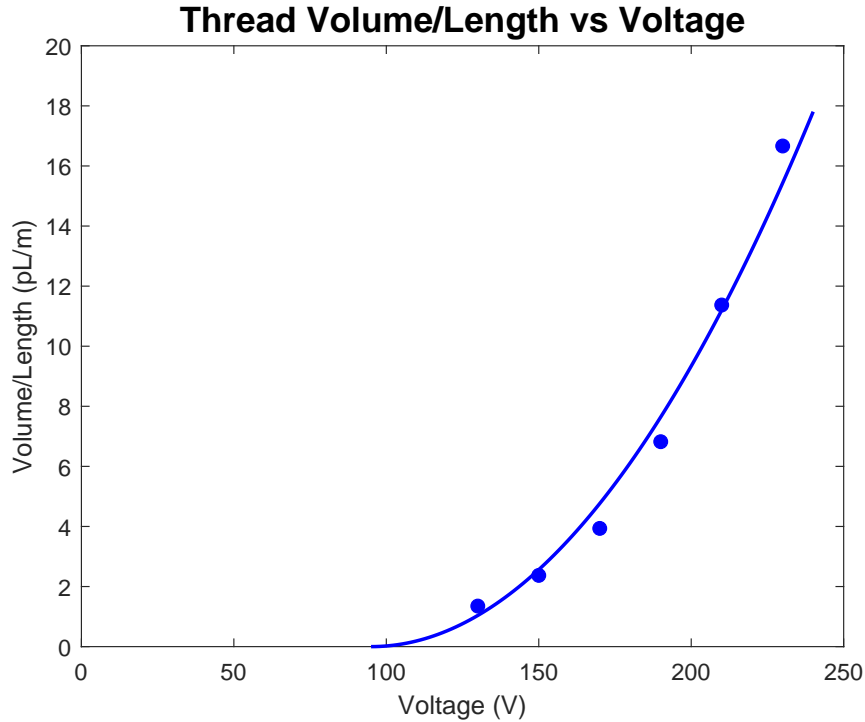


Figure 8.4: Thread width vs Voltage - Decanol 1kHz

Figure 8.4 shows the thread volume per length for the connected threads at various voltages. Like in section 8.2.2, there is a certain threshold voltage which is needed to produce a thread to begin with, but once that has been achieved there is a voltage squared dependence on the volume past the threshold voltage: $\text{Volume} \propto (V - V_0)^2$, where V_0 is 95V in this case.

8.3 Liquid thread dynamics

In this subsection, we examine the time-dependent behaviour of liquid threads. We look at how their lengths increase and decrease as a function of time under different applied voltages.

8.3.1 Dynamic evolution of a non-volatile liquid thread

Once the static behaviour of liquid threads had been established, the dynamic behaviour of non-volatile liquid threads was studied. For voltages ranging from 120V to 250V at 1kHz, liquid threads were recorded being pulled out of a parent droplet of decanol. ImageJ was used to measure the thread's length at each frame as a function of time. Figures 8.5 and 8.6 show the thread length versus time for several different voltages.

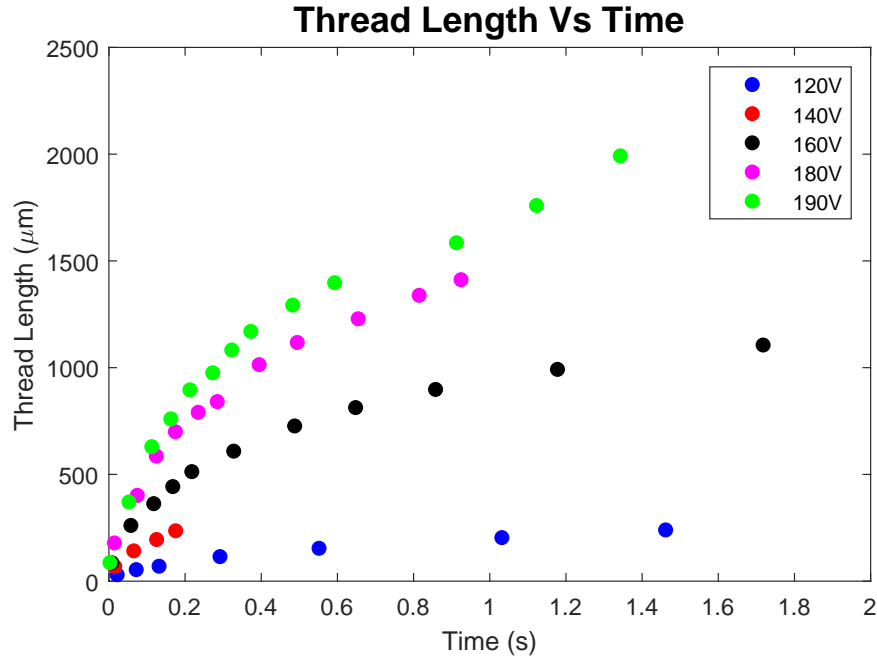


Figure 8.5: Thread length vs Time for lower voltages - Decanol 1kHz

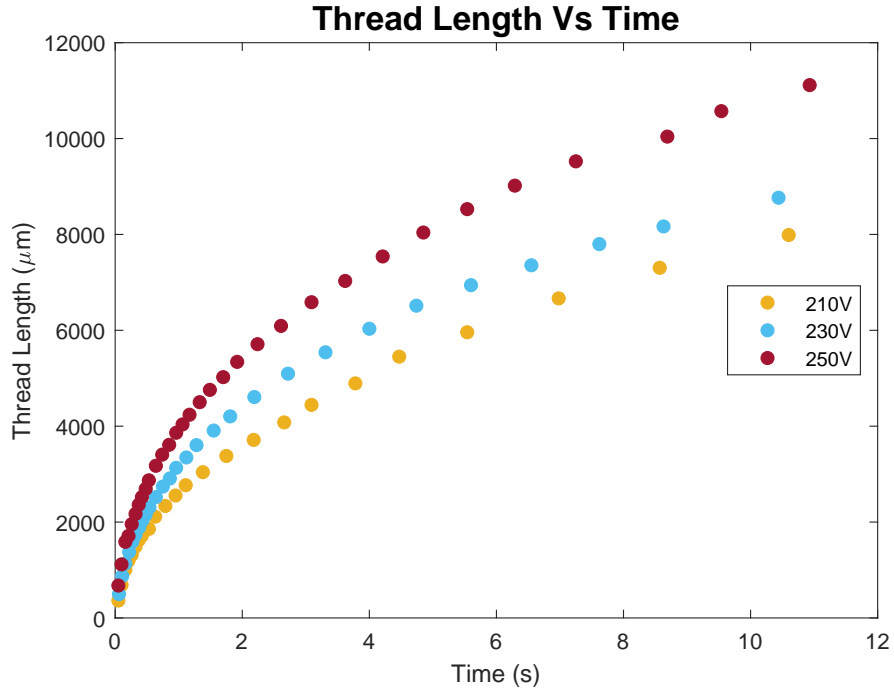


Figure 8.6: Thread length vs Time for higher voltages - Decanol 1kHz

It is clear that the speed at which the thread evolves increases strongly with voltage. In addition, the gradient of the length versus time plot does not remain constant, slowly decreasing until tapering off to zero, which is when we arrive at the static thread regime (section 8.2.1). The similarities of the liquid thread dynamics to Washburn Law's 2.2.7 were very telling from these plots, so thread length squared versus time was plotted for each voltage to see if they satisfied the Lucas-Washburn equation.

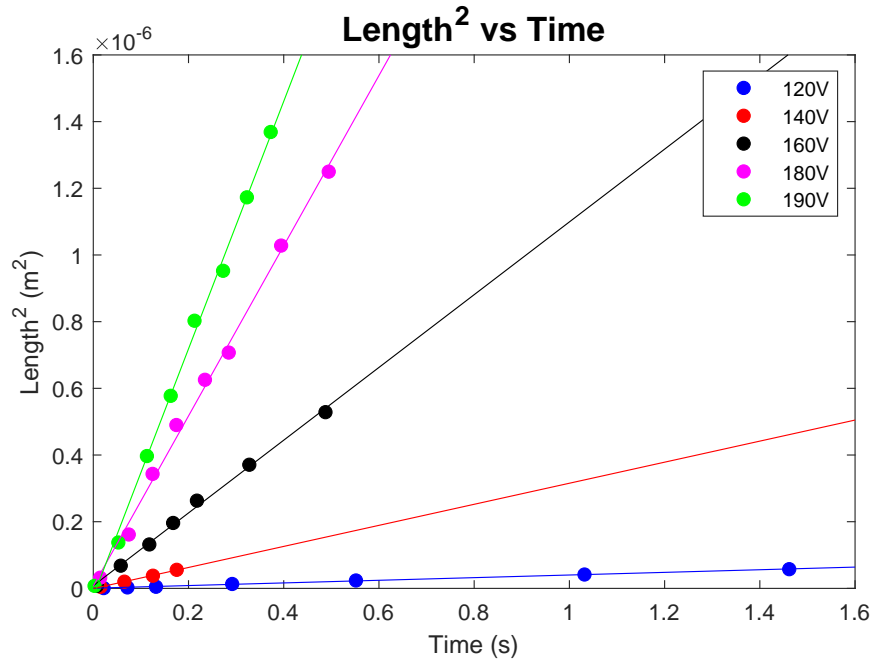


Figure 8.7: Thread length squared vs Time for lower voltages - Decanol 1kHz

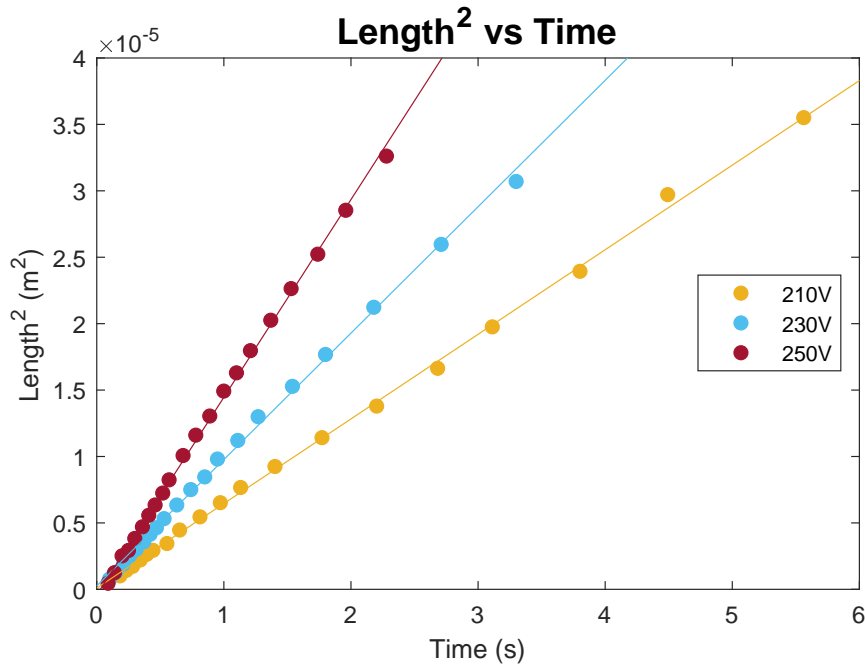


Figure 8.8: Thread length squared vs Time for higher voltages - Decanol 1kHz

Figures 8.7 and 8.8 show the plots of thread length squared vs time for each voltage. Each plot produces a strong linear relationship between length squared and time, satisfying the

Lucas-Washburn equation $L = (D_w t)^{1/2}$, where D_w is a simplified diffusion coefficient. The value for the diffusion coefficient is therefore the gradient of the length squared vs time graph, which can be plotted as a function of voltage (figure 8.9).

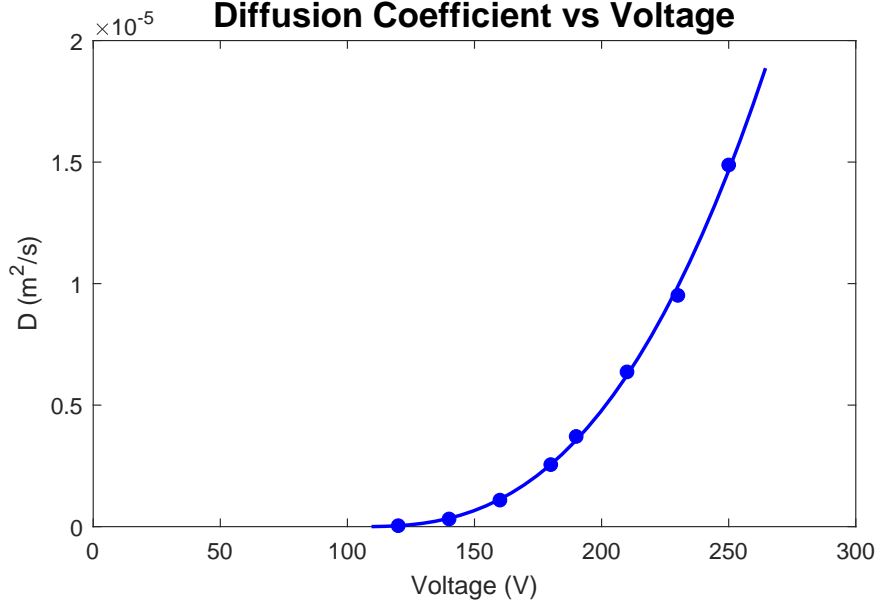


Figure 8.9: Washburn diffusion coefficient vs Voltage for decanol threads

Similarly to the static case (section 8.2.1), the threshold voltage must be determined so that a better physical understanding of the system can be obtained. At this threshold voltage, V_0 , it is assumed that all resisting forces are equal and opposite to the DEP force, resulting in no net movement of liquid. Once V_0 is surpassed, the net force on the tip of the liquid thread becomes positive and therefore there is movement of the liquid. As the thread grows, the DEP force required to pull the thread longer increases; so for a given voltage the forces will eventually balance out again and the thread growth will taper off as seen in figures 8.5 and 8.6. In a perfect system, the thread would grow at an ever-decreasing rate indefinitely, but since in reality the surface is not perfect and due to pinning, the thread eventually reaches a static equilibrium.

From figure 8.9, a threshold voltage of $V_0 = 110\text{V}$ was estimated. This value was then used in the following equation:

$$L^2/(V - V_0)^2 = t \quad (8.1)$$

which was used to collapse figures 8.7 and 8.8 into a single graph in figure 8.10.

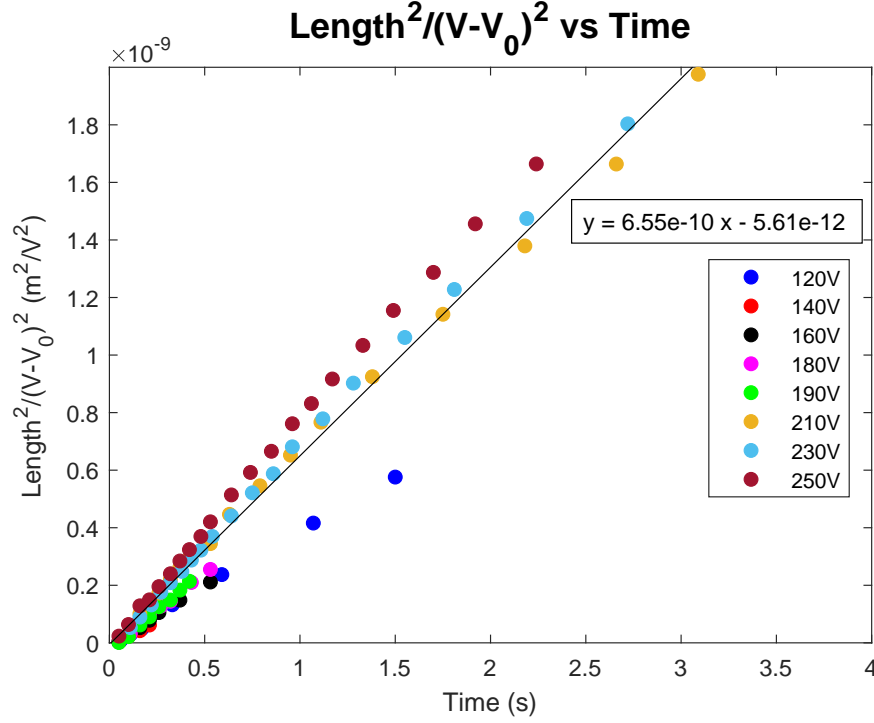


Figure 8.10: Figures 8.7 and 8.8 have been divided by $(V - V_0)^2$ and plotted on the same graph. In this example, a V_0 value of 110V was chosen. The line of best fit has been calculated to find a single diffusion coefficient for the thread dynamics.

From figure 8.10, a single diffusion coefficient was calculated by finding the line of best fit across all the voltages combined. The diffusion coefficient had a value of $m_d = 6.55 \times 10^{-10} \text{ sV}^2/\text{m}^2$ from the gradient of the best-fit line. There was also a small offset term of $c = 5.61 \times 10^{-12}$, but this can be assumed to be zero in a Washburn relationship.

8.3.2 Controlled detwetting of non-volatile liquid threads

In section 8.3.1, the dynamic evolution of a single non-volatile liquid thread was shown to exhibit the behaviour of a Washburn relationship. In this case, the pressure difference created at the tip of the thread via the DEP force was greater than that of the resisting forces, causing the thread to grow. In this section, we begin with an existing thread of length L_0 , which is

produced and held in place by a higher initial voltage V_i . The voltage is then switched to a lower voltage V , which lies somewhere in between the maximum Rayleigh-Plateau break-up voltage and the minimum voltage required to see any substantial dewetting of the thread. For example, if $V_i = 180V$, switching the voltage to $50V$ will be below the break-up voltage and therefore not be useful for this experiment. Meanwhile, switching from $180V$ to $170V$ will not produce enough pressure difference to overcome any pinning or contact angle hysteresis.

This thread dewetting experiment was initially attempted using the thin threads produced along one edge of the electrode as used in previous experiments. However, the dewetting rate was very practically zero. Using electrodes which had two edges patterned sufficiently close together so that two thin threads were able to merge into one single ‘wide thread’, it became possible to see the controlled dewetting dynamics of microscopic liquid threads.

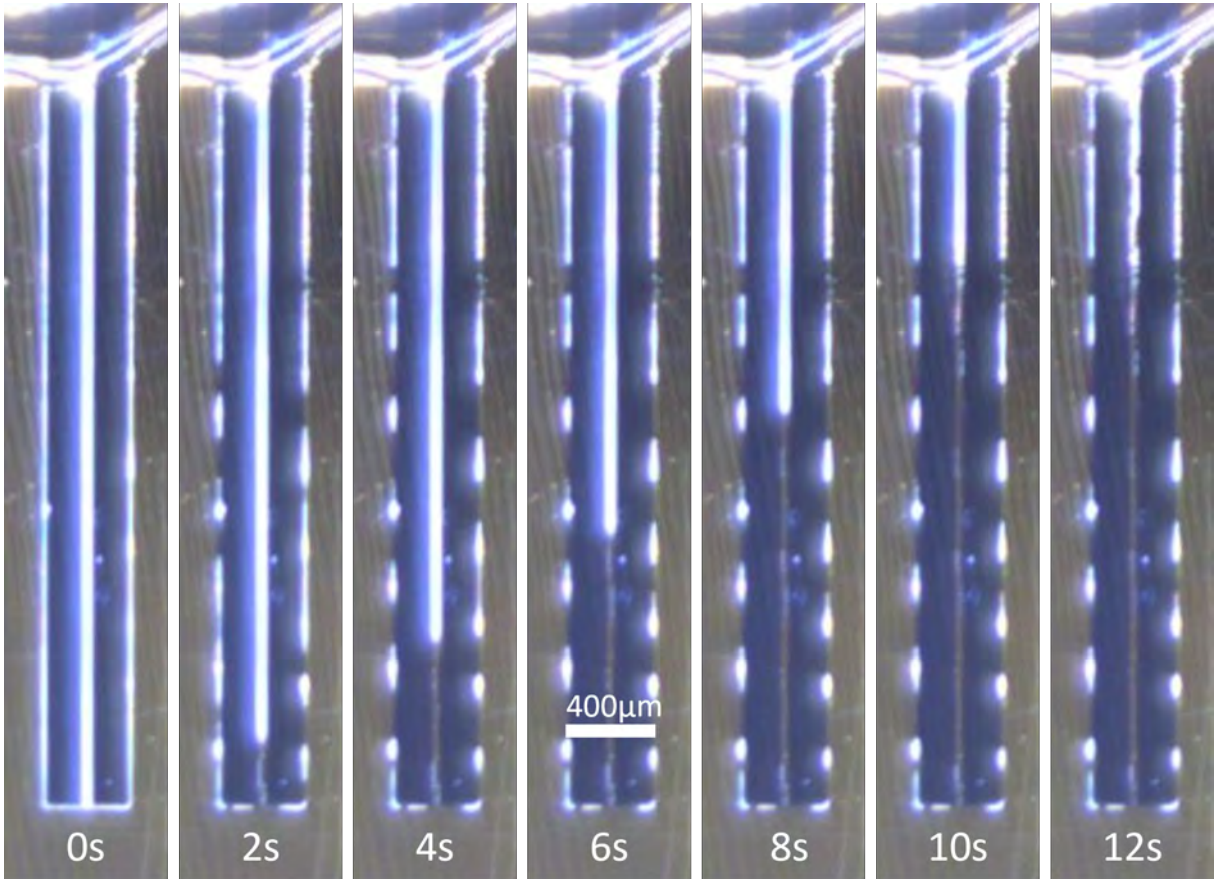


Figure 8.11: Dewetting of wide thread from 180V to 120V - Decanol 1kHz

Figure 8.11 shows the dewetting of ‘wide threads’ of decanol along the middle of the images. In this case, the long gold stripe on which the thread is created is at a width of $20\mu m$. By starting with an initial voltage of $180V$ and then instantly reducing it to $120V$, the thread begins to recede slowly towards the parent droplet, before receding more quickly the closer it gets. This was tested for three different final voltages ($120V$, $133V$ and $145V$), which influenced the speed at which the thread receded. Figure 8.12 shows the thread length vs time for each voltage. This gave a similar feel to the Washburn relationship for threads in section 8.3, so the length squared was plotted against time in figure 8.13.

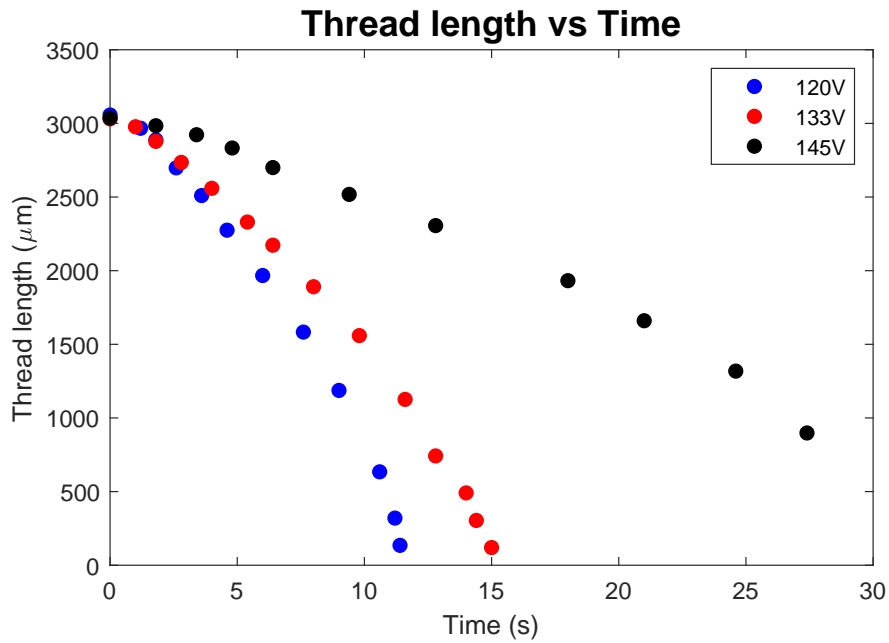


Figure 8.12: Dewetting of wide decanol threads at fixed voltages - Length vs Time

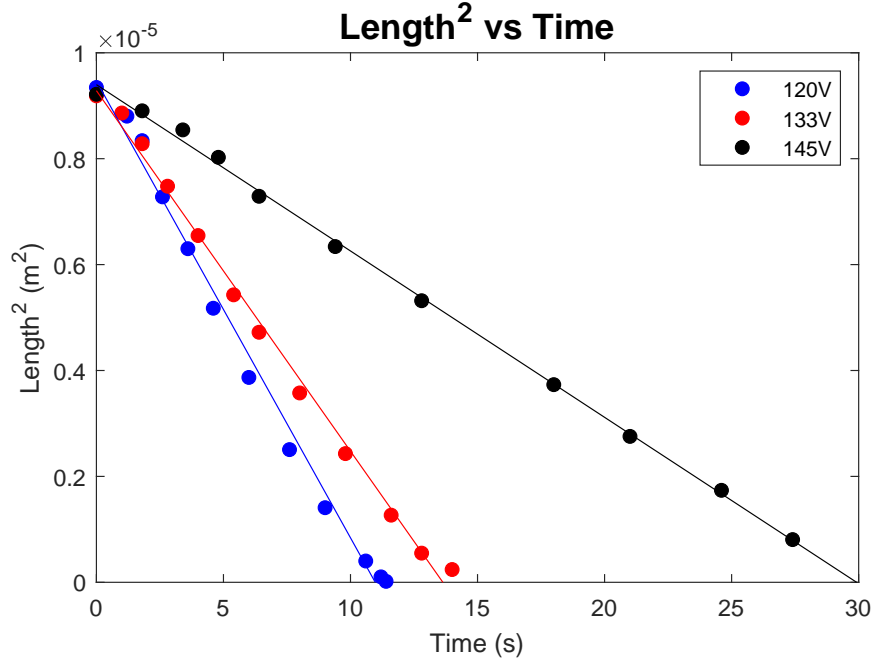


Figure 8.13: Dewetting of wide decanol thread at fixed voltages - L^2 vs Time

Figure 8.13 reveals how there is a so-called ‘Reverse Washburn’ relationship [176] for the thread dewetting process, in which the speed of recession increases as it gets shorter.

8.4 Liquid thread evaporation

Until now, this chapter has documented the static and dynamic behaviour of non-volatile decanol liquid threads. At room temperature, the decanol has such a slow evaporation rate that even the thinnest threads with tiny amounts of decanol would take several minutes to evaporate. This section examines the behaviour of liquid threads when using a much more volatile liquid. Isopropyl alcohol (IPA) turned out to be a good candidate for this study, both due to its high evaporation rate at room temperature and its ability to form liquid threads in a suitable frequency range (2kHz-30kHz) on the devices used. Since the devices tended to heat up once they got to frequencies above 10kHz at 200V, the frequency chosen for the evaporation experiments was set to 7.5kHz so that the temperature of the device did not change as the voltage was increased, preventing additional variables from being introduced.

8.4.1 Static length equilibrium of evaporating thread

Something that immediately became apparent was that evaporating liquid threads tended to maintain a consistent length for a given voltage, revealing that the flow rate into the thread from the parent droplet was in a balanced equilibrium with the total thread evaporation rate. This does not necessarily have to be the case. Instead, one can imagine a scenario where the length of the thread oscillates back and forth as the evaporation and flow rate increase and decrease depending on the length of the thread. To show how consistent the length of the threads remained throughout the entire evaporation of the parent droplet, a video was taken over 90 seconds and the thread length was measured using ImageJ at 5-second intervals. Figure 8.14 shows a snapshot of the video for 150V at 7.5kHz. It can be seen how the thread of IPA is much wider than that of a decanol one, and there tends to be more of a taper with some ripples along its length.

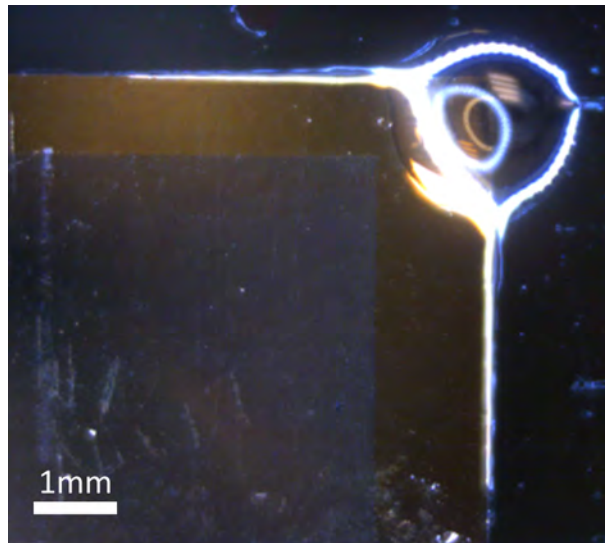


Figure 8.14: Image of two evaporating IPA threads from parent droplet - 150V at 7.5kHz

Figure 8.15 shows a graph of thread length vs time at three different applied voltages. The values on the y-axis represent the average lengths of the two individual threads protruding from the parent droplet.

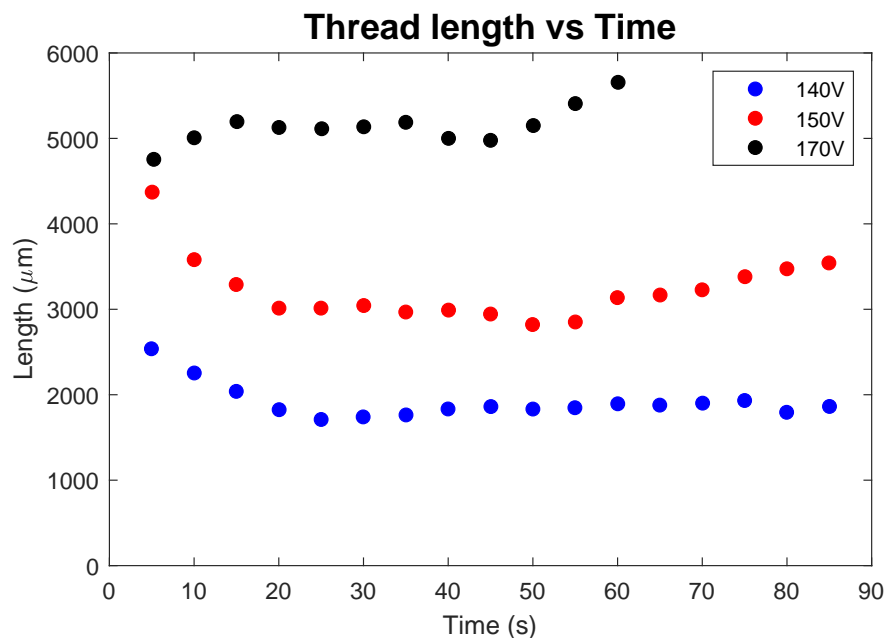


Figure 8.15: Final length of IPA threads over time as they evaporate

To quantify the variation in thread length over this time, the average deviation of the length was divided by the average length and multiplied by 100 to get the value as a percentage for each voltage. These percentages come out as 6.8% for 140V, 8.4% for 150V and 2.9% for 170V, showing a very consistent thread length over the entire evaporation of the parent droplet.

Once it was established that the flow rate into the thread was in a balanced equilibrium with the evaporation rate of the thread, the voltage dependence for the length of an evaporating thread could be studied. Like non-volatile liquids, the thread length was expected to grow as a function of voltage in some way since the dielectrophoretic force at the tip of the thread is proportional to the voltage squared. In the case of the non-evaporating threads, the limiting factor of the thread length is speculated to be a combination of pinning and the reduction in flow described by Poiseuille's law (see section 2.2.6) that reduces linearly with length. In the case of isopropyl alcohol, it seems that the thread is not able to reach that limiting length before fully evaporating. This gives a different length dependence to what is seen with non-evaporating threads.

To test the length vs voltage dependence, a $4\mu\text{L}$ droplet of isopropyl alcohol was placed on the edge of the electrode and several voltages were applied at 7.5kHz. To prevent pinning at lower voltages, the thread was first pulled out to a longer length at 210V and then the voltage was reduced in steps of 10V down to 90V, at which there was no longer enough dielectrophoretic force to overcome the surface tension of the droplet to pull out a thread. The length of the thread was always measured from the point at which it protruded from the droplet, which was pulled slightly further outwards at higher voltages. This experiment was performed five times with a new droplet each time to show repeatability and achieve conclusive results. Figure 8.16 shows how the equilibrium length varies at several voltages.

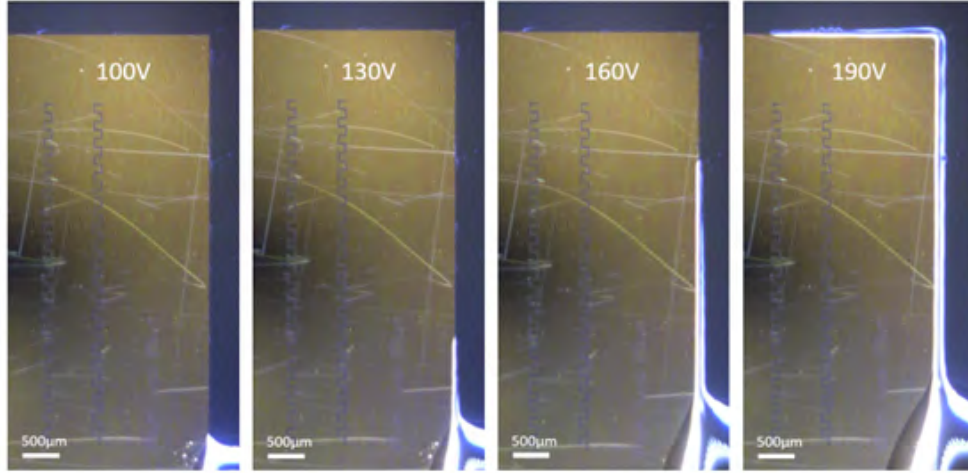


Figure 8.16: Images of evaporating IPA threads from parent droplet at various voltages

Figure 8.17 shows the plot of the equilibrium length vs voltage for an evaporating thread of IPA at 7.5kHz. Like non-volatile threads, there is a minimum threshold voltage to pull out any thread. After this voltage, there is a power law relationship between the length of the thread and the voltage. In this case, the length had a weaker voltage dependence than the decanol threads, which is assumed to be because as the threads get longer there is more evaporation and therefore the equilibrium thread length will be smaller compared to threads that do not evaporate.

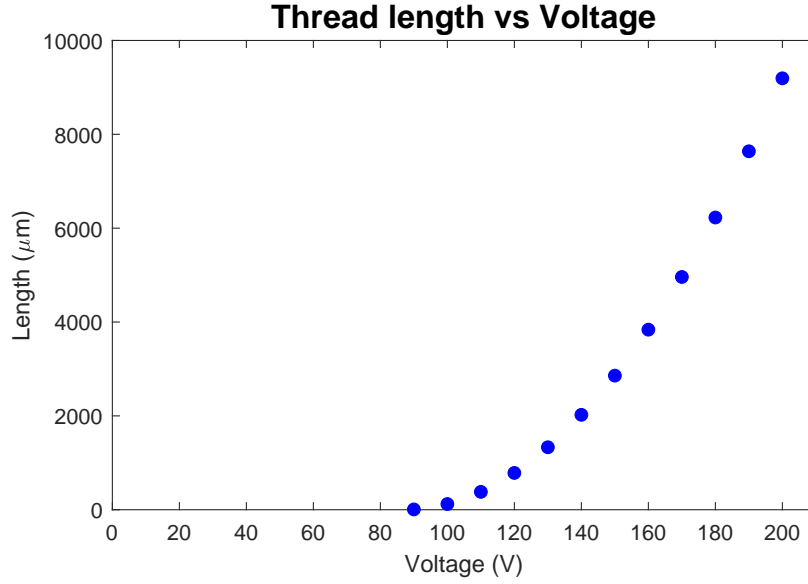


Figure 8.17: Evaporating thread length vs voltage in static equilibrium - IPA 7.5kHz

8.4.2 Dynamic evolution of evaporating thread

In section 8.3.1 the dynamic evolution of non-volatile liquid threads was determined by capturing a video and recording the thread length versus time at various voltages, which gave almost perfect Washburn relationships (see section 2.2.7). In this section, the same experiment was done for evaporating IPA threads at 7.5kHz. Figure 8.18 shows the length versus time plot of this experiment for a few voltages.

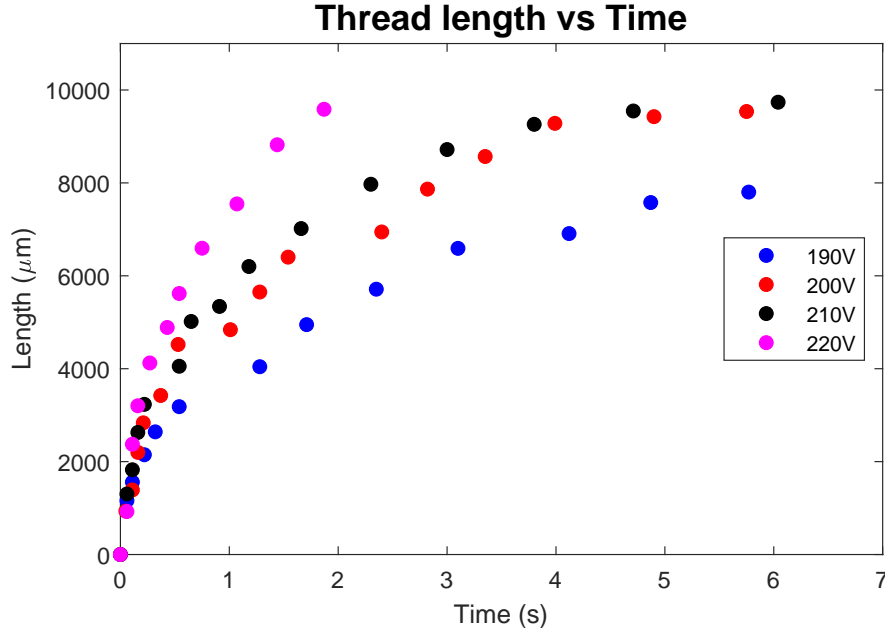


Figure 8.18: Evaporating thread length vs time - IPA 7.5kHz

The length squared was plotted against time to determine whether evaporating threads also followed a Washburn relationship, which would give straight line graphs as seen in figures 8.7 and 8.8. Figure 8.19 shows this plot. The plot shows that evaporating threads do not follow a Washburn relationship like non-volatile threads. Instead, they start with a Washburn-like behaviour, in which best-fit lines have been plotted to the first second of their evolution, but then their L^2 vs time dependence goes sub-linear. This is to be expected since as they get longer they begin to evaporate more before reaching a balanced equilibrium length in which the evaporation rate is equal to the flow rate from the parent droplet.

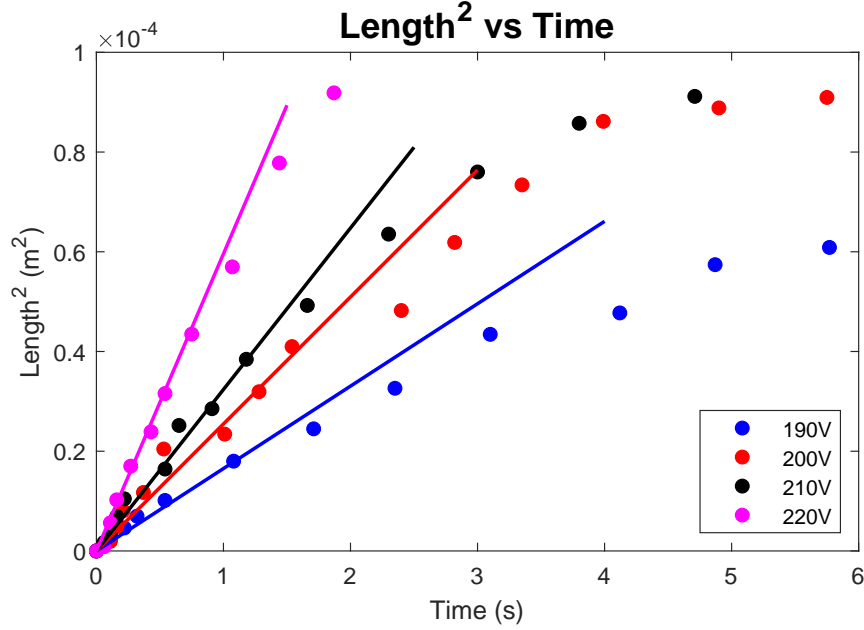


Figure 8.19: Evaporating thread length squared vs time - IPA 7.5kHz

8.5 Microdroplet spreading

Once a liquid thread had been pulled out of a parent droplet and allowed to break up via the Plateau–Rayleigh instability [175], a long line of tiny ‘microdroplets’ were produced along the edge of the gold/silicon oxide interface. These droplets could then be spread again by applying a voltage. Due to their small size, it was impossible to get a side view to measure their contact angle like in section 7.1, so only their length could be measured from above. Due to the nature of the breakup process, it was difficult to get the droplets to all be exactly the same size, so several droplets of differing sizes were averaged to get the overall trend (figure 8.22). The main observation was that the microdroplets grew very little at first until around 100V at which point there became a strong voltage dependence on the length. In addition, larger droplets tended to spread more easily than small droplets, although this wasn’t a strict rule of thumb as seen in figure 8.21.

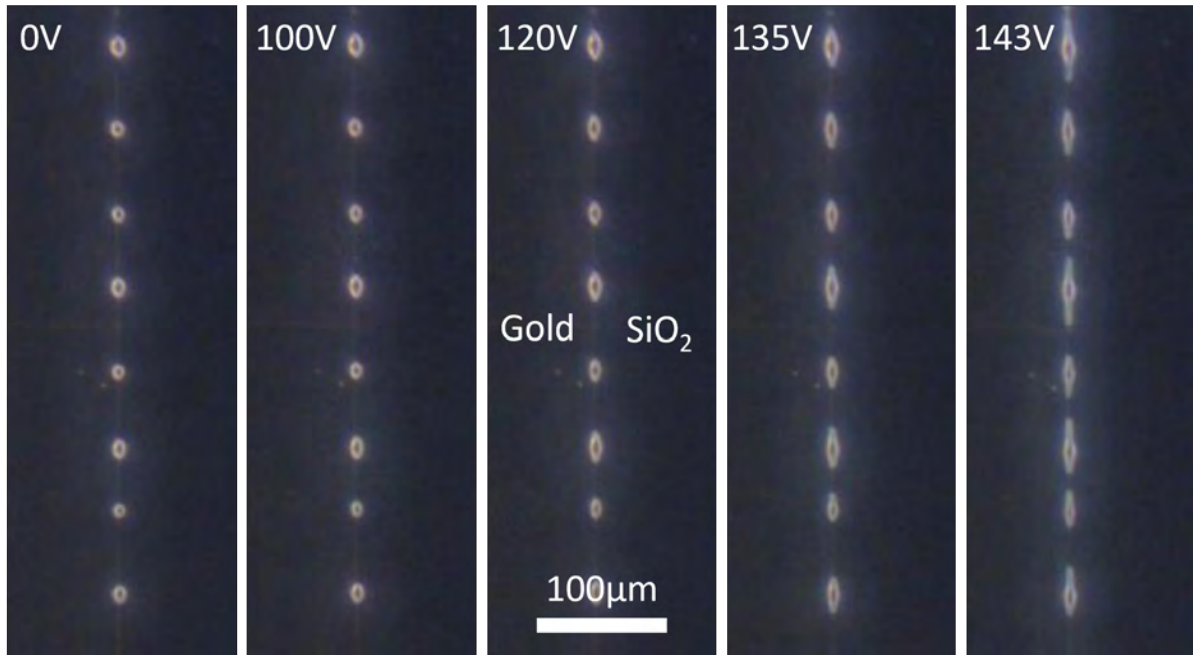


Figure 8.20: Spreading of microdroplets along gold/silicon oxide electrode edge

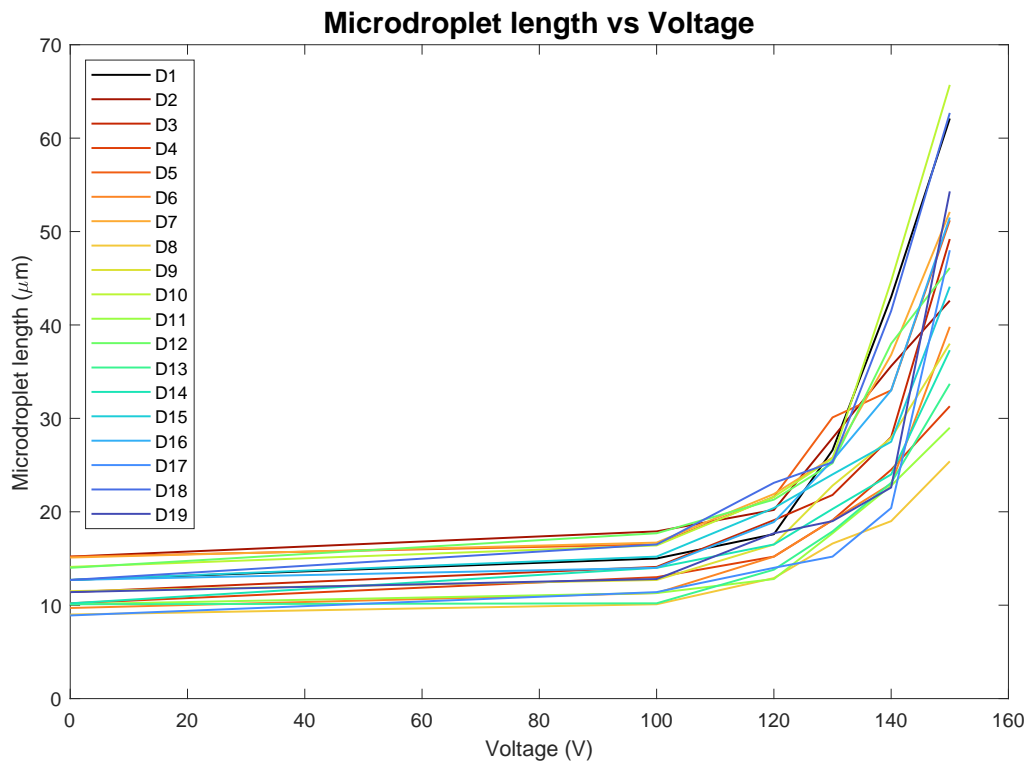


Figure 8.21: Length vs voltage for all microdroplets

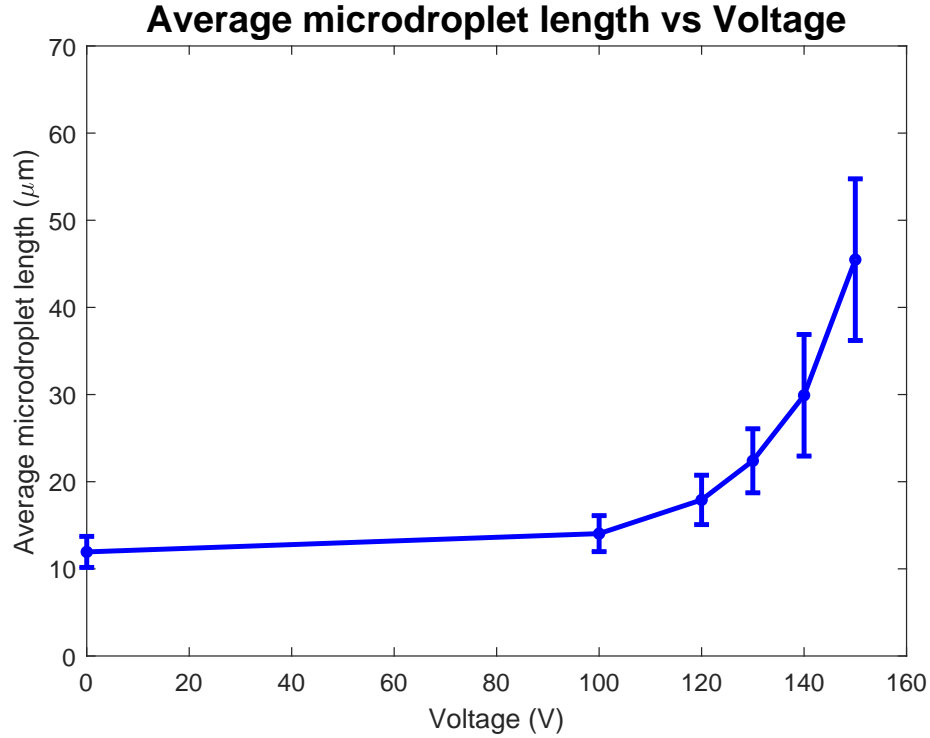


Figure 8.22: Average length vs voltage of microdroplets

Dr Elfego Gutierrez of Newcastle University was kindly able to create some simulations in his free time to model the spreading of microdroplets along the electrode edge in the MOS capacitor geometry. Figure 8.23 shows the simulated droplet at three points in time as an electric potential is applied across the metal electrode (red) and the underside of the device (black), which are separated by the oxide layer (clear). The simulation shows the DEP force acts strongest at the point of contact between the droplet contact line and the metal/oxide interface. This simulation gives very good qualitative agreement with the microdroplet spreading at the time of writing this thesis, and more quantitative work is possible.

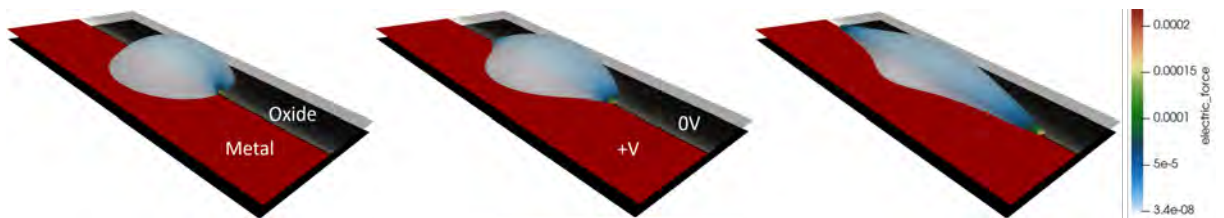


Figure 8.23: Simulation of microdroplet spreading along electrode edge

9 Particle dielectrophoresis

This chapter focuses on the use of the novel MOS geometry to manipulate polystyrene microspheres via the DEP force. First, we look at the effects of how the particles behave along one edge of an electrode, then how they behave in the striped geometry, then how they behave in the hexagonal array of circles geometry, before finally looking at some ways in which the thickness of the liquid film can affect their behaviour. As discussed in section 4.2, dielectric particles can undergo both negative and positive dielectrophoresis depending on the electrical permittivities, conductivities and frequency of the applied electrical field. Since the dielectric constant of the $10\mu m$ polystyrene microspheres ($\epsilon_r = 2.5$) used throughout these experiments was always lower than that of the decanol ($\epsilon_r = 8$), we would expect nDEP in the higher frequency limit of the Clausius-Mossotti factor (equation 4.2). Simply put, the particles should move away from the edge of the electrode where the electric field is strongest when a high-frequency electric field is applied. How low the crossover frequency is should depend on the conductivities of both the liquid and particles.

9.1 Particle DEP along a single edge

Testing the movement of the particles along a single electrode edge was the most straightforward approach to determine the type of particle dielectrophoresis we would get and the crossover frequency of the system. $1\mu L$ of the particle/liquid suspension (see section 6.1.3) was dispensed onto the edge of the gold electrode, and a 1mm thick glass slide was placed on top of it to flatten it into a cylinder. The glass slide had $70\mu m$ thick Kapton (polyimide) tape stuck underneath each end to produce a $70\mu m$ gap between the surface of the device and the underside of the glass, hence resulting in a liquid cylinder height of $70\mu m$. The top camera could then be focused through the glass and liquid to see the device's surface and microspheres sitting just above it.

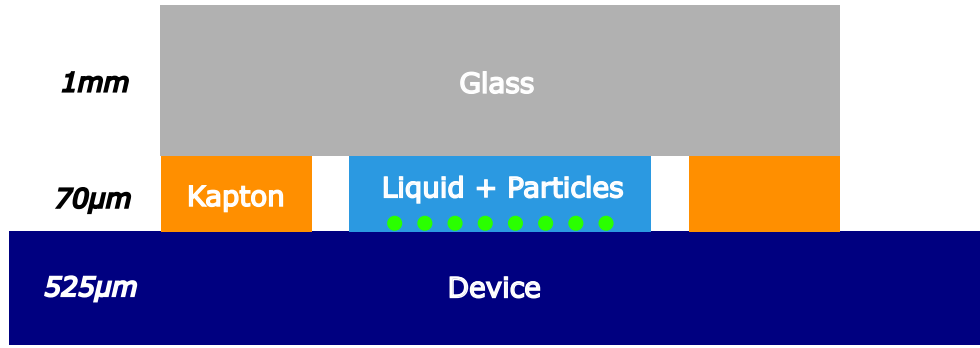


Figure 9.1: Particle DEP $70\mu m$ capped side view diagram

9.1.1 Initial movement of particles

When the decanol/particle suspension was first placed onto the substrate and capped to form a circular cylinder of $70\mu m$ in height, the particles spread out evenly across the entire surface. Besides the occasional clumps of particles in which the sonication process had not fully separated them, the majority of the particles were single entities before any voltage was applied. Using a 5x lens on the top view camera the single edge of one of the $9\times 7mm$ gold electrodes was viewed through the glass slide, and a voltage was applied across the device at several frequency voltage combinations. It soon became apparent that no matter what voltage or frequency was applied the particles would always move away from the electrode edge, which implies negative dielectrophoresis. A couple of examples are shown in figure 9.2, which shows the $10\mu m$ polystyrene microspheres in decanol along a single edge.

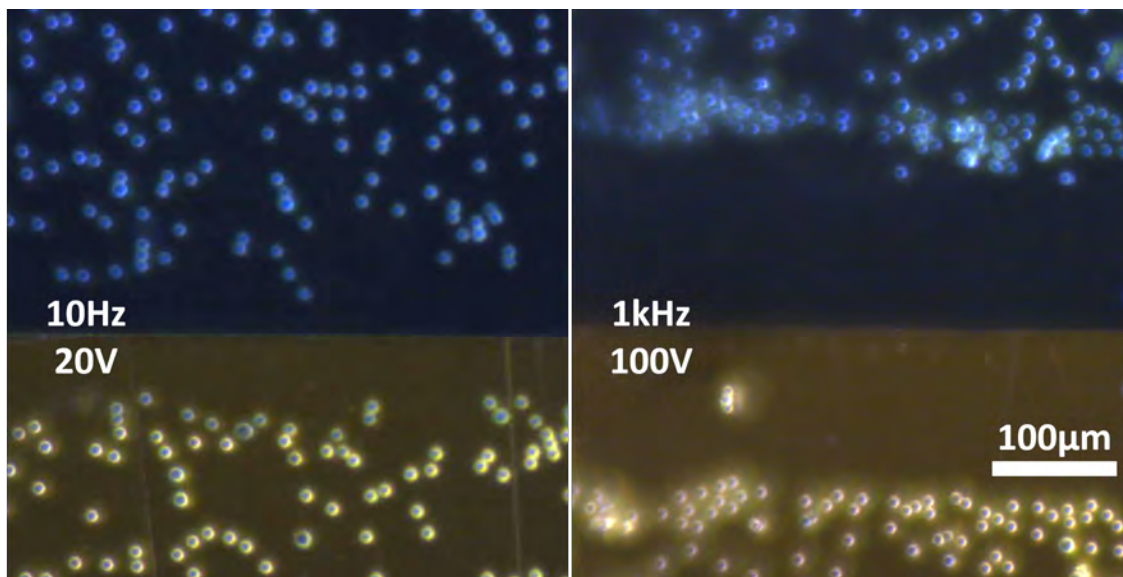


Figure 9.2: Particle DEP along a single edge at two frequency/voltage combinations. The blue half is the silicon oxide and the gold shows the metal electrode, the microspheres appear a different colour depending on which surface they are above. In both cases, they move away from the electrode edge when a voltage is applied.

As stated at the beginning of section 9, since the particles have a lower dielectric constant than decanol, negative dielectrophoresis is to be expected at higher frequencies. What the CM factor does not predict is for negative DEP to also occur at frequencies as low as 10Hz, which was assumed to be below the crossover frequency for positive DEP to occur. However, the experiments show this is not the case, and the particles always undergo negative DEP. The discrepancy between the theoretical and experimental crossover frequency has been emphasised before [177], particularly with particle sizes above $5\mu m$ in diameter [178].

Although there was a voltage and frequency dependence on how quickly and how far the particles moved away from the edge of the electrode, it was decided to not pursue this quantitatively due to more interesting studies that could be done during this PhD. In addition to this, the liquid droplet would need replacing for each frequency/voltage, since once the particles had moved, there was no way to get them to return to their original uniformly spread out positions. Thus, changing the droplet every time could lead to significant variations in parameters such as particle concentration near the electrode edge and liquid conductivity due to the sensitivity of the system.

9.1.2 Particle chains at low frequencies

An interesting effect that was noticed along the single edge is that at very low frequencies ($<50\text{Hz}$), after the initial movement seen in section 9.1.1, the particles tended to form long chains that were always perpendicular to the gold/silicon interface, even when the interface was curved (see figure 9.3). There was always a bias for the chains to prefer to be on the gold side of the edge as opposed to the silicon. These chains show very similar behaviour to the ‘pearl chains’ previously seen in the literature (see section 4.3.4).

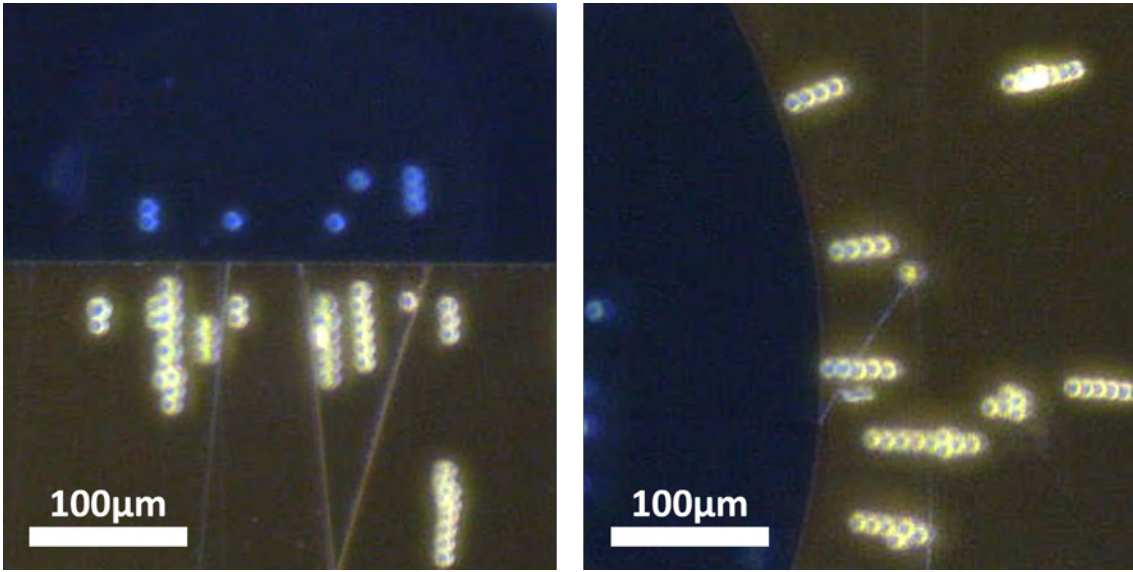


Figure 9.3: Long chains of particles form perpendicular to edge at low frequencies (50V/20Hz)

9.2 Particle DEP on striped geometry

Although the behaviour of the particles along the single electrode edge in section 9.1 showed little frequency dependence due to it always exhibiting negative DEP behaviour, some interesting effects were observed on the more complex geometries, including the striped geometry. To test the striped geometry the setup was identical to that of the single edge geometry, where a 1mm thick glass slide with $70\mu\text{m}$ Kapton tape was used to cap a $1\mu\text{L}$ droplet of decanol/-particle suspension (figure 9.1), except this time the droplet was placed onto the centre of

the 5x5mm striped electrode pattern. Two stripe widths were tested, $40\mu m$ and $20\mu m$, each exhibiting slightly different results. It is important to note that in these more complex geometries, there are a lot of factors at play, so being able to replicate the exact results of an experiment with the same frequency/voltage combinations with a different droplet, or even the same droplet a day later, was very unlikely. This is discussed more in the conclusion.

9.2.1 40 micron wide stripes

Being only $40\mu m$ apart, it was already established in section 7.1 (table 2) that the electric fields from neighbouring stripes have some effect on each other. It did therefore not take much stretch of the imagination to assume that the particle effect would be altered by bringing two edges this close together. Of course, they were not expected to suddenly go from exhibiting negative to positive dielectrophoresis just because the two edges were brought close together. Instead, it was interesting to see how the edges interacted and caused the particles to behave in certain ways depending on the voltage and frequency applied.

For the $40\mu m$ stripe width it was found that the particles tended to get “trapped” in certain positions depending on both the frequency and voltage. The effect was much more pronounced at lower voltages, which can be seen in figure 9.4 at 25V. The x-axis is a logarithmic scale for the frequency of the voltage applied and the y-axis shows how far the centre of the average particle is from the centre of the silicon stripe. A value of $0\mu m$ on the y-axis would mean that all of the particles are trapped perfectly in the centre of the silicon stripes, whilst $40\mu m$ would mean they are all trapped perfectly in the centre of the gold stripes. $20\mu m$ with small error bars would indicate they are attracted to the edge of the gold/silicon interface, whilst $20\mu m$ with large error bars would indicate a completely random scatter.

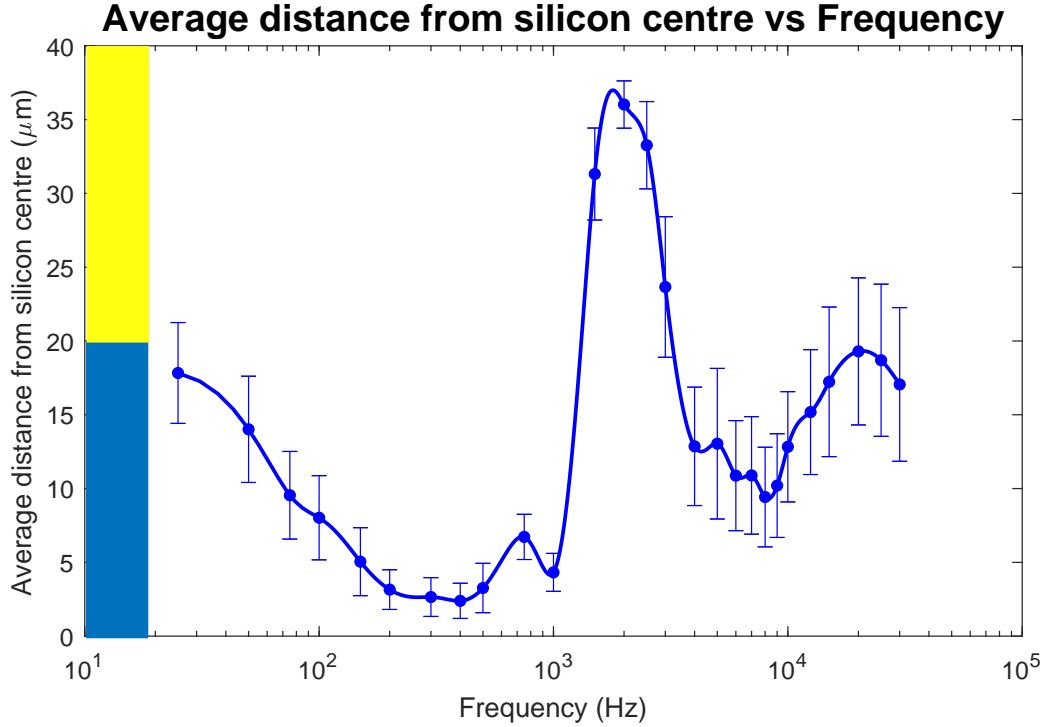
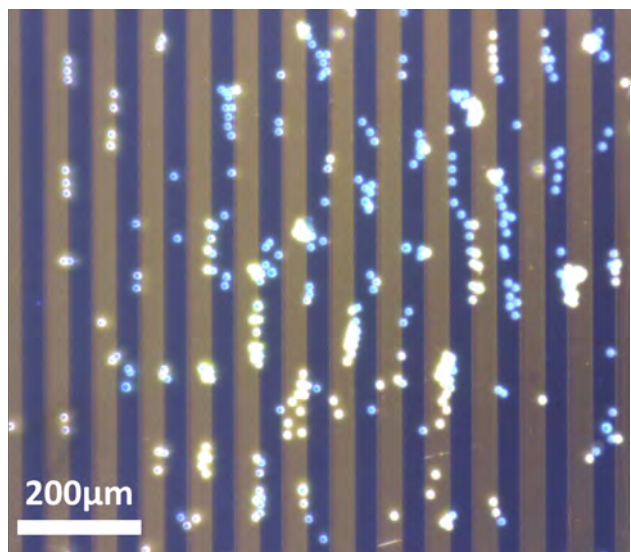


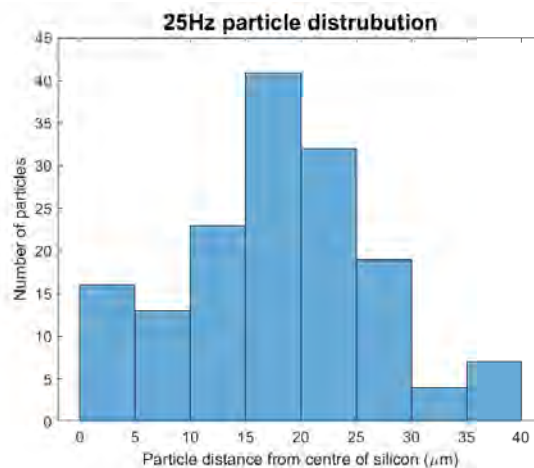
Figure 9.4: $40\mu\text{m}/25\text{V}$: Average particle distance from centre of silicon

In addition to the plot of average particle location vs frequency, figures 9.5-9.8 show the images and histograms of the particles for 25Hz, 200Hz, 2000Hz and 20kHz. These are four areas of interest as they show different regimes for the system. Note that the number of particles in the histogram changes due to the number of single particles that can be analysed in each image.

At 25Hz (figure 9.5) there is the regime in which the particles tended to be weakly attracted to the gold/silicon interface. This is not so obvious in this image or data set but was seen in other experiments (figure 9.9).



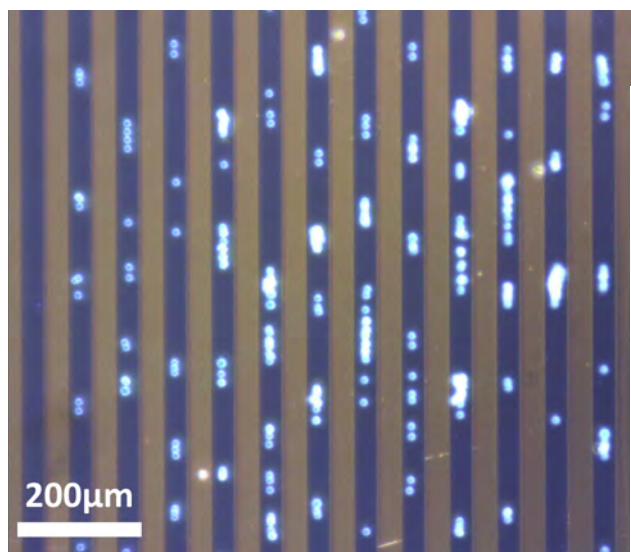
(a) No obvious arrangement of particles



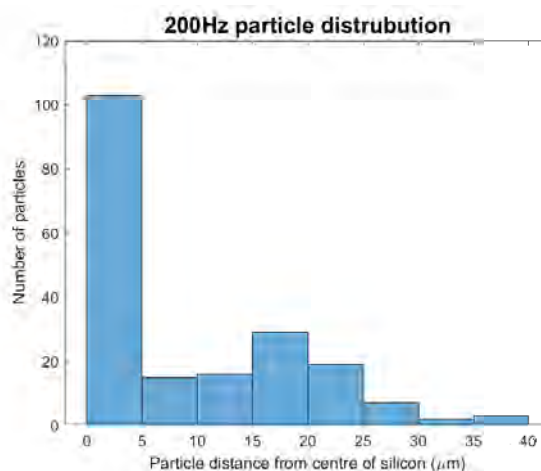
(b) Particle distribution at 25Hz

Figure 9.5: $40\mu\text{m}$ stripes at 25V: Particle distribution at 25Hz

At 200Hz (figure 9.6) there is the regime in which the particles were strongly attracted to the centre of the silicon stripes. This regime was the most reproducible experimentally, and always tended to occur in the region of 100Hz-1kHz, although sometimes it extended lower and higher. Increasing the voltage also made this regime more dominant.



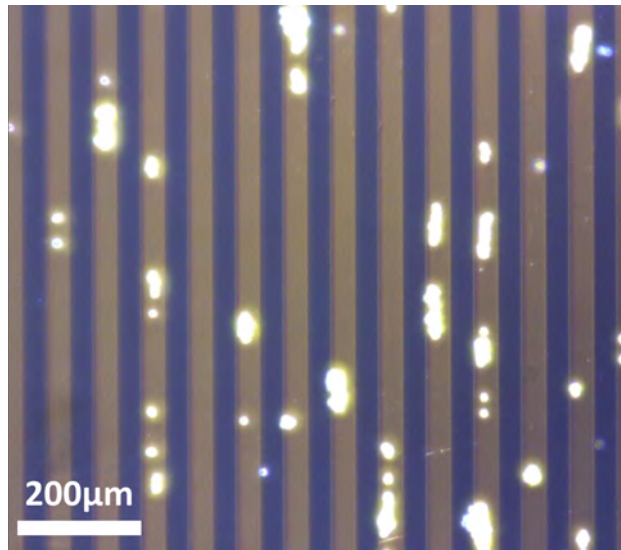
(a) Particles strongly attracted onto silicon



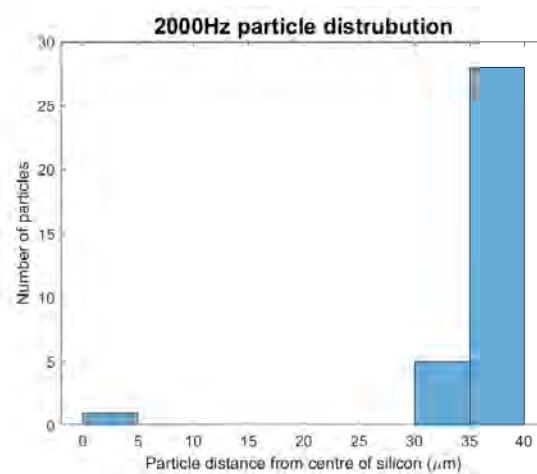
(b) Particle distribution at 200Hz

Figure 9.6: $40\mu\text{m}$ stripes at 25V: Particle distribution at 200Hz

At 2000Hz (figure 9.7) there is the regime in which the particles were attracted to the centre of the gold stripes. This result was not always reproducible and only happened at lower voltages.



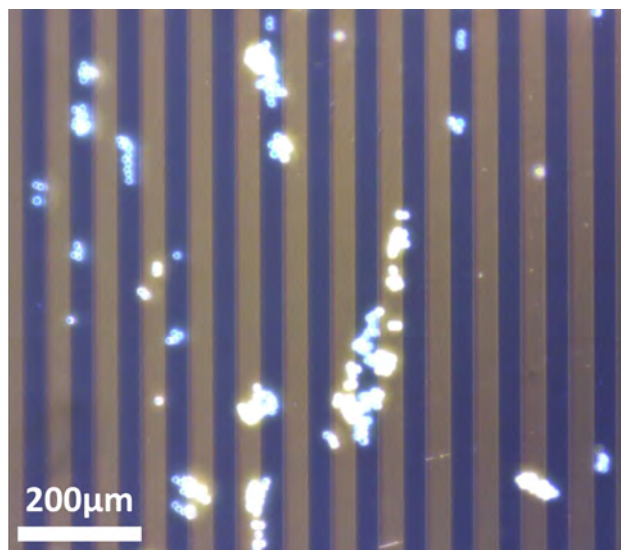
(a) Particles strongly attracted onto gold



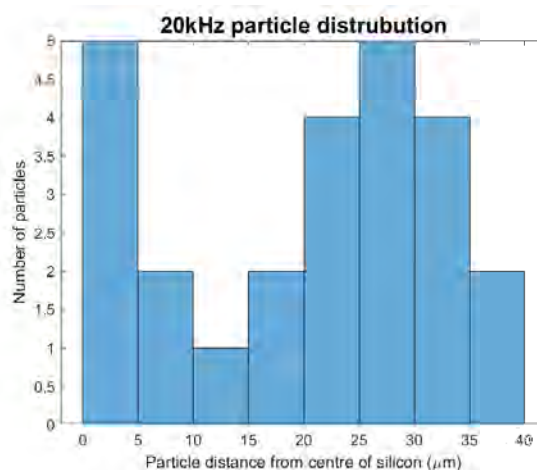
(b) Particle distribution at 2000Hz

Figure 9.7: $40\mu\text{m}$ stripes at 25V: Particle distribution at 2000Hz

At 20kHz (figure 9.8) there is the regime in which the particles clumped together and drifted around randomly without being trapped or attracted to a particular location.



(a) No arrangement of particles



(b) Particle distribution at 20000Hz

Figure 9.8: $40\mu\text{m}$ stripes at 25V: Particle distribution at 20000Hz

Figure 9.9 shows another experiment where the particles were more sparse in the area being examined. When a low voltage and frequency were applied, the particles were weakly attracted to the edge of the gold/silicon interface. It could be argued that this is positive DEP and that the conductivities are now playing a larger role due to the lower frequencies, changing the direction of the DEP force (see section 4.2). However, this is in direct contradiction to the single edge experiments in section 9.1, so there are more electrohydrodynamic (EHD) effects happening than just dielectrophoresis.

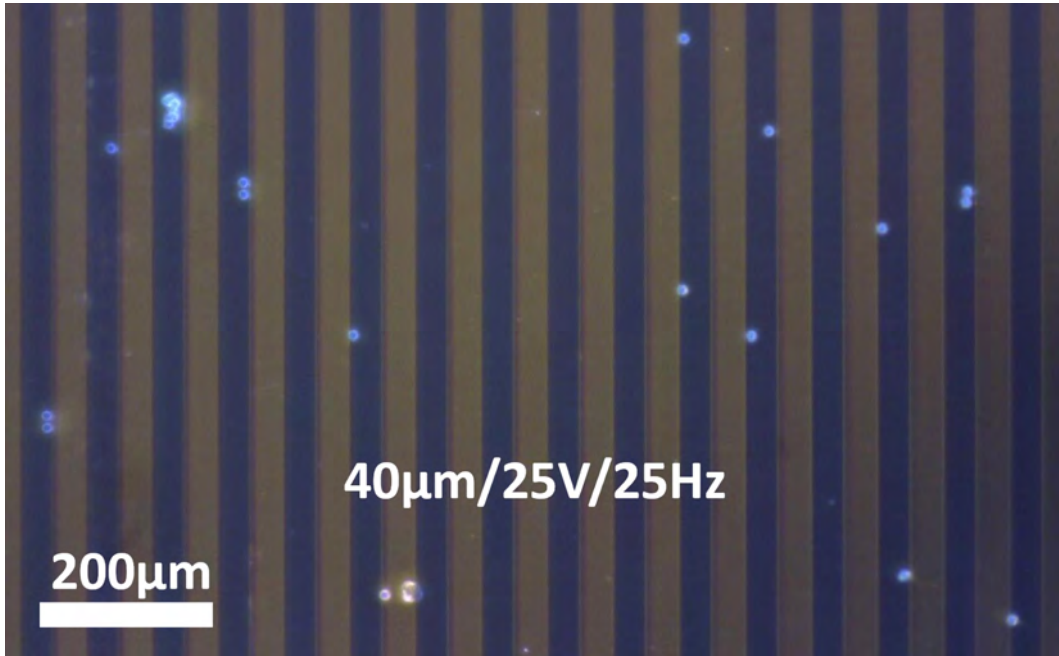


Figure 9.9: Image showing the particles being attracted to the gold/silicon interface at $40\mu\text{m}/25\text{V}/25\text{Hz}$ in an experiment with fewer particles.

9.2.2 20 micron wide stripes

As seen in section 7.1, a stripe width of $20\mu\text{m}$ causes an even greater interference between the neighbouring stripes than the $40\mu\text{m}$ ones. Therefore, it only made sense to test this stripe width to see if they yielded different results than the previous section. The same suspension of decanol and $10\mu\text{m}$ polystyrene microspheres were tested using the same $70\mu\text{m}$ tape method used for the $40\mu\text{m}$ stripes.

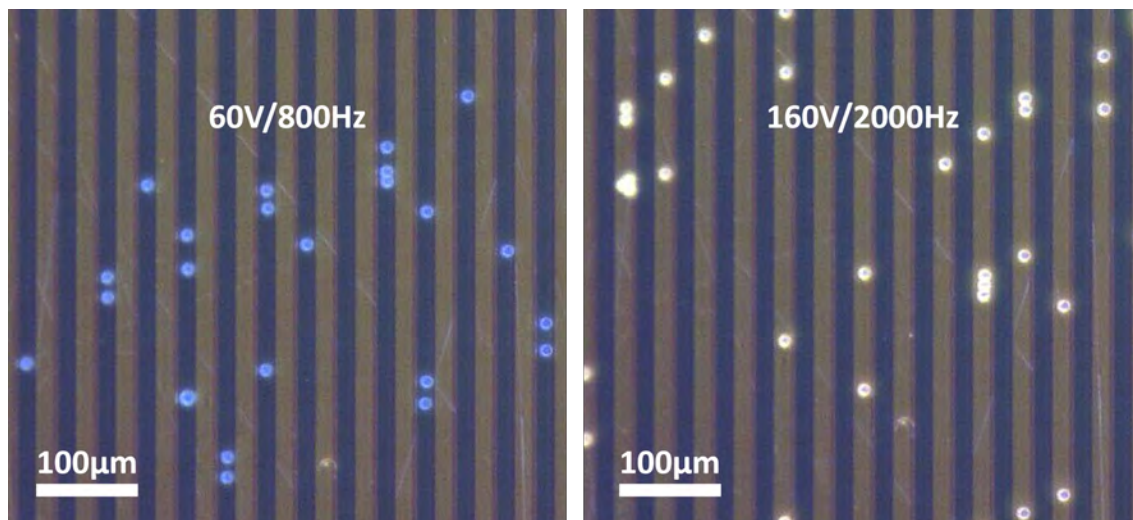


Figure 9.10: Particle DEP on $20\mu\text{m}$ stripes

For the $20\mu\text{m}$ stripes it was found that more voltage/frequency combinations determined where the particles got trapped. Figure 9.11 shows a frequency sweep from 800Hz to 10kHz for voltages from 60V to 180V^2 .

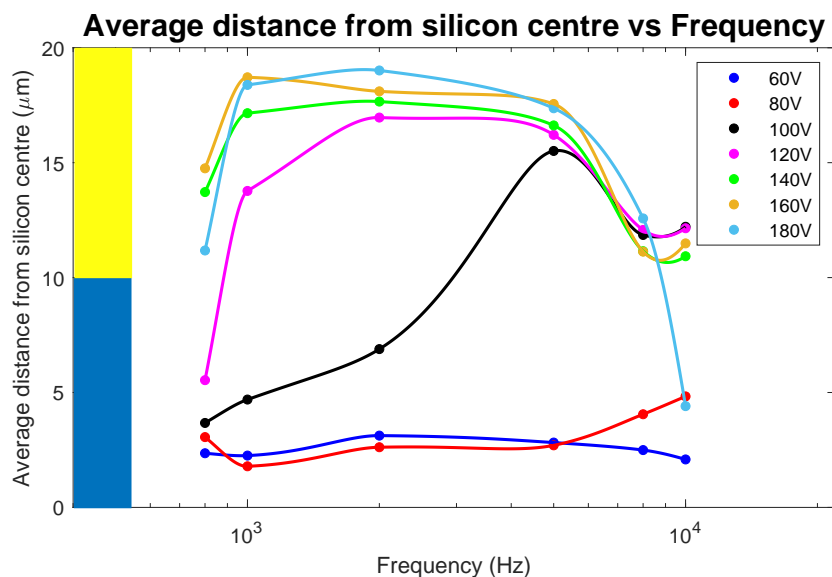


Figure 9.11: $20\mu\text{m}$: Average particle distance from the centre of silicon for several voltages

This experiment showed some contrasting results to the $40\mu\text{m}$ stripes in section 9.2.1, with

²The frequency sweep range was not as wide due to this experiment being done much earlier on in the PhD before the full extent of the low-frequency effects were known.

the lower voltages causing the particles to stay trapped above the silicon region whilst the higher voltages caused them to be trapped above the gold. In the middle voltage ranges (100-160V), frequencies above 8kHz tended to cause the particles to drift without necessarily being strongly trapped above one particular region. There was never any evidence that the particles were getting trapped along the edge of the stripes (pDEP) for any frequency/voltage combination, and the data in figure 9.11 that appears to converge on the edge of the stripes is solely because it is the average position of randomly floating particles, as seen in figure 9.12. In summary, there were only ever 3 configurations for the $20\mu m$ stripes: trapped above silicon, trapped above gold, or not trapped and floating freely.

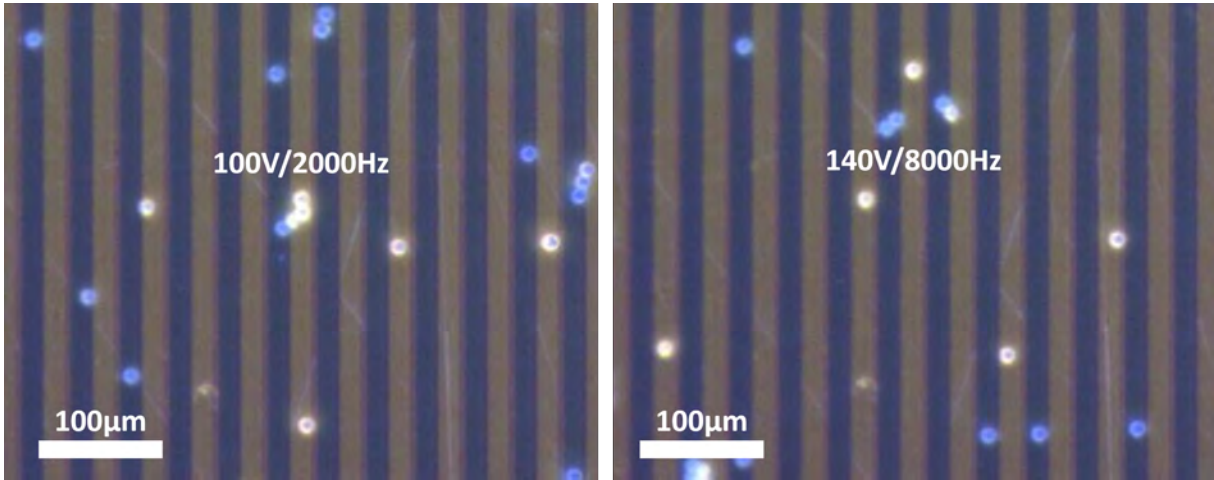


Figure 9.12: Particles drift at random at some voltage/frequencies

9.3 Particle DEP on hexagonal array of circles

In this subsection, we review how the polystyrene microspheres reacted in decanol when they were subjected to the same test as in section 9.2 but instead with the hexagonal patterned array of circles, which gives a more complex 2-dimensional system. Although more complex, one advantage of this geometry is that the particles do not tend to clump together as much and are easier to separate by applying a voltage if they do so.

9.3.1 Large circles (C3A)

To follow a similar logic to section 9.2, we first look at the circles with the largest diameter, also known as pattern C3A. The circles have a pitch of $60.5\mu m$ and a diameter of $40.4\mu m$. See figures 9.14-9.17 to get a visual representation of this pattern. Similarly to the stripes, with the edges being only $40.4\mu m$ apart there will be interaction between the fringing fields expected. In addition, we expect negative DEP at higher frequencies so that the particles would be repelled away from the edges of the circles. Meanwhile, at lower frequencies, we expect to see positive DEP, and hence the particles are attracted towards to edges of the circles. Of course, this is a simplified picture and not only dielectrophoresis can be taken into account, due to the other EHD effects that could be happening simultaneously [179].

One voltage (100V) was tested across a wide range of frequencies from 40Hz to 30kHz and the average distance from the centre of the nearest circle of the particles has been plotted in figure 9.13. The error bars show the standard deviation of the data for this experiment. Again, there appeared to be both similarities and differences than the results of the striped geometry. For frequencies in the range 200Hz-2kHz the particles were strongly attracted into the circles, with there being a sudden spike around the 4-6kHz mark where they were pushed out of the circles onto the gold. Then at 7kHz and above they were strongly attracted back inside the circle again, this time even closer to the centre than before. At <100 Hz there was a slightly weaker attraction to the edge of the circle on the gold. Is this weak attraction at lower frequencies positive DEP? It seems to back up the effects seen in figure 9.9, but then contradicts what was seen at low frequencies along a single edge in section 9.1, so it is still inconclusive.

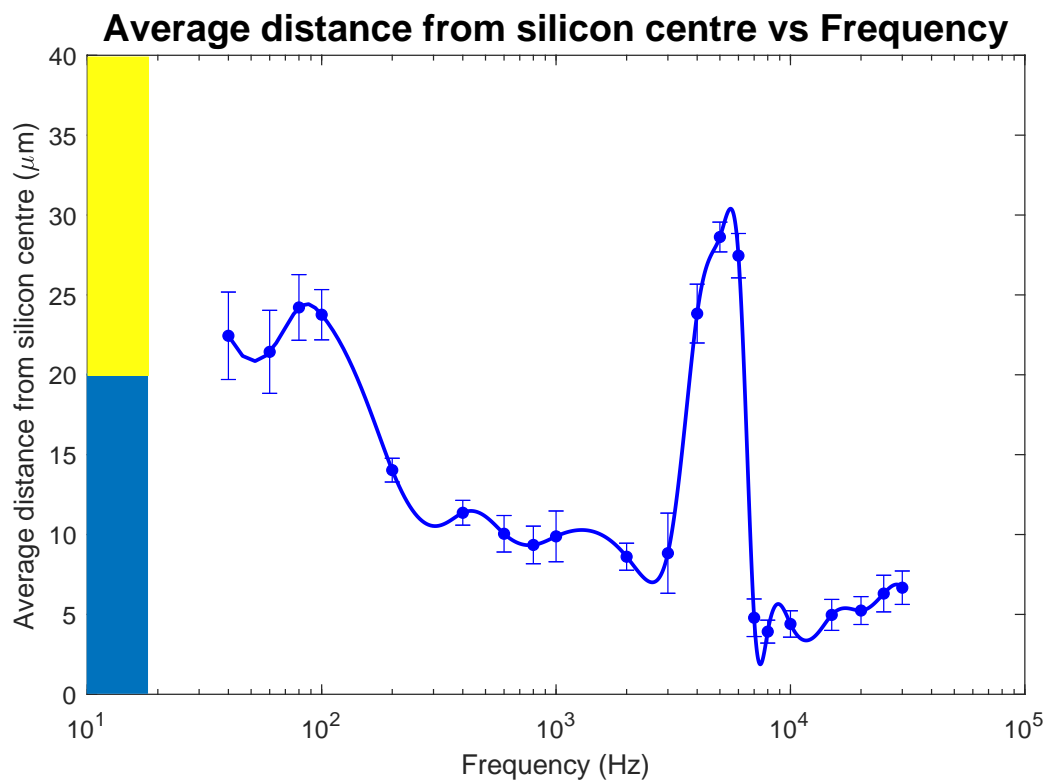


Figure 9.13: C3A/100V: Average particle distance from the centre of large circles vs frequency

Figure 9.14 shows the image and histogram of the distribution of the particles at 100Hz. It shows that they tend to be attracted to the edge of the circles on the gold.

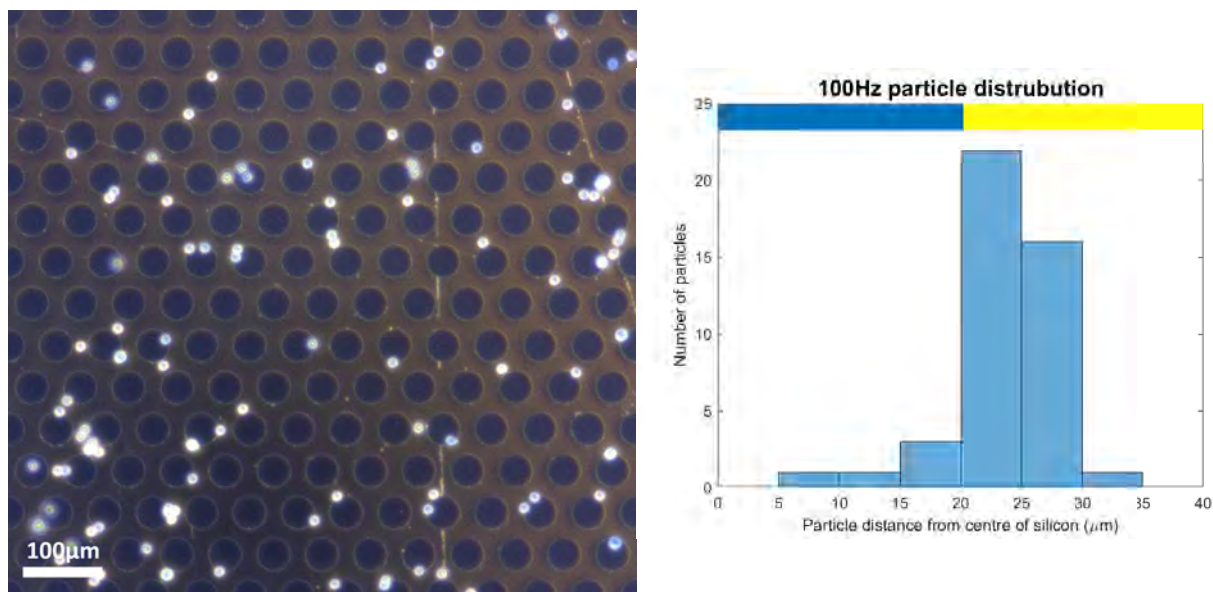


Figure 9.14: C3A/100V: Particle distribution at 100Hz

Figure 9.15 shows the image and histogram of the distribution of the particles at 1000Hz. It shows that they have a tendency to be attracted inside the circle, but not directly in the centre.

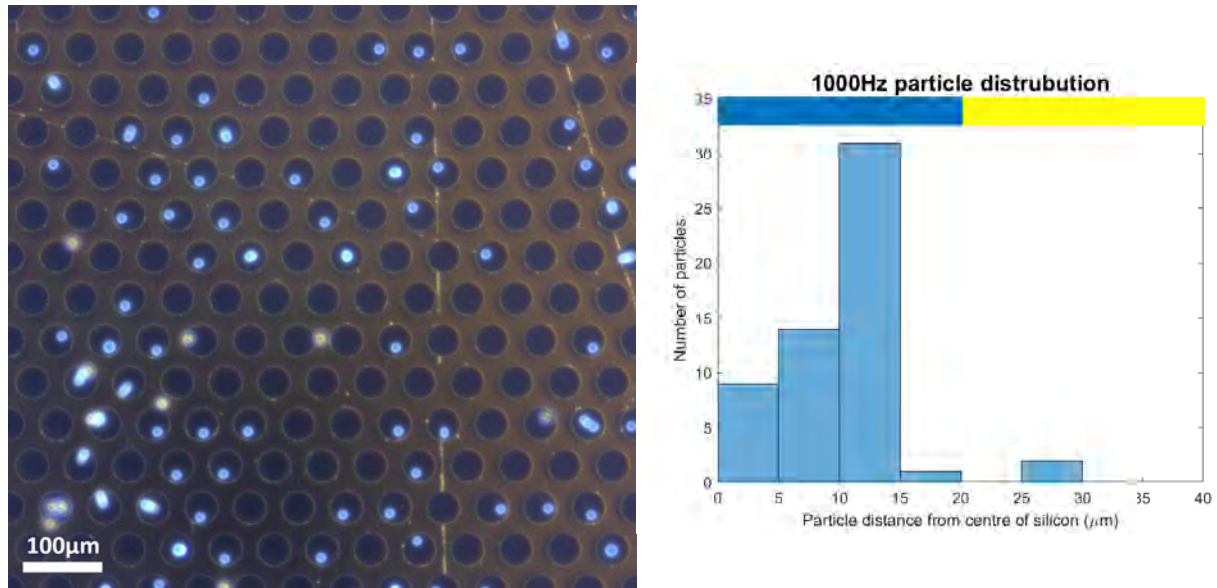


Figure 9.15: C3A/100V: Particle distribution at 1000Hz

Figure 9.16 shows the image and histogram of the distribution of the particles at 5000Hz. It shows that they tend to be pushed onto the gold.

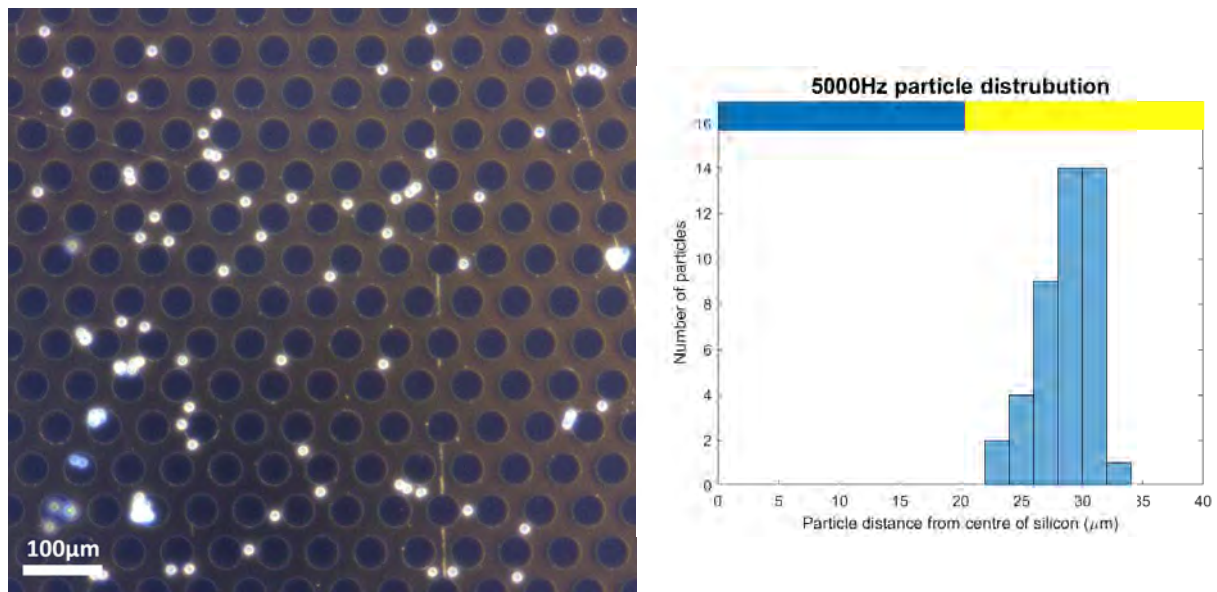


Figure 9.16: C3A/100V: Particle distribution at 5000Hz

Figure 9.17 shows the image and histogram of the distribution of the particles at 10kHz. It shows that they tend to be attracted inside the circle, and much closer to the centre than with 1000Hz.

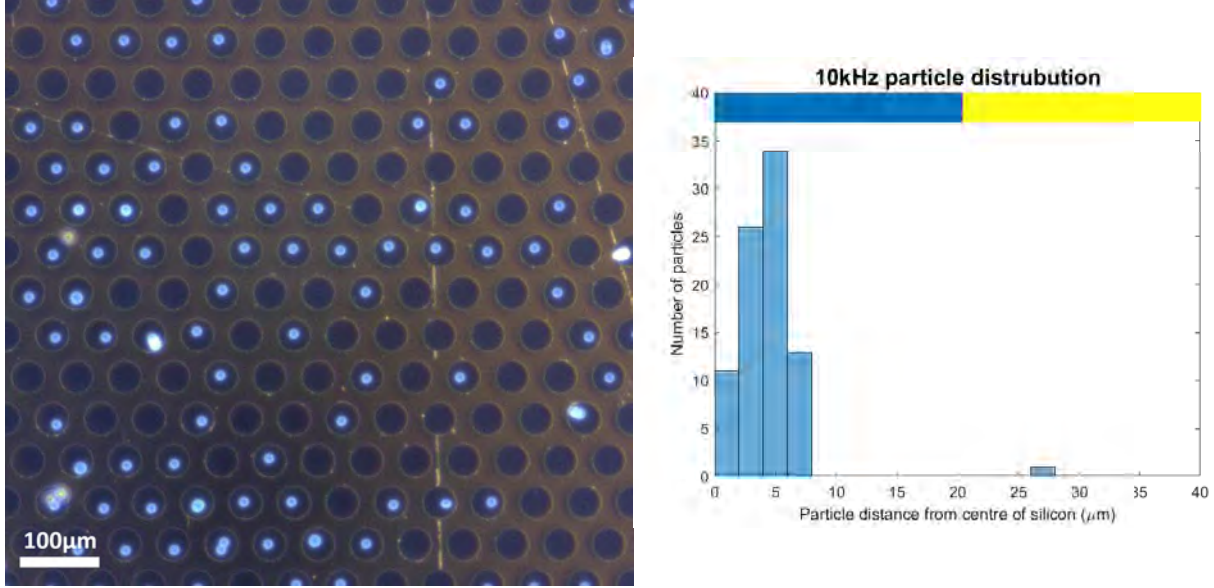


Figure 9.17: C3A/100V: Particle distribution at 10kHz

9.3.2 Small circles (C3B)

Here we take a look at how the microspheres behaved when using the geometry with smaller circles and a smaller pitch, also known as C3B. Similar to how the $20\mu\text{m}$ stripes gave differing results to the $40\mu\text{m}$ stripes due to the closer proximity of the edges as well as being closer to the size of the actual particles, this was also the case for the smaller circles. The C3B geometry consists of a hexagonal array of circles with a diameter of $22.6\mu\text{m}$ and a pitch of $45.3\mu\text{m}$. See figure 9.18 to get a visual idea of the size and spacing of the circles relative to the microspheres for this geometry.

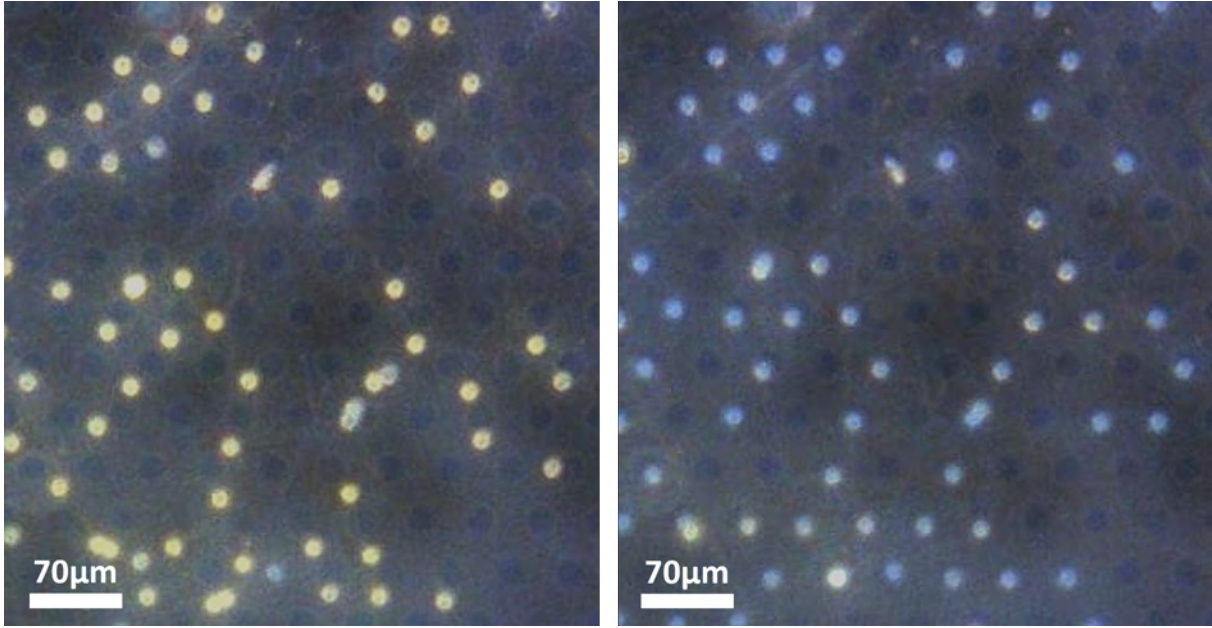


Figure 9.18: Image of particle DEP using C3B geometry

A frequency sweep from 100Hz to 10kHz was done for four different voltages and the average distance from the centre of the circles was plotted against the frequency in figure 9.19. It can be seen how there was both a voltage and frequency dependence on the position of the particles. In this geometry, there was much more consistency across all the particles and there was never a voltage/frequency combination when they appeared to be floating randomly which can be interpreted from the relatively small error bars in the data, which show the standard deviation of the average particle distance from their nearest circle centre.

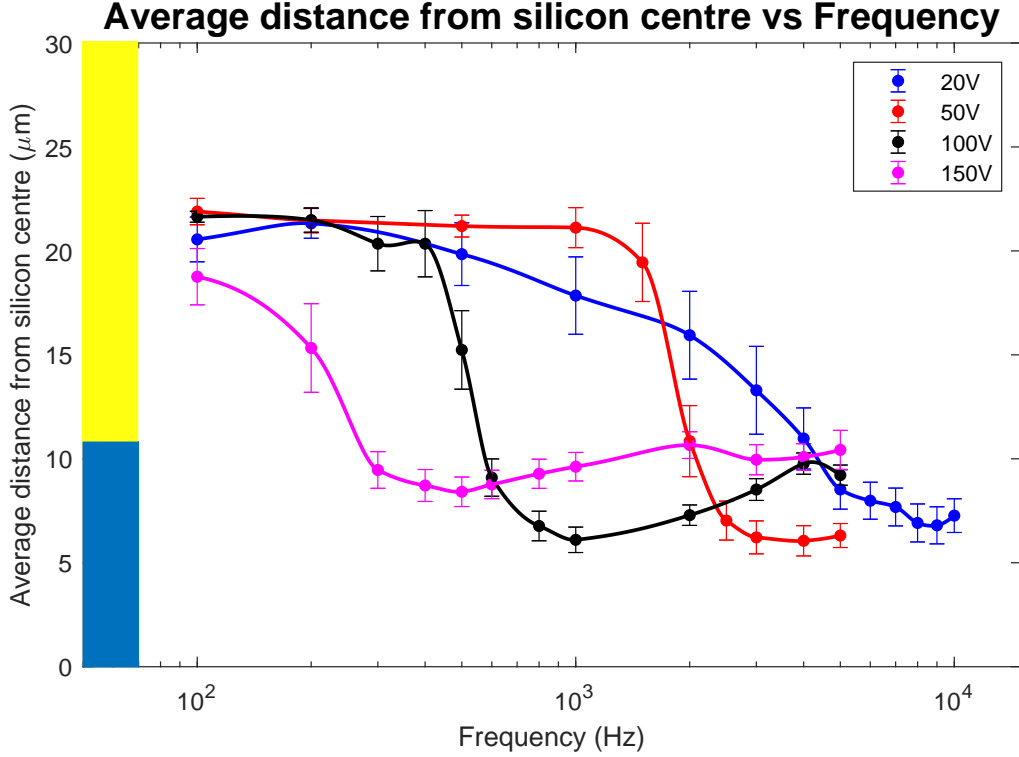


Figure 9.19: C3B: Average particle distance from the centre of small circles vs frequency

This data further reinforces the hypothesis that it is not only particle dielectrophoresis at play in this system since the crossover frequency is also voltage-dependent, which is not included in the Clausius-Mossotti factor.

9.4 Particle DEP liquid film thickness dependence

The final effect discussed in this chapter is that of a liquid film thickness dependence on the position of the particles, even under the same voltage and frequency. This effect was first noticed when a glass coverslip with no Kapton spacers was placed on top of a droplet of particle/liquid suspension on the 5x5mm C3B pattern at 100V/1000Hz. At the outside edge of the glass coverslip (seen as the curved white line in figure 9.20 due to it not being scribed and snapped straight) some of the liquid had spread and formed a relatively thick film of estimated thickness $200\mu m$, and all the particles were attracted onto the silicon inside the

circles (top left). Right underneath the inside edge of the coverslip, the film was very thin with an estimated thickness of less than $30\mu m$. Now the particles had all been pushed onto the gold instead, forming rings around the circles. Finally, the bottom right side of figure 9.20 shows the zone in which the liquid film was estimated to have gotten thick enough for the effect to reverse and the particles to move into the circles again. To test this systematically, the film thickness needed to be controlled and measured.

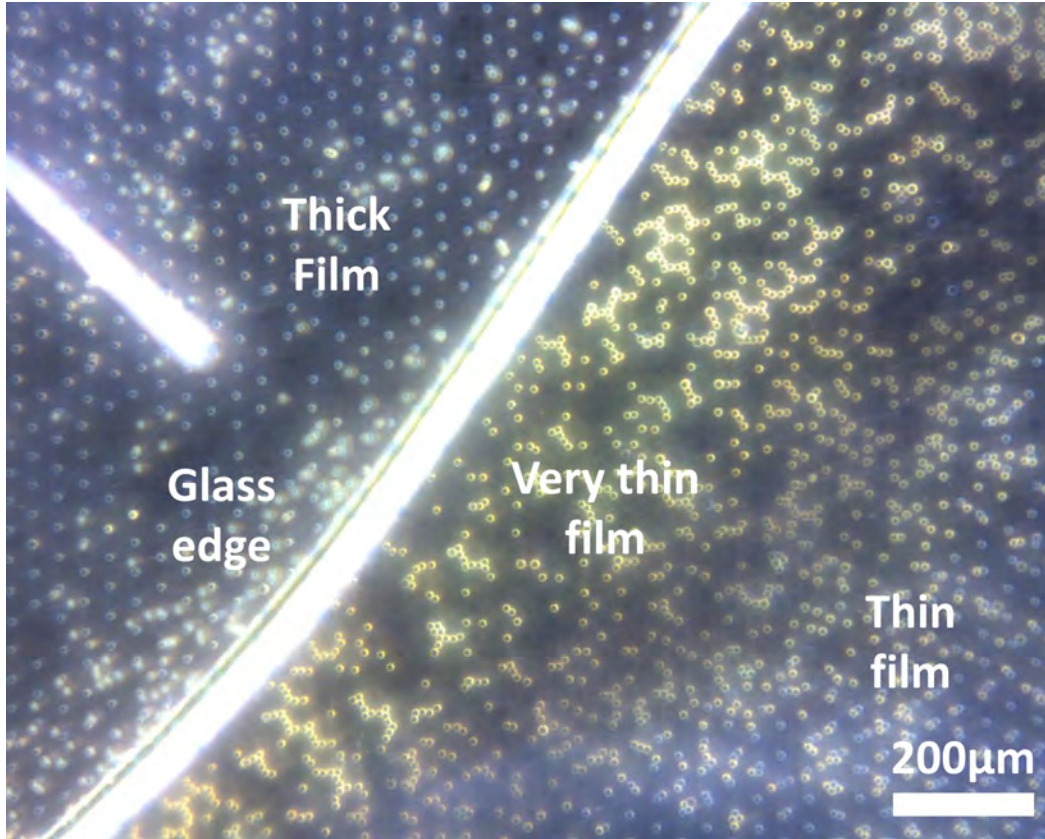


Figure 9.20: Initial discovery of film thickness effect

For all the previous sections up until now (sections 9.1-9.3) there has been a liquid film thickness of $70\mu m$ with a glass slide to cap it, as seen in figure 9.1. It was proven in simulations using ANSYS (see table 1) that the vast majority of the electric field energy is stored well below the $100\mu m$ zone, so $70\mu m$ was deemed suitable for this. However, once the film thickness is reduced it is conceivable that the presence of the glass slide, which has a different dielectric permittivity to the liquid, would have an effect on the electrical properties of the system and therefore change the way the particles behave. Not only this, but the

glass would also change the way any convection currents from other EHD effects, such as electroosmosis, would affect the particles.

To measure the film thickness dependence whilst keeping all other variables fixed, a glass slide was attached to a holder on a fine adjustable stage that had rotation in the x-z plane. This meant that it could be slanted in such a way that the liquid film was slightly thinner on one end of the 5x5mm electrode pattern than the other. Therefore, by using one droplet of particle/liquid suspension and applying just one voltage/frequency combination the only differing variable would be the film thickness.

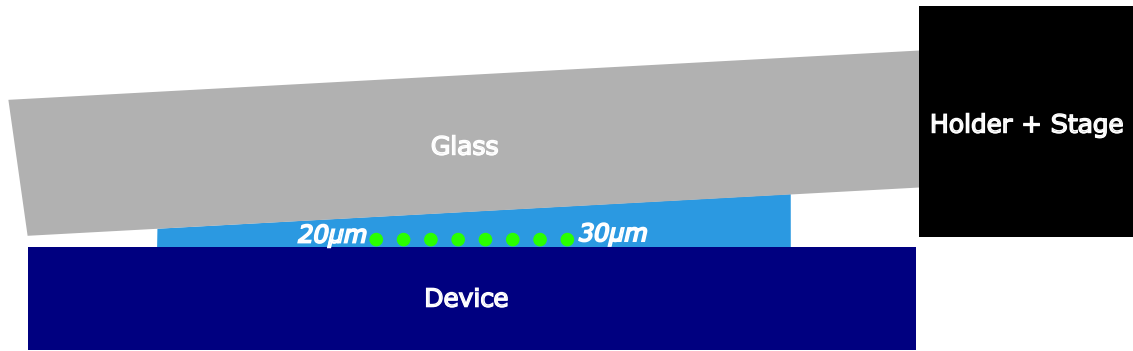


Figure 9.21: Particle DEP for film thickness side view diagram

Like before, $1\mu L$ of particle/decanol suspension was placed onto the 5x5mm array of small circles (C3B pattern), and then the glass slide was slowly lowered onto it as horizontally as possible at first. This was because if there was too much of an angle between the glass slide and the device surface the liquid would quickly slide toward the narrowest part of the gap. This effect is due to the instability of liquid bridges on non-parallel hydrophilic surfaces [180]. Once the droplet was sandwiched between the glass slide and the device, it was slowly squeezed until roughly $100\mu m$ in thickness when looking from a side view camera. It was at this point when the instability of the liquid bridge started to become more prominent, so finer adjustment was needed. A Thorlabs electronic z-stage was then used to slowly move the device upwards whilst the rotation of the glass was tweaked by hand. This process took some trial and error, but after several attempts a relatively uniformly sloped film along the x-axis was formed, as seen in figure 9.22. It shows how the liquid does indeed move towards the

smallest gap between the glass slide and the device, but if the angle and thickness are tuned correctly it is possible to systematically measure the film thickness dependence of this effect. It can be seen from figure 9.22 how the bottom area of the film has a slight yellow hue whilst the top has a slightly blue hue. This is because the particles are trapped above the gold at the bottom and trapped above the silicon at the top. Meanwhile, there is a brown/orange hue in the centre area, which suggests a combination of the two and no trapping at all.

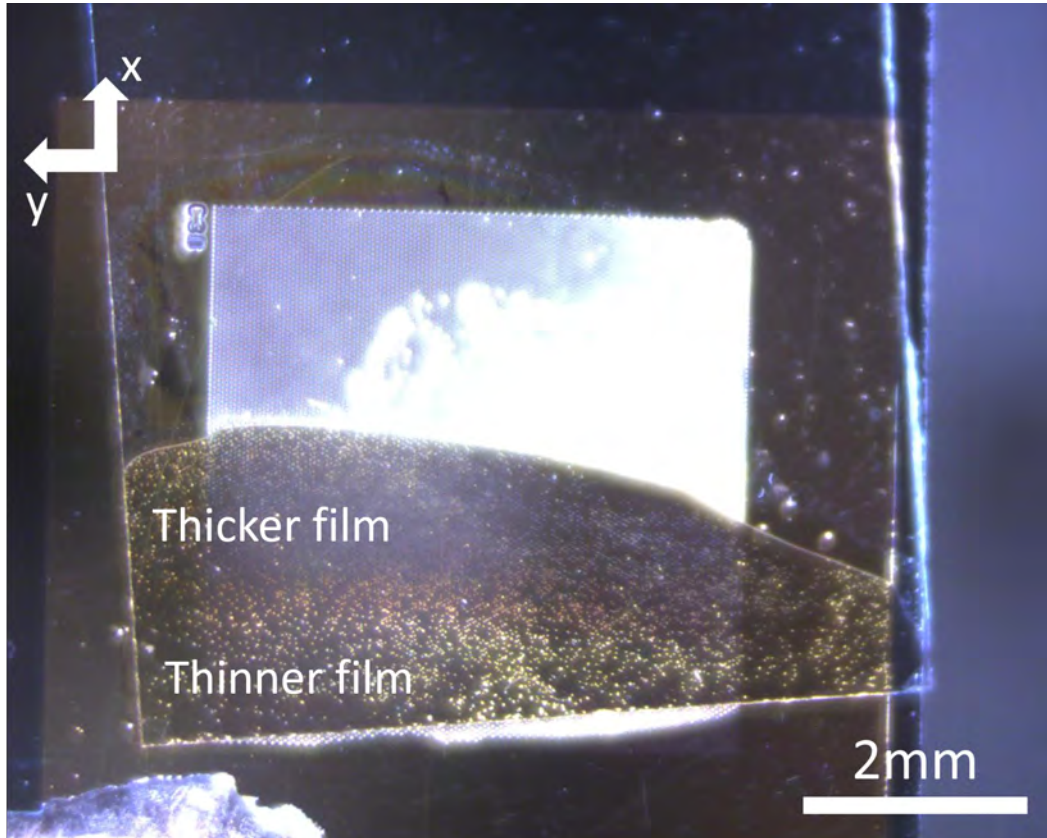


Figure 9.22: Particle DEP for film thickness top view image

To get accurate estimates of the film thickness, a 20x lens was used and the top-view camera was set up onto an electronic fine adjustable stage (ThorLabs apt DC Servo Controller). This was so it could be finely adjusted to focus on the device surface or the underside of the glass slide. By subtracting the z-distance that the camera had to move between these two points of reference, the film thickness could be calculated.

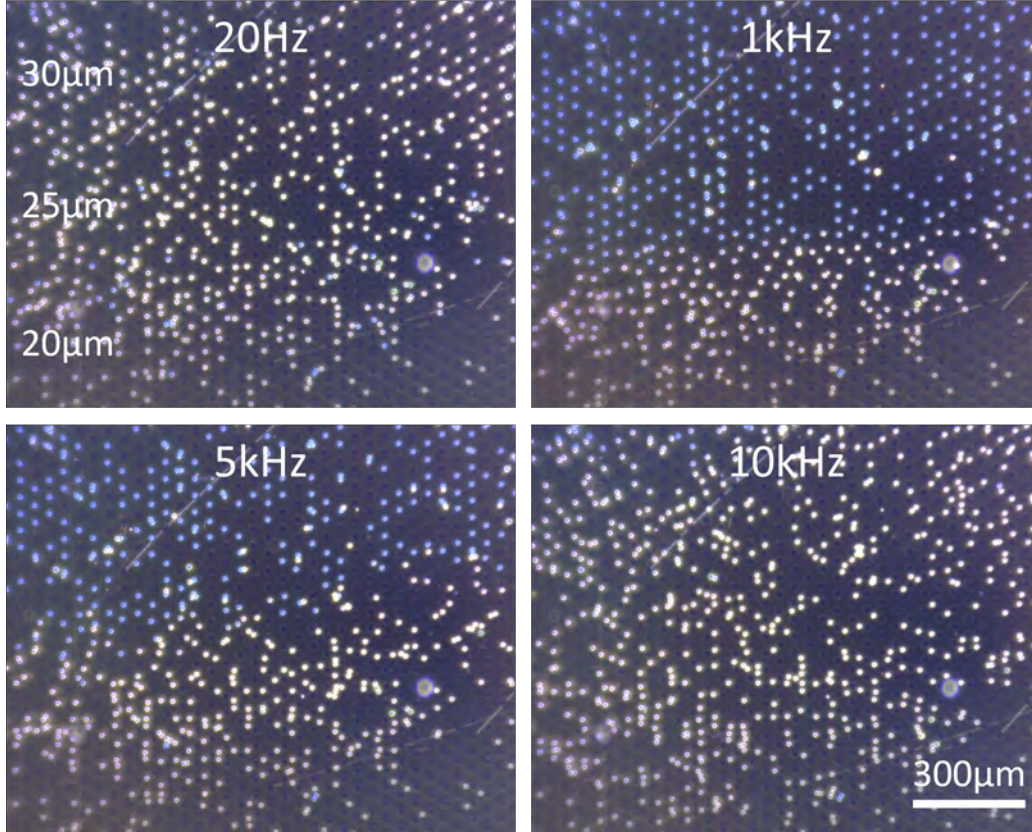


Figure 9.23: Particle DEP for film thickness zoomed images - C3B Decanol 100V

Figure 9.23 shows some zoomed-in images of the liquid film thickness dependence experiment with decanol at 100V in the C3B geometry. Using the focusing technique mentioned above, the measured film thickness was $30(\pm 2.5)\mu m$ in the top third, $25(\pm 2.5)\mu m$ in the middle third and $20(\pm 2.5)\mu m$ in the bottom third of the image. Keeping everything else fixed a frequency sweep was performed and the average particle distance from the centre of its nearest circle was plotted against frequency for the three film thickness zones. The results are shown in figure 9.24. It reveals how at the thicker film region ($30\mu m$) the particles will still exhibit some frequency dependence, but this then gets diminished as the film gets thinner ($25\mu m$) until it does not show any frequency dependence once it gets to $20\mu m$ or below.

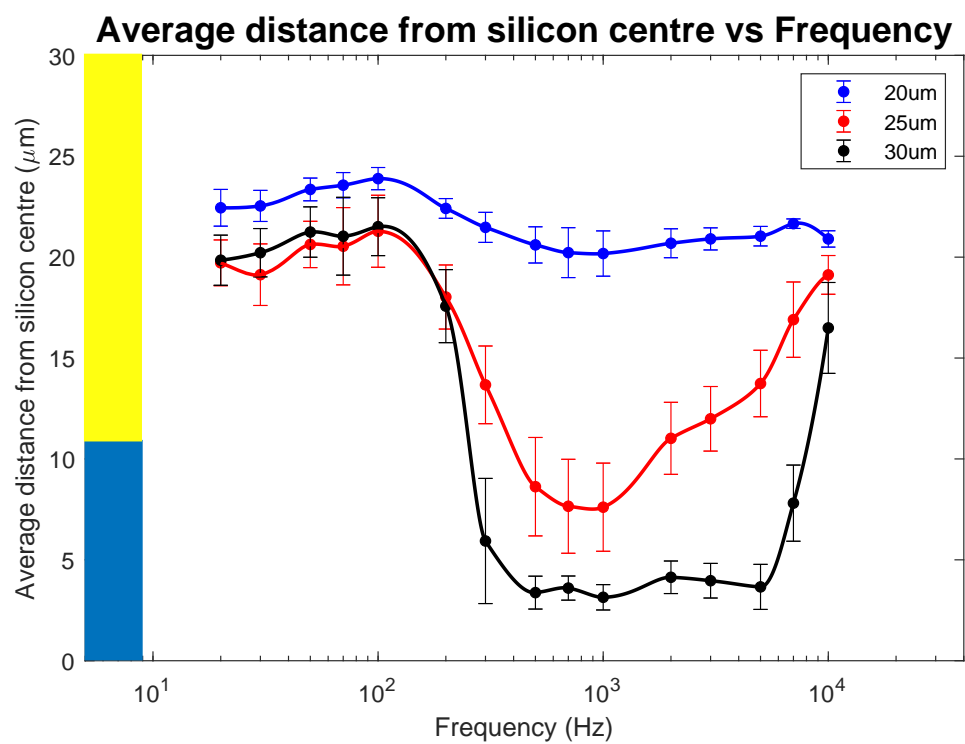


Figure 9.24: Liquid film thickness dependence on C3B geometry at 100V

10 Microdroplet arrays

This chapter focuses on the formation and evaporation of 5x5mm arrays of tightly packed microdroplets using the MIS geometry. These arrays were formed by first spreading a parent droplet into a thin film across the entire 5x5mm area and then, while the voltage was still applied, blowing the vast majority of the excess liquid off so that only a tiny amount remained trapped by the fringing fields at the electrode edges. When the voltage was switched off, the remaining liquid dewetted into an array of microdroplets whose size and pitch mirrored that of the underlying electrode pattern.

10.1 Formation of microdroplet arrays

To produce an array of microdroplets that last for any substantial amount of time to be photographed or measured, a liquid with a low enough evaporation rate was required. It turned out that decanol was the perfect candidate for this. For all practical purposes in the PhD up until this point, decanol had been considered a non-volatile liquid due to the fact it would practically take days to evaporate just a single microlitre-sized droplet at room temperature. However, once we get down to picolitre-sized droplets evaporation starts to become more important, even for a liquid like decanol. The effects of evaporation will be discussed more in section 10.2.

10.1.1 Creating a microdroplet array

The geometry best suited for the creation of microdroplet arrays was that of the hexagonal lattice of circles, which was used in the particle dielectrophoresis chapter (see section 9). This is because liquid got trapped in the strong fringing fields along the inside edges of the circles when the rest of the film was blown away. Once the voltage was turned off, the

most favourable way for the liquid to dewet was towards the centre of the circle to form a microdroplet. This meant that the x-y positions of the microdroplet centres were always in the circle centres of the array. There was also a correlation between the size of the circle and the size of the final microdroplet, with larger circles leading to larger microdroplets.

To create the array of microdroplets, a $1\mu\text{L}$ droplet of decanol was deposited onto the $5\times 5\text{mm}$ patterned area of the electrode. A voltage was then applied to the device to wet the droplet into a thin film. A frequency/voltage combination of $8\text{kHz}/180\text{V}$ was used. Due to the stagnation lines discussed in section 7.2.1, the droplet often needed some help spreading completely into a thin film by blowing it gently on a low setting using a Dorobeen electronic air duster. Once the liquid had formed a uniform thin film across the entire $5\times 5\text{mm}$ area, and whilst the voltage was kept on, the air duster was turned to its high setting and the excess liquid was blown from the 'right side' until $5\times 5\text{mm}$ area appeared uniformly white to the naked eye. This typically took about 5 seconds on the highest power with the nozzle at a distance of 5cm . The voltage was then switched off and the remaining liquid dewet to form the array of microdroplets.

10.1.2 Droplet size consistency across array

The first systematic study done on microdroplet arrays was to determine the consistency of the size of the microdroplets across the entire array. Due to the resolution of the camera system, it was not possible to get accurate measurements of the whole $5\times 5\text{mm}$ array in one photo, so 9 zoomed-in images with a $10\times$ lens had to be taken. An example of this is shown in figure 10.1. These zones are labelled with names such as 'top left' and 'bottom right', with the most important thing to note being that the air was always blown from the right side for every experiment in chapter 10. This has significance when considering any bias to droplet size or evaporation rate in section 10.2.

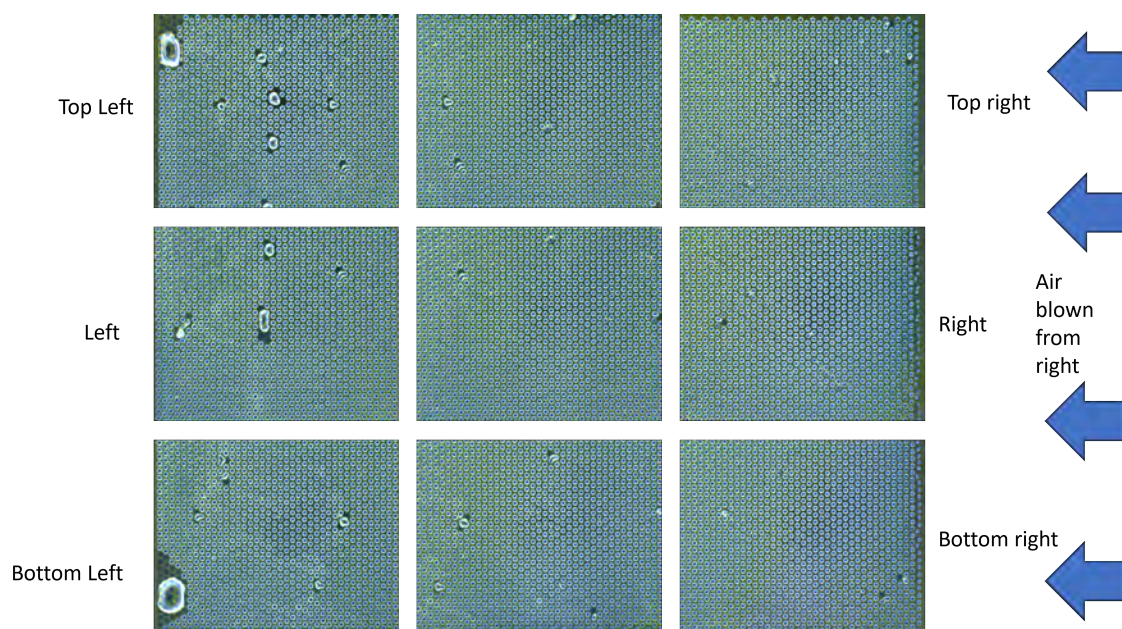


Figure 10.1: 9 zones of C3A microdroplet array

There was often some overlap between each zone from the zoomed-in images, but it was decided that there was no need to crop the images to prevent the overlap since this meant that they would often be different sizes. After all, we are not interested in the overall count of microdroplets in each zone or the entire array but instead want an idea of the size distribution of the microdroplets in those areas, so some overlap was not seen as an issue. The images were taken from right to left within a 2-minute window, starting at the top right and ending at the bottom left. This attempted to minimise the time that the microdroplets would spend evaporating between the first and last photo.

To get a size distribution the thresholding method documented in methods section 6.2.4 was used. This allowed for quick and easy radius measurements of microdroplets in the whole image at once. There were some slightly unfocused microdroplets at the corners of the image due to field curvature [181] which may have caused some artificial scatter in the data, but the vast majority of the image was in focus and some good results were obtained from this experiment as seen in figure 10.2.

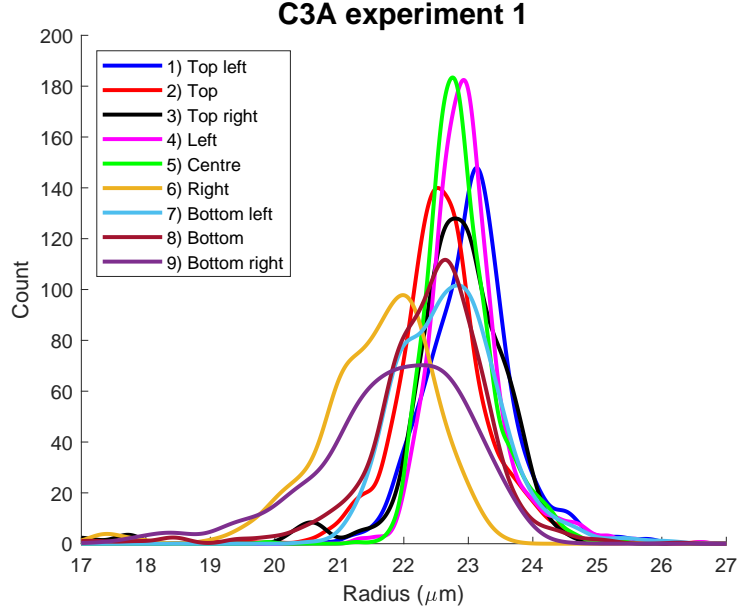


Figure 10.2: C3A experiment 1: Droplet size distribution in each zone

The first electrode pattern tested was the C3A array. The underlying electrode circles have a pitch of $60.5\mu m$ and a radius of $20.2\mu m$, which was the largest of the available designs on the photomask. Figure 10.2 is a fit of the histograms for the first attempt at creating a uniform array of microdroplets using the C3A geometry. The x-axis shows the radius of the microdroplets and the y-axis shows the count. Since it would be impractical to plot nine histograms on top of one another, instead a ‘kernel’ distribution was fitted to each histogram to give a better way of comparing all nine zones of the array at once. Another important thing to note is that any droplets with radii much larger than the size of the underlying pattern were not plotted, as they were considered outliers due to scratches and other defects on the surface. This is analysed further in section 10.1.4.

The first thing that is apparent from figure 10.2 is how the peaks of the bottom right and right zones are shifted to the lower radius values, as well as having a wider distribution. The reason for this was attributed to two mechanisms: The first being that the array was blown from the right-hand side, and therefore the droplets in the far right of the array had evaporated due to the air-blowing process. The second is that the droplets from the right side are closer to the nozzle of the air blower and therefore more liquid is removed from the

surface prior to the voltage being switched off. Besides this, all other zones appear to show very consistent microdroplet radii and width distributions across the array, averaging around the $23\mu m$ mark with average deviations ranging from $0.4\mu m$ to $0.8\mu m$.

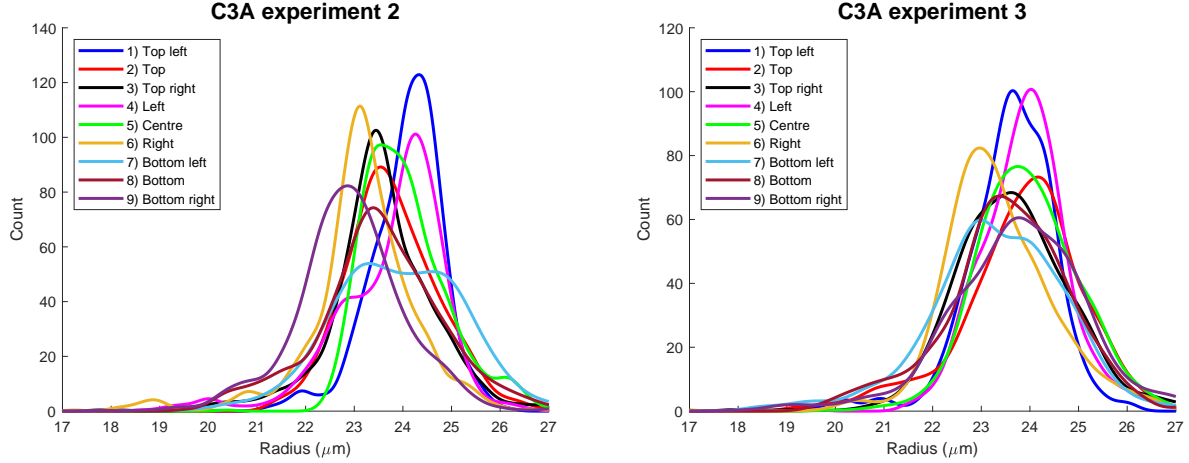


Figure 10.3: C3A experiment 2/3: Droplet size distribution in each zone

The second experiment for spatial consistency across the C3A array is shown in figure 10.3 (left). This time there was still some bias of the bottom right and right zones towards smaller radii, but also this time the three left zones had a bias towards larger radii which further backs up the evaporation/liquid removal hypothesis. The third experiment for spatial consistency across the C3A array is shown in figure 10.3 (right). This was the most consistent of all three attempts for the average radii for the nine zones. However, the width of the distribution was wider than in the first experiment. This may have been caused by focusing issues such as the camera not being completely perpendicular to the plane of the device, causing an artificial wider distribution across each zone. It could have also been caused by turbulence in the blown air, causing an uneven distribution of droplet sizes across the array (seen as ripples in figure 10.7).

10.1.3 Droplet size consistency over multiple experiments

The droplet radius data from section 10.1.2 can be taken from all 3 experiments and plotted on separate graphs for each of the 3 columns (left, centre and right) of the array, so it is easier to compare droplet size consistency across multiple attempts at creating the arrays in each area. The plots are shown in figures 10.4 and 10.5.

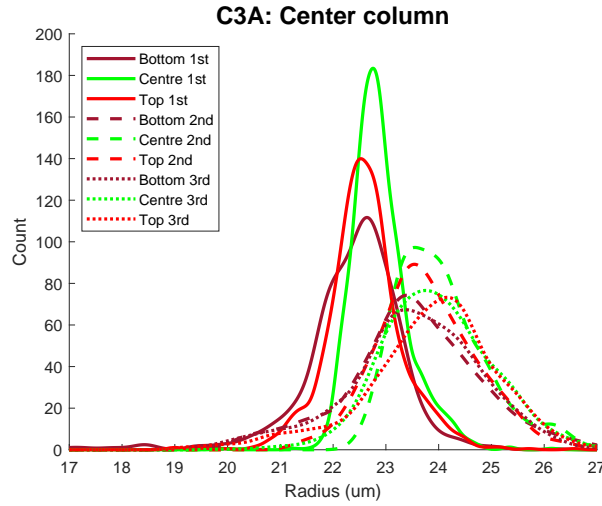


Figure 10.4: Droplet size distribution over 3 experiments for middle column

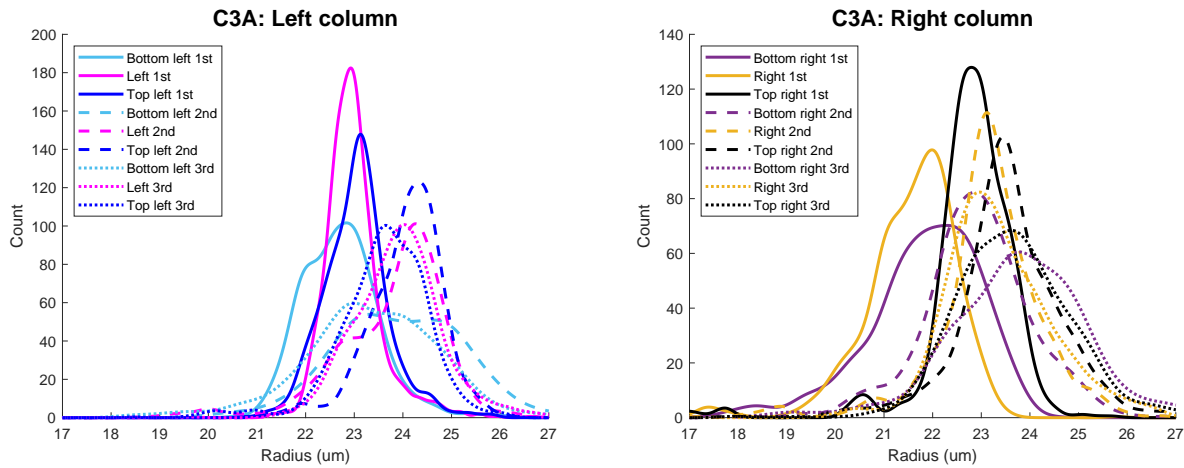


Figure 10.5: Droplet size distribution over 3 experiments for left and right columns

The plots show a maximum average radius difference of roughly $2\mu m$ between the three experiments on the C3A array across all nine sections of the array. The main reason for this

is thought to be the amount of time spent blowing the liquid off to create the array. The longer spent on blowing liquid off, the more liquid that is trapped by the strong fringing fields will evaporate and therefore leave smaller microdroplets when the voltage is switched off.

10.1.4 Large defects in microdroplet arrays

In addition to the general distribution of microdroplet size that was discussed in sections 10.1.2 and 10.1.3, there were also large defects present in the microdroplet arrays that were often caused by damage to the Novec 2702 coating, debris on the surface, or simply where the liquid had not been properly blown off in the corners of the array. This caused droplets to form that were larger and often non-circular in shape after the voltage had been switched off. To determine a size for the defects since they were often not circular, the area A was found using the thresholding method as seen in section 6.2.4 and then the ‘effective radius’ of the defect was found using the formula $r = (A/\pi)^{1/2}$. A histogram for the large defects of effective radii larger than $30\mu m$ has been plotted in figure 10.6. It reveals that the first experiment on the new surface had fewer large defects than the subsequent ones. The C3A array has 6940 droplets in total, so for the first experiment, a total of only 26 large defects was considered to be quite successful. In the second and third experiments, a total of 106 and 83 large defects were present. A more in-depth study on the surface degradation over time was not pursued due to other work higher in priority.

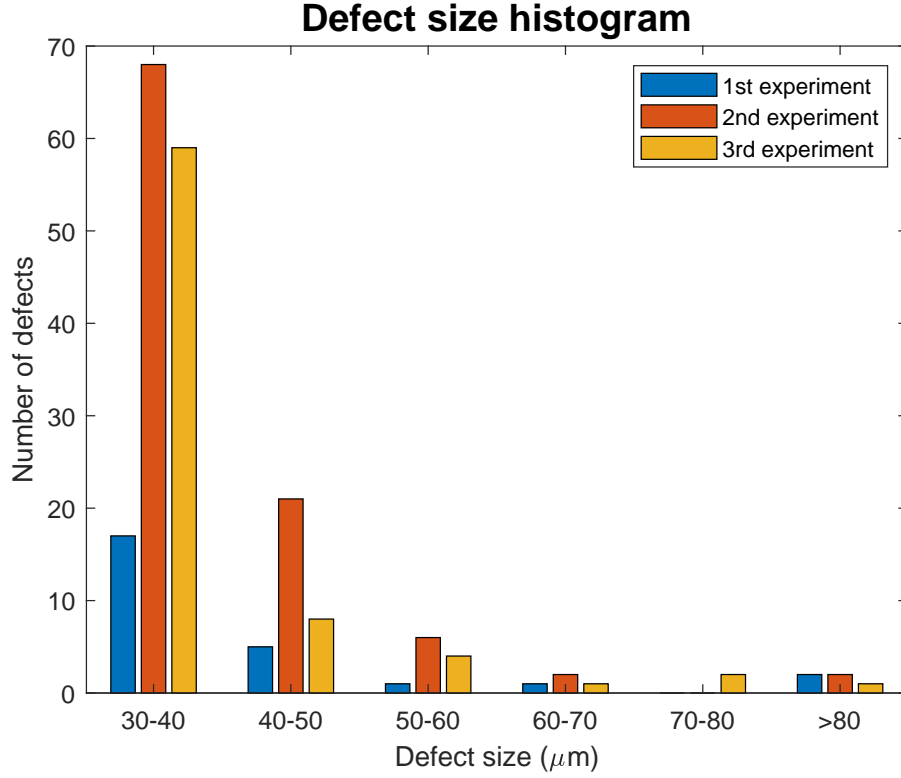


Figure 10.6: Large defect count over multiple droplet array experiments

10.2 Evaporation of microdroplet arrays

While droplet printers can be used to print uniform arrays to study the evaporation of larger droplets [77], there is currently no way to get such uniform arrays of microdroplets. Whilst inkjet printing technology can indeed create droplets in the picolitre range [182], the time taken to print an array of 100x100 microdroplets would mean that the first droplet had already evaporated well before the last one has been printed. Using the new technique to quickly and reliably create microdroplet arrays allowed us to study the evaporation of thousands of tightly packed microdroplets.

10.2.1 C3A evaporation

The first array size tested for evaporation was the C3A array. This gave the largest microdroplets which took the longest time to evaporate, but due to their size more accurate data of droplet radii could be obtained across a wider area of the array at once. Using the same technique described in section 10.1.1, a 5x5mm array of microdroplets was produced on the C3A electrode pattern. This led to an average microdroplet base radius of around $21\mu\text{m}$ across the array with a pitch of $60.5\mu\text{m}$. For the first experiment, a zoomed-out image of the entire array was taken at regular time intervals. This did not allow us to see individual droplets for droplet radius measurements but instead allowed for droplet lifetime measurements since it was clear when a microdroplet had fully evaporated due to the change in colour from light to dark. As seen in figure 10.7, the microdroplets take a long time to evaporate for such a small amount of liquid. This is a consequence of the low volatility of decanol. The temperature in the lab during this experiment was 19°C and the humidity was 45%.

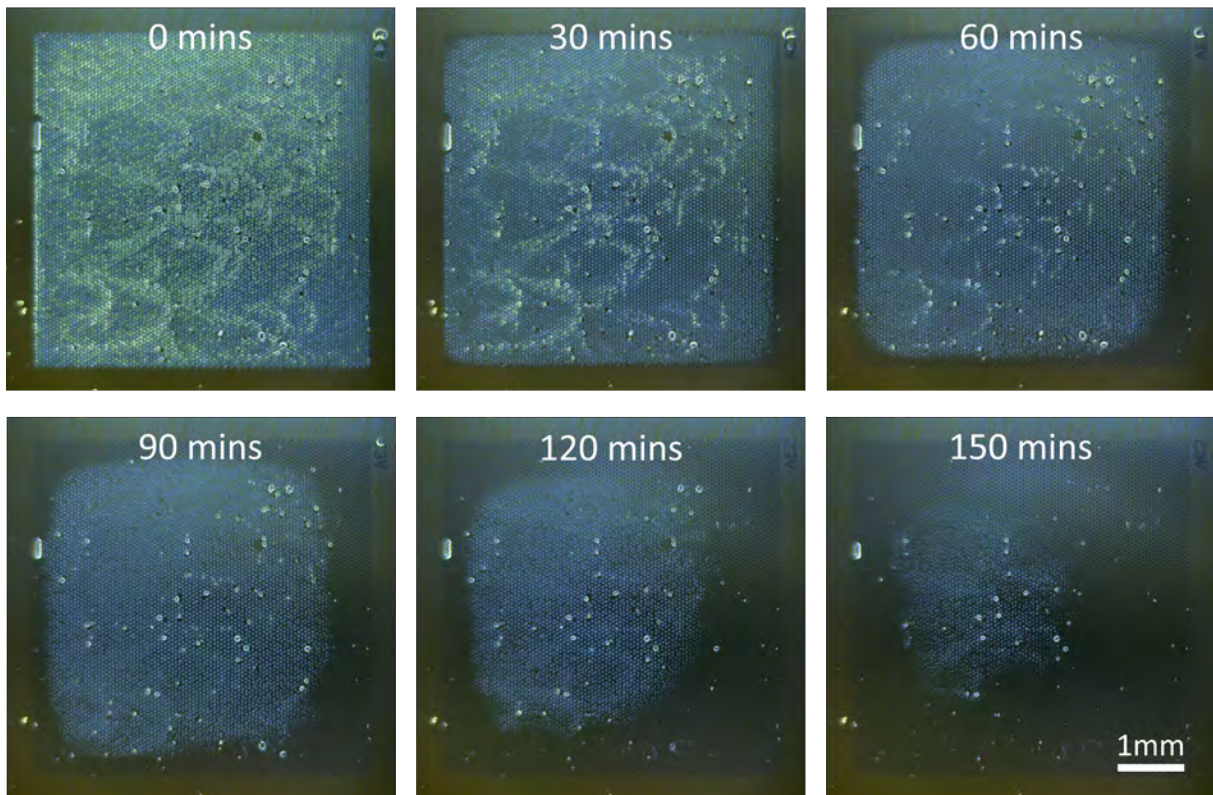


Figure 10.7: Images of C3A microdroplet array evaporation

To compare experimental data to theory, the time of the experimental data was normalised by dividing the droplet lifetimes by the lifetime of the final droplet to evaporate, which was 170 minutes in this case. A contour plot (figure 10.8a) can then be used to show the normalised droplet lifetimes of the experimental data as the array evaporates. A python simulation based on the Masoud theory (see section 2.3.4), which was created by Joey Kilbride for his PhD, was run using the same C3A array pitch (s), droplet base radius (R) and a contact angle of 40° . The density or diffusion coefficient constants for decanol were not required in the simulation since the evaporation time would have scaled linearly with these constants and been normalised regardless.

Figure 10.8b shows the normalised lifetime plot for this simulation.

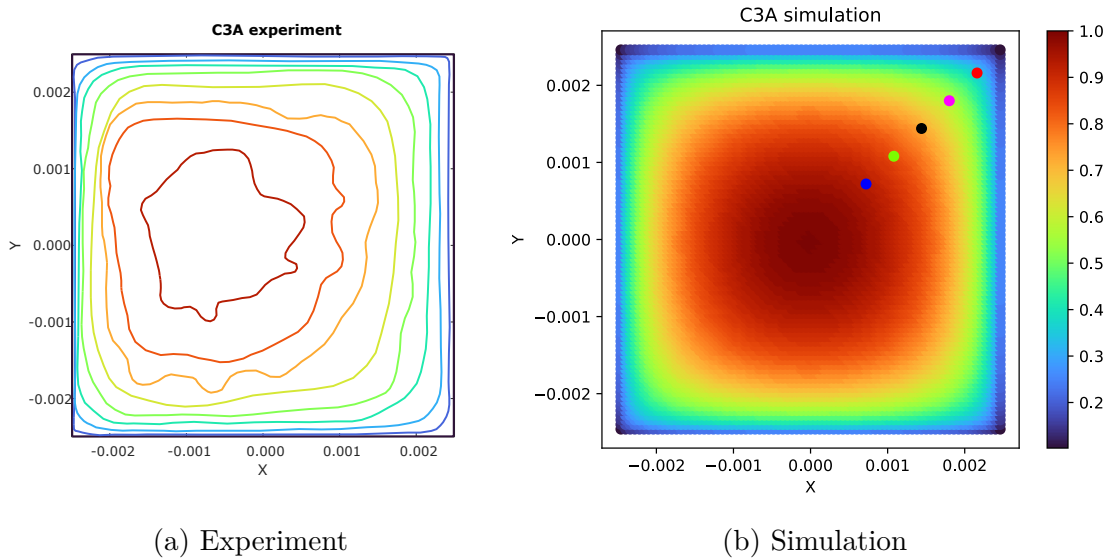


Figure 10.8: Experimental and simulated normalised droplet lifetimes for C3A array. Coloured dots on the simulation plot represent the lines in figure 10.9. Droplet lifetime is normalised with respect to the time it takes for the entire array to evaporate.

Figure 10.8 allows us to compare and contrast the experimental data of the microdroplets and the Masoud theory side by side using normalised droplet lifetimes, where blue shows the first droplets to evaporate and red shows the last. Something first noticed in the experimental data that points to evidence of diffusive evaporation is that the corners of the square array begin to evaporate first, quickly becoming more rounded before at later stages tending towards a

more rounded shape. Since the Masoud theory only considers diffusive evaporation this is also seen in the simulation, giving both plots very similar-looking shapes.

One difference between the two plots in figure 10.8 is how the experimental data is not smooth at later times. This is due to the variation in droplet size which can be seen in the top left image of figure 10.7, which is probably due to some air turbulence when blowing the film off. This meant that as the droplets evaporated some areas had longer lifetimes, which is shown as unevenness in the contour plot. Meanwhile, the simulation is perfectly symmetrical as one might expect. Another difference between the experimental data and simulation is that there is a clear bias in the direction of how the microdroplets evaporate. In every evaporation experiment, the droplets always tended to have a bias to evaporate towards the left of the centre last. It is suspected that the reason for this is due to the air is blown from right to left (see figure 10.1), and therefore there would be some decanol on the device to the left side of the array, in addition to there being some slightly larger droplets along the left side of the array. This would create a higher vapour concentration on the left side than on the right side, which would slow down the net rate of evaporation on the left compared to the right, therefore creating a bias which is reflected in the data.

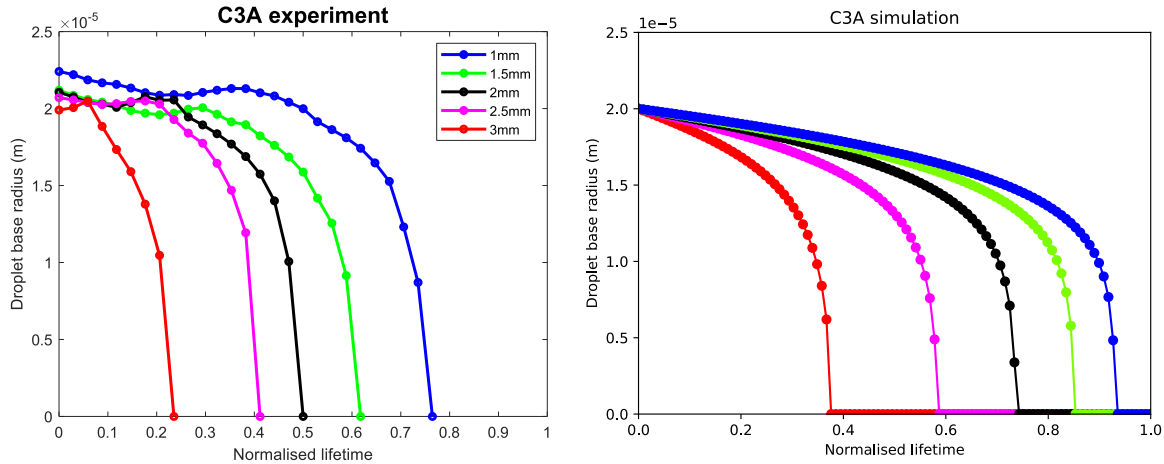


Figure 10.9: Droplet base radius vs normalised lifetime along diagonal for C3A array. The colour of each line corresponds to a single droplet location as shown by the coloured dots in figure 10.8b. Droplet lifetime is normalised with respect to the time it takes for the entire array to evaporate.

Figure 10.9 shows the experimental and simulated data for the droplet base radius vs time at five equally spaced points along the top-right diagonal corner whose positions are also shown in figure 10.8b. For the experimental data, the average base radius of a cluster of seven microdroplets was measured using the thresholding technique shown in figure 6.7 at regular time intervals. Since the evaporation times were getting normalised to compare to the simulation regardless, it was not seen as an issue that the zoomed-out droplet lifetime measurements and zoomed-in droplet base radius measurements were not taken during the same experiment.

Much like the lifetime plot, the base radius vs time plot shows many similarities to the Masoud simulation. Although the relative timescales at which the droplets evaporate are off due to the direction of the evaporation bias, the shape of the curve is indicative of the constant contact angle (CA) mode of diffusive evaporation (eqn 2.23). The shielding effect is also obvious from this graph, in which the droplets near the centre evaporate at a much slower rate to begin with. There does appear to be a subtle difference between the experiment and simulation, in which there appears to be a very slight amount of droplet growth before they begin shrinking again. Whether this is due to an actual increase in volume due to condensation which is a phenomenon that has been seen in exhaled breath [183], the droplet base radius growing slightly due to increased wetting on the surface over time, or simply the change in lighting levels as the array evaporates causing the thresholding method to give slightly inaccurate results, this apparent growth should not be ignored and can lead way to future studies (see section 12.4).

10.2.2 C3B evaporation

The same experiment was done on the C3B array, which produced microdroplets smaller in radius of roughly $16\mu m$, but at a closer pitch of $45.3\mu m$. To get more precise measurements of the droplet radii, a higher magnification was used, meaning less of the array was able to be measured for the radius plots in figure 10.12a. Like always, the thin film was blown off from right to left, which caused a bias in the evaporation. Figure 10.10 shows some images

of the whole array as it evaporated. Similarly to the C3A array, it shows signs of diffusive evaporation as the corners evaporate first and it becomes rounded. The C3B took less time to evaporate, most likely because the droplets are smaller and therefore have less liquid (see eqn 2.21).

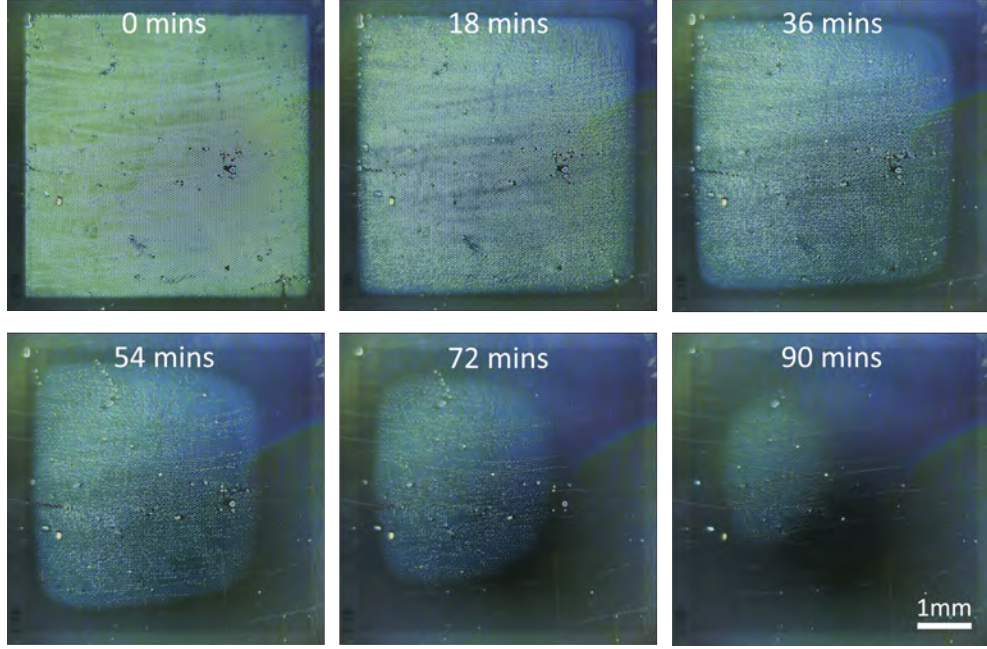


Figure 10.10: Images of C3B microdroplet array evaporation

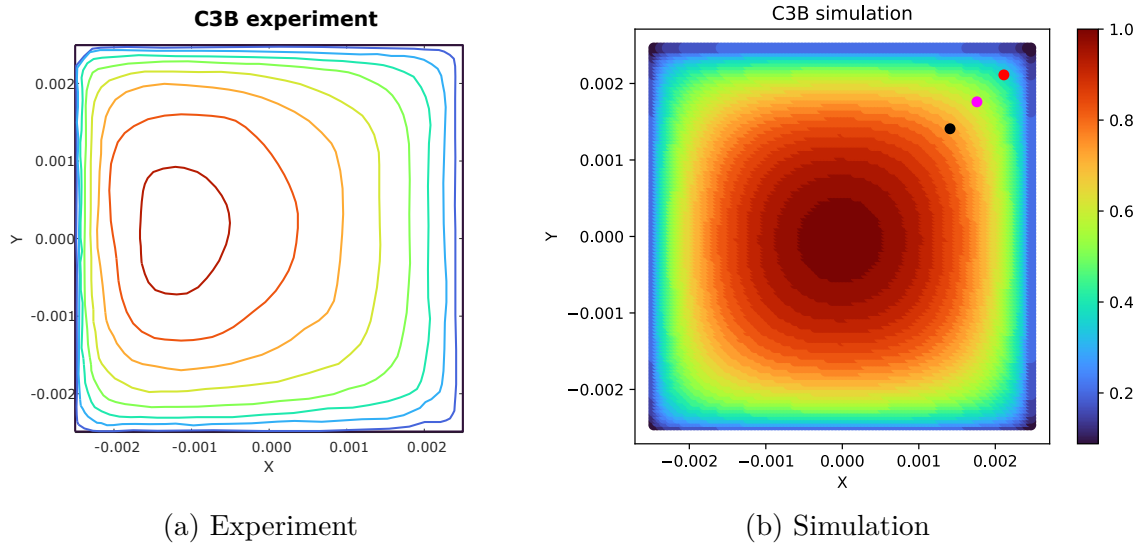


Figure 10.11: Experimental and simulated normalised droplet lifetimes for C3B array. Coloured dots on the simulation plot represent the lines in figure 10.12. Droplet lifetime is normalised with respect to the time it takes for the entire array to evaporate.

Similarly to the C3A array in the previous section, the radii of the C3B droplets followed a relationship similar to that predicted by the simulation based on Masoud theory, as seen in figure 10.12. Due to the right-to-left bias in the evaporation, the experimental droplets evaporate faster than those predicted by the theory, but this could be accounted for by adding a bias to the simulation in future work.

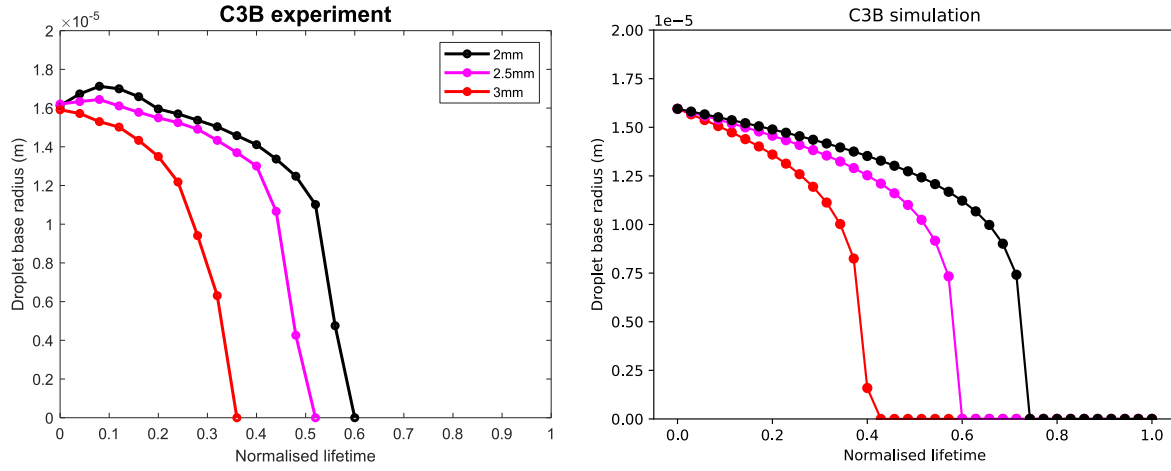


Figure 10.12: Droplet base radius vs normalised lifetime along diagonal for C3B array. The colour of each line corresponds to a single droplet location as shown by the coloured dots in figure 10.11b. Droplet lifetime is normalised with respect to the time it takes for the entire array to evaporate.

11 Conclusions

When using liquids with low conductivity, such as decanol and TMPTGE, the novel MOS geometry was able to produce some very effective and reliable liquid dielectrophoresis phenomena, ranging from uni-directional wetting to alter the contact angle of a sessile droplet, to pulling out microscopic liquid threads that obey fluid dynamic principles such as Washburn's law. In contrast, the geometry did not work well with water, even when deionised at $18M\Omega.cm$, which ultimately limits any practical real-world applications in which its feasibility with water is a must. The geometry was able to produce some interesting effects with the polystyrene microspheres. Unlike liquid DEP, there was less reproducibility for the particle DEP experiments, and the exact physical mechanisms causing the particle behaviour is not conclusive. The ability to create microdroplet arrays that ultimately allowed for the self-contained microdroplet evaporation study was another advantage of the unique electrode designs that are only possible due to the nature of the MOS geometry.

11.1 Dielectrowetting conclusions

Chapter 7 explored the phenomenon of dielectrowetting. Starting with the most basic of uni-directional dielectrowetting in section 7.1, a linear relationship between the cosine of the contact angle and the voltage squared was found. This was compared to theory using a model based on parallel microstrip capacitors, which gave good agreement (eqn 7.1 in section 7.1.2). This $\cos(\theta) \propto V^2$ dependence had been seen multiple times before in both electrowetting and dielectrowetting [149], and is derived from the relationship between the interfacial energies and dielectric energies of the system. In section 7.2 the MOS geometry was utilised to its full potential, and several different electrode patterns were tested in the axi-symmetric droplet spreading experiments. It was found that the droplets spread along both axes, loosely following the underlying symmetry of the pattern, before finally becoming a thin uniform film to cover the whole patterned area of the electrode. There was an effect

discovered with ‘stagnation lines’, in which the liquid could not spread across from one shape to another, therefore limiting the pattern design somewhat. Section 8.5 then analysed the spreading of microdroplets along a single electrode edge and found a very strong voltage dependence on the growth past a certain threshold voltage.

11.2 Liquid threads conclusions

Chapter 8 looked into the formation and behaviour of both non-volatile and volatile liquid threads. In section 8.1 the formation of thin liquid threads along a single electrode edge is introduced. It is believed that the mechanism of action is a DEP force at the tip of the thread which creates a pressure gradient from one end to the other, much like for flow in a pipe or capillary flow, which causes liquid to flow down the length of the thread. In section 8.2, the length, width and volume of single-edge non-evaporating decanol threads were measured as a function of voltage once they had reached a static equilibrium. In the case of thread length vs voltage (section 8.2.1), the final length was influenced by the point at which it got pinned by the surface, so it was not the most reproducible experiment and needed to be averaged to get a relationship. The experimental relationship between the static equilibrium thread length and voltage depends on several factors such as pinning, thread shape/flow profile and liquid properties. In sections 8.2.2 and 8.2.3 two separate single-edge decanol threads were connected from two parent droplets so that they formed a connected thread of uniform width. This gave a strong linear relationship of thread width vs voltage past a certain threshold voltage. The volume of the thread was found to be proportional to the voltage squared.

In section 8.3.1 the dynamics of single-edge decanol liquid threads were studied. In this study, a very strong Washburn relationship for the thread length vs square root of time ($L \propto t^{1/2}$) was discovered for multiple voltages. This experiment further backs up the notion that the mechanism of action is similar to that of pipe flow and capillary flow since the Washburn relationship is also prevalent in those areas of physics. Section 8.3.2 then looked into the

controlled dewetting dynamics of wider decanol threads. Wider threads could be produced if two thinner threads were drawn out in close enough proximity to one another so that they coalesced into one. By starting with a thread of fixed length and a high voltage and then switching to a lower voltage so that it did not break up due to the Rayleigh instability, it was possible to control the speed at which the thread receded into its parent droplet. This experiment also gave a Washburn relationship but in reverse.

The final work on threads was documented in section 8.4. It looked into both the static and dynamic behaviour of evaporating IPA liquid threads, which was then compared to the behaviour of non-volatile liquid threads. Unlike non-volatile threads that eventually stop growing due to pinning on the surface, evaporating threads stop growing where the evaporation rate of the thread reaches an equilibrium with the flow rate from the parent droplet. The equilibrium length of an evaporating thread can be controlled by the voltage applied. The dynamic behaviour of evaporating threads was then examined. The results showed that although they begin with a Washburn-like relationship in the early stages, the length squared versus time plot goes sub-linear as the thread grows, which is due to the fact it has a higher evaporation rate the longer it gets.

11.3 Particle dielectrophoresis conclusions

Chapter 9 delved into the behaviour of $10\mu m$ polystyrene microspheres using the novel MOS geometry in decanol. In general, it was difficult to pinpoint the exact electrodynamical mechanism causing their behaviour and it is speculated to be a combination of several including dielectrophoresis, electroosmosis, pearl chain formation, thermal convection and particle trapping in convective cells.

In section 9.1 the particles always moved away from the strongest electric fields at the electrode edge, regardless of voltage/frequency. It is believed this was caused by negative DEP, particularly at higher frequencies, since the permittivity of the particles was lower than that of decanol. At very low frequencies ($< 50\text{Hz}$) there was still net movement away from the

edge, but long chains of particles formed perpendicular to the edge of the electrodes. It is speculated that these ‘pearl chains’ are caused by particle/particle interaction along the field lines via induced dipoles or the effects of electroosmosis acting perpendicular to the electrode edge.

Section 9.2 explored the behaviour of the microspheres on the striped geometry for the wider $40\mu m$ and narrower $20\mu m$ stripes. There was a frequency and voltage dependence that determined where the particles tended to get trapped in regions above the stripes. The voltage/frequency combinations that determined whether the particles got trapped above the silicon, gold, closer to the stripe edges or simply didn’t get trapped at all varied from one experiment to another, and a clear-cut relationship was not easy to pinpoint. Some trends that did occur were that low frequencies ($<50\text{Hz}$) tended to attract the particles to the edge of the stripes, middle frequencies (100Hz - 1000Hz) tended to attract the particles over the silicon and high frequencies ($>5000\text{Hz}$) tended to favour the particles moving either onto the gold or not being trapped at all.

Section 9.3 gave similar results to the previous section, but this time on the circular geometry. The large circles from the C3A array in section 9.3.1 gave similar results to the wider stripes. The small circles in the C3B geometry in section 9.3.2 provided the most consistent results from the particle DEP chapter. Figure 9.19 shows how the crossover frequency is affected by the voltage. Since the Clausius-Mossotti factor (eqn 4.3) has no voltage dependence, this is further evidence that dielectrophoresis is not the only EHD effect taking place in this situation.

Finally, section 9.4 looked at the film thickness dependence for the position of the particles. It shows how even at the same voltage/frequency it is possible to change the location of where the particles get trapped simply by changing the thickness of the liquid film. This could be due to convection cells that form within the circles being disrupted as the film thickness is reduced.

11.4 Microdroplet array conclusions

Chapter 10 explored the formation and evaporation of decanol microdroplet arrays, just 5x5mm in size and containing more than 10000 droplets of only 0.1pL in volume. By first forming a thin film across the entire 5x5mm patterned area and by keeping the voltage switched on, it was possible to blow the vast majority of the liquid off with an electric air duster so that only a small amount remained trapped by the fringing fields at the patterned electrode edge. Once the voltage was then switched off, this remaining liquid then dewet into the equally spaced array of relatively uniform microdroplets.

In section 10.1 it was found that the size consistency for the microdroplets across the array was good in general, with the biggest issues being the droplets on the right were about $1 - 2\mu m$ smaller in average radii due to the direction of the blowing process and some large droplets formed due to imperfections on the surface, which degraded over time. For droplet size consistency across multiple experiments, there was evidence of up to $2\mu m$ difference in average droplet radii which has been attributed to how long the liquid was being blown away for.

In section 10.2 the evaporation of the decanol microdroplet arrays was documented. Although a 1μL decanol droplet would most likely take days or even weeks to evaporate at room temperature, 0.1pL droplets evaporate in a matter of minutes when isolated and the whole array had a lifespan of about 1-3 hours due to the shielding effect from neighbouring droplets. The experimental results for both the C3A and C3B arrays were compared to simulations based on Masoud's theory from their 2021 paper. Although they did not give exact quantitative matches due to a bias in evaporation direction, the evidence of diffusive evaporation was clear. In the lifetime plots of the whole array the corners of the square first round off until the array becomes more circular. In droplet base radius vs time measurements along the diagonal of the array, we get a relationship similar to that of the constant contact angle (CA) mode of diffusive evaporation with $R = R_0(1 - \beta t)^{1/2}$, as seen in equation 2.23.

12 Future work

12.1 Gradient wetting

In chapter 7 the effects of uni-directional and axi-symmetric dielectrowetting were studied. Due to the symmetry of the electrode pattern, the droplet would always dewet into the same position as it started once the voltage had been switched off, leading to no net movement of the droplet. It is conceivable that with asymmetric electrode designs, such as those seen in figures 12.1 and 12.2, there would be a bias towards a given direction when spreading under an applied voltage. This bias would lead to a net movement of the droplet over several voltage on/off cycles. This mechanism could lead to some interesting areas of research in droplet transport. Other groups have done similar using varying wettability methods [184][185], SLIPS surfaces [186][187] and electrowetting techniques [188][189].

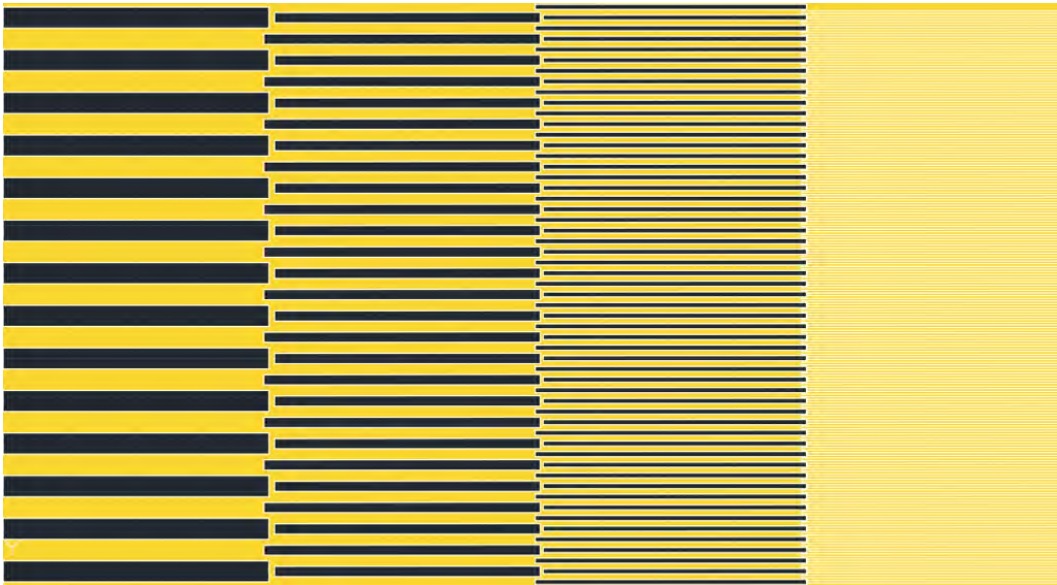


Figure 12.1: Gradient wetting - Thinning stripes from left to right

Figure 12.1 shows a simple striped design, in which the stripes get thinner and more numerous as you move from left to right. Due to thinner stripes having a stronger wetting effect as

seen in section 7.1, there should be a tendency for the liquid to spread more strongly on the thinner stripes than the thicker ones. Therefore, it should be possible to start with a small droplet on the thicker stripes, apply a voltage so that it wets onto its thinner neighbours, and then turn the voltage off so that the net position of the dewetted droplet has moved onto the thinner stripes. This cycle can then be repeated to transport the droplet across the entire striped pattern.

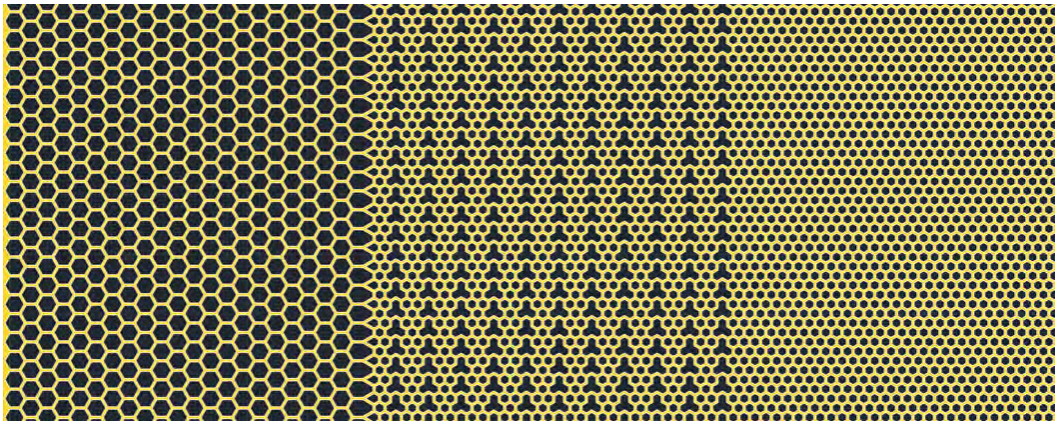


Figure 12.2: Gradient wetting - Hexagon and caltrop design

The pattern in figure 12.2 works similarly, except it combines the hexagonal and caltrop patterns as seen in section 7.2. Like before, since the wetting effect would be stronger for the smaller hexagons due to them having more electrode edges per unit area, it should be possible to start with a small droplet on the larger hexagons and then move onto the smaller ones, with the interlocking caltrop/hexagon design serving as an intermediate between two hexagon sizes.

12.2 Liquid threads

To expand on the work done on liquid threads, more in-depth modelling of the system can be done. Dr Elfego Gutierrez has already done some modelling of the microdroplet spreading (see section 8.5), and in the future, this could be expanded to model the behaviour of the threads. To further work on the theory of both non-volatile and volatile liquid threads,

more systematic experiments could be done. These include using different liquids for varying electrical permittivity, viscosity and density, controlling the temperature to alter the viscosity and/or evaporation rate of the thread, and varying the width of the ‘wide’ threads.

A pilot study into the temperature dependence of the dynamic evolution of decanol liquid threads was done. Whilst fixing the voltage at 240V and frequency of 1kHz, the temperature of the decanol could be controlled by attaching the device to an RS Pro Peltier Module using some thermal tape and paste. A thermal camera was used to measure the device’s temperature. Figure 12.3 shows the results of this study.

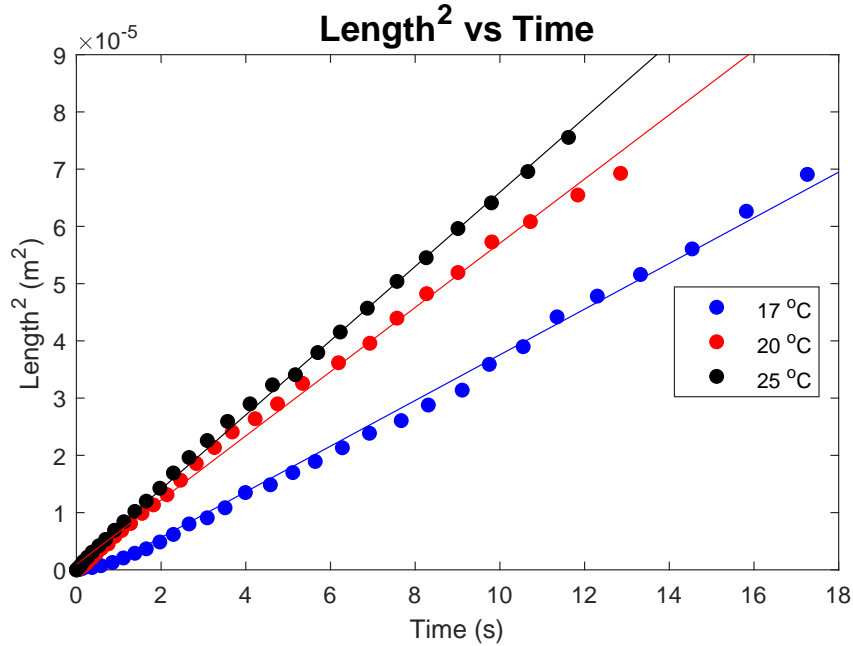


Figure 12.3: Temperature dependence of decanol liquid thread at 240V

It reveals how the thread grows at a slower rate as the temperature decreases and vice versa. This is expected since the viscosity will be higher at a lower temperature, thus making it more difficult for the liquid to flow for a given dielectrophoretic force provided by the voltage. Temperatures higher than 25°C were tested, but this started to have a strong effect on the evaporation rate of the decanol, not allowing the threads to grow much before evaporating. This temperature dependence on the length of evaporating threads could further advance the thread evaporation work.

12.3 Particle DEP

Due to the complexity of the particle DEP system, it made it difficult to conclude what exactly was happening in chapter 9. Future work on this topic should put constraints on the system and use more powerful measuring techniques, such as OCT to get better z-positions of the microspheres above the surface. Experimentation with different particle sizes, changing the conductivity and permittivity of the liquid, particle surface treatments to control conductivity, and different electrode geometries could all be done to constrain specific parameters and get a better understanding of the system.

12.4 Different sized microdroplet evaporation

In chapter 10 the formation and evaporation of microdroplet arrays was documented. The arrays were 5x5mm squares and the microdroplets were all the same size in a hexagonal lattice structure. However, in reality, droplets are never completely uniform in size and spacing. There is often competitive evaporation between droplets causing larger droplets to grow as the smaller ones evaporate [190][88] with an example being human breath in cold and humid air [183].

A potential future pathway for microdroplet evaporation research could be to make and study the evaporation of arrays of varying-sized droplets and droplet spacings. Figure 12.4 shows an array made from the ‘octagon and square’ geometry seen in section 7.2. Larger droplets form above the larger octagons whilst smaller droplets form above the smaller squares. Other potential pathways could also include different shaped and sized arrays and measuring the temperature dependence of evaporation.

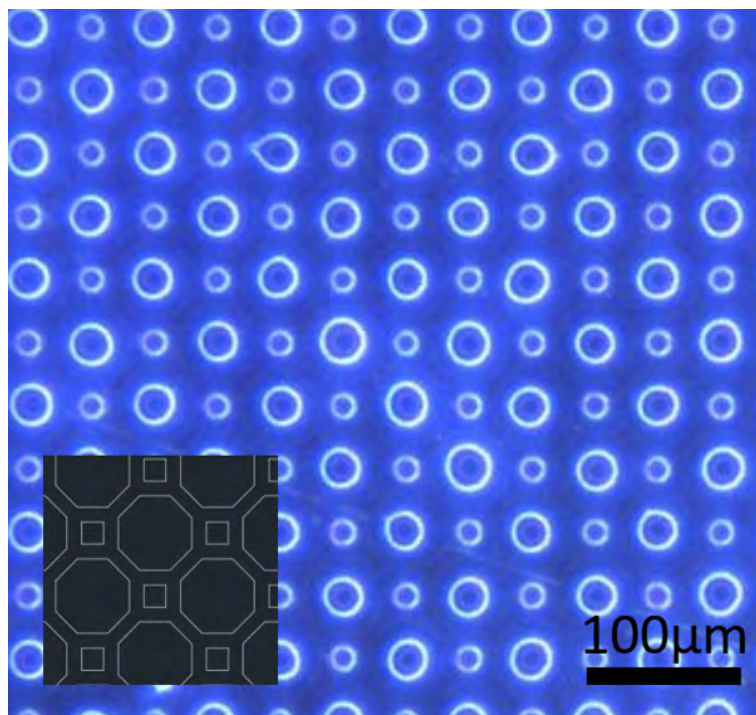


Figure 12.4: Microdroplets of different sizes in same array

Bibliography

- [1] Chih-Cheng Cheng, C Alex Chang, and J Andrew Yeh. Variable focus dielectric liquid droplet lens. *Optics express*, 14(9):4101–4106, 2006.
- [2] H Geng, J Feng, L M Stabryla, and S K Cho. Droplet manipulations by dielectrowetting: Creating, transporting, splitting, and merging. In *2017 IEEE 30th International Conference on Micro Electro Mechanical Systems (MEMS)*, pages 113–116, 2017.
- [3] George M Whitesides. The origins and the future of microfluidics. *Nature*, 442(7101):368–373, 2006.
- [4] R Ahmed and T B Jones. Optimized liquid DEP droplet dispensing. *Journal of Micromechanics and Microengineering*, 17(5):1052, 2007.
- [5] Karan V. I. S. Kaler, Ravi Prakash, and Dipankar Chugh. Liquid dielectrophoresis and surface microfluidics. *Biomicrofluidics*, 4(2):022805, 6 2010.
- [6] Jakub Novotný and František Foret. Fluid manipulation on the micro-scale: Basics of fluid behavior in microfluidics. *Journal of Separation Science*, 40(1):383–394, 1 2017.
- [7] Dongkyu Lee, Bohyun Hwang, and Byungkyu Kim. The potential of a dielectrophoresis activated cell sorter (DACS) as a next generation cell sorter. *Micro and Nano Systems Letters*, 4(1):2, 2016.
- [8] G R Ballantyne and P N Holtham. Application of dielectrophoresis for the separation of minerals. *Minerals Engineering*, 23(4):350–358, 2010.

- [9] Kai Zhao and Dongqing Li. Continuous separation of nanoparticles by type via localized DC-dielectrophoresis using asymmetric nano-orifice in pressure-driven flow. *Sensors and Actuators B: Chemical*, 250:274–284, 2017.
- [10] Xinbo Qiu, Xiliang Gong, Xiaoyu Zhang, and Weitao Zheng. Ink-Jet Printing towards Ultra-High Resolution: A Review. *Coatings*, 12:1893, 12 2022.
- [11] Jungho Kim. Spray cooling heat transfer: The state of the art. *International Journal of Heat and Fluid Flow*, 28(4):753–767, 2007.
- [12] Rajneesh Bhardwaj and Amit Agrawal. Likelihood of survival of coronavirus in a respiratory droplet deposited on a solid surface. *Physics of Fluids*, 32(6):061704, 6 2020.
- [13] J A Pople. The Electronic Structure and Polarity of the Water Molecule. *The Journal of Chemical Physics*, 21(12):2234–2235, 12 2004.
- [14] Bin Chen, Ivaylo Ivanov, Michael L Klein, and Michele Parrinello. Hydrogen Bonding in Water. *Physical Review Letters*, 91(21):215503, 11 2003.
- [15] Slawomir Grabowski. *Hydrogen Bonding—New Insights*, volume 3. Springer, 1 2006.
- [16] N B Vargaftik, B N Volkov, and L D Voljak. International Tables of the Surface Tension of Water. *Journal of Physical and Chemical Reference Data*, 12(3):817–820, 7 1983.
- [17] R Strey and T Schmeling. Surface Tension Measurements for the n-Alcohols in the Temperature Range from -40°C to $+40^{\circ}\text{C}$. *Berichte der Bunsengesellschaft für physikalische Chemie*, 87(4):324–327, 4 1983.
- [18] Shirong Zhu, Kaibin Xie, Qiaoli Lin, Rui Cao, and Feng Qiu. Experimental determination of surface energy for high-energy surface: A review. *Advances in Colloid and Interface Science*, 315:102905, 2023.
- [19] Siddharth Misra and Yuteng Jin. Chapter 5 - Effects of wettability of conductive and nonconductive particles on the multifrequency electromagnetic response of porous material. In Siddharth Misra, Yifu Han, Yuteng Jin, and Pratiksha Tathed, editors,

- Multifrequency Electromagnetic Data Interpretation for Subsurface Characterization*, pages 145–170. Elsevier, 2021.
- [20] C G Jothi Prakash and R Prasanth. Approaches to design a surface with tunable wettability: a review on surface properties. *Journal of Materials Science*, 56(1):108–135, 2021.
 - [21] V Adrian Parsegian. *Van der Waals Forces: A Handbook for Biologists, Chemists, Engineers, and Physicists*. Cambridge University Press, Cambridge, 2005.
 - [22] J J Dannenberg. An Introduction to Hydrogen Bonding By George A. Jeffrey (University of Pittsburgh). Oxford University Press: New York and Oxford. 1997. ix + 303 pp. \$60.00. ISBN 0-19-509549-9. *Journal of the American Chemical Society*, 120(22):5604, 6 1998.
 - [23] P. G. de Gennes. Wetting: statics and dynamics. *Reviews of Modern Physics*, 57(3):827–863, 7 1985.
 - [24] Thomas Young. III. An essay on the cohesion of fluids. *Philosophical Transactions of the Royal Society of London*, 95:65–87, 1 1805.
 - [25] T S Chow. Wetting of rough surfaces. *Journal of Physics: Condensed Matter*, 10(27):L445, 1998.
 - [26] Hans-Jürgen Butt, Jie Liu, Kaloian Koynov, Benedikt Straub, Chirag Hinduja, Ilia Roisman, Rüdiger Berger, Xiaomei Li, Doris Vollmer, Werner Steffen, and Michael Kappl. Contact angle hysteresis. *Current Opinion in Colloid & Interface Science*, 59:101574, 2022.
 - [27] L J Clancy. *Aerodynamics*. Pitman aeronautical engineering series. Pitman, 1975.
 - [28] Joseph Pedlosky. *Geophysical fluid dynamics*. Springer Science & Business Media, 2013.
 - [29] James G. Speight. The properties of water. *Natural Water Remediation*, pages 53–89, 2020.

- [30] ahepp. www.simscale.com/forum/t/what-is-incompressible-flow/70493, 6 2017.
- [31] University College London. www.ucl.ac.uk/~uceseug/Fluids2/Notes_Momentum.pdf, 2023.
- [32] D. J. Acheson. *Elementary Fluid Dynamics*. Oxford University Press, 1990.
- [33] Grzegorz Łukaszewicz and Piotr Kalita. Equations of Classical Hydrodynamics. In Grzegorz Łukaszewicz and Piotr Kalita, editors, *Navier–Stokes Equations: An Introduction with Applications*, pages 11–37. Springer International Publishing, Cham, 2016.
- [34] Cüneyt Sert. Governing Equations of Fluid Flow and Heat Transfer. In *ME 582 Finite Element Analysis in Thermofluids*. Middle East Technical University, 2023.
- [35] Atul Bhattad. Review on viscosity measurement: devices, methods and models. *Journal of Thermal Analysis and Calorimetry*, 148(14):6527–6543, 2023.
- [36] John R. Rumble, David R. Lide, and Thomas J. Bruno. *CRC Handbook of Chemistry and Physics*. CRC Press/Taylor & Francis, 99th edition, 2018.
- [37] J B Segur and Helen E Oberstar. Viscosity of Glycerol and Its Aqueous Solutions. *Industrial & Engineering Chemistry*, 43(9):2117–2120, 9 1951.
- [38] S Yanniotis, S Skaltsi, and S Karaburnioti. Effect of moisture content on the viscosity of honey at different temperatures. *Journal of Food Engineering*, 72(4):372–377, 2006.
- [39] J Frenkel. The Viscosity of Liquids. *Nature*, 125(3154):581–582, 1930.
- [40] Saheed Adewale Adio, Mohsen Sharifpur, and Josua P Meyer. Investigation Into Effective Viscosity, Electrical Conductivity, and pH of γ -Al₂O₃-Glycerol Nanofluids in Einstein Concentration Regime. *Heat Transfer Engineering*, 36(14-15):1241–1251, 9 2015.
- [41] Bill Rehm, Drilling Consultant, Arash Haghshenas, Amir Saman Paknejad, and Jerome Schubert. CHAPTER TWO - Situational Problems in MPD. In Bill Rehm, Jerome Schubert, Arash Haghshenas, Amir Saman Paknejad, and Jim Hughes, editors, *Managed Pressure Drilling*, pages 39–80. Gulf Publishing Company, 2008.

- [42] S P Suter and R Skalak. The History of Poiseuille’s Law. *Annual Review of Fluid Mechanics*, 25(1):1–20, 1 1993.
- [43] George Stokes. On the Theories of the Internal Friction of Fluids in Motion, and of the Equilibrium and Motion of Elastic Solids. In George Gabriel Stokes, editor, *Mathematical and Physical Papers*, volume 1 of *Cambridge Library Collection - Mathematics*, pages 75–129. Cambridge University Press, Cambridge, 2009.
- [44] John X J Zhang and Kazunori Hoshino. Chapter 3 - Microfluidics and Micro Total Analytical Systems. In John X J Zhang and Kazunori Hoshino, editors, *Molecular Sensors and Nanodevices*, pages 103–168. William Andrew Publishing, Oxford, 2014.
- [45] Edward W Washburn. The Dynamics of Capillary Flow. *Physical Review*, 17(3):273–283, 3 1921.
- [46] Richard Lucas. Ueber das Zeitgesetz des kapillaren Aufstiegs von Flüssigkeiten. *Kolloid-Zeitschrift*, 23(1):15–22, 1918.
- [47] Mingchao Liu, Jian Wu, Yixiang Gan, Dorian A H Hanaor, and C Q Chen. Evaporation Limited Radial Capillary Penetration in Porous Media. *Langmuir*, 32(38):9899–9904, 9 2016.
- [48] Jean-François Louf, Yi Zheng, Aradhana Kumar, Tomas Bohr, Carsten Gundlach, Jesper Harholt, Henning Friis Poulsen, and Kaare H Jensen. Imbibition in plant seeds. *Physical Review E*, 98(4):42403, 10 2018.
- [49] S Leelajariyakul, H Noguchi, and S Kiatkamjornwong. Surface-modified and micro-encapsulated pigmented inks for ink jet printing on textile fabrics. *Progress in Organic Coatings*, 62(2):145–161, 2008.
- [50] S Takahashi and A R Kovscek. Spontaneous countercurrent imbibition and forced displacement characteristics of low-permeability, siliceous shale rocks. *Journal of Petroleum Science and Engineering*, 71(1):47–55, 2010.
- [51] Max Gong and David Sinton. Turning the Page: Advancing Paper-Based Microfluidics for Broad Diagnostic Application. *Chemical Reviews*, 117, 6 2017.

- [52] Abdullah Alghunaim, Suchata Kirdponpattara, and Bi-min Zhang Newby. Techniques for determining contact angle and wettability of powders. *Powder Technology*, 287:201–215, 2016.
- [53] Jianchao Cai, Tingxu Jin, Jisheng Kou, Shuangmei Zou, Junfeng Xiao, and Qingbang Meng. Lucas–Washburn Equation-Based Modeling of Capillary-Driven Flow in Porous Systems. *Langmuir*, 37(5):1623–1636, 2 2021.
- [54] C H Bosanquet. LV. On the flow of liquids into capillary tubes. *The London, Edinburgh, and Dublin Philosophical Magazine and Journal of Science*, 45(267):525–531, 3 1923.
- [55] Joachim Schoelkopf, Patrick A C Gane, Cathy J Ridgway, and G.Peter Matthews. Practical observation of deviation from Lucas–Washburn scaling in porous media. *Colloids and Surfaces A: Physicochemical and Engineering Aspects*, 206(1):445–454, 2002.
- [56] George Emanuel. Chapter 16 - Couette Flow. In *Analytical Fluid Dynamics*, pages 511–518. CRC Press, 2nd edition, 2000.
- [57] C Paterson, S K Wilson, and B R Duffy. Pinning, de-pinning and re-pinning of a slowly varying rivulet. *European Journal of Mechanics - B/Fluids*, 41:94–108, 2013.
- [58] Abdulwahed S Alshaikhi, Stephen K Wilson, and Brian R Duffy. Rivulet flow over and through a permeable membrane. *Physical Review Fluids*, 6(10):104003, 10 2021.
- [59] Cyril Deroy, Nicholas Stovall-Kurtz, Federico Nebuloni, Cristian Soitu, Peter R Cook, and Edmond J Walsh. Predicting flows through microfluidic circuits with fluid walls. *Microsystems & Nanoengineering*, 7(1):93, 2021.
- [60] Jue Nee Tan and Adrian Neild. Microfluidic mixing in a Y-junction open channel. *AIP Advances*, 2:032160, 8 2012.
- [61] Miguel A Herrada, A S Mohamed, José M Montanero, and A M Gañán-Calvo. Stability of a rivulet flowing in a microchannel. *International Journal of Multiphase Flow*, 69:1–7, 2015.

- [62] Qing Zhu, Yuanyuan Shen, Aili Zhang, and Lisa X Xu. Numerical study of the influence of water evaporation on radiofrequency ablation. *BioMedical Engineering OnLine*, 12(1):127, 2013.
- [63] Alok Prakash, Chaitali Patil, S Vinodhini, A Panneerselvam, and V Devi Rajeswari. 1 - Engineering Approach in Beverage Industry. In Alexandru Mihai Grumezescu and Alina Maria Holban, editors, *Engineering Tools in the Beverage Industry*, pages 1–25. Woodhead Publishing, 2019.
- [64] Ioana Naşcu, Nikolaos A Diangelakis, Salvador García Muñoz, and Efstratios N Pistikopoulos. Advanced model predictive control strategies for evaporation processes in the pharmaceutical industries. *Computers & Chemical Engineering*, 173:108212, 2023.
- [65] Tatsiana Dudzina, Elena Garcia Hidalgo, Natalie von Goetz, Christian Bogdal, and Konrad Hungerbuehler. Evaporation of decamethylcyclopentasiloxane (D5) from selected cosmetic products: Implications for consumer exposure modeling. *Environment International*, 84:55–63, 2015.
- [66] Jeongbeom Cha, Haedam Jin, Mi Kyong Kim, Jong Hwan Park, and Min Kim. Evaporation-controlled spray deposition process achieving ultrasMOOTH photoactive layer for efficient organic solar cells. *Surfaces and Interfaces*, 28:101669, 2022.
- [67] Antonio A Cantú. A study of the evaporation of a solvent from a solution—Application to writing ink aging. *Forensic Science International*, 219(1):119–128, 2012.
- [68] N Bouhssira, S Abed, E Tomasella, J Cellier, A Mosbah, M S Aida, and M Jacquet. Influence of annealing temperature on the properties of ZnO thin films deposited by thermal evaporation. *Applied Surface Science*, 252(15):5594–5597, 2006.
- [69] N Kapilan, Arun M Isloor, and Shashikantha Karinka. A comprehensive review on evaporative cooling systems. *Results in Engineering*, 18:101059, 2023.
- [70] Goutam Konapala, Ashok K Mishra, Yoshihide Wada, and Michael E Mann. Climate change will affect global water availability through compounding changes in seasonal precipitation and evaporation. *Nature Communications*, 11(1):3044, 2020.

- [71] Lu Wang, Xinglong Ma, Hui Kong, Rihui Jin, and Hongfei Zheng. Investigation of a low-pressure flash evaporation desalination system powered by ocean thermal energy. *Applied Thermal Engineering*, 212:118523, 2022.
- [72] F Mandl. The Maxwell velocity distribution. In *Statistical Physics*, Manchester physics series, chapter 7. Wiley, 1971.
- [73] Max Born and H S Green. A kinetic theory of liquids. *Nature*, 159(4034):251–254, 1947.
- [74] Christopher Auyeung. www.ck12.org/c/chemistry/evaporation/lesson/Evaporation-CHEM/, 2020.
- [75] Christian Diddens, Simon Hartmann, Maziyar Jalaal, and Uwe Thiele. Sessile drop evaporation in a gap – crossover between diffusion-limited and phase transition-limited regime. *Journal of Fluid Mechanics*, 960:A32, 2023.
- [76] Irving Langmuir. The Evaporation of Small Spheres. *Physical Review*, 12(5):368–370, 11 1918.
- [77] Azmaine Iqtidar, Joseph J Kilbride, Fouzia F Ouali, David J Fairhurst, Howard A Stone, and Hassan Masoud. Drying dynamics of sessile-droplet arrays. *Physical Review Fluids*, 8(1):13602, 1 2023.
- [78] Mounir Aytouna, Daniel Bonn, Odile Carrier, Jens Eggers, Mehdi Habibi, Noushine Shahidzadeh-Bonn, and Rojman Zargar. Evaporation of water: evaporation rate and collective effects. *Journal of Fluid Mechanics*, 798:774–786, 2016.
- [79] Robert D Deegan, Olgica Bakajin, Todd F Dupont, Greb Huber, Sidney R Nagel, and Thomas A Witten. Capillary flow as the cause of ring stains from dried liquid drops. *Nature*, 389(6653):827–829, 1997.
- [80] Taewoong Lim, Sewoon Han, Jaewon Chung, Jin Taek Chung, Seunghwan Ko, and Costas P Grigoropoulos. Experimental study on spreading and evaporation of inkjet printed pico-liter droplet on a heated substrate. *International Journal of Heat and Mass Transfer*, 52(1):431–441, 2009.

- [81] Duyang Zang, Sujata Tarafdar, Yuri Tarasevich, Moutushi Choudhury, and Tapati Dutta. Evaporation of a Droplet: From physics to applications. *Physics Reports*, 804, 2 2019.
- [82] Stephen K Wilson and Hannah-May D’Ambrosio. Evaporation of Sessile Droplets. *Annual Review of Fluid Mechanics*, 55(1):481–509, 1 2023.
- [83] R G Picknett and R Bexon. The evaporation of sessile or pendant drops in still air. *Journal of Colloid and Interface Science*, 61(2):336–350, 1977.
- [84] Dinghua Hu, Huiying Wu, and Zhenyu Liu. Effect of liquid–vapor interface area on the evaporation rate of small sessile droplets. *International Journal of Thermal Sciences*, 84:300–308, 2014.
- [85] C Bourges-Monnier and M E R Shanahan. Influence of Evaporation on Contact Angle. *Langmuir*, 11(7):2820–2829, 7 1995.
- [86] Md Syam Hasan, Konstantin Sobolev, and Michael Nosonovsky. Evaporation of droplets capable of bearing viruses airborne and on hydrophobic surfaces. *Journal of Applied Physics*, 129:024703, 1 2021.
- [87] C Schäfle, C Bechinger, B Rinn, C David, and P Leiderer. Cooperative Evaporation in Ordered Arrays of Volatile Droplets. *Physical Review Letters*, 83(25):5302–5305, 12 1999.
- [88] M Sokuler, Günter Auernhammer, Chuanjun Liu, Elmar Bonaccorso, and H-J Butt. Dynamics of condensation and evaporation: Effect of inter-drop spacing. <http://dx.doi.org/10.1209/0295-5075/89/36004>, 89, 2 2010.
- [89] Odile Carrier, Noushine Shahidzadeh-Bonn, Rojman Zargar, Mounir Aytouna, Mehdi Habibi, Jens Eggers, and Daniel Bonn. Evaporation of water: Evaporation rate and collective effects. *Journal of Fluid Mechanics*, 798:774–786, 7 2016.
- [90] Feargus G H Schofield, Alexander W Wray, David Pritchard, and Stephen K Wilson. The shielding effect extends the lifetimes of two-dimensional sessile droplets. *Journal of Engineering Mathematics*, 120(1):89–110, 2020.

- [91] Alexander Wray, Brian Duffy, and Stephen Wilson. Competitive evaporation of multiple sessile droplets. *Journal of Fluid Mechanics*, 884, 2 2020.
- [92] Andrew M J Edwards, Jack Cater, Joseph J Kilbride, Pierre Le Minter, Carl V Brown, David J Fairhurst, and Fouzia F Ouali. Interferometric measurement of co-operative evaporation in 2D droplet arrays. *Applied Physics Letters*, 119(15):151601, 10 2021.
- [93] Hassan Masoud, Peter Howell, and Howard Stone. Evaporation of multiple droplets. *Journal of Fluid Mechanics*, 927, 11 2021.
- [94] J J Kilbride, K E Fagg, F F Ouali, and D J Fairhurst. Pattern-Distortion Technique: Using Liquid-Lens Magnification to Extract Volumes of Individual Droplets or Bubbles within Evaporating Two-Dimensional Arrays. *Physical Review Applied*, 19(4):44030, 4 2023.
- [95] David Fairhurst. Predicting evaporation rates of droplet arrays. *Journal of Fluid Mechanics*, 934, 3 2022.
- [96] John Daintith. *A Dictionary of Physics*. Oxford University Press, 6 edition, 2009.
- [97] Edward M Purcell and David J Morin. *Electricity and Magnetism*. Cambridge University Press, Cambridge, 3 edition, 2013.
- [98] Huray P. Foundations of Maxwell’s Equations. In *Maxwell’s Equations*, pages 1–22. Wiley, 10 2010.
- [99] Michael Faraday. Experimental Researches in Electricity. In *Experimental Researches in Electricity*, volume 1, pages 122–124. Richard and John Edward Taylor, London, 1839.
- [100] Dinesh Kumar and Mohit Johari. Characteristics of silicon crystal, its covalent bonding and their structure, electrical properties, uses. In *American Institute of Physics Conference Series*, volume 2220 of *American Institute of Physics Conference Series*, page 40037, 5 2020.

- [101] Marius Grundmann. Electronic Defect States. In Marius Grundmann, editor, *The Physics of Semiconductors: An Introduction Including Nanophysics and Applications*, pages 179–221. Springer International Publishing, Cham, 2021.
- [102] C Gatel, R Serra, K Gruel, A Masseboeuf, L Chapuis, R Cours, L Zhang, B Warot-Fonrose, and M. J. Hÿtch. Extended Charge Layers in Metal-Oxide-Semiconductor Nanocapacitors Revealed by Operando Electron Holography. *Physical Review Letters*, 129(13):137701, 9 2022.
- [103] Bart Van Zeghbroeck. https://km2000.us/franklinduan/articles/ecee.colorado.edu/~bart/book/book/chapter6/ch6_2.htm, 2011.
- [104] Abdussamad Muntahi and Shaikh Ahmed. https://nanohub.org/resources/32905/download/MOSCap_Tool_Primer.pdf, 2012.
- [105] Hiroyuki Ohshima. Electrical Double Layers. In Tharwat Tadros, editor, *Encyclopedia of Colloid and Interface Science*, pages 342–361. Springer Berlin Heidelberg, Berlin, Heidelberg, 2013.
- [106] Chenxu Liu and Yonggang Meng. Tribology at charged solid-liquid interfaces. In Klaus Wandelt and Gianlorenzo Bussetti, editors, *Encyclopedia of Solid-Liquid Interfaces (First Edition)*, pages 581–588. Elsevier, Oxford, 2024.
- [107] K Pate and P Safer. 12 - Chemical metrology methods for CMP quality. In Suryadevara Babu, editor, *Advances in Chemical Mechanical Planarization (CMP)*, pages 299–325. Woodhead Publishing, 2016.
- [108] Herbert A. Pohl. The Motion and Precipitation of Suspensoids in Divergent Electric Fields. *Journal of Applied Physics*, 22(7):869–871, 7 1951.
- [109] Herbert A. Pohl and Ira Hawk. Separation of Living and Dead Cells by Dielectrophoresis. *Science*, 152(3722):647–649, 4 1966.
- [110] Nurhaslina Abd Rahman, Fatimah Ibrahim, and Bashar Yafouz. Dielectrophoresis for Biomedical Sciences Applications: A Review. *Sensors*, 17:449, 5 2017.

- [111] Ronald Pethig. Review—Where Is Dielectrophoresis (DEP) Going? *Journal of The Electrochemical Society*, 164:B3049–B3055, 5 2017.
- [112] Hongyao Geng and Sung Kwon Cho. Dielectrowetting for Digital Microfluidics: Principle and Application. A Critical Review. *Reviews of Adhesion and Adhesives*, 5(3):268–302, 9 2017.
- [113] Thomas B Jones. *Electromechanics of Particles*. Cambridge University Press, Cambridge, 1995.
- [114] Abdelhadi Mortadi, A Melouky, El Chahid, Reddad el moznine, and Omar Cherkaoui. Studies of the Clausius–Mossotti factor. *Journal of Physical Studies*, 20, 5 2016.
- [115] Michael P. Hughes. Fifty years of dielectrophoretic cell separation technology. *Biomeicrofluidics*, 10(3):032801, 5 2016.
- [116] Herbert Ackland Pohl. *Dielectrophoresis: The Behavior of Neutral Matter in Nonuniform Electric Fields*. Cambridge University Press, 1978.
- [117] Jonathan A R Price, Julian P H Burt, and Ronald Pethig. Applications of a new optical technique for measuring the dielectrophoretic behaviour of micro-organisms. *Biochimica et Biophysica Acta (BBA) - General Subjects*, 964(2):221–230, 1988.
- [118] Akihiko Irimajiri, Tetsuya Hanai, and Akira Inouye. A dielectric theory of “multi-stratified shell” model with its application to a lymphoma cell. *Journal of Theoretical Biology*, 78(2):251–269, 1979.
- [119] Tadaaki Kakutani, Shigeo Shibatani, and Makoto Sugai. Electroration of non-spherical cells: theory for ellipsoidal cells with an arbitrary number of shells. *Bioelectrochemistry and bioenergetics*, 31(2):131–145, 1993.
- [120] Vladimir L Sukhorukov, Gustav Meedt, Markus Kürschner, and Ulrich Zimmermann. A single-shell model for biological cells extended to account for the dielectric anisotropy of the plasma membrane. *Journal of Electrostatics*, 50(3):191–204, 2001.

- [121] Torsten Müller, Stefan Fiedler, Thomas Schnelle, Kai Ludwig, Hartmut Jung, and Günter Fuhr. High frequency electric fields for trapping of viruses. *Biotechnology Techniques*, 10(4):221–226, 1996.
- [122] Bashar Yafouz, Nahrizul Adib Kadri, Hussin A Rothan, Rohana Yusof, and Fatimah Ibrahim. Discriminating dengue-infected hepatic cells (WRL-68) using dielectrophoresis. *ELECTROPHORESIS*, 37(3):511–518, 2 2016.
- [123] Mohammed Alshareef, Nicholas Metrakos, Eva Romito, Fadi Azer, Fang Yang, Xiaoming Yang, and Guiren Wang. Separation of tumor cells with dielectrophoresis-based microfluidic chip. *Biomicrofluidics*, 7, 1 2013.
- [124] Paul V Jones, Gabriel L Salmon, and Alexandra Ros. Continuous separation of DNA molecules by size using insulator-based dielectrophoresis. *Analytical chemistry*, 89(3):1531–1539, 2017.
- [125] Georg R Pesch and Fei Du. A review of dielectrophoretic separation and classification of non-biological particles. *ELECTROPHORESIS*, 42(1-2):134–152, 2021.
- [126] Herbert Ackland Pohl. Some effects of nonuniform fields on dielectrics. *Journal of Applied Physics*, 29(8):1182–1188, 1958.
- [127] Herbert A Pohl and Charles E Plymale. Continuous separations of suspensions by nonuniform electric fields in liquid dielectrics. *Journal of The Electrochemical Society*, 107(5):390, 1960.
- [128] Qiaoying Chen and Yong J Yuan. A review of polystyrene bead manipulation by dielectrophoresis. *RSC Advances*, 9(9):4963–4981, 2019.
- [129] N G Green and H Morgan. Dielectrophoretic investigations of sub-micrometre latex spheres. *Journal of Physics D: Applied Physics*, 30(18):2626, 1997.
- [130] Michael Pycraft Hughes and Nicolas Gavin Green. The influence of Stern layer conductance on the dielectrophoretic behavior of latex nanospheres. *Journal of colloid and interface science*, 250(1):266–268, 2002.

- [131] Clyde Midelet, Bruno Le Pioufle, and Martinus H V Werts. Brownian Motion and Large Electric Polarizabilities Facilitate Dielectrophoretic Capture of Sub-200 nm Gold Nanoparticles in Water. *ChemPhysChem*, 20(24):3354–3365, 2019.
- [132] Nicholas R Wood, Amanda I Wolsiefer, Robert W Cohn, and Stuart J Williams. Dielectrophoretic trapping of nanoparticles with an electrokinetic nanoprobe. *Electrophoresis*, 34(13):1922–1930, 2013.
- [133] Linbo Liu, Ke Chen, Nan Xiang, and Zhonghua Ni. Dielectrophoretic manipulation of nanomaterials: A review. *Electrophoresis*, 40(6):873–889, 2019.
- [134] Benjamin D Smith, Theresa S Mayer, and Christine D Keating. Deterministic assembly of functional nanostructures using nonuniform electric fields. *Annual review of physical chemistry*, 63:241–263, 2012.
- [135] N G Green and H Morgan. Separation of submicrometre particles using a combination of dielectrophoretic and electrohydrodynamic forces. *Journal of Physics D: Applied Physics*, 31(7):L25, 1998.
- [136] Chester T O’Konski. Electric properties of macromolecules. V. Theory of ionic polarization in polyelectrolytes. *The Journal of Physical Chemistry*, 64(5):605–619, 1960.
- [137] Adrienne R Minerick, Ronghui Zhou, Pavlo Takhistov, and Hsueh-Chia Chang. Manipulation and characterization of red blood cells with alternating current fields in microdevices. *Electrophoresis*, 24(21):3703–3717, 2003.
- [138] Antonio Ramos, Hywel Morgan, Nicolas Green, and Antonio Castellanos. AC Electrokinetics: A Review of Forces in Microelectrode Structures. *Journal of Physics D-applied Physics - J PHYS-D-APPL PHYS*, 31:2338–2353, 9 1998.
- [139] Ming Li, Weihua Li, Jun Zhang, Gursel Alici, and Wenli Wen. A review of microfabrication techniques and dielectrophoretic microdevices for particle manipulation and separation. *Journal of Physics D Applied Physics*, 47, 1 2014.
- [140] Chia-lun J Hu and Frank S Barnes. A simplified theory of pearl chain effects. *Radiation and Environmental Biophysics*, 12(1):71–76, 1975.

- [141] V Giner, M Sancho, R S Lee, G Martinez, and R Pethig. Transverse dipolar chaining in binary suspensions induced by rf fields. *Journal of Physics D Applied Physics*, 32(10):1182–1186, 5 1999.
- [142] Richard D Stoy. Interactive dipole model for two-sphere system. *Journal of Electrostatics*, 33(3):385–392, 1994.
- [143] Robert Kretschmer and Wolfgang Fritzsche. Pearl Chain Formation of Nanoparticles in Microelectrode Gaps by Dielectrophoresis. *Langmuir*, 20(26):11797–11801, 12 2004.
- [144] Carl V Brown, Glen McHale, and Christophe L Trabi. Dielectrophoresis-Driven Spreading of Immersed Liquid Droplets. *Langmuir*, 31(3):1011–1016, 1 2015.
- [145] H Pellat and C. R. Seances. 119, 675. *Seances, Acad. Sci., Paris*, 1894.
- [146] Thomas B. Jones, Michael P. Perry, and James R. Melcher. Dielectric Siphons. *Science*, 174(4015):1232–1233, 12 1971.
- [147] Jitesh Barman, Wan Shao, Biao Tang, Dong Yuan, Jan Groenewold, and Guofu Zhou. Wettability Manipulation by Interface-Localized Liquid Dielectrophoresis: Fundamentals and Applications. *Micromachines*, 10(5):329, 5 2019.
- [148] T. B. Jones, M. Gunji, M. Washizu, and M. J. Feldman. Dielectrophoretic liquid actuation and nanodroplet formation. *Journal of Applied Physics*, 89(2):1441–1448, 1 2001.
- [149] A.M.J. Edwards, C.V. Brown, M.I. Newton, and G. McHale. Dielectrowetting: The past, present and future. *Current Opinion in Colloid & Interface Science*, 36:28–36, 7 2018.
- [150] C. V. Brown, G. G. Wells, M. I. Newton, and G. McHale. Voltage-programmable liquid optical interface. *Nature Photonics*, 3(7):403–405, 7 2009.
- [151] G. McHale, C. V. Brown, M. I. Newton, G. G. Wells, and N. Sampara. Dielectrowetting Driven Spreading of Droplets. *Physical Review Letters*, 107(18):186101, 10 2011.

- [152] M A Quetzeri-Santiago, J R Castrejón-Pita, and A A Castrejón-Pita. Controlling droplet splashing and bouncing by dielectrowetting. *Scientific Reports*, 11(1):21410, 2021.
- [153] F. F. Reuss. Sur un Nouvel Effet de l’électricité Galvanique. *Mem. Soc. Imp. Natur. Moscou*, 2:327–337, 1809.
- [154] R J Fritsch and I Krause. ELECTROPHORESIS. In Benjamin Caballero, editor, *Encyclopedia of Food Sciences and Nutrition (Second Edition)*, pages 2055–2062. Academic Press, Oxford, 2003.
- [155] M. von Smoluchowski. Contribution à la théorie de l’endosmose électrique et de quelques phénomènes corrélatifs. *Bull. Int. Acad. Sci. Cracovie*, 184, 1903.
- [156] Makio Naito, Toyokazu Yokoyama, Kouhei Hosokawa, and Nogi Kiyoshi. Chapter 3 - Characteristics and Behavior of Nanoparticles and Its Dispersion Systems. In Makio Naito, Toyokazu Yokoyama, Kouhei Hosokawa, and Kiyoshi Nogi, editors, *Nanoparticle Technology Handbook (Third Edition)*, pages 119–120. Elsevier, 2018.
- [157] Gabriel Lippmann. Relations entre les phénomènes électriques et capillaires. *Ann. Chim. Phys*, 5(11):494–549, 1875.
- [158] Fritz Scholz. *Electroanalytical Methods: Guide to Experiments and Applications*. Springer, 1 2002.
- [159] Frieder Mugele and Jean-Christophe Baret. Electrowetting: from basics to applications. *Journal of Physics: Condensed Matter*, 17(28):R705–R774, 7 2005.
- [160] B Berge. Electrocapillarité et mouillage de films isolants par l’eau. *C. R. Acad. Sci.*, 317(157), 1993.
- [161] Yong Hyub Won, Junoh Kim, Cheoljoong Kim, Junsik Lee, Doseub Shin, Gyohyun Koo, and Jee Hoon Sim. Autostereoscopic three-dimensional displays based on electrowetting liquid lenses. *Optical Engineering*, 57(6):061618, 5 2018.

- [162] William M Abbott, Christopher P Murray, Sorcha Ní Lochlainn, Frank Bello, Chuan Zhong, Christopher Smith, Eoin K McCarthy, Clive Downing, Dermot Daly, Amanda K Petford-Long, Cormac McGuinness, Igor Igorovich Chudin, John F Donegan, and David McCloskey. Comparison of Metal Adhesion Layers for Au Films in Thermo-plasmonic Applications. *ACS Applied Materials & Interfaces*, 12(11):13503–13509, 3 2020.
- [163] Alexandre Rothen. The Ellipsometer, an Apparatus to Measure Thicknesses of Thin Surface Films. *Review of Scientific Instruments*, 16(2):26–30, 12 2004.
- [164] Royal Society of Chemistry. www.rsc.org/periodic-table/element/49/indium.
- [165] G. McHale, C. V. Brown, and N. Sampara. Voltage-induced spreading and super-spreading of liquids. *Nature Communications*, 4(1):1605, 6 2013.
- [166] Andrew M. J. Edwards, Rodrigo Ledesma-Aguilar, Michael I. Newton, Carl V. Brown, and Glen McHale. Not spreading in reverse: The dewetting of a liquid film into a single drop. *Science Advances*, 2(9), 9 2016.
- [167] Andrew M.J. Edwards, Rodrigo Ledesma-Aguilar, Michael I. Newton, Carl V. Brown, and Glen McHale. Electrostatic control of dewetting dynamics. *Applied Physics Letters*, 116(25), 6 2020.
- [168] Edward M Purcell and David J Morin. Electric fields around conductors. In *Electricity and Magnetism*, pages 150–152. Cambridge University Press, 1 2013.
- [169] J. F. Joanny and P. G. de Gennes. A model for contact angle hysteresis. *The Journal of Chemical Physics*, 81(1):552–562, 7 1984.
- [170] S. K. Kwok, K. F. Tsang, and Y. L. Chow. A novel capacitance formula of the microstrip line using synthetic asymptote. *Microwave and Optical Technology Letters*, 36(5):327–330, 3 2003.
- [171] Mirko Barbuto, Andrea Alù, Filiberto Bilotti, Alessandro Toscano, and Lucio Vegni. Characteristic impedance of a microstrip line with a dielectric overlay. *COMPEL: The*

- International Journal for Computation and Mathematics in Electrical and Electronic Engineering*, 32(6):1855–1867, 11 2013.
- [172] É Ruiz-Gutiérrez, P J Baker, A M J Edwards, M I Newton, I C Sage, R Ledesma-Aguilar, G McHale, and C V Brown. Dielectrowetting on curved surfaces. *Applied Physics Letters*, 120(19):191601, 5 2022.
- [173] Peter J Mohr, Barry N Taylor, and David B Newell. CODATA recommended values of the fundamental physical constants: 2006a). *Journal of Physical and Chemical Reference Data*, 37(3):1187–1284, 7 2008.
- [174] A C Russell, W L Hsieh, K C Chen, and J Heikenfeld. Experimental and numerical insights into isotropic spreading and deterministic dewetting of dielectrowetted films. *Langmuir*, 31(1):637–642, 2015.
- [175] Bastian E Rapp. Chapter 23 - Plateau-Rayleigh Instability. In Bastian E Rapp, editor, *Microfluidics: Modelling, Mechanics and Mathematics*, pages 467–477. Elsevier, Oxford, 2017.
- [176] S Castonguay, Y Temiz, E Delamarche, and T Gervais. Reverse Washburn dynamics induces flow acceleration during capillary filling. *Physics of Fluids*, 35(11):112107, 11 2023.
- [177] Yun-Wei Lu, Chieh Sun, Ying-Chuan Kao, Chia-Ling Hung, and Jia-Yang Juang. Dielectrophoretic Crossover Frequency of Single Particles: Quantifying the Effect of Surface Functional Groups and Electrohydrodynamic Flow Drag Force. *Nanomaterials*, 10(7), 2020.
- [178] In Soo Park, Se Hee Park, Dae Sung Yoon, Sang Woo Lee, and Beop-Min Kim. Direct measurement of the dielectrophoresis forces acting on micro-objects using optical tweezers and a simple microfluidic chip. *Applied Physics Letters*, 105(10):103701, 9 2014.
- [179] Antonio Ramos, Hywel Morgan, Nicolas G Green, and Antonio Castellanos. AC

- Electric-Field-Induced Fluid Flow in Microelectrodes. *Journal of Colloid and Interface Science*, 217(2):420–422, 1999.
- [180] Mohammad Ataei, Huanchen Chen, Tian Tang, and Alidad Amirfazli. Stability of a liquid bridge between nonparallel hydrophilic surfaces. *Journal of colloid and interface science*, 492:207–217, 2017.
- [181] Discover Digital Photography. www.discoverdigitalphotography.com/2015/lens-problems-field-curvature/, 2015.
- [182] Nanoscience Instruments. www.nanoscience.com/products/attension-tensiometers/optical-tensiometers/picoliter-dispenser/, 2023.
- [183] Chong Shen Ng, Kai Leong Chong, Rui Yang, Mogeng Li, Roberto Verzicco, and Detlef Lohse. Growth of respiratory droplets in cold and humid air. *Physical Review Fluids*, 6(5):54303, 5 2021.
- [184] Zexin Cai, Faze Chen, Yanling Tian, Dawei Zhang, Zhongxu Lian, and Moyuan Cao. Programmable droplet transport on multi-bioinspired slippery surface with tridirectionally anisotropic wettability. *Chemical Engineering Journal*, 449:137831, 2022.
- [185] Gaby Launay, Muhammad Subkhi Sadullah, Glen McHale, Rodrigo Ledesma-Aguilar, Halim Kusumaatmaja, and Gary G Wells. Self-propelled droplet transport on shaped-liquid surfaces. *Scientific Reports*, 10(1):14987, 2020.
- [186] Finn Box, Chris Thorogood, and Jian Hui Guan. Guided droplet transport on synthetic slippery surfaces inspired by a pitcher plant. *Journal of The Royal Society Interface*, 16(158):20190323, 9 2019.
- [187] Kai Zhuang, Yao Lu, Xiaolei Wang, and Xiaolong Yang. Architecture-Driven Fast Droplet Transport without Mass Loss. *Langmuir*, 37(43):12519–12528, 11 2021.
- [188] M Pollack, Alexander Shenderov, and Richard Fair. Electrowetting-based actuation of droplets for integrated microfluidics. *Lab on a Chip*, 2:96–101, 6 2002.

- [189] W Wang and T B Jones. Microfluidic actuation of insulating liquid droplets in a parallel-plate device. *Journal of Physics: Conference Series*, 301:012057, 6 2011.
- [190] A M Lacasta, I M Sokolov, J M Sancho, and F Sagués. Competitive evaporation in arrays of droplets. *Physical Review E*, 57(5):6198–6201, 5 1998.